Superfluid Transition, Topological Vortices, and Magneto-hydrodynamic Simulations for Relativistic Heavy-ion Collisions

By

Shreyansh Shankar Dave

PHYS07201204003

Institute of Physics, Bhubaneswar

A thesis submitted to the

Board of Studies in Physical Sciences

In partial fulfillment of requirements

For the Degree of

DOCTOR OF PHILOSOPHY

of

HOMI BHABHA NATIONAL INSTITUTE

July, 2018

Homi Bhabha National Institute

Recommendations of the Viva Voce Committee

As members of the Viva Voce Committee, we certify that we have read the dissertation prepared by Mr. Shreyansh Shankar Dave entitled "Superfluid Transition, Topological Vortices, and Magneto-hydrodynamic Simulations for Relativistic Heavy-ion Collisions", and recommend that it may be accepted as fulfilling the dissertation requirement for the Degree of Doctor of Philosophy.

Am Jayannavar 4/1/19

Chairman - Prof. Arun M. Jayannavar Date:

Ajit M. Srivastava 4-1-19

Guide /Convener - Prof. Ajit M. Srivastava Date:

Co-guide (if any) Date:

V. Ravi 4.1.19.

Examiner - Prof. V. Ravishankar Date:

4-1-19

Member 1 - Prof. Pankaj Agrawal Date:

Subhasish Basak 4/1/19.

Member 2 - Prof. Subhasish Basak (NISER) Date:

Final approval and acceptance of this thesis is contingent upon the candidate's submission of the final copies of the dissertation to HBNI.

I/We hereby certify that I/we have read this thesis prepared under my/our direction and recommend that it may be accepted as fulfilling the thesis requirement.

Date: 4-1-19

Place: IOP, Bhubaneswar

Ajit M. Srivastava

Co-guide (if applicable) **Guide**

STATEMENT BY AUTHOR

This dissertation has been submitted in partial fulfillment of requirements for an advanced degree at Homi Bhabha National Institute (HBNI) and is deposited in the Library to be made available to borrowers under rules of the HBNI.

Brief quotations from this dissertation are allowable without special permission, provided that accurate acknowledgement of source is made. Requests for permission for extended quotation from or reproduction of this manuscript in whole or in part may be granted by the Competent Authority of HBNI when in his or her judgment the proposed use of the material is in the interests of scholarship. In all other instances, however, permission must be obtained from the author.

Shreyansh Shankar Dave

DECLARATION

I, Shreyansh Shankar Dave, hereby declare that the investigations presented in the thesis have been carried out by me. The matter embodied in the thesis is original and has not been submitted earlier as a whole or in part for a degree/diploma at this or any other Institution/University.

Shreyansh Shankar Dave

List of Publications arising from the thesis

Published/Accepted for publication/Preprint

a) *Towards Laboratory detection of topological vortices in Superfluid Phases of QCD*, Arpan Das, **Shreyansh S. Dave**, Somnath De, and Ajit M. Srivastava, Mod. Phys. Lett. A **32**, 1750170 (2017), arXiv: 1607.00480.

b) *Effects of magnetic field on the plasma evolution in relativistic heavy-ion collisions*, Arpan Das, **Shreyansh S. Dave**, P. S. Saumia, Ajit M. Srivastava, Phys. Rev. C **96**, 034902 (2017), arXiv: 1703.08162.

c) *Formation of topological vortices during superfluid transition in a rotating vessel*, **Shreyansh S. Dave**, Ajit M. Srivastava, arXiv: 1805.09377 (Submitted to Phys. Rev. B).

2. Conference/Workshop

a) Talk given on *Probing Color Superconducting Phases and Neutron Superfluidity via Hydrodynamic evolution at FAIR and NICA*, in the Conference, 6^{th} **Asian Triangular Heavy Ion Conference, ATHIC-2016**, 15- 19 February 2016, at India International Center, New Delhi, India.

b) Talk given on *Effects of magnetic field on plasma evolution in relativistic heavy-ion collisions*, in the Conference, 15^{th} **International Conference on QCD in Extreme Conditions (XQCD 2017)**, 26-28 June 2017, at University of Pisa, Italy.

c) Talk given on *Probing Superfluid Phases of QCD in Heavy Ion Collision Experiment*, in Workshop on **High Energy Physics Phenomenology (WHEPP) XV-2017, Group IV**, 14-23 December 2017, at IISER Bhopal, India.

d) Talk given on *Formation of skyrmions (baryons) and superfluid vortices during phase transitions in presence of external field*, in **CNT Workshop on Effective Field Theory of Hadrons: Vacuum to Medium**, 12-17 March 2018, VECC, Kolkata, India.

Shreyansh Shankar Dave

In the memory of my father,

Shri Anand Shankar Dave

Acknowledgement

It is a great opportunity for me to acknowledge people who played a very important role in the completion of this work. Firstly, I would like to thank my parents for their enormous supports and help at every stages of my academic carrier. I am highly obliged for their dedication and sacrifices for my study. At this moment, I am missing my father. He always encouraged me for doing study and gave me very important suggestions and mental supports on many occasions whenever I needed. I also want to thank my other family members for their help and supports.

The most important person for completion of a Ph.D always be the supervisor. Without his/her guidance it is impossible to finish Ph.D work. I learned lot of things from my supervisor Prof. Ajit M. Srivastava. His physics understanding, amazing intuition, so much excitement in physics, and interest in other subjects, always encouraged me to understand the thing properly, and to learn other subjects also. For a student, it is very important to have a development of correct scientific attitude, which I guess, I never be able to gain by any other person. Not only physics, I also learned many other things related with the social issues by him - equality in human being irrespective of religion, cast, poverty, and sex is one of them.

I would like to thank my collaborators Srikumar Sengupta, P.S. Saumia, Partha Bagchi, Somnath De, Oindrila Ganguly, Arpan Das for fruitful physics discussions. It is always a pleasure to work with them. I want to give my special thank to P.S. Saumia, Abhishek Atreya and Minati Biswal for wonderful physics discussion, their help, supports and encouragement for my research work and this thesis. Their nice behavior always make me free to discuss on academic as well as on non-academic issues with them.

I also want to thank my other close friends Jim Chacko, Trilochan Bagarti and Bharat Kumar. These people always helped me whenever I needed. I am lucky that I got such a great seniors like Jim da and Trilocha da. Their various suggestions were very useful for me in my entire reasearch work. After dinner various personal conversations with Bharat was helpful to express my emotions in front of at least someone in IoP. I thank him for being such a nice friend with me.

I would like to thank my predoc batch-mates, specially Priyo Shankar Paul and

Puspendu Guha for their helps at various stages. I also like to thank Vanraj da, Pramita di, Indrani di, and Shalik da for nice conversations on various topics during tea sessions. I also want to thank my M.Sc. friends T. Sonamani and M. Apparao (BHU). Their help and encouragement during my M.Sc. time made me able to reach at this Institute and pursue my research carrier.

I would like to thank all the faculty members of IoP for great teaching during my predoc course. I specially enjoyed the course of Prof. Somen Bhattacharjee, Prof. Arun M. Jayannavar, Prof. Sudipta Mukharji, and Prof. Ajit M. Srivastava. I also want to mention that I always get irritated with the course of computational physics from my M.Sc. days. But I think this was the only course, taught by Prof. Shikha Verma in my predoc course, which I used mostly in my research work. Her calm and relaxed stile of teaching helped me to learn such a useful subject without in much hurry. I also thank Shikha madam for saving me many times whenever my supervisor wanted to pull my leg during the tea session in the canteen.

I am also thankful to SERC school organization committee for giving me the opportunity to attend preparatory school and main schools on high energy physics. SERC schools give a fantastic platform to learn basic as well as advance topics in high energy physics.

I would like to express my gratitude to IoP and HBNI for their financial support to attend conferences within and outside India. My humble regard to all the staff members of the library and the computer section who have maintained the excellent facilities at IoP. My thanks goes to all the administrative and non-academic staffs for their support, cooperation and help at every stages.

I would like to thank Prof. Sudhakar Panda, Director of this institute, for providing me the financial support for eight months from his J.C. Bose fellowship.

The campus of IoP is very beautiful and I will miss it wherever I go. For maintaining such a beautiful campus, I would like to thank gardeners of the institute.

Shreyansh Shankar Dave

Contents

Synopsis

The *spontaneous symmetry breaking (SSB) phase transitions* and the *hydrodynamic equations* are some of the most important tools of *statistical physics* which are extensively used, irrespective of the energy scale of the system, from condensed matter physics to the high energy physics. In the condensed matter physics, ferromagnetism, superfluidity, superconductivity, etc., correspond to spontaneous symmetry broken phases. In the high energy physics also the whole evolution of the Universe is affected by such kind of phase transitions. The GUT phase transition, at the energy scale of 10^{15} GeV, and the *electroweak* phase transition, at the energy of about 100 GeV are the examples of SSB phase transition in the early Universe. The confining transition, from quark-gluon plasma (QGP) phase of QCD to the hadronic phase, is a cross-over transition. All these transitions lead to interesting stages during the evolution of the Universe. Similarly, hydrodynamics is also used in almost every branch of physics. The description of the flow of water, and evolution of the cosmic plasma during early stages of the Universe, both are governed by hydrodynamics equations, although former is a non-relativistic system while latter is a relativistic system, and equation of state for both the systems are quite different. In this thesis we discuss SSB phase transition of the superfluid systems, and hydrodynamics & magneto-hydrodynamics evolution of QCD matter in relativistic heavy-ion collision experiments.

The concepts of topology are also very extensively used in many branches of physics. There are many physical situations where topology plays a very important role, e.g., Aharonov-Bohm effect, topological phase transitions, QCD instanton processes, Skyrmion picture of baryons in linear sigma model, Berry phase, superfluid vortices, flux tubes in superconductor, and cosmic strings, domain walls, monopoles in the early Universe etc.. In this thesis we are interested in *topological defects*, mainly in the formation of *topological vortices* during superfluid transition. We study the formation of vortices in the ^4He system, and QCD matter at high baryon density.

There are many ways by which a topological defect can form. In this thesis we are interested in the formation of the topological defects during the SSB phase transitions. If the order parameter space of a system is topologically non-trivial, then topological defects can exist in the physical space [1], and a symmetry breaking phase transition can lead to the formation of *topological defects*. The formation of these defects during a phase transition is described by the *Kibble mechanism* which has been tested experimentally [2]. In the case of superfluid transitions this lead to the formation of topological vortices. These vortices have important implications in the condensed matter as well for neutron star physics. The most important property of superfluid vortices, which makes these defects different from the topological defects in other systems, is the rotation of superfluid components about these vortices. This property of rotation arises due to the quantum nature of superfluidity and due to the non-trivial order parameter field configuration about the superfluid vortex. Therefore these vortices carry (quantized) angular momentum and are protected by topology. The appearance of superfluid vortices in the superfluid phase makes this phase qualitatively distinct from the normal fluid.

The search of the *quark-gluon plasma* and its possible probes in the relativistic heavy-ion collisions is one of the exciting area of research. Although the zero chemical potential quark-gluon plasma phase is of interest for the early Universe, quark-gluon plasma at finite chemical potential contains very rich physics and is of tremendous interest for the physics of neutron star. There are several exiting phases of Quantum Chromodynamics (QCD) possible in this regime of high baryon density at sufficiently low temperatures. The physics of BCS theory is directly applicable in this regime and formation of Cooper pairs, both, in the confined phase and deconfined phase lead to the emergence of superfluidity and superconductivity in the QCD matter. These phases play a very important role in the dynamics, like glitches, and cooling process of neutron star.

In the low energy heavy-ion collisions if any superfluid phase of QCD arises, via spontaneous symmetry breaking phase transitions, then it affects the hydrodynamics evolution of the system due to the formation of topological vortices [3]. In such an energy regime there is a strong possibility that, in the case of non-central collisions, the formed medium may get rotation due to surface tension. Therefore in such situation the superfluid phase transition will occur in the presence of a rotation. This is a similar situation as occurs in the case of neutron star superfluid transition, as in that case also neutron superfluid transition occurs in the presence of rotation of the star. In the condensed matter system, such as ^4He, superfluid transitions in the presence of rotation is routinely studied experimentally. The formation of these vortices during the phase transition is governed by the Kibble Mechanism. The Kibble mechanism predicts the equal formation probabilities of defects and anti-defects [2]. But the above phase transitions, in the presence of rotation, requires a biasing in the formation of vortices over anti-vortices or vise-versa. In this thesis, we address this issue for superfluid ^4He transition by modifying the Kibble mechanism in the presence of such external influence so that it can account for the required biases, see Ref. [4]. As discuss above, this has important applications for the case of neutron star and heavy-ion collision physics. Note that there are other situations where such kind of modification in the Kibble mechanism is required, for example, formation of flux-tubes during the superconducting transition in the presence of magnetic field, and formation of baryons (Skyrmions) at finite chemical potential during chiral transition in linear-sigma model, requires more number of one kind of topological object than other one (note that the baryon production is restricted by the baryon number conservation, see Ref. [5]). All these issues can be handled by modifying the main ingredients of the Kibble mechanism which are the *domain structure* and the *geodesic rule*. In this thesis, we propose such kind of modification for the case of superfluid transition in the presence of a rotation which lead to the biasing in the formation of topological vortices [4]. If such a modification of the domain structure and geodesic rule is confirmed in the experiments then one can extend such approach to the other systems also.

The spontaneous symmetry breaking occurs when the ground state of the theory does not follow the full symmetry of the Lagrangian or Hamiltonian. To discuss the finite temperature phase transition of a system in the high energy physics, we use the effective potential of the system at the finite temperature, and the free energy density in the condensed matter. A phase transition leads to the formation of correlation domains in the physical space. The Kibble mechanism utilizes a picture of domain formation during the phase transition and describe how the topological defects form during the SSB phase transition [2]. *Topological defects* are the locations in the physical space where the order parameter field becomes singular (ill defined) [1]. This singularity is topologically protected and can not be removed by local deformation of the order parameter field configuration. The order parameter configuration corresponds to the mapping from the physical space to the order parameter space which forms shrinkable/non-shrinkable loops. There can be many different kind of mappings from the physical space to the order parameter space which are distinguished by the winding number (for superfluid ^4He case) and are characterized by the homotopy classes of the loops. These homotopy mappings form a group structure under the combination law of homotopy classes, which is known as the *fundamental group*. If this fundamental group is non-trivial for an order parameter space of the system, i.e. if it is not isomorphic to the trivial group (consisting of only the identity element), then this ensures that in the physical space topological vortices or line defects will exist [1].

The main physics of the Kibble mechanism lies in the formation of a domain structure, where all domains are considered to be independent and have random order parameter values, while in each domain order parameter field is considered to be uniform (with small fluctuations). The second, very important consideration of the Kibble mechanism is the way the order parameter field interpolates in between two successive domains. The order parameter field interpolates in between two successive domains such that it traverses the shortest path on the order parameter space, usually known as the *geodesic rule* [2]. Both these ingredients of the Kibble mechanism, the uniform domain structure and the geodesic rule, are based on the free energy minimization of the system and therefore considered to be naturally valid assumptions. For $U(1)$ SSB phase transitions, the Kibble mechanism predicts the probability of formation of topological vortices in the two space dimension to be $1/4$ per domain if three domains meet at a point, while $\sim 1/3$ per domain if four domains meet at a point. The formation probabilities of both defects and anti-defects on an average are equal in this mechanism.

In this thesis we are interested in the formation of superfluid vortices during the superfluid transitions. Superfluidity arises when a bulk of bosonic gas or Cooper pairs near the Fermi surface, undergoes Bose-Einstein condensation. The bosons in the condensate (superfluid components) flow in space without loosing their energy and momentum. The superfluid component is described by the multi-particle wave function. The quantum probability current for this wave function ultimately gives a macroscopic motion to the superfluid with a curl free velocity profile. This special property of the superfluid, which arises due to its quantum nature, makes its motion highly restrictive and does not allow any rotation below a critical angular velocity of the vessel. Above the critical velocity, superfluid start rotating by following a curl free velocity profile given by, $\vec{v} = \frac{1}{r}\hat{\theta}$, in region away from the center of vessel. All these facts can be explained by the energy minimization of the system, see Ref. [6]. This is the nucleation of a vortex at the center of the vessel. When one increases the angular velocity of the vessel further, more number of vortices start nucleating and form a (rotating) vortex-lattice. This method of generation of the superfluid vortices is completely different from the Kibble mechanics. In the former case, vortices arises when the system is already in the superfluid phase while in the Kibble mechanism, vortices arise during the normal to superfluid transition. In this thesis, we address the issue that how superfluid vortices will form if the superfluid transition occurs in the presence of a rotation. The rotation of the vessel will lead to the formation of more number of vortices than anti-vortices. The standard Kibble mechanism can not capture this feature, it predicts the formation of defects and anti-defects with equal probabilities.

In this thesis, we have proposed a modification of the Kibble mechanism which accounts for such biases in the formation of topological vortices. For this, we considered that, during the transition from normal to superfluid, the momentum carried by the normal fluid component gets transferred to the superfluid such that the curl free property of the superfluid remains satisfied in a given domain, and angular momentum of the whole system remain conserved. This induces a systematic order parameter variation inside each domain. We have taken the variation of the order parameter inside each domain such that the free energy of the system is minimized. The free energy density for superfluid transition in the presence of a rotation is given by, see Ref. [4],

$$f' = \alpha|\Psi|^2 + \frac{\beta}{2}|\Psi|^4 + \frac{\hbar^2}{2m}\Psi_0^2|\vec{\nabla}\theta|^2 - \Omega\rho_s r\frac{\hbar}{m}|\vec{\nabla}\theta|, \tag{0.1}$$

where α and β are phenomenological coefficients, m is the mass of ^4He atom, Ω is the angular velocity of the vessel, and ρ_s is the superfluid mass density. $\Psi = \Psi_0 e^{i\theta}$ is the wave function of superfluid condensate. For temperatures less than the superfluid transition temperature, $\alpha < 0$ and we determine the local value of condensate density Ψ_0 by minimizing the free energy neglecting the rotation. With constant superfluid density Ψ_0, we minimize this free energy density with respect to $|\vec{\nabla}\theta|$ and get,

$$|\vec{\nabla}\theta|_{bias} = \frac{m\Omega r}{\hbar}. \tag{0.2}$$

This shows that the equilibrium configuration of Ψ requires a non-zero value of $|\vec{\nabla}\theta|$ in the presence of rotation. (Note, for the non-rotating case, we get θ = constant, as is assumed inside a domain in the conventional Kibble mechanism.) Note that $|\vec{\nabla}\theta|_{bias}$ is proportional to the distance from the origin. Therefore larger r domains will have more variation of order parameter than the lower one. Eventually, this gives the biasing in the formation of the vortices over anti-vortices. We also see, again by minimization of the free energy, that geodesic rule also gets modified. Even if we have larger path variation on the order parameter space to connect two successive domains, such variation may be allowed supporting the formation of vortices over anti-vortices. With all these features, we performed the simulation in two dimension and got a systematic bias in the formation of vortices over anti-vortices with the increasing angular velocity of the vessel. We also see that the correlation in the formation of vortices and anti-vortices get suppressed with the angular velocity. The probabilities of the formation of vortices and anti-vortices also increase, but differently, with the angular velocity of the vessel, see Ref. [4].

To summarize this part of the thesis, we have proposed a modification in the conventional Kibble mechanism for the situation of production of topological defects when physical situation requires excess of winding of one sign over the opposite ones. We have considered the case of formation of vortices for superfluid ^4He system when the transition is carried out in a rotating vessel. As our results show, this biased formation of defects can strongly affect the estimates of net defect density. Also, these studies may be crucial in discussing the predictions relating to defect-anti-defect correlations. The modified Kibble mechanism we presented here has very specific predictions about net defect number which shows a clear pattern of larger fluctuations (about mean value governed by the net rotation) compared to the conventional Kibble prediction. This can be easily tested in experiments. Further, even the average net defect number deviates from the number obtained from energetics considerations, especially for low values of Ω. This implies that exactly at the time of transition, a different net defect number will be formed on the average, which will slowly evolve to a value obtained from energetic considerations, see Ref. [4].

In our other study in this thesis, we consider the possibility of the superfluid phases of QCD in heavy-ion collision experiments. QCD has mainly two superfluid phases, one is in the confined phase, which is the neutron superfluid for which we have performed UrQMD (Ultra-relativistic Quantum Molecular Dynamics) simulations to check whether such phase is possible in the low energy heavy-ion collision experiment. We get that temperature and the baryon density are very close to the neutron superfluid transition point and conclude that such superfluid phase may be possible if one collides neutron rich nuclei, such as $^{238}U_{92}$, at sufficiently low energy, $\sim 50A\ MeV$. The other superfluid phase of QCD lies in the deconfined phase which is known as the *color-flavor locked* (CFL) phase, see Ref. [7]. The symmetry breaking pattern from QGP to CFL phase is, $SU(3)_c \times SU(3)_L \times SU(3)_R \times U(1)_B \rightarrow SU(3)_{c+L+R} \times \mathcal{Z}_2$. This symmetry breaking arises due to the formation and Bose-Einstein condensation of the quark-quark Cooper pairs near the Fermi surface. The quark-quark anti-symmetric color combination have attractive interaction and therefore only this combination of the quarks can form the Cooper pairs and condense near the Fermi surface. Therefore ground state of this phase becomes colored thereby breaking color gauge symmetry of the QCD Lagrangian. These pairs also break chiral symmetry of the theory, but in different ways from quark-antiquark pairs in the usual chiral transition. This phase is a superfluid phase because quark-quark pairs also break $U(1)_B$ global symmetry to $\mathcal{Z}_2$. This symmetry breaking makes the order parameter space of this system topologically non-trivial and thus, in this phase topological vortices can exist. This phase is supposed to occur at very high chemical potential regime, about 1500 MeV baryon chemical potential (500 MeV quark chemical so that with respect to this, masses of all three quarks u, d, and s can be neglected) and at temperature lower than about 50 MeV. Though there is not much hope that such a phase can arise in heavy-ion collisions, in our work, we consider the possibility of both the superfluid phases of QCD in heavy-ion collision experiments. The method for the detection of these phases which we propose, in this thesis, is universal for both the phase, i.e., appearance of the superfluid vortices when the superfluid medium forms. This generates a local rotation in the medium which affects the hydrodynamic evolution at least at the initial stages and may be detected in the experiment by its effect on the flow pattern [3].

The energy momentum conservation for the ideal hydrodynamics is given by,

$$\partial_\mu T^{\mu\nu} = 0; \quad T^{\mu\nu} = (\rho + p)u^\mu u^\nu - p\eta^{\mu\nu}, \tag{0.3}$$

where ρ and p are the energy density and pressure of the fluid which are related by the equation of state of the fluid, we assume the ideal gas equation of state $\rho = 3p$, u^μ is the 4-velocity of the fluid and $\eta^{\mu\nu}$ is the Minkowski tensor, which here we have taken $\eta^{\mu\nu} = \text{diag}(1, -1, -1, -1)$. For the hydrodynamic evolution of the fluid, we need initial energy density profile, which in this work we have considered to be a woods-saxon distribution. To account for the fluctuations, we put few Gaussian of small width on the top of this woods-saxon distribution. We have taken, in the superfluid phase, the initial velocity profile of a superfluid vortex or vortices. To account for the linear momentum conservation, when superfluid vortices form, normal components also start rotating about the vortex in the opposite direction, this leads to the generation of a strong elliptic flow (a hydrodynamic quantity which characterizes the momentum anisotropy of the fluid evolution) see Ref. [3]. Using hydrodynamic simulations, we show that vortices can qualitatively affect the power spectrum of flow fluctuations, e.g. elliptic flow. Even if the plasma region in the transverse plane is isotropic, a strong elliptic flow can be generated due to formation of superfluid vortices. We also see that in the presence of pair of vortices, the power spectrum of flow can show differences in the power of even and odd flow coefficients. In the case of non-central collisions we have negative value of elliptic flow, arising due to specific configuration of vortex pairs. This can give unambiguous signal for superfluid transition resulting in vortices, allowing for check of defect formation theories in a relativistic quantum field theory system, and the detection of superfluid phases of QCD. Detection of nucleonic superfluid vortices in low energy heavy-ion collisions will give opportunity for laboratory controlled study of their properties, providing crucial inputs for the physics of pulsars. We also study the possibility of formation of neutron superfluidity in the low energy heavy-ion collisions. We see that it is a good possibility to have neutron superfluidity in the this experiment at the sufficiently low energy collisions of neutron rich nuclei. The detection of these in laboratory experiments will strengthen our understanding of pulsar dynamics. The signals we have discussed show qualitatively new features in flow anisotropies signaling the presence of vortices and the underlying superfluid phase in the evolving plasma. These qualitative features are expected to be almost model independent, solely arising from the vortex velocity fields.

One of the most important probes of the medium formation in the heavy-ion collisions is the *elliptic flow* which characterizes the momentum anisotropy of the medium evolution. By fitting the elliptic flow from the experiment data in the *viscous hydrodynamics* simulations, one is able to extract out the viscosity of the quark-gluon plasma. The determination of the viscosity depends upon the various parameters of the simulation, e.g. initial energy density, thermalization time, equation of state, etc. In heavy-ion collisions due to the opposite motion of nuclei, magnetic field also get generated. Its survival until the formation of the thermal medium and its effects on the medium dynamics is an exciting area of research. In this thesis, by performing the magneto-hydrodynamics simulations, we show that the magnetic field can affect the fluid dynamics in heavy-ion collisions. In particular, it changes the elliptic flow depending upon the impact parameter of the collisions. We also study other possible effects of magnetic field on the fluid dynamics and back effect of dynamics of fluid on the magnetic field evolution, see Ref. [8].

In this work we have generated the initial energy density profile by using the *Glauber model*. We use *optical Glauber model* for smooth profile and *Glauber Monte Carlo* for energy density profile with fluctuations. We have generated the initial magnetic field, by doing the Lorentz transformation for velocities of nuclei along $\pm z$-axis, on the rest frame electric field of a uniformly charged nuclei. We have calculated the magnetic field at the thermalization time and assumed that it gets trapped in the fluid due to medium conductivity. The conservation of total energy momentum tensor (for QGP as well as the magnetic field) is given by [8],

$$\partial_\alpha T^{\alpha\beta} = 0; \quad T^{\alpha\beta} = (\rho + p_g + |b|^2)u^\alpha u^\beta - b^\alpha b^\beta + (p_g + \frac{|b|^2}{2})\eta^{\alpha\beta}, \tag{0.4}$$

where ρ and p_g are the energy density and pressure of the fluid which are related by the equation state of the fluid, we assume the ideal gas equation of state $\rho = 3p$, u^α is the 4-velocity of the fluid and $\eta^{\alpha\beta}$ is the Minkowski tensor, which here we have taken

$\eta^{\alpha\beta} = \text{diag}(-1,1,1,1)$. The Maxwell's equations are,

$$\partial_\alpha(u^\alpha b^\beta - b^\alpha u^\beta) = 0. \tag{0.5}$$

Here the 4-vector b^α is related to the magnetic field $\vec{B}$ and fluid velocity by, $b^\alpha = \gamma[\vec{v}.\vec{B}, \frac{\vec{B}}{\gamma^2} + \vec{v}(\vec{v}.\vec{B})]$, where γ is the Lorentz factor for velocity $\vec{v}$ and we have $|b|^2 \equiv b^\alpha b_\alpha = \frac{|\vec{B}|^2}{\gamma^2} + (\vec{v}.\vec{B})^2$. In this work, we carry out relativistic magnetohydrodynamics (RMHD) simulations to study the effects of this magnetic field on the evolution of the plasma using above equations and study resulting flow fluctuations in the ideal RMHD limit. We have demonstrated qualitatively new effects on the flow pattern of QGP in the presence of initial magnetic field. These qualitative patterns may be able to provide clear signal for the presence of strong magnetic field during early stages of the evolution, though actual value of magnetic field etc. will depend on more reliable numerical estimates of the numbers. Our results show that magnetic field leads to enhancement in elliptic flow for small impact parameters while it suppresses the elliptic flow for large impact parameters (which may provide a signal for initial stage magnetic field). This result on the enhancement of elliptic flow in the presence of magnetic field confirms earlier expectation in Refs. [4, 6]. At the same time our simulation also points out that the effects of magnetic field on elliptic flow are much more complex than envisaged in simple arguments of Ref. [4], as in some situations one finds decrease in the elliptic flow. This may resolve the discrepancy between the results of Refs. [4, 6] and Ref. [7] (see, also Refs. [19, 20]). The strong suppression of elliptic flow for large impact parameters can provide a signal for strong magnetic field at initial stages. Interestingly, we find that magnetic field in localized regions can temporarily increase in time as evolving plasma energy density fluctuations lead to reorganization of magnetic flux. This can have important effects on chiral magnetic effect. Magnetic field has non-trivial effects on the power spectrum of flow fluctuations. For very strong magnetic field case one sees a pattern of even-odd difference in the power spectrum of flow coefficients arising from reflection symmetry about the magnetic field direction if initial state fluctuations are not dominant. We discuss the situation of nontrivial magnetic field configurations arising from collision of deformed nuclei and show that it can lead to anomalous elliptic flow. Special (crossed body-body) configurations of deformed nuclei collision can lead to presence of quadrupolar magnetic field which can have very important effects on the rapidity dependence of transverse expansion (similar to *beam focusing* from quadrupole fields in accelerators), see Ref. [8].

The deformed nucleus collisions in relativistic heavy-ion collisions leads to even more interesting possibilities related with the shape anisotropy of the plasma in the transverse plane and the direction of magnetic field. The dependence of the elliptic flow on the impact parameter, in the body-body collisions (where impact parameter is along the semi-major axis of both the nuclei), with and without magnetic field, becomes dramatically different from the spherical nucleus collisions case [14].

We have performed RMHD simulations for the case of deformed nucleus-nucleus collisions for the case of Uranium nuclei. We have generated the initial energy density by Glauber model, and magnetic field profile (following Ref. [15]) appropriate for Uranium-Uranium collisions. We have performed the RMHD simulations for the body-body collisions. Due to deformation of the nuclei, even in the zero impact parameter case there is spatial anisotropy in the plasma such that the semi-major axis of the ellipse lies along the x-axis therefore we get negative elliptic flow; in this case there is no magnetic field present. When we increase the impact parameter by a small amount, magnetic field gets generated along the y-axis (semi-minor axis of the plasma), due to which, overall magnitude of the elliptic flow gets suppressed. When we increase the impact parameter further at a particular impact parameter, plasma region becomes isotropic in the transverse plane. For such case ideal hydrodynamics gives zero value of the elliptic flow, but due to presence of the magnetic field in the fluid in this case, we get non zero elliptic flow showing that magnetic field itself can generate momentum anisotropy in the plasma. When we increase impact parameter further, the situation becomes similar as in the case of the spherical nuclei collisions and we first get enhancement and then suppression in the elliptic flow [14].

Bibliography

[1] N.D. Mermin, Rev. Mod. Phys. **51**, 591 (1979).

[2] T.W.B. Kibble, J. Phys. A **9**, 1387 (1976); Phys. Rept. **67**, 183 (1980).

[3] A. Das, S.S. Dave, S. De, A.M. Srivastava, Mod. Phys. Lett. A **32**, 1750170 (2017).

[4] S.S. Dave and Ajit M. Srivastava, **arXiv:** 1805.09377.

[5] V.S. Kumar, B. Layek, A.M. Srivastava, S. Sanyal, and V.K. Tiwari, IJMP A **21**, 1199-1219 (2006).

[6] E.M. Lifshitz and L. P. Pitaevskiĭ, **Statistical Physics, Part 2, Theory of the Condensed State**, Pergamon Press (1980).

[7] M.G. Alford, A. Schmitt, K. Rajagopal, T. Schäfer, Rev. Mod. Phys. **80**, 1455 (2008).

[8] A. Das, S.S. Dave, P.S. Saumia, and A.M. Srivastava, Phys. Rev. C **96**, 034902 (2017).

[9] R. K. Mohapatra, P. S. Saumia, and A. M. Srivastava, Mod. Phys. Lett. A **26**, 2477 (2011).

[10] K. Tuchin, J. Phys. G **39**, 025010 (2012).

[11] G. Inghirami et al. arXiv: 1609.03042; Eur. Phys. J. C **76**, 659 (2016).

[12] L.G. Pang, G. Endrodi, and H. Petersen, Phys. Rev. C **93**, 044919 (2016).

[13] S. Pu and D.L. Yang, Phys. Rev. D **93**, 054042 (2016).

[14] S.S. Dave, talk on **Effects of magnetic field on plasma evolution in relativistic heavy-ion collisions** in the Conference, *The 15th International Conference on QCD in Extreme Conditions (XQCD-2017), 26-28 June 2017* at University of Pisa, Italy, on 27th June 2017.

[15] O.D. Kellogg, *Foundations of Potential Theory*, Springer-Verlag (1967).

List of Figures

List of Tables

Chapter 1

Introduction

Though the motivation of the development of quantum mechanics came from the particle nature of electromagnetic radiation (photon), there is no prescription available in quantum mechanics, by which one can quantize the electromagnetic field [1]. The formal description of particle creation and annihilation is also not available in quantum mechanics [1]. The quantum field theory takes care of all these issues in a very systematic way. In the quantum field theory, there are prescriptions by which field can be quantized which creates multi-particle states. There are loop diagrams, which arise due to quantum nature of the theory. Such loop processes generally have divergences. To take care of these divergences regularization and renormalization prescription are followed.

The effective potential of a theory incorporates all possible quantum corrections, arising from the interaction, on the top of the classical potential [2]. Due to the quantum corrections (loop diagrams), the classical potential can get modified qualitatively. The vacuum energy density and vacuum expectation value, both get modified due to such quantum corrections. The effective potential provides the actual ground state of the theory and its symmetries. Hence effective potential plays a very important role in the study of spontaneous symmetry breaking. The field configuration obtained by minimizing the effective potential, gives translation and Lorentz invariant vacuum state of the theory.

In spontaneous symmetry breaking, ground state of the theory does not follow the full symmetry of the Lagrangian. This phenomena happens only if ground state has some degeneracy, in which system chooses one particular ground state spontaneously. There are numerous examples where ground state only breaks part of the full symmetry group G of the Lagrangian and remains invariant under the subgroup H of the full symmetry group G. For example, in the case of para-magnetic to ferro-magnetic transition, magnetization density breaks $SO(3)$ symmetry of the theory, but remains invariant under $SO(2)$ transformations. Similarly, in the case of chiral transition of QCD, $\langle\bar{\psi}\psi\rangle$ chiral condensate breaks $SU(2)_V \otimes SU(2)_A$ symmetry of the theory to $SU(2)_V$ subgroup. In the electro-weak phase transition, $SU(2)_L \otimes U(1)_Y$ breaks to $U(1)_{e.m.}$. In superconducting transitions, Cooper pair condensate breaks $U(1)_{e.m.}$ gauge symmetry to $\mathcal{Z}_2$ symmetry. There are also systems where the symmetry group G is completely broken (to trivial group). The ^4He superfluid system is the simplest example where Bose condensation of helium atoms breaks $U(1)$ global symmetry completely.

The spontaneous symmetry breaking phase transition happens in the many-body system where statistical field theory or thermal field theory is used. The effective potential at finite temperature and/or finite density describes such kind of phase transition, and plays similar role in the field theoretical system as played by free energy density in the Ginzburg-Landau theory in a condensed matter system. The spontaneous symmetry breaking in general is not necessarily associated with a phase transitions and can happen even in non-equilibrium systems also. The quantum field theoretical systems at $T = 0$ and $\mu = 0$ usually allows such kind of possibility. In this thesis we will focus on the spontaneous symmetry breaking (SSB) for a thermal (many-body) system. This is known as the SSB phase transitions. The phase transitions in condensed matter systems is described by the Taylor's series expansion of free energy density in terms of the order parameter field. Writing free energy density in such a way captures phenomenological aspects of the phase transition dynamics. This is known as the Ginzburg-Landau theory of phase transitions. In high-energy physics effective potential at finite temperature or finite density is calculated from the first principle, which describes the symmetry breaking phase transition in the quantum field theoretical systems.

A system undergoes phase transition, when at a given value of state variable, e.g. at a particular temperature, the partition function of the system becomes non-analytical. Generally, a phase transition is characterized by an order parameter, which distinguishes two phases by taking non-zero value in the symmetry broken phase (also known as the ordered phase) and zero value in the other (disordered phase). In the case of first order phase transition, free energy density or effective potential has a metastable state. Due to this, dynamics of this phase transition is quite different from the continuous phase transition, in which case there is no metastable state. In the case of a first order phase transition, order parameter changes discontinuously to a non-zero value from the zero value at the transition point (by changing the temperature). In the case of continuous phase transition order parameter changes continuously from zero value to the non-zero value in the ordered phase. The continuous phase transition encounters *critical point*, where correlation length of the system becomes divergent. In the *critical* or *Ginzburg region*, the effect of thermal fluctuations ($k_B T$) are strong and due to this, there is no possibility of having ordering, even though the symmetry remains broken in this region. Below the *Ginzburg temperature*, where fluctuations become suppressed in a correlated volume, the ordering establishes and domain structure forms - as happens in the case of ferromagnetic systems. In the case of first order phase transition, there is no critical region. In this case, just below the transition temperature, bubbles of ordered phase nucleate in the background of disordered phase. If the size a bubble is bigger than the critical size, then bubble grows in size and fill up nearby space with ordered phase. Ultimately whole space is filled up with the phase of ordered phase in both kinds of phase transitions. In Chapter 3 we discuss that due to random variation of order parameter in these domains or bubbles, when they meet at a junction point there is a possibility of formation of *topological defect*. The kind of defects formed during the phase transition, depends upon the order parameter space of the theory and spatial dimensions of the system, see Chapter 2.

As we have mentioned, in the case of spontaneous symmetry breaking, ground state does not remain invariant under full symmetry transformations in G as followed by Lagrangian of the theory. However, in the case of explicit symmetry breaking, symmetry breaks at the Lagrangian level itself. In such situation, no SSB phase transition occurs. In the absence of a genuine phase transition, the system undergoes, the so called *cross-over transition*. The best example is the *Heisenberg model* in the presence of (external) magnetic field term. This term breaks $SO(3)$ symmetry to $SO(2)$ explicitly. Similarly in the chiral model, masses of u and d quarks break chiral symmetry explicitly.

Now, we briefly discuss about the hydrodynamics description of thermal systems. The long wavelength dynamics of a thermal medium is governed by the hydrodynamic (fluid dynamic) equations. The ideal hydrodynamic description of system demands (at least) local thermodynamic equilibrium. The hydrodynamics describes, if there are pressure variations in the system, then along the pressure gradient, there will be a flow of fluid elements. To have full ideal hydrodynamics description of a system, the macroscopic length and time scale of the fluid evolution should be much greater than the microscopic length scale (mean free path) and (interaction) time scale of the system, such that the local thermodynamic equilibrium remains maintained throughout the evolution of the fluid. In such situation, one can define local thermodynamic quantities, such as energy density, pressure, temperature etc. at each space-time points. The hydrodynamic description requires equation of state of the system also. This requirement arises because number of independent variables are more in hydrodynamics equations than the number of equations. Since equation of state of a system depends upon the microscopic interactions of its constituents, therefore only at this place, the actual property of the system enters in the ideal hydrodynamics equations, and gives quantitatively different evolution for different systems. More specifically, fluid velocity in hydrodynamic description is directly related with the sound speed in the medium, which varies from system to system. But it should be noted that, the overall hydrodynamics description does not depends upon whether constituents of the fluid elements are quantum or classical in nature. The hydrodynamics equation requires relativistic description, if either fluid elements are relativistic or its constituents are relativistic particles. The formalism of the relativistic hydrodynamics has been discussed in Chapter 6 and its application in the context of relativistic heavy-ion collision is discussed in the Chapter 8.

The *spontaneous symmetry breaking (SSB) phase transitions* and the *hydrodynamic equations* are some of the most important tools of *statistical physics* which are extensively used, irrespective of the energy scale of the system, from condensed matter physics to the high energy physics. In the condensed matter physics, ferromagnetism, superfluidity, superconductivity, etc., arise due to spontaneous symmetry breaking phase transitions. In the high energy physics also the whole evolution of the Universe is affected by such kind of phase transitions. The GUT phase transition, at the energy scale of 10^{15} GeV, and the *electroweak* phase transition, at the energy of about 100 GeV are the examples of SSB phase transition in the early Universe. The confining transition, from quark-gluon plasma (QGP) phase of QCD to the hadronic phase, is a cross-over transition. All these transitions lead to interesting stages during the evolution of the Universe. Similarly, hydrodynamics is also used in almost every branch of physics. The description of the flow of water, and evolution of the cosmic plasma during early stages of the Universe, both are governed by hydrodynamics equations, although former is a non-relativistic system while latter is a relativistic system, and equation of state for both the systems are quite different also. In this thesis we discuss SSB phase transition of the superfluid systems, and hydrodynamics & magneto-hydrodynamics evolution of QCD matter in relativistic heavy-ion collision experiments.

The concepts of topology are also very extensively used in many branches of physics. There are many physical situations where topology plays a very important role, e.g., Aharonov-Bohm effect, topological phase transitions, QCD instanton processes, Skyrmion picture of baryons in the linear-sigma model, Berry phase, superfluid vortices, flux tubes in superconductor, and cosmic strings, domain walls, monopoles in the early Universe etc. The main essence of the topology is in the continuity, specifically, continuous deformations of a map. This is explored in much more detail in Chapter 2. In this thesis we are interested in *topological defects*, mainly in the formation of *topological vortices* during superfluid transition. We study the formation of vortices in the ^4He system, and in QCD matter at high baryon density.

Topological defects are the locations in the physical space where the order parameter field becomes singular (ill defined) [3]. This singularity is topologically protected and can not be removed by local deformation of the order parameter field configuration. The order parameter configuration corresponds to the mapping from the physical space to the order parameter space which forms shrinkable/non-shrinkable loops. There can be many different kind of mappings from the physical space to the order parameter space which are distinguished by the winding number (for superfluid ^4He case) and are characterized by the homotopy classes of the loops. These homotopy mappings form a group structure under the combination law of homotopy classes, which is known as the *fundamental group*. If this fundamental group is non-trivial for an order parameter space of the system, i.e. if it is not isomorphic to the trivial group (consisting of only the identity element), then this ensures that in the physical space topological vortices or line defects will exist [3]. For the detail discussion see Chapter 2.

There are many ways by which a topological defect can form. In this thesis we are interested in the formation of the topological defects during the SSB phase transitions. This, we have explored in detail in Chapter 3. If the order parameter space of a system is topologically non-trivial, then topological defects can exist in the physical space [3], and a symmetry breaking phase transition can lead to the formation of *topological defects*. The formation of these defects during a phase transition is described by the *Kibble mechanism* [4], which is very well tested experimentally. A phase transition leads to the formation of correlation domains in the physical space. The Kibble mechanism utilizes a picture of domain formation during the phase transition and describes how topological defects form during the SSB phase transition [4], see Chapter 3 also. In the case of superfluid transitions this leads to the formation of topological vortices. These vortices have important implications in the condensed matter as well for neutron star physics. The most important property of superfluid vortices, which makes these defects different from the topological defects in other systems, is the rotation of superfluid components about these vortices. This property of rotation arises due to the quantum nature of superfluidity and due to the non-trivial order parameter field configuration about the superfluid vortex. Therefore these vortices carry (quantized) angular momentum and are protected by topology. The appearance of superfluid vortices in the superfluid phase makes this phase qualitatively distinct from the normal fluid. This also we have discussed in Chapter 3.

The search of the *quark-gluon plasma* and its possible probes in the relativistic heavy-ion collisions is one of the exciting area of research. Although, the zero chemical potential quark-gluon plasma phase is of interest for the early Universe, quark-gluon plasma at finite chemical potential contains very rich physics and is of tremendous interest for the physics of neutron star. There are several exiting phases of Quantum Chromodynamics (QCD) possible in this regime of high baryon density at sufficiently low temperatures. The physics of BCS theory is directly applicable in this regime and formation of Cooper pairs, both, in the confined phase and deconfined phase lead to the emergence of superfluidity and superconductivity in the QCD matter. These phases play a very important role in the dynamics, like glitches, and cooling process of a neutron star. The Quantum Chromodynamics (QCD) and its phases, specially superfluid phases, has been discussed in Chapter 5.

In the low energy heavy-ion collisions, if any superfluid phase of QCD arises via spontaneous symmetry breaking phase transitions, then it affects the hydrodynamics evolution of the system due to the formation of topological vortices [5]. This we discuss in Chapter 9 in detail. In such an energy regime, there is a strong possibility that, in the case of non-central collisions, the formed medium may get rotation due to surface tension. Therefore in such situation the superfluid phase transition will occur in the presence of a rotation. This is a similar situation as occurs in the case of neutron star superfluid transition, as in that case also neutron superfluid transition occurs in the presence of rotation of the star. In the condensed matter system, such as ^4He, superfluid transitions in the presence of rotation is routinely studied experimentally. The formation of these vortices during the phase transition is governed by the Kibble mechanism, which predicts the equal formation probabilities of defects and anti-defects [4]. However the above phase transitions, in the presence of rotation, requires a biasing in the formation of vortices over anti-vortices or vise-versa. In this thesis, we address this issue for superfluid ^4He transition by modifying the Kibble mechanism in the presence of such external influence, so that it can account for the required biases, see Ref. [6] and Chapter 4. As discussed above, this has important implications in the case of neutron star and heavy-ion collision physics. Note that there are other situations where such kind of modification in the Kibble mechanism is required. For example, formation of flux-tubes during the superconducting transition in the presence of magnetic field, and formation of baryons (Skyrmions) at finite chemical potential during chiral transition in the linear-sigma model, requires more number of one kind of topological object than other one (note that the baryon production is restricted by the baryon number conservation, see Ref. [7]). All these issues can be handled by modifying the main ingredients of the Kibble mechanism which are the *domain structure* and the *geodesic rule*. In Chapter 4, we have discussed such kind of modification for the case of superfluid transition in the presence of a rotation which lead to the biasing in the formation of topological vortices [6]. If such a modification of the domain structure and geodesic rule is confirmed in the experiments then one can extend such approach to the other systems also.

One of the works presented in this thesis relates to formation of superfluid vortices in ^{4}He system in a rotating vessel. This is presented in Chapter 4. It is well known fact that when one increases the angular velocity of the vessel containing superfluid, a (rotating) vortex-lattice forms. This method of generation of the superfluid vortices is completely different from the Kibble mechanics. In the former case, vortices arises when the system is already in the superfluid phase while in the Kibble mechanism, vortices arise during the normal to superfluid transition. In Chapter 4, we address the issue that how superfluid vortices will form if the superfluid transition occurs in the presence of a rotation. The rotation of the vessel will lead to the formation of more number of vortices than anti-vortices. The standard Kibble mechanism can not capture this feature. In fact, it predicts equal formation probabilities of defects and anti-defects. In Chapter 4, we have proposed a modification of the Kibble mechanism which accounts for biases in the formation of topological vortices during the superfluid transition in the presence of rotation.

Another work discussed in this thesis relates to the possibility of detecting superfluid phases of QCD in the heavy-ion collision experiments. This is presented in Chapter 9. We also investigate whether neutron superfluidity is possible in the low energy heavy-ion collisions. For this we have performed ultra-relativistic quantum molecular dynamics (UrQMD) simulations. Though there is not much hope that color-flavor locked (CFL) phase, which is also a superfluid phase of QCD, can arise in heavy-ion collisions. In our work, we have considered the possibility of both the superfluid phases of QCD (neutron superfluid and CFL) in heavy-ion collision experiments. The method for the detection of these phases, which we propose in Chapter 9, is universal for both the phase, i.e., appearance of the superfluid vortices when the superfluid medium forms. This generates a local rotation in the medium which affects the hydrodynamic evolution at least at the initial stages and may be detected in the experiment by its effect on the flow pattern [5].

One of the most important probes of the medium formation in the heavy-ion collisions is the *elliptic flow* which characterizes the momentum anisotropy of the medium evolution. By fitting the elliptic flow with the experiment data in the *viscous hydrodynamics* simulations, one is able to extract out the viscosity of the quark-gluon plasma. The determination of the viscosity depends upon the various parameters of the simulation, e.g. initial energy density, thermalization time, equation of state, etc. In heavy-ion collisions due to the opposite motion of nuclei, magnetic field also get generated. Its survival until the formation of the thermal medium, and its effects on the medium dynamics is an exciting area of research. In Chapter 10, by performing the magneto-hydrodynamics simulations, we show that the magnetic field can affect the fluid evolution in heavy-ion collisions. In particular, it changes the elliptic flow depending upon the impact parameter of the collisions. We also study other possible effects of magnetic field on the fluid dynamics and effect of dynamics of fluid on the magnetic field strength at the center of the system, see Ref. [8].

The deformed nucleus collisions in relativistic heavy-ion collisions leads to even more interesting possibilities related with the shape anisotropy of the plasma in the transverse plane and the direction of magnetic field. The dependence of the elliptic flow on the impact parameter, in the body-body collisions (where impact parameter is along the semi-major axis of both the nuclei), with and without magnetic field, becomes dramatically different from the spherical nucleus collisions case [9]. We have discussed this also in Chapter 10.

Chapters in this thesis are organized in the following manner. In Chapter 2, starting by motivating the study of topology and discussing some basic notions of topology, we discuss the order parameter space for various systems. We also discuss the coset space for a medium in the symmetry broken phase (coset space of a system is homeomorphic to the order parameter space [3]). Then we discuss topological defects and first homotopy group for the classification of line-like defects.

Chapter 3 is devoted to the Kibble mechanism, superfluidity and a very brief discussion on the vortex model and its experiment study. In Chapter 4, we have proposed a modification of the Kibble mechanism which accounts for the biases in the formation of topological vortices during the superfluid transition in the presence of rotation.

Chapter 5 is dedicated for a brief review of Quantum Chromodynamics (QCD) and its phases. In this chapter by introducing QCD and its formal description, we discuss its global symmetries. Then we introduce very briefly QCD at finite temperature and discuss, by showing Lattice results, the QCD phase transition at zero chemical potential. Then we discuss the superfluid phases of QCD. Here we introduce color-flavor locked phase and neutron superfluid phase. Finally we discuss the QCD phase diagram.

Chapter 6 and Chapter 7 are devoted for formal theory of ideal relativistic hydrodynamics and magneto-hydrodynamics. In Chapter 8, we introduce the physics of heavy-ion collisions (HIC). Here we discuss about various stages of the system evolution in HIC and possible probes for the medium formation. Then we have discussed the application of ideal relativistic hydrodynamics for heavy-ion collisions, and discuss a very important probe for the medium formation in the experiment, which is the elliptic flow. We discuss the Fourier analysis of the azimuthal particle momentum distribution function in HIC. We end this chapter by discussing about the production of magnetic field in HIC and its effects in the system evolution in this experiments.

In Chapter 9, we propose the possibility of neutron superfluidity in low energy HIC experiments and discuss if any of the superfluid phase arise in such experiment then how to detect it. We propose the probe for the appearance of the superfluidity in the HIC experiments via discussing the hydrodynamic evolution of the system in the presence of superfluid vortices.

In Chapter 10, we have discussed ideal relativistic magneto-hydrodynamics simulations and have given results in the context of HIC experiments. We show that presence of magnetic field can change the elliptic flow qualitatively. We see the enhancement in the elliptic flow at low impact parameter regime, while there is strong suppression in the elliptic flow at high impact parameter regime. By showing our other results, we end the chapter with our extension of this work in the case of deformed nucleus collision, where we have shown our preliminary results for such case.

Finally, we summarize the thesis in Chapter 11.

Bibliography

[1] A. Lahiri and P.B. Pal, **A First Book of Quantum Field Theory**, Second Edition, Narosa (2004).

[2] R.H. Brandenberger, Rev. Mod. Phys. **57**, 3985 (1985).

[3] N.D. Mermin, Rev. Mod. Phys. **51**, 591 (1979).

[4] T.W.B. Kibble, J. Phys. A **9**, 1387 (1976); Phys. Rept. **67**, 183 (1980).

[5] A. Das, S.S. Dave, S. De, A.M. Srivastava, Mod. Phys. Lett. A **32**, 1750170 (2017).

[6] S.S. Dave and Ajit M. Srivastava, **arXiv:** 1805.09377.

[7] V.S. Kumar, B. Layek, A.M. Srivastava, S. Sanyal, and V.K. Tiwari, IJMP A **21**, 1199-1219 (2006).

[8] A. Das, S.S. Dave, P.S. Saumia, and A.M. Srivastava, Phys. Rev. C **96**, 034902 (2017).

[9] S.S. Dave, talk on **Effects of magnetic field on plasma evolution in relativistic heavy-ion collisions** in the Conference, *The 15th International Conference on QCD in Extreme Conditions (XQCD-2017), 26-28 June 2017* at University of Pisa, Italy, on 27th June 2017.

Chapter 2

Basics of Topology, Homotopy Theory, Order Parameter Spaces, and Topological Defects

Topology deals with continuous functions, the continuous deformation of maps from one topological space to other, and also deformation of topological spaces into each other. Topology is the generalization of Euclidean geometry where there is no distinction between spaces which can be continuously deformed to each other. So topology does not distinguish between a circle and a square but it distinguishes a sphere and a torus. Spaces which are continuous deformable to each other are called *Homeomorphic*.

One of the example in which continuous deformation plays a very important role is the *Cauchy's residue theorem* discussed in [1]. In the complex plane a line integral of a *meromorphic function* from one point to the other is independent from the path chosen for the integration until and unless it does not cross any pole. If there is no pole in the region, continuous deformation of the path is allowed and integration remains independent of the path chosen. If a path crosses a pole then integration value gets changed in accordance with the *Cauchy's residue theorem*.

We give one example which can provide an understanding of the concept of *topological invariance*. Consider a *disc* B^2 (a two dimensional bounded space) and consider

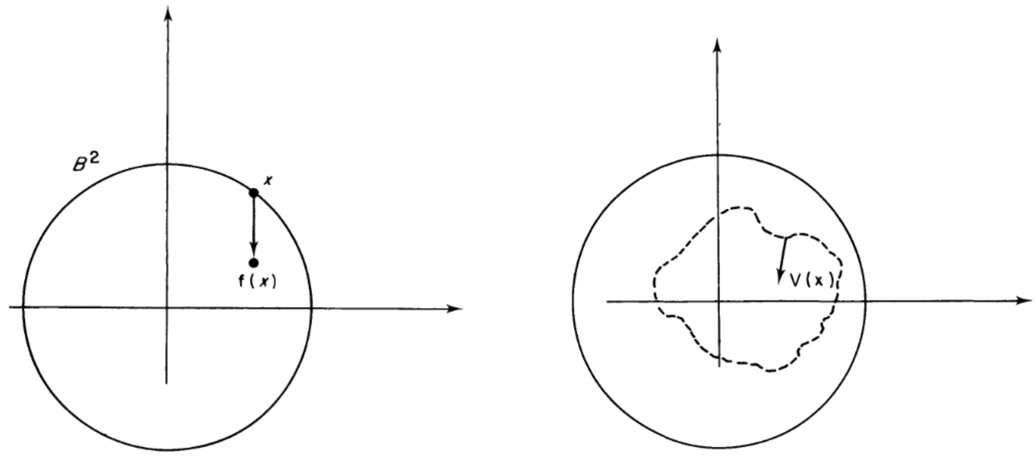

Figure 2.1: Left figure shows the vector field $\mathbf{v}(x)$ drawn from boundary point x to $f(x)$ (interior of B^2). Right figure shows that a continuous deformation of the boundary can not change the index of vector field $\mathbf{v}(x)$, hence index of a vector field is a *topologically invariant* quantity. Figure has been taken from Ref. [1].

a function $f(x)$ which maps points from B^2 into itself, with the condition that boundary of B^2 always get mapped to the interior of B^2. Let us consider a vector $\mathbf{v}(x)$ pointing from x to $f(x)$ as shown in the left Fig.2.1,

$$\mathbf{v}(x) = x - f(x),$$

where x are the boundary points of B^2 and function $f(x)$ maps boundary points x of B^2 into its interior. With this definition of $\mathbf{v}(x)$, if points x are rotated by 2π about the center, then it is certain that $\mathbf{v}(x)$ will also rotate by 2π about the center. It implies that that $\mathbf{v}(x)$ has index one (winding number one), which is an integer number. The index of a field configuration is a *topologically invariant* quantity. To verify the topological invariance of an index, let us continuously deform the boundary of B^2 as shown by dotted loop in the right Fig.2.1. One can check that under this deformation, the index of vector field $\mathbf{v}(x)$ does not change, therefore the index of a vector field is a *topologically invariant* quantity. If continuous deformations cannot change the index of a field configuration, then the field configuration is known as a topologically invariant configuration.

2.1 Basic Notions of Topology

In this section, by following the discussion from Ref. [1], we discuss few basic definitions which are useful in the discussion of topological defects. A *topological space* is a set on which continuity of a function is defined. The exact definition of a *topological space* is as follow [1] :

A set $\mathcal{A}$ along with a finite or infinite collection of subsets of $\mathcal{A}$, $\mathcal{U} = \{\mathcal{A}_\alpha\}$ forms a *topological space*, if the collections $\mathcal{U}$ satisfies following conditions:

a) $\phi \in \mathcal{U}, \ \mathcal{A} \in \mathcal{U}$
b) Any finite or infinite subcollection $\{\mathcal{C}_\alpha\}$ of the $\mathcal{A}_\alpha$ has the property that $\bigcup \mathcal{C}_\alpha \in \mathcal{U}$
c) Any finite subcollection $\{\mathcal{C}_{\alpha_1}, ..., \mathcal{C}_{\alpha_n}\}$ of the $\mathcal{A}_\alpha$ has the property that $\bigcap \mathcal{C}_{\alpha_i} \in \mathcal{U}$

If the above conditions are satisfied, then $\mathcal{A}$ and $\mathcal{U}$ form a *topological space* $(\mathcal{A}, \mathcal{U})$, and the subsets $\mathcal{A}_\alpha$ are called *open sets*. The choice of $\mathcal{U}$ satisfying above conditions is said to give a topology to $\mathcal{A}$.

We give an example in which a set $\mathcal{A}$ may or may not form topological space depending upon the collection $\mathcal{U}$. Let us take a set $\mathcal{A} = \{1, 2, 3, 4\}$, it does not form a topological space for the collection $\mathcal{U} = \{\phi, \mathcal{A}, \{1, 2\}, \{2, 3\}\}$, because second and third conditions are not satisfied. On the other hand, if we take $\mathcal{U} = \{\phi, \mathcal{A}, \{1, 2\}, \{3, 4\}\}$, then one can check that this collection of subsets gives topology to $\mathcal{A}$. Subsets $\{1, 2\}$ and $\{3, 4\}$ are called open sets.

Continuous Function: Consider a function f defining a map from topological space $(\mathcal{A}, \mathcal{U}_\mathcal{A})$ to topological space $(\mathcal{B}, \mathcal{U}_\mathcal{B})$. f is said to be continuous if under the map, the inverse image of any open set in $(\mathcal{B}, \mathcal{U}_\mathcal{B})$ is an open set in $(\mathcal{A}, \mathcal{U}_\mathcal{A})$ [1].

According to the definition, function f is continuous if and only if the inverse mapping from topological space $(\mathcal{B}, \mathcal{U}_\mathcal{B})$ to $(\mathcal{A}, \mathcal{U}_\mathcal{A})$ maps open sets to the open set. It can be seen, that this definition reduces to the conventional ϵ-δ definition for continuous and discontinuous functions defined on real line $\mathcal{R}$. For a discontinuous function, inverse map of an open set, which lies about the discontinuous branch of the function f, does not remain an open set.

The purpose of the topological spaces is to describe continuity of functions. The above definition of topological space is an appropriate mathematical structure to discuss the continuity or discontinuity of a function. Continuity of a function completely depends upon the topology associate with a set; a discontinuous function may become continuous from one topology to other. For example if we consider a collection of all 2^n subsets of a given set $\mathcal{A}$ with n number of elements (the *power set* of $\mathcal{A}$, $\mathcal{P}(\mathcal{A})$), then in the topological space $(\mathcal{A}, P(\mathcal{A}))$ each and every function will become continuous. This is called the *discrete topology* of $\mathcal{A}$. This is not a useful topology because every function is continuous in this space. Similarly, for a given set $\mathcal{A}$, collection $\mathcal{U} = \{\phi, \mathcal{A}\}$ give the topology to $\mathcal{A}$, but it is too restrictive as almost every function become discontinuous. This is called the *indiscrete or trivial topology.*

Here we list some basic definitions which may be used in the discussion of topological defects.

Neighbourhoods: For a topological space $(\mathcal{A}, \mathcal{U}_{\mathcal{A}})$, $\mathcal{N}$ is a neighbourhood of a point $x \in \mathcal{A}$, if $\mathcal{N}$ is a subset of $\mathcal{A}$ which also contains some open sets $\mathcal{A}_\alpha$ to which x belongs.

Closed Sets: Any subset $\mathcal{X}$ of $\mathcal{A}$ is said to be closed if complement of $\mathcal{X}$ (denoted by $\mathcal{A} - \mathcal{X}$) is an open set. ϕ and $\mathcal{A}$ both are open sets as well as closed sets as both are complements of each other.

Closure of a Set: Consider a collection of closed sets $\{F_\alpha\}$, such that each F_α contains a set U. Then the $\bigcap F_\alpha$ is called *closure* of set U and denoted by $\overline{U}$. For a real line $\mathcal{R}$, if $U = (a, b)$ then $\overline{U} = [a, b]$, a close set.

Interior and Boundary: The *interior* of a set U is the union of all open subsets of U. Let us take open subsets of U to be $\mathcal{O}_\alpha$, then *interior* of U is $U^0 = \bigcup_\alpha \mathcal{O}_\alpha$. For example if U is a closed set B^2 of unit radius in $\mathcal{R}^2$, then U^0, the *interior*, will be $x^2 + y^2 < 1$.

The *boundary* of set U is the complement of the *interior* of the *closure* of U, i.e. the *boundary* $b(U) = \overline{U} - U^0$. So in the above example $b(U)$ is $x^2 + y^2 = 1$; a circle is the *boundary* of B^2.

Cover and Compactness: Consider a collection of sets $F = \{F_\alpha\}$. If union of these sets, i.e. $\bigcup F_\alpha$ contains a set U, then F is said to be the *cover* of U. If all the sets F^α are open sets, then the *cover* F is called an *open cover* of U.

For a give set U, there can be many *open covers*. If for every *open cover* F with $\bigcup F_\alpha \supset U$, there exist a finite subcovering $\{F_{\alpha_1}, ..., F_{\alpha_n}\}$ of U such that $F_{\alpha_1} \bigcup F_{\alpha_2} ... \bigcup F_{\alpha_n}$ $\supset U$, then set U is called compact.

In $\mathcal{R}^2$, all the sets with infinite area are non-compact, as although one can get open cover of the set such that union of them contain the infinite area which the given set has (in fact equal to the area of set), but no finite subcollection can exist which can give infinite area of the given set, and therefore can not cover the set. So to have finite subcovering, the area of the set should be finite and also the set should be closed. So a set is compact if it is bounded and closed. For example open set B^2 on $\mathcal{R}^2$ is non-compact because not all open cover of B^2 has a finite subcovering of B^2; but closed set B^2 is compact.

Connectedness: A set $\mathcal{A}$ is said to be *connected*, if it cannot be written in terms of completely disjoint peaces (with empty intersection), i.e. a connected set $\mathcal{A}$ can not be written as $\mathcal{A} = \mathcal{A}_1 \bigcup \mathcal{A}_2$, where $\mathcal{A}_1$ and $\mathcal{A}_2$ both are open and $\mathcal{A}_1 \bigcap \mathcal{A}_2 = \phi$; otherwise the set is called *disconnected*.

Homeomorphism: Homeomorphism divides *topological spaces* into *equivalence classes*. Two *topological spaces* are said to be *homeomorphic* if there exist a continuous map α which maps one space into the other, and its inverse α^{-1} also exists which is also a continuous map. *Homeomorphic* spaces are continuously deformable to each other and lie in the same *equivalency class*. Two *non-homeomorphic* spaces belong to different *equivalency classes*. *Homeomorphism* between two *topological spaces* $\mathcal{A}$ and $\mathcal{B}$ is defined as,

$$\alpha : \mathcal{A} \to \mathcal{B}$$

where α is a continuous map such that α^{-1} also exist and is a continuous map. Therefore if $\mathcal{A}$ is *homeomorphic* to $\mathcal{B}$ then reverse is also true. If there are three *topological spaces* and first is *homeomorphic* to second and second is *homeomorphic* to third then first will also be *homeomorphic* to third. As $\mathcal{A}$ is homeomorphic to $\mathcal{A}$, we see that homeomorphism is an equivalence relation.

If $\mathcal{A}$ and $\mathcal{B}$ are *homeomorphic* topological spaces, then if $\mathcal{A}$ is *compact* then $\mathcal{B}$ has to be *compact* and if $\mathcal{A}$ is *connected* then $\mathcal{B}$ has to be *connected*. Therefore *compactness* and *connectedness* are *topological invariants*.

Dimension of $\mathcal{R}^n$ is a *topological invariant number*; there can not be a continuous function which can map $\mathcal{R}^n$ to $\mathcal{R}^m$, where $n \neq m$. Therefore spaces $\mathcal{R}^n$ and $\mathcal{R}^m$, with $n \neq m$, are not *homeomorphic*.

Homotopy of Maps: Let us consider two continuous maps from *topological space* $\mathcal{A}$ to $\mathcal{B}$,

$$\alpha_1 : \mathcal{A} \to \mathcal{B}$$
$$\alpha_2 : \mathcal{A} \to \mathcal{B}.$$

α_1 and α_2 are said to be *homotopic* to each other if they can be continuously deformed to each other. This means there exist a continuous map $\mathcal{F}$:

$$\mathcal{F} : \mathcal{A} \times [0,1] \to \mathcal{B}$$

such that $\mathcal{F}$ satisfies

$$\mathcal{F}(x,0) = \alpha_1(x)$$
$$\mathcal{F}(x,1) = \alpha_2(x).$$

Therefore for $t \in [0,1]$, $\mathcal{F}(x,t)$ varies such that when t varies from 0 to 1, $\mathcal{F}(x,t)$ continuously deforms from α_1 to α_2. It is easy to see that homotopy is an equivalence relation. Therefore *homotopy* divides maps into different *equivalence classes*. While *homeomorphism* generates *equivalence classes* of *topological spaces*, *homotopy* generates *equivalence classes* of continuously deformable maps.

Equivalence classes generated by *homotopy* are themselves unchanged by continuous deformation of *topological spaces*, i.e. *homeomorphic topological spaces* have the same *homotopy equivalence classes*. Therefore *homotopy equivalence classes* are *topological invariants* for *pair* of spaces $\mathcal{A}$ and $\mathcal{B}$. No continuous maps (deformation) is possible which can map one *homotopy equivalence class* to the other. This shows that there is *topological obstruction* between different *equivalence classes* which leads to *topological invariants* of *homotopy equivalence classes*.

Simply Connected Space: A *topological space* is called *simply connected* if any *closed path or loop* can be shrinkable on the space. For example, $\mathcal{R}^2 - \{0\}$ is not a simply connected space, while $\mathcal{R}^3 - \{0\}$ is.

Relative Topology: Suppose $\mathcal{A}'$ is a subset of a *topological space* $\mathcal{A}$. If the *open sets* of $\mathcal{A}$ are $\{\mathcal{A}_\alpha\}$, then $\mathcal{A}'$ is called *relative topology* of $\mathcal{A}'$ to $\mathcal{A}$, if *open sets* $\{\mathcal{A}'_\alpha\}$ of $\mathcal{A}'$ are intersections of $\mathcal{A}_\alpha$ and $\mathcal{A}'$, i.e. $\{\mathcal{A}'_\alpha\} = \{\mathcal{A}_\alpha \bigcap \mathcal{A}'\}$.

2.2 Order Parameter and Order Parameter Spaces

As we have discussed in the Chapter 1, a phase transition from one phase to the other is described by Landau-Ginzburg theory, where free energy density is written in terms of a power series of order parameter field. An *order parameter* characterizes two distinct phases by having non-trivial (non-zero) value in one of the phase, while being zero in the other phase. In the case of spontaneous symmetry breaking phase transitions, order parameter takes non-zero value in the symmetry broken phase; symmetry broken phase being known as the *ordered medium*. In an *ordered medium* order parameter field, say $f(r)$, is defined at every point and can vary in space continuously (except where *topological defects* are present as discussed latter). The possible values of *order parameter* constitute a space known as the *order parameter space* (or *manifold of internal states*) [2].

An *ordered medium* is characterized by a continuous order parameter field which has its well defined value at every points in the space (apart from location of any possible topological defect). Typically, in condensed matter system, order parameter fields arise after coarse-graining of some microscopic degrees of freedom. For example, in the case of magnetic systems, microscopic constituents are spins, while order parameter field for this medium is taken to be magnetization density which is the coarse-grained field of these microscopic constituents. In the construction of *order parameter space*, for most of the cases, all possible orientation of microscopic constituents are used. Though we should emphasize that each point on the order parameter space corresponds to a local average of these microscopic variables. Note that the length scale of the variation of an order parameter field and microscopic variables are completely different. Below we present few examples of order parameter and order parameter spaces:

1. Planar Spins: In this system, spin vectors are restricted to a plane therefore the order parameter field (magnetization) is a vector of fixed magnitude lying in a plane. Since all possible orientations of the order parameter field are parameterized by an angle between 0 to 2π, therefore the order parameter space here is a circle S^1.

2. Superfluid Helium-4: The superfluid phase arises due to Bose-Einstein condensation, which has a non-zero condensate density. The order parameter field, which characterizes this phase is a complex scalar field $\psi = \psi_0 e^{i\theta(r)}$ with a fixed magnitude ψ_0, where $|\psi_0|^2$ is the condensate density and $0 \leq \theta \leq 2\pi$. Therefore order parameter space for this system is a circle S^1 in the complex plane.

3. Ordinary Spins: In this case, spin vectors can take any possible 3-dimensional orientation, therefore order parameter, which is the magnetization density with fixed magnitude, also can have any possible orientation in 3-dimensional space. The order parameter space for this system is therefore the surface of 2-sphere S^2.

4. Superconductor: For conventional BCS superconductors, order parameter field is also characterized by a complex scalar field. This is the field of the condensate of *cooper-pairs* which also break $U(1)$ symmetry as in the case of superfluid (though here it is local gauge symmetry). Here $U(1)$ local symmetry breaks to Z_2. Therefore, the order parameter space in this case is a circle with opposite points are identified, i.e. S^1/Z_2. This space is *homeomorphic* to a circle, therefore in this case also the order parameter space is a circle S^1.

5. Nematic Liquid Crystals: This system consists of a collection of long ellipsoidal molecules which can locally align in the symmetry broken phase. These molecules have orientation like an ordinary spin vector but without any arrowhead. Thus the order parameter space for this system is a surface of 2-sphere with diametrically opposite points identified, i.e. S^2/Z_2. This space is known as the *real projective plane* RP^2 which is a *non-orientable manifold.*

For more examples of order parameter and spaces, see Ref. [2].

2.2.1 Coset space and order parameter space

Let G be a group and H a subgroup of G. Let $g \in G$ and $h_i \in H$. Then set of all elements gh_i is called the *coset* of H (*left coset*), denoted by symbol gH. It can be shown that, if g_1 and g_2 are two distinct elements of G then cosets g_1H and g_2H are always either completely identical or completely disjoint sets. The space of these cosets is called *coset space* and denoted by the symbol G/H [2].

In the case of spontaneous symmetry breaking, G is the symmetry group of the Lagrangian or Hamiltonian, while H (subgroup of G) is the symmetry group (remaining symmetry) of the ground state after the symmetry breaking. Under the transformation of H, a specific value f of the order parameter does not change, therefore H in this case is called the *isotropy subgroup* corresponding to f. Note that g transforms f into a different order parameter value if $g \notin H$. It has been shown in Ref. [2] that the *coset space* G/H is *homeomorphic* to the *vacuum manifold* or the *order parameter space* of the theory. As we have discussed above, two *homeomorphic spaces* have the same *homotopy equivalence classes* (homeomorphism does not change homotopy classes), therefore homotopy equivalence classes of the coset space and of the order parameter space are the same.

For example, in the case of *planar spin* and *superfluid* $SO(2)$ and $U(1)$ symmetries break completely. Therefore in both the cases isotropy subgroup H is the *identity.* Therefore coset space G/H in both the cases is the group manifold of $SO(2)$ and $U(1)$ which is a circle S^1. In the case of *ordinary spin* in 3-dimensions, $SO(3)$ symmetry breaks to $SO(2)$, therefore coset space G/H in this case is $SO(3)/SO(2)$ which is a surface of 2-sphere S^2.

2.3 Topological Defects

Topological defects are the *order parameter field* configurations, of topological origin, which can not be removed by local deformation of the field configuration. To remove it, the field configuration has to be changed globally (which costs energy, scaled with the system size). The *defect* regions are singular regions where order parameter field has singularity (ill defined). The gradient term of the order parameter field, present in the *free energy* of the theory, becomes divergent at defect location, and it is energetically more favorable that order parameter field leave the vacuum manifold (and become zero at the center of defect). Because of this, defects region have higher energy than the background. The zero magnitude value of the order parameter field corresponds to symmetry restored phase, and that is why it is called a defect, which is topologically protected, and hence *topological defect*.

We follow the discussion from Ref. [2] to describe the *topological defects* by considering a simple example of planar spin system in two dimensional space, where order parameter is a vector $s(x, y)$ of unit magnitude in a plane. The order parameter space of this system is a circle S^1. We will argue, by just following the argument of continuity, that for a given field configuration $s(x, y)$, on a hypothetical circle of radius d about a point P, one can predict that whether the field value somewhere inside the circle is singular or not.

Let us consider one of the order parameter field configurations given in Fig.2.2 on a (hypothetical) circle about point P with radius d. By traversing on the circle in the counterclockwise direction, if the mapped field configuration from physical space to order parameter space (S^1) also changes in the counterclockwise direction, then, by convention, we count it as a positive variation, while if it changes in the clockwise direction on S^1, we count it as a negative variation. Now since field $s(x, y)$ is continuous and single valued on the circle, therefore in traversing a full close path on circle, the variation in the field has to be integral multiple of 2π, i.e. $2\pi n$, where $n = 0, 1, 2, \ldots$. The integer n is known as the *winding number* of the *topological defect*.

For a given non-trivial field configuration (with non-zero winding number) on the circle, to discuss whether there is any singularity at point P or not, we continuously

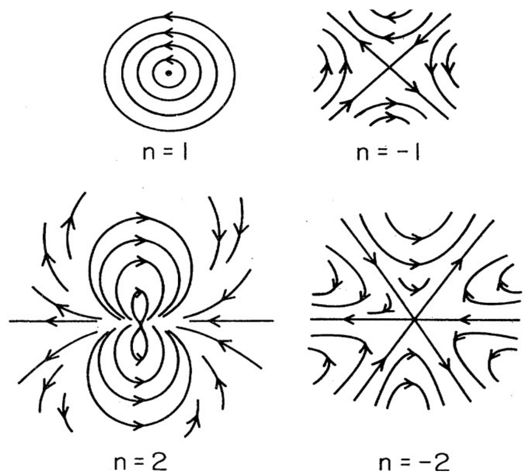

Figure 2.2: Figures show different winding number order parameter field configurations in the physical space. To realize the winding number, traverse counterclockwise about the center of configuration and observe in which direction field is changing on the order parameter space, and how many times field configuration wraps up around the order parameter space S^1. Figure has been taken from Ref. [2].

shrink the circle to a smaller radius. Since the deformation is continuous, therefore the total variation of field on the new circle will also remain invariant and it still will have the same winding number n. As the net winding number can not change even if we shrink the circle to a very small radius, therefore the gradient of field on the smaller circle will become very large. Therefore by the continuous shrinking of circle, when we reach at the point P, derivative of order parameter field becomes singular. Hence we conclude that if there is a non-trivial winding configuration of order parameter field about a point P in the physical space, then there will be a *singular* point somewhere inside this configuration which is a *topological defect.*

For $n = 0$ case also, it is possible that by pinching the field configuration one can achieve singularity at P. But this singularity *always* can be removed by local *continuous* deformation of field without affecting outer field configuration. In this sense $n = 0$ singularity is said to be *removable* or *topologically unstable*, while $n \neq 0$ singularity as a *topologically stable* singularity.

Now we discuss the mapping of the field configuration from physical space to the order parameter space and discuss the existence of the *topological defects* in the physical space on the basis of continuity of mappings in the order parameter space.

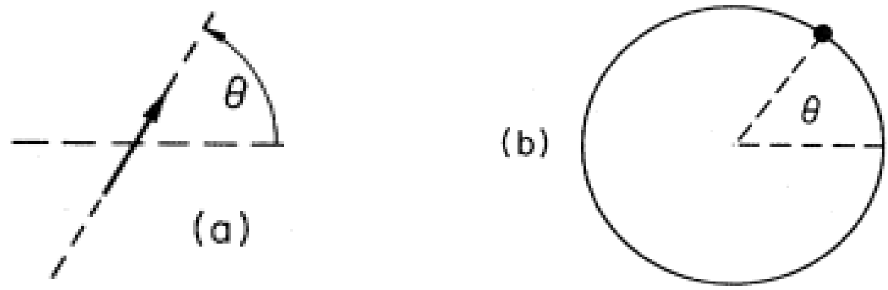

Figure 2.3: (a) shows the orientation of order parameter field at point (x, y) in the physicals space.(b) shows the mapping $s(x, y)$ of the order parameter field to the order parameter space. This mapping is represented by a point on the order parameter space with the same angle θ as in the physical space. Figure has been taken from Ref. [2].

First we define the mapping by saying that the order parameter field in the physical space has some orientation (direction of the spin vector) which is mapped to the order parameter space to a point by following the orientation of the field in physical space. This defines $s(x, y)$ as a mapping from physical space to order parameter space, see Fig. 2.3. We are interested in the mapping from a circle in the physical space, on which we want to investigate winding of field configuration around a point, to the order parameter space for the existence of a *topological defect*. The order parameter field on the circle in physical space get mapped either to a loop or to a point in the order parameter space. The key statement is, *if this loop is shrinkable on the order parameter space, then on the circle in physical space, order parameter field configuration will have zero winding and therefore there will not be a stable topological defect in the region inside this circle, while if the loop in the order parameter space is not shrinkable, then on the circle in the physical space, field configuration will have a non-trivial winding and hence inside the region of the circle there will be a topological defect*, see Fig. 2.4 in this regard.

The *winding number* n is determined by the number of times a non-trivial loop in the order parameter space wraps up around the order parameter space. Positive and negative windings, by convention, are defined by counterclockwise and clockwise wrapping, respectively. If two mappings (loops) are deformable to each other then they are called *homotopic* to each other and they give same kind of *topological defect* in

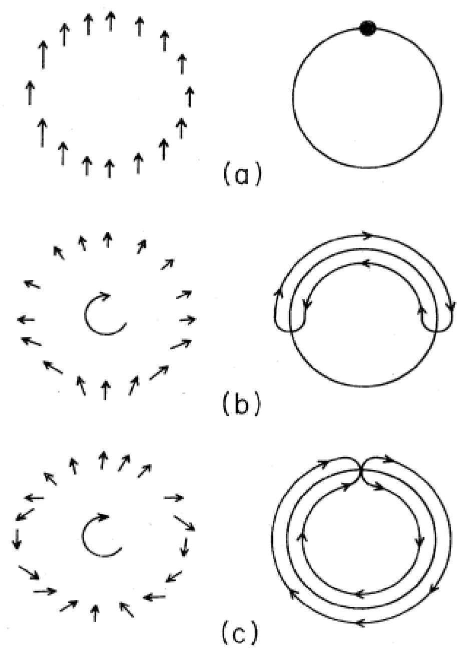

Figure 2.4: In all the cases left figures show the field configuration in the physical space and right show corresponding mapping of these configurations in the order parameter space.(a) Shows the mapping of a uniform field configuration into the order parameter space.(b) Shows mapping of spatially varying order parameter field configuration into the order parameter space which clearly has $n = 0$ winding configuration.(c) shows winding number 2 configuration. Figure has been taken from Ref. [2].

the physical space. In other words, we can say that if we can construct a *continuous family of mappings*, $h_t(x, y)$ between two maps $s_1(x, y)$ and $s_2(x, y)$ in the order parameter space (mapping from the circle in physical space to order parameter space), such that $h_0(x, y) = s_1(x, y)$ and $h_1(x, y) = s_2(x, y)$, where $t \in [0, 1]$, then $s_1(x, y)$ and $s_2(x, y)$ are said to be *homotopic maps*; $h_t(x, y)$ is called the *homotopy* between two maps which is continuous in both (x, y) and t.

The statement, that a shrinkable loop in the order parameter space corresponds to a *unstable singularity* in the physical space, can be understood by considering a map by using the polar coordinates $s(r, \theta)$, where r can play a role of parameter t of the *homotopy* discussed above. Suppose we have a field configuration such that at the larger value of r there is no winding of this configuration on the circle, but there is a singularity at the origin. When we decrease the r, it will generate a family of homotopic maps to the previous map (with larger r), therefore new map will also have the same winding number (because deformation is continuous in r as in the analogous parameter t of homotopy), which is zero in this case. Even if we reach very close to the origin winding number still will be zero because of the fact that all the maps are *homotopic* and hence this singularity can not have any non-trivial winding of field configuration at any r, therefore it can be removed by local deformations. In the similar way we can show that if the field configuration has a non-trivial winding around a point in a large radius circle, then it will also have the same winding in a circle of infinitesimally small radius about the origin; this shows that there will be a *stable singularity* at the origin which is a *topological defect.*

Now we discuss the *homotopy equivalence classes* of defects. Here we mention that different field configurations with the same winding number in the core region of singularity (around a point P) can be continuously deformed to each other such that they become identical. We can see this in Fig. 2.5, where a continuous deformation of the field configuration in the core region of one defect is shown to become the same as the core configuration of the other defect, where both the defects have the same winding number. The different winding number field configurations do not have this feature. Thus for the same winding configurations there is no *topological barrier* for going from one configuration to other, while for different winding configurations

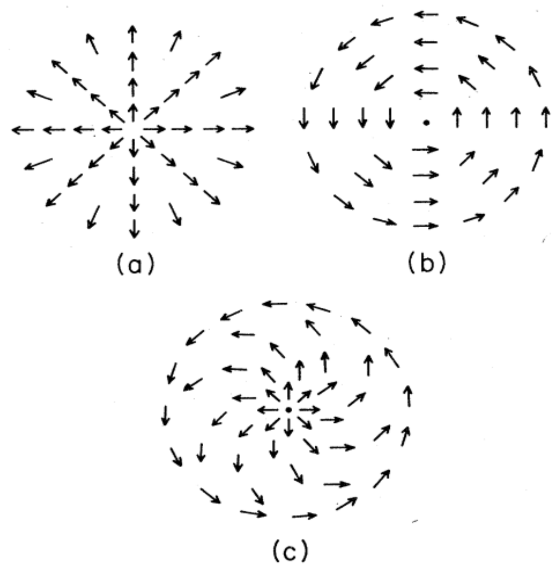

Figure 2.5: (a) and (b) are winding number one field configurations. (c) shows after performing a continuous deformation of (b) field configuration in the core region, one can achieve (a) configuration, while outer region still have configuration of (b). Figure has been taken from Ref. [2].

there is a *topological barrier*, and therefore by performing local continuous deformation, one can not achieve different winding number configurations. This shows that corresponding loops in the order parameter space form *equivalence classes*. In a given equivalence class, two loops can be continuously deform to each other, while in different classes they can not. These classes are called *homotopy equivalence classes* which classifies the *singularities* in physical space for a given order parameter space. Singularities in the same class are called *topologically equivalent*.

We have seen that the *winding number* is a *topological conserved number*. If we have two nearby topological defects with winding number n and m, then a circle encircling both the defects will have winding number $n+m$. In this regard, it is also possible that winding number n and m defects can merge into a single defect with winding number $n + m$. This is shown in Fig. 2.6 where two topological defects, both with winding number one, merge into a single defects with winding number two. This can be in the reverse also; single higher winding defect can split into multiple defects with lower winding number by preserving the initial winding. Defects (winding

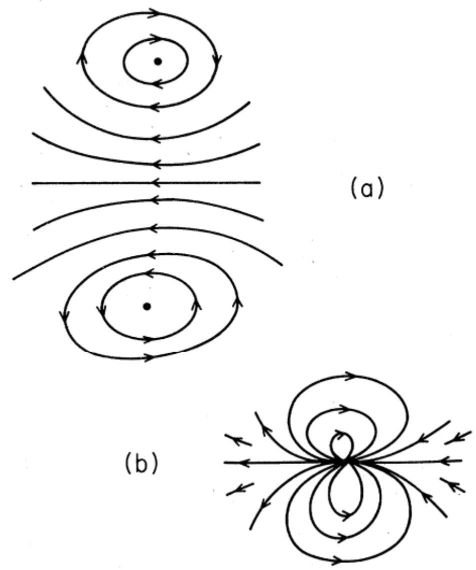

Figure 2.6: (a) shows two nearby topological defects with winding number +1. (b) shows that defect configuration in (a) is *topologically equivalent* to a single defect with winding number +2. Figure has been taken from Ref. [2].

number $+n$) and anti-defects (winding number $-n$) can annihilate to each other to a *singularity free* configuration and vice-versa. This feature shows a group-theoretical structure of the classification of defects, which we discuss in the next section.

The classification scheme of defects depends upon the structure of the order parameter space. If we consider ordinary spin in 3-dimensions instead of planar spin, then in this case order parameter space is a surface of 2-sphere. It can be shown that the topological defects what we have discussed above are unstable in this space because every loop in this space is shrinkable. Note that for a 3-dimensional system, a wrapped *balloon* on the surface of 2-sphere is not shrinkable. This leads to the *monopole defects* in the physical space. Therefore the defect classification differs from one order parameter space to other (non-homeomorphic) order parameter space.

2.4 Homotopy Theory

Homotopy theory provides a classification of topological defects in the ordered media. It also gives a systematic description for crossing of two topological line defects. If for a given order parameter space homotopy group is non-trivial, it will have an important consequence in the physical space in terms of existence of topological defects. For example, if fundamental group of the order parameter space is non-trivial it ensures the existence of the line defects in 3-dimensions and point defects in 2-dimensions. First we discuss the *fundamental group* (also known as *first homotopy group*), then we briefly discuss about the *higher homotopy groups* and list possible topological defects and objects for a given order parameter space.

2.4.1 The Fundamental Group

In the last section we have discussed the classification of defects in 2-dimensional space for a planar spin for which order parameter space is S^1. In general, there is no reason to restrict ourselves to 2-dimension and for a specific order parameter space; in fact, different media can have different spatial dimensions and order parameter spaces. In general, one can classify the topological defects in any spatial dimensions with the study of equivalence classes of maps from physical space to the order parameter space. As we have discussed that within a given homotopy equivalence class, loops in order parameter space can be continuously deformed to each other, while maps belonging to different homotopy equivalence classes can not be deformed into each other. This introduces the notion of topological barrier (topological invariants) and some kind of discreteness which is known as the winding number associated with each equivalence class. These equivalence classes form a group structure, which we discuss below, called homotopy group. The combination law of two defects is associated with the combination law of elements of the homotopy group. The fundamental group is the first homotopy group; first homotopy means we study the group of equivalence classes whose elements are the one dimensional loops. For higher dimensional surfaces in order parameter space, we have higher homotopy groups accordingly.

First we begin by considering loops which have a common point in the order parameter space and show that equivalences classes of these loops form a group structure known as *based homotopy group.* Then we discuss that, if the order parameter space is *path connected*, then no point in this space is special and the choice of one point over the other in this space do not change the group structure and hence this group is associated with the order parameter space overall. A *path connected* space is a space in which any two points can be continuously joined by a path lying in the order parameter space. Mathematically, if there are two points x and y in the order parameter space then there is a continuous mapping f which maps interval $[0,1]$ into the order parameter space($f : [0,1] \to S$; S is the order parameter space) such that $f(0) = x$ and $f(1) = y$. Note that the consideration of *path connected* order parameter space does not loose the generality of our next discussions, as even in the case when order parameter space has disjoint pieces (in terms of path connectedness), the field configuration at a circle in the physical space is always mapped into a path connected part of the order parameter space, and for that our entire following discussion will go through. Note that if two different maps from the physical space to the order parameter space lie in two disjoint pieces of the order parameter space then they belong to different equivalence classes, and therefore there is no homotopy between these two maps [2].

A. Fundamental Group at a point

In this section we discuss the homotopy between loops which have one point common in the order parameter space. The common point is called the *base point* and the homotopy between loops at the *base point* is called the *based homotopy.* The *based homotopy* of loops form a group structure for a given order parameter space known as *based homotopy group.* In the next section we discuss that in the path connected order parameter space, no point is special and each based homotopy group (discussed below) are isomorphic. The homotopy without any base point is known as *free homotopy.*

Let us begin by defining a loop at a base point x. A loop at base point x can be describe by a continuous maps $f(z)$ which maps the interval $[0,1]$ $(0 \leq z \leq 1)$ from physical space to the order parameter space such that $f(0) = f(1) = x$. Note that the increase in z in the physical space is represented by direction of arrow on the loop in the order parameter space.

The homotopy between the two continuous maps f and g which have common base point x is describe by a family of continuous maps (both in t and z) $h_t(z)$ $(h_t(z) : [0,1] \times [0,1] \to S)$ such that $h_0(z) = f$ and $h_1(z) = g$ and also $h_t(0) = x$ and $h_t(1) = x$. In Fig.2.7 the based homotopy between family of loops has been shown.

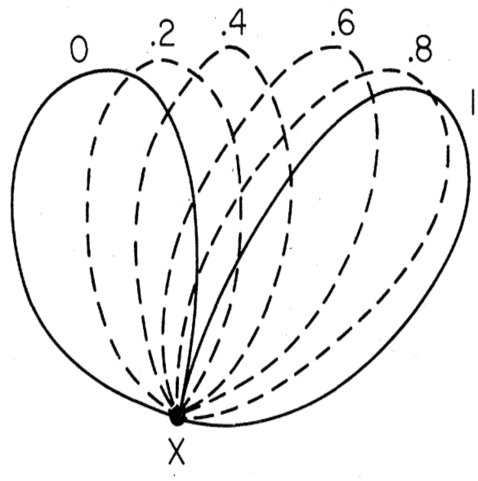

Figure 2.7: Figure shows the based homotopy between family of loops. Figure has been taken from Ref. [2].

Now, to describe the group-theoretical structure, we first discuss the combination law. We here note that it is difficult to parameterize the combination of two loops. This difficulty arises because of too much restrictive condition put by above parameterization than required. Let us discuss one possible parameterization of combination of two loops,

$$\begin{aligned} f \circ g(z) &= f(2z), \quad 0 \leq z \leq \tfrac{1}{2}; \\ &= g(2z-1), \quad \tfrac{1}{2} \leq z \leq 1. \end{aligned}$$

In this parameterization, at $z = \frac{1}{2}$, loops always has to reach at the base point x. This is an unnecessary restrictive constraint, since we know that loop $f \circ g(z)$ is homotopic to a loop which start and end at x and has the same winding number as of the combination of loops f and g. Also, there is a serious problem related with the associative law with the above parameterization for combination law. This kind of parameterization does not follow the associative law.

Therefore we do not consider the combination law of two loops (which gives more restrictive condition than required). Instead of the combination of loops, we consider combination of equivalence classes (at x). This is appropriate for the formation of group structure of equivalence classes at x. This consideration is quite natural since the equivalence classes are the one which characterize topological defects.

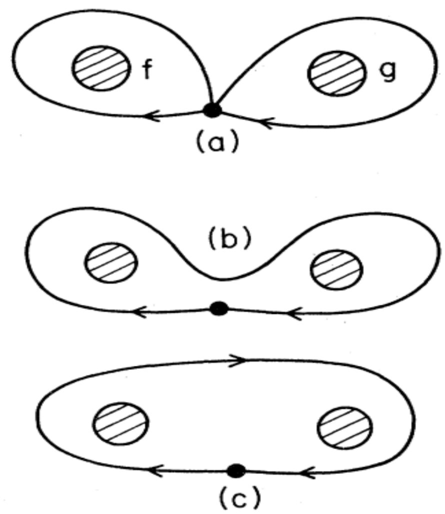

Figure 2.8: Figure shows the combination of two loops f and g following the definition of combination of equivalence classes. Since in this definition there is no any issue of parametrization, therefore this definition allows the homotopy in between the loop $[f] \circ [g]$ in (a) and loop $[f \circ g]$ in (c). Figure has been taken from Ref. [2].

We represent a homotopic equivalence class at x by $[f]$, where f is a loop in the equivalence class $[f]$ and a representative of it. We now define combination law (product) of two equivalence classes by,

$$[f] \circ [g] = [f \circ g].$$

This combination law is independent from the representative of the classes $[f]$ and $[g]$; if $f \sim f'$ and $g \sim g'$ then $[f \circ g] \sim [f' \circ g']$ ($\sim$ represents *homotopic to at* x). This definition of combination law is also independent from any parametrization. Fig.2.8 shows the combination of two loops f and g following the above definition. In the above definition, there is no any issue of parametrization, and therefore above definition allows the homotopy in between the loop $[f] \circ [g]$ in Fig.2.8(a) and loop $[f \circ g]$ in Fig.2.8(c).

With the above combination law of homotopy classes at base point x, we can now discuss the group-theoretical structure of homotopy classes. Homotopy classes at the base point x of an order parameter space S form a group which is known as the *fundamental group* at point x, and written as $\pi_1(S, x)$. To verify the group structure of homotopy classes, our first observation is that the combination law given above satisfies closure property, as $[f] \circ [g] = [f \circ g]$, which is also a homotopy class of maps from physical space to the order parameter space.

If we consider one representative loop, say $f,\ g,\ h$, from each classes $[f],\ [g],\ [h]$, then they satisfy associative law because, $f \circ \Big(g \circ h\Big)$ and $\Big(f \circ g\Big) \circ h$ are only different in their parametrization, and such parametrization does not affect the homotopy between two maps. So these maps belong to same homotopy class, and hence homotopy classes satisfy associative law $[f] \circ \Big([g] \circ [h]\Big) = \Big([f] \circ [g]\Big) \circ [h]$ under the given combination law.

There is always a map $e(z)$ exist which can map the field configuration in the physical space to a point x in the order parameter space. This map is known as the constant map. There can also be maps whose image can be shrink to a point x. All these maps are homotopic to the constant maps and form a homotopy class $[e]$. The combination law of $[e]$ with the other homotopy class, say $[f]$, simply follows,

$$[e] \circ [f] = [f] \circ [e] = [f],$$

and therefore $[e]$ is the identity element in the set of homotopy classes.

Suppose f^{-1} is a loop at x in the order parameter space (here we are representing map f by its image) which traverses in the opposite direction to the loop f, therefore its paramterization is,

$$f^{-1}(z) = f(1-z), \quad 0 \leq z \leq 1.$$

Now if loops f and g are homotopic loops then it can be shown that f^{-1} and g^{-1} are also homotopic to each other and therefore they also form a homotopic class such that,

$$[f]^{-1} = [f^{-1}].$$

Now to show that $[f]^{-1}$ is an inverse of $[f]$, it is easy to verify that loop $f^{-1} \circ f = f \circ f^{-1}$ is homotopic to a constant map at x which is obvious as f^{-1} traverses in the opposite direction to f, so combination of these two is shrinkable to a point. This homotopy can be represented in the parameter form as,

$$\begin{aligned} h_t(z) &= f(2zt), && 0 \leq z \leq \tfrac{1}{2}; \\ &= f(2t(1-z)), && \tfrac{1}{2} \leq z \leq 1. \end{aligned}$$

Therefore $[f]^{-1} \circ [f] = [f] \circ [f]^{-1} = [e]$; inverse of each homotopy class exists.

This shows that homotopy classes of loops at x in the order parameter space S form a group which is denoted by $\pi_1(S, x)$ and is called *fundamental group* or *first homotopy group*. Subscript 1 denotes that fundamental group is a group of homotopic maps of one dimensional surface (loops) from physical space to the order parameter space. There can be mapping of higher dimensional surfaces also which form higher homotopy groups, $\pi_n(S, x)$, where $n > 1$.

B. Fundamental Group of a path connected space

Now we discuss the isomorphism between fundamental groups based at two different points in the order parameter space. As we are considering path connected order parameter space, therefore there is always a path which can connect any two points in the order parameter space. This allows to construct loop at any point in the order parameter space for a given loop at a base point, say y, see Fig. 2.9. In fact, all homotopic loops at y remain homotopic loops at other base point in the order parameter space under the mapping shown in Fig. 2.9; this mapping preserves homotopy classes. This mapping also preserves the group theoretical structure of the based fundamental group at y, in particular the combination law. This brings a one to one correspondence between fundamental groups at different base points in the path connected order parameter space. This correspondence between fundamental groups at different base points is a path isomorphism between the based fundamental groups. Thus only one based fundamental group is good enough to give an appropriate classification of topological defects for a given path connected order parameter space.

For an abelian fundamental group, all paths uniquely define the isomorphism between two based fundamental groups, see Ref. [2]. Thus, in the case of abelian fundamental group, there is always path independent correspondence in between two based loops in the order parameter space. In the case of non-abelian fundamental group it is not true. But still all fundamental groups, including non-abelian, are path isomorphic. The reason is that two different paths which connect the loops at different base points only differ by *inner automorphism* (path dependent mappings always can be connected through *inner automorphism* between them), and inner automorphism

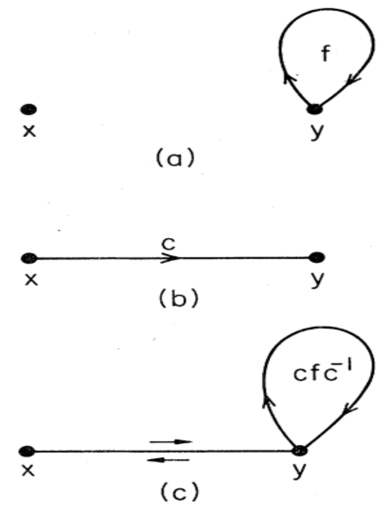

Figure 2.9: (a) shows two points x and y in the order parameter space, at point y there is a loop f. (b) since order parameter space is assumed to be path connected, therefore there will be always a path c which connects points x and y. (c) shows that $c \circ f \circ c^{-1}$ is a loop at x, which establishes the isomorphism between fundamental group at y and x. Figure has been taken from Ref. [2].

does not change the *conjugacy class* of the group, see details in Ref. [2]. Here we note that most of the order parameter spaces of physical systems have abelian fundamental group. Bi-axial nematic liquid crystal is an example where one gets non-abelian fundamental group.

C. Fundamental Group and free homotopic classes

To identify topological defects in the physical space, one takes mapping of order parameter field configurations on a hypothetical circle (of varying radius about a point) into the order parameter space. This does not require that all possible mappings around that region should have a common fixed point (base point) in the order parameter space. This mapping is free from any such kind of restriction and therefore topological defects actually should be characterized by *freely homotopic loops*, not by *based homotopy*.

When the restriction of base point is released then two loops f and g which lie at the same point, say x, are said to be *free homotpic maps* if they belong to the same conjugacy class of the group $\pi_1(S, x)$, i.e. if they are related by a relation $f \sim bgb^{-1}$. On the other hand if two loops do not lie at the same point, then there will be always a path $c(z)$ which can connect these two points. It should be noted that g is always freely homotopic to cgc^{-1}, and therefore if f is homotopic to cgc^{-1} (at the same point), i.e. $f \sim cgc^{-1}$, then f and g are said to be freely homotopic to each other (although at different points).

Equivalently we can say that a loop f at x is freely homotopic to loop g at y if and only if there is a *path isomorphism* $c(z)$ between homotopy class $[f]$ of based fundamental group $\pi_1(S, x)$ and homotopy class $[g]$ of $\pi_1(S, y)$. There can be many paths which can establish path isomorphism between these two homotopy classes. The set of all such path isomorphisms establishes a unique connection between the conjugacy classes of based fundamental groups at x and y such that it only rearrange the elements (loops) within a conjugacy class, without changing elements from one conjugacy class to other. Therefore classes of freely homotopic loops are labeled by conjugacy classes of fundamental group $\pi_1(S)$.

In the case of abelian fundamental group, each conjugacy class of the group consists only one element. Therefore line defects in the physical space has one to one correspondence with each element of the fundamental group (with appropriate winding number). Therefore fundamental group completely characterizes the topological defects. Two defects which belong to distinct elements of the group, can not continuously deform to each other by local deformation. The product of two non-trivial elements of the fundamental group gives a new element of the group (this loop will be freely homotopic to the combination of original pair of loops) which corresponds to different winding number defect in the physical space. This shows how two different winding number defects get combined to give a new kind of defect in the physical space, and vice-versa. We conclude that for media with the abelian fundamental group, when pair of defects combined, the byproduct of these two will have the winding number by simply addition of winding numbers of the original pair of defects.

In the case of media which has non-abelian fundamental group, a defect is characterized by the conjugacy classes of the fundamental group (classes of freely homotopic loops) and therefore the combination of the conjugacy classes gives a new conjugacy class (conjugacy class multiplication) which characterizes a new defect in the physical space; byproduct of combination of the pair of defects.

D. Examples

Fundamental group for order parameter space S^1 (for planar spin and superfluid) contains elements of homotopy classes which are characterized by winding number n. Combination of two homotopy classes with winding number n and m, gives a homotopy class with winding number $n + m$ and this combination is commutative, therefore fundamental group of S^1 is an abelian group, and is *isomorphic* to additive group of integers Z. Therefore, $\pi_1(S^1) = Z$. If the order parameter space is a surface of 2-sphere, all loops are shrinkable to a point in this space, therefore fundamental group of S^2 only contains one element, identity, which for an additive group is represented by 0. Therefore, $\pi_1(S^2) = 0$. This implies that no line defects are possible for a media which has order parameter space S^2.

If the fundamental group of a connected space is trivial (contains only identity), then the space is said to be *simply connected space*. S^2 is a simply connected space while S^1 is not.

Summary and some important points:

1. Coset space and order parameter space: All possible values of order parameter form a space known as the *order parameter space*. In the case of spontaneous symmetry breaking, if G is the symmetry group of the Lagrangian or Hamiltonian and H is the *isotropy subgroup* of G for a given value of order parameter, then *coset space*, G/H, is identified as the *order parameter space* or the *vacuum manifold* of the theory, as both spaces are *homeomorphic* to each other.

For example, in the case of *planar spin* and *superfluid* ^4He, respectively, $SO(2)$ and $U(1)$ symmetries break completely in the ordered phase. Therefore in both the cases isotropy subgroup H is an *identity*. Therefore coset space G/H in both cases is the group manifold of $SO(2)$ and $U(1)$ which is a circle S^1. In the case of *ordinary spin* in 3-dimensions, $SO(3)$ symmetry breaks to $SO(2)$, therefore coset space G/H in this case is $SO(3)/SO(2)$ which is a surface of 2-sphere S^2.

2. Meaning of topological defects: A topological defect corresponds to a singularity of the order parameter field in the physical space which is topologically protected - it can not be removed by local continuous deformation of the field configuration. A line topological defect arises due to non-trivial order parameter field configuration around a point in the physical space, which is characterized by a topological number known as winding number in the order parameter space. The mapping of this non-trivial field configuration in the order parameter space forms a non-shrinkable loop. Hence this is related with the non-trivial property of the order parameter space, which is characterized by the first homotopy group of the order parameter space.

3. Homotopy group and the dimensions of topological defects:

a) For a disconnected order parameter space, zeroth-homotopy group $\pi_0(S)$ is non-trivial. For example in the case of *Ising-model*, order parameter space is z_2, which is a disconnected space. In such a case, surface defects exist called *domain wall defects*.

$$\pi_0(S) \neq 0 \Longrightarrow \text{Domain wall/surface defects can exist.}$$

b) If the first homotopy group, i.e. fundamental group, of the order parameter space is non-trivial, e.g. in the case of circle S^1 order parameter space (planar spin and superfluid), then line defects (string defects) can exist. In the case of superfluid system these are called *superfluid vortices* and in the case of superconductor they are called *flux tube defects*.

$$\pi_1(S) \neq 0 \Longrightarrow \text{String/line defects can exist.}$$

c) If the second homotopy group is non-trivial for an order parameter space (as in the case of S^2), then a point defects can exist.

$$\pi_2(S) \neq 0 \Longrightarrow \text{Monopole/point defects can exist.}$$

d) If third homotopy group of the order parameter space is non-trivial, then a topological object can exist in the physical space, called *Skyrmion*, which also can be characterized by a winding number.

$$\pi_3(S) \neq 0 \Longrightarrow \text{Skyrmion, a topological object can exist.}$$

For example, in the case of linear-sigma model order parameter space is S^3, which has non-trivial third homotopy group. In the linear-sigma model skyrmions are identified with the *Baryons*. These objects are realized by a *stereographic projection* of S^3 to R^3. Skyrmions are the compact objects which only contains the gradient energy of the Lagrangian density or free energy density of the system.

Skyrmions can also exit in the lower space dimension. For example in the case of ordinary spin system, order parameter space is S^2 for which second homotopy group is non-trivial. In this case, therefore, a mapping from S^2 to compactified R^2 (if the physical space is of two dimension) gives skyrmions in the two dimension called *baby skyrmions*. Similarly, mapping from S^1, for which $\pi_1(S)$ is non-trivial, to compactified R^1 gives skyrmions in one dimension.

Bibliography

[1] C. Nash and S. Sen, **Topology and Geometry for Physicists**, Academic Press, Inc. (1987).

[2] N.D. Mermin, Rev. Mod. Phys. **51**, 591 (1979).

Chapter 3

Kibble Mechanism and Superfluidity

3.1 Topological Defects in Physical System

In the last chapter, we have discussed that topological defects are locations in the physical space where order parameter field becomes singular (ill defined) and this singularity can not be removed by a continuous local deformation and therefore is topologically protected. In a given phase of the physical system, free energy of the system should be minimized. Let us consider the $U(1)$ global theory, where in the symmetry broken phase, order parameter space is a circle which is parameterized by a phase θ. The order parameter field is a complex field, $\phi = \phi_0 e^{i\theta}$ with magnitude ϕ_0. In the equilibrium, order parameter field takes its value such that the free energy of the system gets minimized. The lowest free energy is obtained, when magnitude of the field $|\phi| = \phi_0$ lies on the vacuum manifold (a circle in our case). As we mentioned, at the location of topological defect, derivative of the order parameter (in this case phase θ) becomes singular. In such situation, to keep the energy density of the system finite, it is energetically favorable that order parameter field leave the minimum of the free energy or potential. By the consideration of the energetics, magnitude of order parameter field decreases towards the location of defect and vanishes at the exact location of the defect. This can be understood by considering the free energy density, as an example,

$$f = |\vec{\nabla}\phi|^2 - \alpha|\phi|^2 + \beta|\phi|^4 = \phi_0^2|\vec{\nabla}\theta|^2 + |\vec{\nabla}\phi_0|^2 - \alpha|\phi|^2 + \beta|\phi|^4 \tag{3.1}$$

Here α, β are the phenomenological constants. The first two terms on right hand side are the gradient energy term of field ϕ. As we mentioned that in the equilibrium ϕ_0 is spatially fixed, therefore one can ignore second gradient energy term in the region away from topological defect. In the near region of a topological defect, $|\vec{\nabla}\phi_0|$ becomes non-zero by the energetics arguments, which we discuss now. When one approaches towards the singular point of the field configuration, $|\vec{\nabla}\theta|$ increases. At the exact the location of topological vortex, if we keep ϕ_0 uniform in space, $|\vec{\nabla}\theta|$ diverges. Therefore it is energetically favorable that field leave the order parameter space and reduces its magnitude towards the location of defect such that $\phi_0^2|\vec{\nabla}\theta|^2$ term remain finite. At the exact location, where $|\vec{\nabla}\theta|$ could be singular, ϕ_0 becomes 0, giving finite energy to the system. The cost of this is that, at location of defect, free energy or potential energy becomes higher compared to the defect free region. Due to this reason, topological defect configurations contain higher energy with respect to rest of the region in the physical space. Since order parameter field is zero at the location of defect, therefore location of defect corresponds to the symmetry restored phase. In fact, topological vortices/strings have a core of size of the order of correlation length of the system. The core of a defect can be effectively considered as the symmetry restored phase. For example, the core of a superfluid vortex contains normal fluid. Thus, in a physical system, there is no actual singularity in the full order parameter field, even though topological defect form. In the location where there is a topological defect, the order parameter field climbs up the hill of the potential or free energy and becomes zero from non-zero value of outer region, see Fig. 3.1.

3.2 Kibble Mechanism

Now we discuss how these topological defects can form during a spontaneous symmetry breaking (SSB) transition due to a domain structure. This is usually known as Kibble mechanism [1] which explains the formation of any kind of topological defect or topological object during a SSB transition. Although the Kibble mechanism for

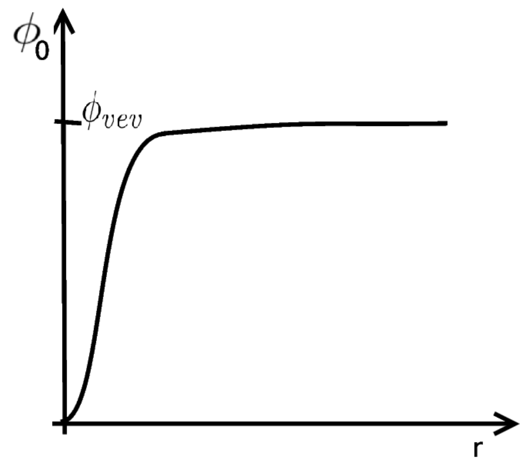

Figure 3.1: Figure shows the core field profile of a topological vortex. Towards the core, magnitude of the field gradually decreases to suppress the dominance of gradient energy of θ field in this region.

the formation of topological defects is quite general (even applicable to domain structure arising from causally disconnected regions), here we will discuss this mechanism in the context of phase transition.

The Kibble mechanism is a very general mechanism for the formation of topological defects during any kind of phase transition, first order as well as continuous phase transitions. In the Fig. 3.2 the dynamics of a first order phase transition has been shown. In the first order phase transition, due to the presence of meta-stable state in the effective potential or free energy density, system may stay for a while in this state. Thermal fluctuations or quantum mechanical tunneling through barrier lead to nucleation of ordered phase (true minimum state) in the background of disordered phase. Since these bubbles corresponds to the phase of ordered phase, therefore has lesser free energy and therefore grow in size with time (bubble of size lesser than a critical size shrinks). These bubbles coalesce with each other and by this, phase transition is completed, and whole space is filled up with ordered phase, except locations where topological defects form.

Let us again consider the $U(1)$ symmetry breaking (first order) phase transition. In this case the order parameter space is a circle which is parameterized by a phase θ. When these bubbles form, there can not be any correlation between any two

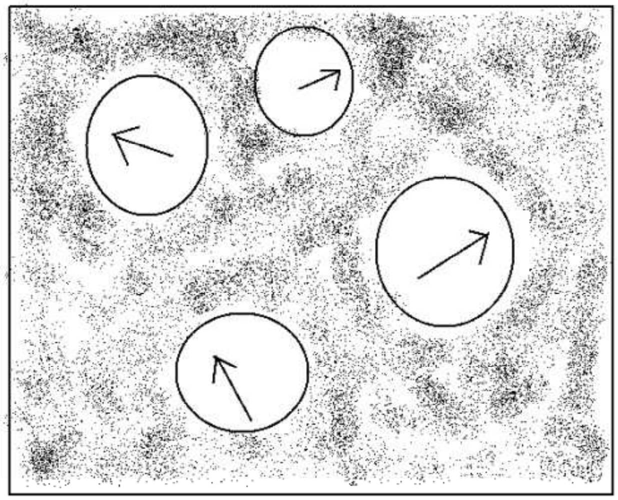

Figure 3.2: Figure shows the dynamics of a first order phase transition. In the first order phase transition, bubbles of ordered phase (arrow region) form in the background of disordered phase (shaded region).

bubbles, and therefore the phase value θ in a bubble is completely independent from the other one. This fact is one of the main ingredient of the Kibble mechanism for the formation of topological defects, which assumes that θ values vary randomly from one bubble to the other. One more important point is that, within a bubble, since order parameter field is correlated, and since free energy density or effective potential (in fact, the gradient energy term) gets minimized if θ does not have any spatial variation, therefore in each bubble θ can be considered to be uniform.

The second ingredient of the Kibble mechanism lies in the fact that, since the value of θ is completely arbitrary between two bubbles, therefore when two bubbles meet, in the intermediate region somehow field has to vary such that θ value of first bubble get connected with the other one. The way field interpolates in the intermediate region is governed by the *geodesic rule*. This rule, again, comes from the fact that total free energy density of the system has to be minimized, and again, in this case also, gradient energy arising due to field variation has to be minimized. As we have considered $U(1)$ symmetry breaking, therefore order parameter space is a circle. Therefore there will be always two paths on this order parameter space by which field can uniformly interpolate in the intermediate region, see Fig.3.3. The geodesic rule says that in the intermediate region field traverses such that it traces the shortest path on the order

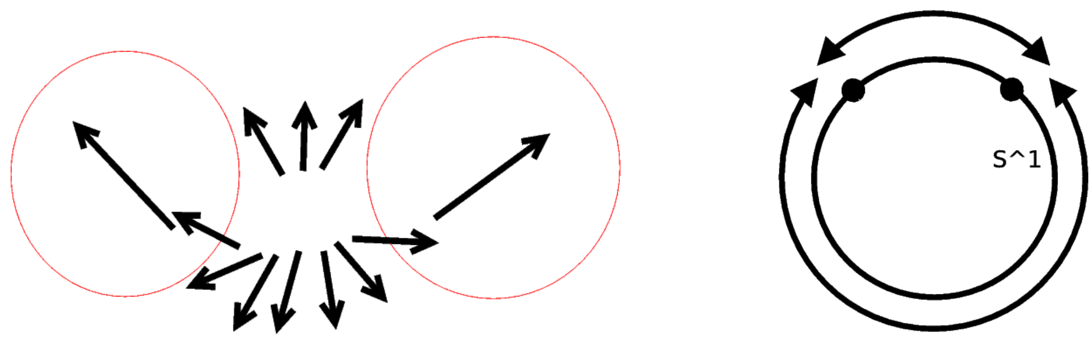

Figure 3.3: Left figure shows the situation when two bubbles, with random phase θ, meet in a region. In the intermediate region, θ can vary in two possible ways. The geodesic rule tells that those θ variation will be preferable whose mapping on the order parameter space traces the shortest path (right figure). Such shortest path minimizes the free energy of the system.

parameter space. It is clear that this gives the lesser gradient energy and therefore should be favored by a system, see Fig. 3.3. If we consider first bubble in the right hand side in the physical space with phase θ_1 and the second bubble in the left hand side with phase θ_2, then there can be two possibilities. First, if $\theta_2 - \theta_1 > 0$, then according to the geodesic rule, in the intermediate region, clockwise variation of θ is preferred if $\theta_2 - \theta_1 > \pi$. Second, if $\theta_2 - \theta_1 < 0$, then anti-clockwise variation of θ is preferred if $\theta_2 - \theta_1 < -\pi$.

If three or four bubbles meet at a point such that they can create a non-trivial winding of field configuration, then at that point topological defect of that winding number forms. Both ingredients of Kibble mechanism, discussed above, determine the formation probability of topological defects. Kibble mechanism predicts a unique probability of formation of defects. In the 2+1 dimensions, when three bubbles meet at a point, then one can calculate the formation probability of topological vortices as follows.

Let us consider three bubbles with phase θ_1, θ_2, and θ_3 meeting at a point, and their position ordering in the physical space is also in the same manner (as written the ordering of phase values) as one moves in anti-clockwise direction around the point (where they meet). Since all these bubbles are independent from each other, therefore phase values will be independent and can have any value on the order parameter space

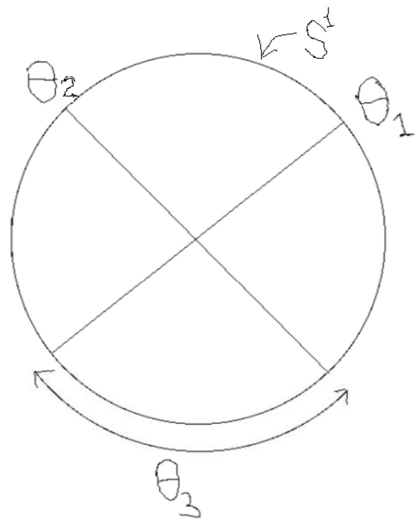

Figure 3.4: Figure shows, if θ_1 and θ_2 of 1^{st} and 2^{nd} bubbles are given, then what will be the possible range of phase, θ_3, of 3^{rd} bubble, such that a non-trivial winding can form around the meeting point.

from 0 to 2π. Let us consider the situation shown in the Fig. 3.4 where θ_1 and θ_2 has been specified on the order parameter space. For the given values of θ_1 and θ_2, according to the geodesic rule, to have a non-trivial winding, phase θ_3 should have value in the range, $\theta_1 + \pi < \theta_3 < \theta_2 + \pi$ (note that this range of θ_3, to have non-trivial winding, is coming due to the consideration of the geodesic rule). For given values of θ_1 and θ_2, the range of θ_3, say $\Delta\theta_3$, for which there can be a non-trivial winding, may have any value ranging from 0 to π. Therefore average value of this range will be $\pi/2$. Now, since θ_3 can take any value in between 0 to 2π, therefore the probability for formation of topological vortices or anti-vortices is $\frac{(\pi/2)}{2\pi} = \frac{1}{4}$ per three bubble junction. For a triangular lattice, number of bubbles is the same as number of junction. So we can conclude that probability of formation of vortices or anti-vortices is $\frac{1}{4}$ per bubble. This is the probability of formation of topological vortices when three bubbles meet at a point. In the case, if four bubbles meet at a point, then due to complexity of the problem, it is difficult to estimate probability of formation of topological vortices analytically. In such case even winding number two defects can form. Simulations show that the formation probability of vortices and anti-vortices in this case is about $\frac{1}{3}$ per bubble which is higher than the case when three bubbles meet.

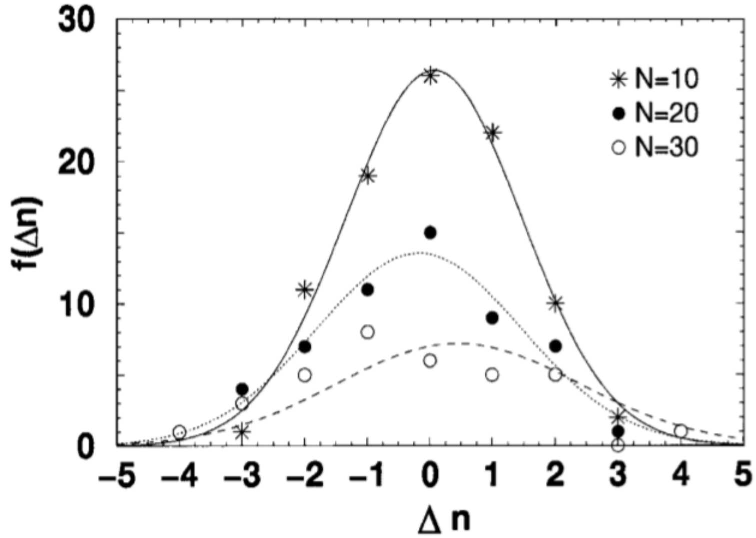

Figure 3.5: Figure shows the experimental result of Δn distribution for three different values of N. Figure has been taken from Ref. [3].

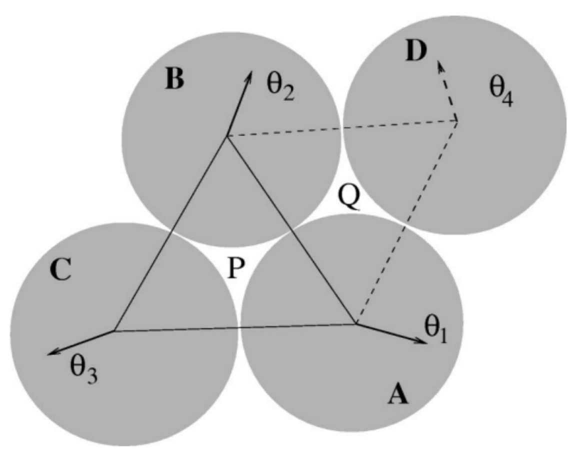

Figure 3.6: Figure shows that when three domains labeled A, B, and C meet at a point P such that they can create a +1 defect, then there is zero probability of having +1 defect at nearby point Q with any phase value in domain D, while there is still 1/4 probability of having -1 defect at this point. This shows that there is correlation between the formation of defects and anti-defects. Figure has been taken from the Ref. [2].

The probabilities of formation of topological vortices and anti-vortices are exactly equal in the Kibble mechanism and therefore there is no preference of one over the other. But, since the formation of topological defects in the Kibble mechanism is a statistical process, therefore in the finite size system, in a single event (phase transition), there can be a mismatch in the formation of number of vortices and anti-vortices. When one performs sufficiently large number of such events, then the difference between vortices and anti-vortices Δn follows a Gaussian distribution of width σ, centered at zero value. The zero mean value of the Gaussian distribution shows that there is no biasing in the formation of topological defects and anti-defects. Even, if one considers a single event, and divide the whole physical system into sub-regions, and calculates the Δn for each sub-region, then in this case also, Δn follows a Gaussian distribution, see Fig. 3.5. The width of this distribution, which we will discuss below, comes out $\sigma \propto N^{1/4}$, where N is the average number of vortices + anti-vortices in sub-regions. We know that, for a random process, width of the probability distribution follows 1/2 power law, while here we get 1/4 power law. This reflects the fact that the formation of vortices and anti-vortices are not completely random. In fact, there is a correlation in the formation of vortices and anti-vortices [2, 3] in the sense that, if a vortex forms, then there is a higher probability that in the nearby region an anti-vortex will form (while lesser probability for formation a vortex in the nearby region). This is shown in the Fig. 3.6 for the triangular lattice case. Therefore, due to this correlation (which reduces the randomness), Gaussian width σ, instead of 1/2, follows 1/4 power law.

Let us consider a finite square sub-region in the physical space. The side of the square is L and area is $A = L^2$. At the boundary of this square, there will be total $4(\frac{L}{\xi} - 1)$ bubbles (or domains) of diameter ξ. In the case of $L \gg \xi$, one can neglect 1 with respect to L/ξ. Therefore at the boundary of each square, there will be $4\frac{L}{\xi}$ number of bubbles. According to Kibble mechanism, phase θ varies randomly from one domain to other (only consider the domains which lie on the boundary of the sub-region). The maximum random variation of θ from one domain to other can be $\pm\pi$, while minimum variation can be 0. Therefore, on an average, from one domain to other, there can be $\pm\pi/2$ random variation of θ. Thus, this is a random walk problem of phase θ with step size $\pm\pi/2$ (note that this random walk of phase θ ultimately gives Δn for the given sub-region). In this random walk, the total number of steps, say N', will be the total number of domains at the boundary. The probability of right step ($+\pi/2$ variation) and left step ($-\pi/2$ variation) is equal, $p = q = 1/2$. Therefore, Gaussian width (of Δn distribution) for such random walker can be obtained by the relation, $\sigma = \sqrt{N'pq} = \sqrt{\frac{L}{\xi}}$. Therefore Gaussian width, in this case, goes as, $\sigma \propto A^{1/4}$ ($A = L^2$). Now if we consider a uniform defect density in the area covered by the sub-region, then $A \propto N$, where N is the total number of defects+anti-defects in that sub-region. This gives the $\sigma \propto N^{1/4}$. We again emphasize that, the exponent 1/4 shows that there is a correlation between the formation of defect and anti-defects in the Kibble mechanism which suppresses the randomness from 1/2 to 1/4 value. In general, σ can be defined by,

$$\sigma = CN^{\nu}, \tag{3.2}$$

where, $C = 0.71$ is obtained from numerical simulations for square domains (square lattice), and $\nu = 1/4$ is the theoretically predicted value by the Kibble mechanism. In Ref. [3], value of ν is observed in the liquid crystal experiment. The observed value of ν in this experiment is $\nu = 0.26 \pm 0.11$ which is very close to the theoretical value 0.25. In the experiment [3], authors plotted the distribution of Δn. The observed Δn follows the Gaussian distribution,

$$f(\Delta n) \propto e^{-\frac{(\Delta n - \overline{\Delta n})^2}{2\sigma^2}}, \tag{3.3}$$

which is shown in the Fig. 3.5.

In the case of continuous phase transition, due to absence of meta-stable state, order parameter field always remain in the minimum free energy state. Therefore, in this phase transition, whole space is filled up with domains of ordered phase (without any background of disordered phase), see Fig. 3.7. At the junction of three or four domains, depending upon phase values, topological defects can form. The arguments of the Kibble mechanism for the production of topological defects are exactly same in this case also, as discussed in the case of first order phase transition. The domain picture and geodesic rule are completely valid and probability of formation of defects and the physics of Δn distribution are also same. The only difference here is that the size of domains depend upon the rate of the phase transition. Note that the size of domains decide the defect density arising during the phase transition. Therefore in

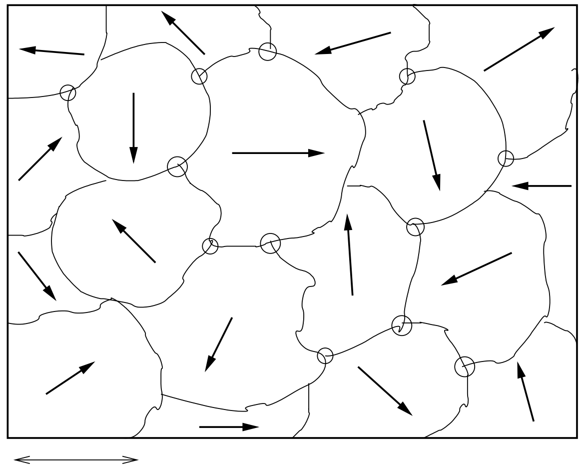

Figure 3.7: Figure shows the dynamics of a continuous phase transition. In the continuous phase transition, whole space is filled up with domains of ordered phase. Small circles show the junction where topological defects have formed.

this case, rate of phase transition decides what will be the topological defect density form during the transition. This physics was explored by Zurek [4], and this mechanism for production of topological defects in continuous transition is known as the *Kibble-Zurek mechanism*.

In Ref. [1], Kibble mentioned that, in the case of continuous transition, since in the critical region (also known as Ginzburg region), thermal fluctuations dominate, so within a domain phase θ never gets settled to a single minimum of the potential (or free energy density). In fact, in the critical region, with time, θ always fluctuates from one minimum to other. Due to this, within a correlated domain well defined phase θ does not exist (in the critical region, ordering never gets establish, although the symmetry breaks). Hence there is no formation of well defined topological defects in the critical region. When temperature reaches a sufficiently low value such that thermal fluctuations get suppressed and depth of the potential-minimum becomes sufficiently large, that total energy required to flip phase θ in a correlated volume starts dominating over the thermal energy present at that temperature, then below this temperature effect of fluctuations becomes sub-dominant and ordering inside domains gets establish. The temperature below which ordering establishes is known as the *Ginzburg temperature* T_G, and the correlation length at this temperature is known as the *Ginzburg correlation length* ξ_G. One can determine the Ginzburg temperature by equating free energy in a correlation volume and thermal energy at that temperature [1],

$$\xi^3 \Delta f = k_B T_G, \tag{3.4}$$

where k_B is the Boltzmann constant.

One should note that the argument presented above is valid, if the rate of phase transition is extremely slow so that, order parameter field gets sufficient time to settle to its equilibrium configuration. Such phase transition is known as the equilibrium phase transition. This picture will not be valid if the rate of transition is faster than the correlation time τ. The correlation time τ is the timescale, which decides, in how much time, a fluctuation in field can be sensed by a whole correlated volume, which can be obtained by dividing correlation length by speed of propagation of information. At the critical point, correlation length diverges and in the critical region its value is very large, generally decreasing with temperature following specific power law. In the context of cosmology, an information may propagate with the speed of light, while in a thermal system the speed of propagation of information is governed by the appropriate speed for relevant degrees of freedom. Therefore correlation time becomes very large in the critical region. Therefore it is clear that if the transition rate is faster than the correlation time, then any fluctuation will not get sufficient time to propagate in the whole correlation volume and remain frozen during the phase transition. Such phase transition is considered to be quench transition (non-equilibrium phase transition). Therefore, in such situation, domain size will not be the actual correlation length at that temperature, but it depends upon the initial temperature T_i of the system from where transition is performed. Below the critical point, phase θ chooses a random value within a domain (of size decided by the correlation length at temperature T_i). Due to fast dynamics of phase transition, this phase remain frozen in the domain, and ultimately give the defect density (different from the standard Kibble mechanism) [4, 5].

3.3 Superfluidity and Superfluid Vortices

Superfluidity arises when a bulk of bosonic particles, or Cooper pairs near the Fermi surface, form Bose-Einstein condensate. The particles, which participate in the condensation, move in space without loosing their energy and momentum. Because of this reason, superfluid has zero viscosity. As we know, Bose-Einstein condensation can be described by spontaneous symmetry breaking phase transition. In the case of ^4He system (and in many other systems also), superfluidity arises when $U(1)$ global symmetry spontaneously breaks. In such case, supefluid phase is characterized by a complex order parameter field. In the case of $U(1)$ symmetry breaking order parameter space is a circle S^1 which is parameterized by an angle θ, and order parameter field in this case is a complex scalar field, $\phi = \phi_0 e^{i\theta}$. As we have discussed in Chapter 2, the fundamental group for S^1 order parameter space is isomorphic to the additive group of integers $\mathcal{Z}$, i.e., $\pi_1(S^1) = \mathcal{Z}$. This implies that topological vortices can exist in such system. These are superfluid vortices. Such kind of superfluid vortices exist in ^4He system, in neutron superfluid phase inside neutron star, and also, in the color-flavor locked phase of QCD.

Superfluid component is characterized by multi-particle condensate wave function,

$$\Psi = \Psi_0 e^{i\theta}, \tag{3.5}$$

where $|\Psi_0|^2 = n_0$ is the number density of superfluid components. A spatial variation of phase θ provides the motion to superfluid. The quantum probability current for this wave function ultimately gives a macroscopic motion of superfluid with a curl free velocity profile. This can be seen by relating macroscopic current density $n_0\vec{v}_s$ with probability current density $(\hbar/m)n_0\vec{\nabla}\theta$ of the above wave function [6], where m is the mass of constituent of condensate. This gives the velocity of superfluid component,

$$\vec{v}_s = \frac{\hbar}{m}\vec{\nabla}\theta. \tag{3.6}$$

This clearly shows that superfluid flow is a potential flow (curl free), since,

$$\vec{\nabla} \times \vec{v}_s = 0. \tag{3.7}$$

This special property of the superfluid, which arises due to its quantum nature, makes its motion highly restrictive and does not allow it to rotate below a critical angular velocity ω_{cr} under a (external) rotation of the vessel [6],

$$\omega_{cr} = \frac{\hbar}{mR^2} \log\left(\frac{R}{a}\right), \tag{3.8}$$

where R is the radius of the vessel, and a is the length scale of the order of atomic distances which still allows for statistical treatment of the system on that length scale. However, it can be shown by energetics arguments [6] that above the critical angular velocity, superfluid start rotating by following a curl free velocity profile given by, $\vec{v} = \frac{1}{r}\hat{\theta}$, in region away from the center of the vessel. This is the nucleation of a superfluid vortex at the center of the vessel. As we have mentioned in the first section of this Chapter, in the core of a superfluid vortex, to minimize gradient energy density, n_0 decreases (fraction of normal component increases). Therefore exactly at the center of a superfluid vortex there is no divergent flow of superfluid, as no superfluid component exist at the center of a superfluid vortex. When one increases the angular velocity of the vessel further, more number of vortices start nucleating and form a (rotating) vortex-lattice. This is known as the *vortex model* for superfluid system in a rotating vessel. It predicts that at large angular velocity ω of the vessel, number of vortices increases with ω as [7],

$$N = mR^2\omega/\hbar. \tag{3.9}$$

In 1967, Hess and Fairbank [8] performed experiment for the verification of vortex model discussed above. To check this model they performed superfluid transition in the presence of rotation. For a given angular velocity of the vessel, they measured angular momentum of the superfluid arising due to the formation of vortices during the superfluid transitions. A superfluid vortex has a quantized angular momentum, so when one increases the angular velocity of vessel, angular momentum of the superfluid increases discontinuously. Fig.3.8 shows the results of Hess and Fairbank experiment. In the plot, along y-axis, measured value of angular momentum of superfluid with respect to angular velocity of vessel has been plotted. Dashed-dotted plot corresponds to the angular momentum of a classical fluid. Solid lines correspond to the prediction of vortex model. Data points are experiment results. Although this experiment gives a good support to the vortex model, there are some data points which show some discrepancy also from the vortex model. This discrepancy could be

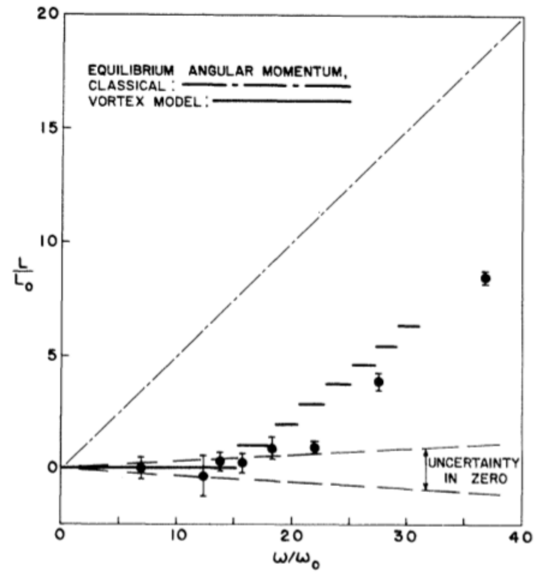

Figure 3.8: Figure shows the experimental result of angular momentum measurement of superfluid component during superfluid transition in a rotating vessel. $L_0 = N_h \hbar \rho_s/\rho$ and $\omega_0 = \hbar/mR^2$, where N_h is the total number of helium atoms. Figure has been taken from Ref. [8].

arising because during the superfluid phase transition, there is no guarantee that one gets exact number of vortices as predicted by the vortex model. As we have discussed that topological defects during a phase transition are formed via the Kibble mechanism. Therefore such superfluid phase transitions will be dominated by the Kibble distribution of vortex as discussed in the last section. This fact may be responsible for such kind of discrepancy observed in the experiment. For detail discussion on this issue see next Chapter.

Bibliography

[1] T.W.B. Kibble, J. Phys. A **9**, 1387 (1976).

[2] R. Ray and A.M. Srivastava, Phys. Rev. D **69**, 103525 (2004).

[3] S. Digal, R. Ray, and A.M. Srivastava, Phys. Rev. Lett. **83**, 5030 (1999).

[4] W.H. Zurek, Nature **317**, 505 (1985).

[5] W.H. Zurek, Phys. Rep. **276**, 177 (1996).

[6] E.M. Lifshitz and L. P. Pitaevskiĭ, **Statistical Physics, Part 2, Theory of the Condensed State**, Pergamon Press (1980).

[7] D.R. Tilley and J. Tilley, **Superfluidity and Superconductivity**, Third Edition, Overseas Press (2005).

[8] G.B. Hess and W.M. Fairbank, Phys. Rev. Lett. **19**, 216 (1967).

Chapter 4

Formation of Topological Vortices during Superfluid Transition in a Rotating Vessel

Formation of topological defects during symmetry breaking phase transitions via the *Kibble mechanism* is extensively used in systems ranging from condensed matter physics to the early stages of the universe. Kibble mechanism uses topological arguments and predicts equal probabilities for the formation of defects and anti-defects. Certain situations, however, require a net bias in the production of defects (or antidefects) during the transition, for example, superfluid transition in a rotating vessel, or flux tubes formation in a superconducting transition in the presence of external magnetic field. In this chapter we present a modified Kibble mechanism for a specific system, ^{4}He superfluid transition in a rotating vessel, which can produce the required bias of vortices over antivortices. Our results make distinctive predictions which can be tested in superfluid ^{4}He experiments. These results also have important implications for superfluid phase transitions in rotating neutron stars and also for any superfluid phases of QCD arising in the non-central low energy heavy-ion collision experiment due to an overall rotation. Results discussed in this chapter have been presented in Ref. [1].

4.1 Introduction and Motivation of the Work

Topological defects arise in a wide range of systems ranging from condensed matter physics to the early stages of the universe. Formation of these defects during symmetry breaking transitions has been a very active area of research, especially in last few decades, bringing out important interconnections between condensed matter physics and particle physics. Indeed, the first detailed theory of formation of topological defects via a domain structure arising during a phase transition was proposed by Kibble [4] in the context of early universe. It was proposed by Zurek that certain aspects of Kibble mechanism can be tested in superfluid helium systems [3]. It is now well recognized that the basic physical picture of the Kibble mechanism applies equally well to any symmetry breaking transition [4, 5] thereby providing the possibility of testing the predictions of Kibble mechanism in various condensed matter systems, see refs. [6–10]. It is particularly important to note that the basic mechanism has many universal predictions making it possible to use condensed matter experiments to carry out rigorous experimental tests of these predictions made for cosmic defects [9, 10]. Defect formation in continuous transitions raises important issues due to critical slowing down. The Kibble-Zurek mechanism incorporates these aspects and leads to specific predictions of the dependence of defect densities on the rate of transition etc. [3, 4].

Basic physics of Kibble mechanism lies in the formation of a domain structure during a phase transition where order parameter field varies randomly from one domain to another. Individual domains represent correlation regions where order parameter field is taken to be uniform. Another important physical input in the Kibble mechanism is the assumption of smallest variation of the order parameter field in between the two adjacent domains (the so called geodesic rule). With these two physical inputs, a geometrical picture emerges for the physical region undergoing phase transition, and straightforward topological arguments can be used to calculate the probability of formation of defects and anti-defects. It is important to note that the probability of defect formation in the Kibble mechanism is calculated *per correlation domain* and it is a universal prediction. Indeed, utilizing this universality, defect formation probability for Kibble mechanism was experimentally tested in liquid crystal experiments [8] for a first order transition case where correlation domains could be directly identified as bubbles of the nematic phase nucleating in the background of isotropic phase. However, for a continuous transition, direct identification of correlation domains is not possible. Further, here effects of critical slowing down introduce dependence of relevant correlation length on the rate of transition [4]. The Kibble-Zurek mechanism incorporates these non-trivial aspects of phase transition dynamics for the case of continuous phase transitions in prediction of defect density [3, 4]. We now note that for the cases under consideration, these topological calculations give equal probability for the formation of defects and anti-defects. Of course this is on the average, and there can be excess of defects or antidefects in a given event of phase transition. Kibble mechanism leads to important predictions about the typical value of this excess which, for the case of U(1) vortices in 2 space dimensions is found to be proportional to $N^{1/4}$ where N is the total number of defects plus antidefects [10].

There are many physical situations which require a net excess of defects or antidefects (i.e. a non-zero value of the average net defect number) in a phase transition due to external conditions. For example, formation of flux tubes in type II superconductors in the presence of external magnetic field will lead to a net excess of flux tubes oriented along the direction of external field. Similarly, a ^{4}He system undergoing a superfluid transition in a rotating vessel will lead to a net excess of vortices. Along with these excess defects (or anti-defects), there will also be a random network of defects/antidefects resulting from domain structure via the conventional Kibble mechanism. Normally, the net defect formation (e.g. superfluid vortex formation in a rotating vessel) is studied using arguments of energetics [11,12]. But the formation of superfluid vortices in a rotating vessel during the superfluid transition also includes contribution from a non-equilibrium defect production process (via the Kibble mechanism) due to which number of formed vortices during the transition can deviate from the vortex model prediction.

In 1967, Hess and Fairbank [14] performed superfluid transitions in a rotating vessel to verify the Landau's irrotational theory of superfluid [15] and Onsager-Feynman vortex model [12]. According to this theory, superfluid component does not rotate if containing vessel rotates with angular velocity smaller than a critical value Ω_{cr}. A single superfluid vortex nucleates if vessel rotates with angular velocity larger than a critical value Ω_{cr} and number of vortices increases with Ω which follow some equilibrium configuration [12]. For experimental verification, Hess and Fairbank [14] performed superfluid transition in the presence of rotation from very low value of $\Omega < \Omega_{cr}$ to some higher values. They concluded from the measurement that there is no rotation of superfluid components below Ω_{cr}. They observed that at higher value of Ω superfluid components have angular momentum and follows the trend of vortex model. At that time Kibble mechanism (1976 [4]) was not available and Zurek' proposal (1985 [3]) for the applicability of this mechanism for the superfluid transition was not present. After the Zurek's proposal Kibble mechanism was tested for superfluid transition in the absence of rotation [6]. Although Hess and Fairbank experiment showed that superfluidity follows Onsager-Feynman vortex model, they also got very strong deviation from the expectation of vortex model, e.g. just above the critical angular velocity they got unexpectedly opposite rotation (antivortex) of superfluid component which can not be explained by the vortex model, similarly, with little higher angular velocity they didn't get expected number of vortices as predicted by vortex model. Their results clearly show that for vortices formation during phase transition energetics arguments (vortex model) can not be applicable, but other mechanism has to be proposed. Hess and Fairbank themselves mentioned in their paper that the discrepancy in their results from vortex model may be coming due to departure from the equilibrium for which Onsager-Feynman vortex model is not applicable.

Kibble mechanism is the mechanism for production of topological defects during a phase transition and one may expect its applicability even in the presence of rotation also with some modifications. Kibble mechanism without any rotation of the vessel, for superfluid transition is very well tested [6]. It predicts that vortex and antivortex formation is completely statistical, and if one performs phase transition sufficiently large number of times then on an average one gets equal number of vortices and antivortices (see Fig.10.1). Hess and Fairbank also took few number of events for their experiment but this number may not be good enough for a good statistics to get exact average value and may be because of this reason they got antivortex and other deviations from the vortex model. In this chapter we present the modified Kibble mechanism in the presence of rotation of the vessel and show that distribution of defects follows gaussian distribution in this case also (see Fig.10.1) which may be able to address the discrepancy of vortices in Hess and Fairbank experiment. As we elaborate below, in the presence of external influence (rotation of initial fluid here, or external field for superconductor) the basic physics of Kibble mechanism needs to be modified.

Two most important ingredients of Kibble mechanism are, existence of correlation domains inside which the order parameter is taken to be uniform, while the order parameter varies randomly from one domain to another, and the geodesic rule which says that the order parameter variation in between two domains is along the shortest path in the order parameter space. (We mention that the geodesic rule becomes ambiguous for the case of superconductors as discussed in [13]. This makes our considerations of the present paper non-trivial for superconductors, we will present it in a follow up work.) We will show below that to get a net excess of defects or antidefects in the presence of external influence (e.g. rotating vessel) both of these aspects of Kibble mechanism need to be modified; a given domain can no longer represent uniform value of the order parameter, rather each domain will have certain systematic variation of the order parameter field originating from the external influence. Further, the same external influence also affects the geodesic rule. In certain situations, the variation of order parameter in between two adjacent domains may trace a longer path on the vacuum manifold in apparent violation of the geodesic rule. We will show that this modified Kibble mechanism leads to reasonable predictions of a net excess of defects, along with a random network of defects/antidefects. Interestingly, it shows very systematic deviations for the random component of the excess of defects or antidefects from the Kibble prediction of $N^{1/4}$. We find that this excess becomes larger with larger external bias. This is an important prediction of the *biased Kibble mechanism* proposed here, and can be tested in experiments. This fluctuation in the net excess of defects resulting from the phase transition, on top of the average net defect number arising from the rotation may account for the experimental results of Hess and Fairbank [14] for superfluid transition in a rotating vessel where deviations from the energetics based net vortex number (at times even negative vortex number) were found.

4.2 Description of the System

Superfluid component is characterized by a multi-particle condensate wave function, $\Psi = \Psi_0 e^{i\theta}$, where Ψ_0^2 gives number density of superfluid component. The superfluid velocity is given by $\vec{v_s} = \frac{\hbar}{m}\vec{\nabla}\theta$, where m is the mass of ^{4}He atom. We use the expression for the free energy of the superfluid system in the presence of rotation [11, 16] as $F' = F - \vec{L}.\vec{\Omega}$, where F is the free energy for superfluid without rotation and $\vec{L} = \rho_s \int (\vec{r} \times \vec{v_s}) d^2x$ is the angular momentum of the superfluid (in the plane perpendicular to the axis of rotation) just after the phase transition generated due to external rotation ($\rho_s = m\Psi_0^2$ is the mass density), $\vec{\Omega}$ being the angular velocity of the vessel containing superfluid. Here we are assuming that part of normal component which undergoes superfluid condensation carries same angular momentum as before the transition. (Though, it may be possible that only a fraction of the momentum of the normal fluid part which is condensing is carried over to the superfluid momentum. Effects of this possibility on our analysis requires a further study. One can determine the value of this fraction experimentally using a rotating annulus of the kind suggested in ref. [3].) In two spatial dimensions, free energy density is given by,

$$f' = f - \rho_s(\vec{r} \times \vec{v_s}).\vec{\Omega}, \tag{4.1}$$

where f is the free energy density of superfluid without any rotation. We thus get [4],

$$f' = \alpha|\Psi|^2 + \frac{\beta}{2}|\Psi|^4 + \frac{\hbar^2}{2m}\Psi_0^2|\vec{\nabla}\theta|^2 - \Omega\rho_s r\frac{\hbar}{m}|\vec{\nabla}\theta|, \tag{4.2}$$

where α and β are phenomenological coefficients. For temperatures less than the superfluid transition temperature, $\alpha < 0$ and we determine the local value of condensate density Ψ_0 by minimizing the free energy neglecting the rotation. (One can discuss the effect of rotation on Ψ_0, even far away from vortices, especially in presence of boundaries. We keep analysis of this issue for future discussions.) With constant superfluid density Ψ_0, we minimize this free energy density with respect to $|\vec{\nabla}\theta|$ and get,

$$|\vec{\nabla}\theta|_{bias} = \frac{m\Omega r}{\hbar}. \tag{4.3}$$

This shows that the equilibrium configuration of Ψ requires a non-zero value of $|\vec{\nabla}\theta|$ in the presence of rotation. (Note, for the non-rotating case, we get $\theta =$ constant, as is assumed inside a domain in the conventional Kibble mechanism.) Note that $|\vec{\nabla}\theta|_{bias}$ is proportional to the distance from the origin, this will play an important role for the biasing in the production of vortices over antivortices as we will see below.

4.2.1 The domain structure in the presence of rotation

One of the main ingredients of Kibble mechanism is the randomness of the condensate phase θ from one correlated domain to other. As we have discussed, for superfluid phase transition in the presence of rotation, order parameter θ cannot be uniform inside any domain, it must vary systematically inside each domain. In this modified domain picture we still use the fact that all domains are independent from each other and have completely random θ value at the center of domain. (This type of picture was invoked in an earlier work by some of us where biased Skyrmion production due to non-zero baryon chemical potential was studied via a modified Kibble mechanism for a toy model in 1+1 dimensions [17].) Further, the order parameter variation inside domain has to be such that it preserve the curl free motion of superfluid. As we have mentioned, here we are assuming that part of normal components which undergoes superfluid condensation carries the same angular momentum as before the transition, and we know that normal components follow rigid-body rotation with velocity given by $\vec{v_n} = \Omega r\hat{\theta}$ which has non-zero curl. With transition to the superfluid phase, we model the domain structure in the presence of initial rotation such that curl free property of superfluid does not get violated inside a domain. We assume that only on the circular arc within a given domain, drawn using the center of the vessel and passing through the center of that domain has superfluid velocity as that was of normal component before the transition. This will give the gradient of θ on that arc to be the same as given by Eq.(4.3). We can see this by relating velocity of superfluid components with normal components on the circular arc, i.e., $v_s = v_n$, which gives $|\vec{\nabla}\theta|_{bias} = \frac{m\Omega r}{\hbar}$, which is the same as earlier obtained by minimizing the free energy density. It means that larger r domain will have more variation in θ than the domains with smaller r. As we will see, this is precisely the feature that will cause the biasing in the formation of vortices over antivortices.

Now as there is no initial radial flow, we don't expect any radial superflow inside a domain also. This means that θ will be uniform in the radial direction inside each domain. With these considerations, we obtain well defined values of θ at every point of a domain. We note that inside a given domain, gradient of θ decreases with increase in r, this domain structure provides curl free motion of superfluid. So with this, for the rotation of the initial normal component whose velocity increases with r, after becoming superfluid, the velocity becomes $1/r$ dependent inside a given domain. This can be viewed as the effect of superfluid transition on the velocity profile inside a given correlation domain. Since with all this, outer domains have stronger variation of θ (see Eq. 4.3), therefore, for the anti-clockwise rotation of vessel, we should get more number of vortices than anti-vortices. This bias will depend upon Ω, system size (r dependence) and also correlation length ξ (large values of ξ will give more $\Delta\theta$ inside a domain). Below we will see that biasing will also depend on the inter-domain separation due to modified geodesic rule.

4.2.2 The geodesic rule in the presence of rotation

We now consider the effect of the rotation on the geodesic rule, the way phase θ interpolates in between two adjacent domains. Conventional Kibble mechanism assumes the *geodesic rule* which states that θ in between two adjacent domains traces the shortest path on the vacuum manifold. Physical motivation for this rule comes from minimizing the free energy in the inter-domain region. (As we mentioned, for gauge case, as for a superconductor, phase variation between two different points is a gauge degree of freedom and has no physical significance like gradient energy. Hence assumption of geodesic rule for gauge case raises conceptual issues, see ref. [13].) One should note that this *conventional* geodesic rule does not require specification of how large the inter-domain region actually is. However, we will see that for the biased case, the physical extent of the inter-domain region becomes an important parameter. We will still follow the physical consideration of minimizing the net free energy in the inter-domain region.

For the inter-domain region also we assume that at the center of this region, the superfluid velocity is the same as the velocity of the initial normal fluid component. For geodesic rule only the gradient terms of free energy density are important, so by ignoring $|\Psi|$ terms from the free energy density we have,

$$f' = a|\vec{\nabla}\theta|^2 - b|\vec{\nabla}\theta|, \tag{4.4}$$

where $a = \frac{\hbar^2}{2m}\Psi_0^2$ and $b = \Omega\rho_s r\frac{\hbar}{m}$. We are interested in gradient in the direction of shortest distance between boundaries of two successive domains. So in this direction gradient can be written as $|\vec{\nabla}\theta| = (\theta_2 - \theta_1)/d$, where θ_1 and θ_2 are the order parameter values at the boundary of 1st and 2nd domain respectively when we traverse, in the physical space, from right to left (anti-clockwise path) and d is the shortest distance between two successive domains. Now we have to determine path for which free energy density gets minimized. There are two possible paths on the order parameter space. If $\theta_2 > \theta_1$, for anti-clockwise path free energy density,

$$f_1' = a(\theta_2 - \theta_1)^2/d^2 - b(\theta_2 - \theta_1)/d \tag{4.5}$$

and for clockwise path,

$$f_2' = a(\theta_2 - \theta_1 - 2\pi)^2/d^2 - b(\theta_2 - \theta_1 - 2\pi)/d. \tag{4.6}$$

Out of these two paths, one of the path will have lower free energy density. Clockwise path will be preferable if condition, $f_2' - f_1' < 0$ get satisfied, which gives, $\theta_2 - \theta_1 > bd/(2a) + \pi$. Putting values of a and b, we get,

$$(\theta_2 - \theta_1) > d|\vec{\nabla}\theta|_{bias} + \pi, \tag{4.7}$$

which is more restrictive condition to have clockwise path on order parameter space than the case when there is no rotation.

Now, if $\theta_2 < \theta_1$, free energy density f_1' given by Eq.(4.5) will be for clockwise path. For anti-clockwise path free energy density will be,

$$f_2' = a(\theta_2 - \theta_1 + 2\pi)^2/d^2 - b(\theta_2 - \theta_1 + 2\pi)/d. \tag{4.8}$$

Now in this case, condition $f_2' - f_1' < 0$ will be for anti-clockwise variation on the order parameter space, which gives,

$$\theta_2 - \theta_1 < d|\vec{\nabla}\theta|_{bias} - \pi, \tag{4.9}$$

which is more supportive condition to have anti-clockwise variation of θ than without any rotation. Thus, in both the cases, rotation of vessel supports anti-clockwise variation of θ on the order parameter space over clockwise variation even though the path is longer. This shows that rotation generates biasing in the geodesic rule also. These modified geodesic rules (Eq.(4.7) and Eq.(4.9)) will also contribute in the biasing of vortices formation over antivortices, along with modified domain structure. Note that for Eq.(4.7) and Eq.(4.9), we have considered that the variation of θ is along the direction of initial flow. If θ variation is considered along a different direction, then suitable projection of $|\vec{\nabla}\theta|_{bias}$ should be taken.

4.3 System parameters and Simulation details

We consider a cylindrical vessel of radius $R = 40\mu m$, and study formation of vortices in an essentially two dimensions system. We have taken such a small vessel because of computational limitations. Note that effective two dimensions requires that the height of the cylinder should be small (i.e. not too large compared to the correlation length). This will avoid string bending and formation of string loops which has to be handled in a full three-dimensional simulation. Certainly, it will be very interesting to see the effects of rotating cylinder in the formation of strings (including string loops) in a full three-dimensional simulations and we plan to investigate it in future. We have taken temperature of the system below the Ginzburg regime. The critical temperature T_c and the Ginzburg temperature T_G for He II system is (Ref. [16]) $2.17K$ and $2.16K$ respectively. The correlation length for this system is given by Ref. [3],

$$\xi = \xi_0 \epsilon^{-\nu}, \tag{4.10}$$

where $\xi_0 = 4\mathring{A}$, $\epsilon = (T_c - T)/T_c$, $\nu = 2/3$. With this expression, the Ginzburg correlation length ξ_G (correlation length at $T = T_G$) for this system can be calculated to be $144\mathring{A}$. As ordered domain structure only can form temperature below T_G, therefore we have taken correlation length ξ of the system $140\mathring{A}$ smaller than ξ_G. We have taken inter-domain distance $d = 10\mathring{A}$ (as a sample value, we will discuss the effect varying d on our results). We have considered anti-clockwise rotational of the vessel with angular velocity $\Omega\hat{z}$. The critical angular velocity for this system, for production of vortices by energetics argument, will be $\Omega_{cr} = \frac{\hbar}{mR^2}\log(R/\xi) \cong 78\ rad\ s^{-1}$ (note that radius of the vessel is very small giving very large Ω_{cr}).

For our two-dimensional simulation, we take a square lattice with the correlated domains centered at the lattice points. Domains are assumed to be square with side ξ so that lattice constant is $(\xi + d)$ with d being the inter-domain separation as mentioned above. We have performed simulation only in the first quadrant of the vessel. So the numbers we get should be multiplied by 4 to get the total number of vortices for the whole vessel. Our focus will be on the probability of vortices per domain. (Note that even for the whole system, the center of the vessel is within a domain so cannot accommodate a vortex at that point.) We take the lattice to start from non-zero coordinates (excluding the x and y axes). For winding number calculations (to locate vortices) we have excluded plaquette which touch the boundary of the vessel.

The essential physics of the Kibble mechanism is implemented by taking random θ value at each lattice points (i.e. at the center of domains). We know from the Eq.(4.3) the gradient of θ at the circular arc, passing through the center of the domain. By knowing the value of θ at the center of the domain, and gradient of θ on this arc, we can determine θ at each point on the arc. With this, by using the fact that there is no flow in the radial direction, so θ is uniform in this direction, we obtain phase value at the domain boundaries which lie on the side of lattice. We also use modified geodesic rule Eq.(4.7) and Eq.(4.9) for variation of θ in the inter-domain region. To implement this rule, as we mentioned, we assume that at the center-point of inter-domain region (which is the middle point of a link) superfluid has same velocity as was of normal components before the transition (given by Eq.(4.3)). We project this velocity along the direction of lattice side to get $\vec{\nabla}\theta$ along the lattice side. With this, and knowing the values of θ at domain boundaries, we implement the modified geodesic rule Eq.(4.7) and Eq.(4.9) to know θ variation in that region. With all this, we calculate winding in each plaquette. Depending upon the winding, at the center of a plaquette we obtain vortex or antivortex.

4.4 Results of Simulation

Now we present the results of our simulation. We consider different values of the angular velocity Ω, and for each Ω we generate 5000 events for defect formation to get good statistics of vortex-anti-vortex production. Fig.10.1 shows the distribution of net defect number Δn (= defect number $-$ anti-defect number) for 5000 events. The left plot shows the distribution without any rotation of vessel ($\Omega = 0$), we get standard distribution as predicted by the Kibble mechanism. This distribution follows Gaussian distribution $f(\Delta n) = ae^{-\frac{(\Delta n - \overline{\Delta n})^2}{2\sigma^2}}$. By fitting the distribution, we obtain the parameters of this Gaussian as: $a = 656.40$, $\overline{\Delta n} \cong 0$, $\sigma = 30.46$ (we have taken bin width 10 with error bars on the plot taken as $[f(\Delta n)]^{1/2}$ for each bin value). Important point to note is that center of Gaussian $\overline{\Delta n}$ has zero value which is the standard prediction of Kibble mechanism; no biasing in the formation of vortices and antivortices (on the average). We obtained average total number of defects from the simulation to be $N = 1857948$. Kibble mechanism makes an important prediction of relation between σ and N Ref. [10], $\sigma = CN^{\nu}$, where value of C for square domains is 0.71. The exponent ν is universal and its theoretical value is $\nu = 1/4$ for the present case. From the obtained value of σ and N with simulation, we derive value of $\nu = 0.2604$, which is quite close to the theoretical value 0.25 and matches well with the experimental value of $\nu = 0.26 \pm 0.11$ obtained for liquid crystal case, see ref. [10].

The right (red) plot in Fig.1 gives the distribution of Δn for the case of vortex formation during superfluid transition in a rotating vessel with angular velocity 10^3 $rad\ s^{-1}$. We see that in this case also we get a Gaussian distribution but shifted with the mean value $\overline{\Delta n} = 25$, which clearly shows that there is a biasing in the formation of vortices over antivortices. For the whole cylinder, we thus expect to get on an average more than 100 vortices over antivortices in the vessel. This bias in the net value of Δn occurs here because of the modification in the domain structure and geodesic rule in the presence of rotation. Thus our proposed modification of the Kibble mechanism, with modified domain structure along with the modified geodesic rule, is able to accommodate the expected bias in the net value of Δn due to the rotation of the vessel.

Table 4.1 shows the obtained values of $\overline{\Delta n}$, σ, and N from simulations at different

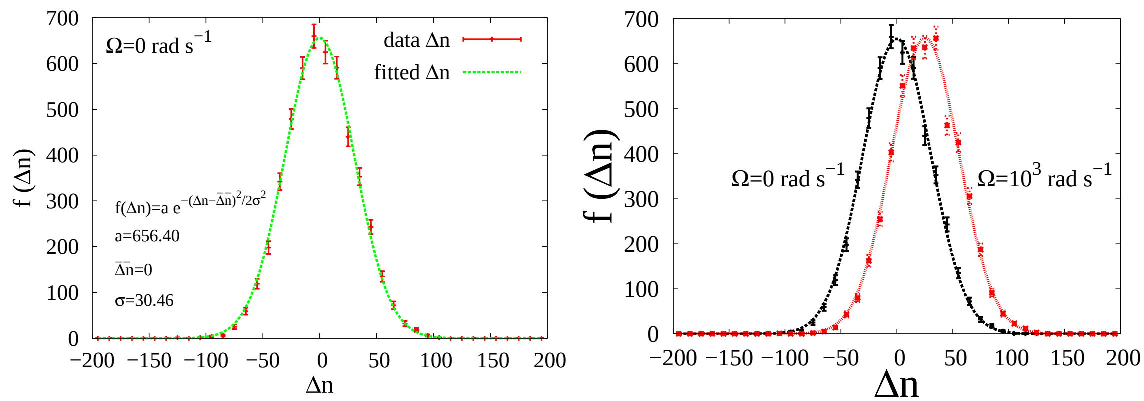

Figure 4.1: Distribution of vortices − antivortices. Left (and black in right) plot shows the case without any rotation of the vessel ($\Omega = 0$) giving the mean value of Gaussian distribution, $\overline{\Delta n} = 0$. Right plot corresponds to the case with angular velocity of the vessel $\Omega = 10^3\ rad\ s^{-1}$ showing that $\overline{\Delta n}$ gets shifted from zero to value 25, showing a net biasing in formation of vortices over antivortices. As we simulate only a quadrant, the full vessel will give value of net $\overline{\Delta n}$ of about 100.

Ω values; note that for each Ω we have generated 5000 events and performed simulations. Values of ν is obtained from the relation $\sigma = CN^{\nu}$, $C = 0.71$. It is very clear that with Ω all the other quantities are increasing.

Fig.10.2 shows the dependence of $\overline{\Delta n}$ on Ω (axes are in log-log scale). This plot clearly shows that $\overline{\Delta n}$ linearly increases with Ω with slope 0.024. Slope will be about 0.1 (4 times higher) for the full cylindrical vessel. As shown in Table 4.1, for $\Omega = 0$ we find $\overline{\Delta n} = 0.0$ as expected from the usual Kibble mechanism. However, the straight line fit in Fig.1 does not pass through the origin (0,0) of the plot, instead it gives $\overline{\Delta n} \simeq 1.0$ for $\Omega = 0$. The best fit line is given by $\overline{\Delta n} = 0.024\Omega + 1.0$. For full vessel this would mean $\overline{\Delta n} \simeq 4$ at $\Omega = 0$. This is clearly due to fluctuations in the simulation results for finite number of runs. With the plot in Fig.2, at the critical angular velocity Ω_{cr} ($\simeq 78$ rad s^{-1} as mentioned earlier) we will have on an average net 12 vortices (for the whole vessel). Note when number of vortices is calculated using only energetics arguments in the vortex model, we expect a single vortex at the critical angular velocity. However, just after the superfluid transition, number of vortices also gets contributions from the Kibble mechanism (suitably modified as

Table 4.1: Effect of rotation on the formation of vortices

Ω	$\overline{\Delta n}$	σ	N	ν
0	0.0	30.46	1857948	0.2604
10^3	25.29±0.44	30.41±0.44	1858005	0.26029
10^4	250.20±0.26	30.90±0.26	1858003	0.2614
10^5	2492.88±0.30	31.42±0.30	1858010	0.26255
5×10^5	12466.9±0.36	31.77±0.35	1858031	0.26332
10^6	24932.8±0.34	35.81±0.32	1858136	0.27161
10^7	240603.±4.96	43.47±0.35	2745682	0.27753

proposed here) whose contributions have a Gaussian spread with σ as given in Table 4.1. Thus the final value of $\overline{\Delta n}$ will be expected to deviate from the vortex model prediction in general. It is still interesting to ask that with proper incorporation of the Kibble vortices, what is the *new* critical angular velocity at which one expects to get $\overline{\Delta n} = 1$. With our results, angular velocity of the vessel will be smaller than a different critical velocity, say, Ω_{Kibble}, which also depends on system parameters system size, the inter-domain separation d, etc. It is very interesting to study the behavior of Ω_{Kibble} in comparison to Ω_{cr} and we plan to study this in future. Especially interesting will be to investigate the dependence of our results on the parameter d. For a first order transition, with a simple situation of nucleation of a large density of critical bubbles (almost at close packing) the value of d will be given by $2\times$ the bubble wall thickness (while ξ corresponds to the bubble diameter). By considering different experimental situations, the ratio d/ξ can be varied and its effects on various results, especially on Ω_{Kibble} can be studied. For a second order transition such a study will be more complicated. In view of these issues, it is clear that a proper interpretation of Hess and Fairbank experiment [14] requires a more detailed analysis. Measurement of average number of vortices in experiment with sufficiently large number of events for superfluid transition with angular velocity just below Ω_{cr} may give a good test for the model here we propose. A non-zero value of angular momentum of superfluid below Ω_{cr} will give a solid support for this model. It will also show that there is a critical angular velocity Ω_{kibble} which is different from Ω_{cr} for the phase transition in the presence of rotation.

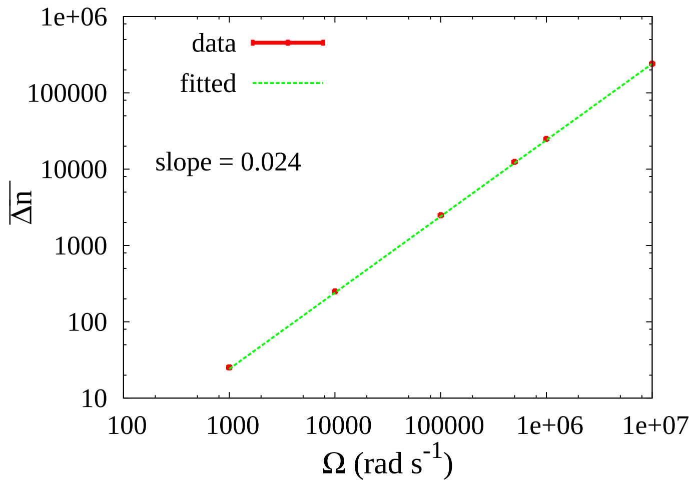

Figure 4.2: Variation of $\overline{\Delta n}$ with Ω in Log-Log scale. This plot shows that $\overline{\Delta n}$ linearly depends on Ω with slope 0.024. Slope will be about 0.1 if simulation perform in full cylinder.

As mentioned above, the best fit line for results in Table 4.1 gives $\overline{\Delta n} = 0.1\Omega$ (ignoring the intercept, hence for large Ω). This matches very well with the vortex model prediction which gives $n \simeq 2\pi R^2 m\Omega/h \simeq 0.1\Omega$ (Ref. [16]). This is expected as for very large Ω, number of vortices should be dominated by the effects of rotation. We again mention that our results depend on various parameters, such as ξ, d etc. Thus one needs to study whether this agreement with the vortex model prediction (for large Ω) is valid in general.

We emphasize that the free energy of individual defects plays no role in the Kibble mechanism (even with the modifications we propose). Still, with our incorporation of initial rotation of the normal fluid (and its some fraction getting transferred to the superfluid flow after the transition) at least some part, if not all, of the "rotation induced vortices" have been included in this proposed modified Kibble mechanism. This point will be particularly important for small rotations where very few vortices are expected from energetics arguments. This modified Kibble mechanism gives defect density right after the transition which will evolve in time, and approach the density expected using equilibrium free energy arguments. Thus, if the (modified) Kibble mechanism gives lesser number of net produced vortices then with time, more number of vortices will get produced and ultimately in the equilibrium, system will have n

number of vortices as predicted by the vortex model using energetics arguments. It is also interesting to study the distribution of vortices and antivortices as a function of distance from center in our model. The equilibrium distribution is uniform but as mentioned above, the distribution right after the transition may be different due to non-equilibrium contributions from the (modified) Kibble mechanism. A non-uniform initial distribution will have very important implications for the case of neutron stars where migration of vortices to achieve uniform (equilibrium) distribution will lead to change in moment of inertia of the neutron star (as in the model discussed in [18]). This requires large statistics and this study is underway.

Fig. 10.3 shows that the width of the Gaussian σ increases with Ω (slowly initially but strongly for large values of Ω). σ represent randomness in the formation of vortices and anti-vortices. If formation of vortices and antivortices is completely uncorrelated then value of σ goes like $\sim N^{1/2}$; width of Binomial distribution. But there is a correlation between production of defect and anti-defects in the Kibble mechanism (Ref. [10]) causing suppression in randomness and hence $\sigma \sim N^{1/4}$. By writing $\sigma \sim N^{\nu}$ we see from the Table 4.1, that ν increases with Ω showing that correlation between production of vortices and antivortices is getting suppressed with Ω. We also fit the dependence of σ on Ω. A reasonable fit for σ as a function of Ω is obtained by $\sigma = a\Omega^p + b$ where fitted values of parameters are found to be $a = 0.004 \pm 0.006, p = 0.51 \pm 0.10, b = 30.30 \pm 0.65$. Even though value of a is entirely dominated by error, this fit does suggest a systematic variation of σ with Ω with exponent $p \simeq 0.5$. We plan to carry out a systematic study of this result and increase of ν with Ω in future.

Fig.10.5-Fig.10.7 presents results for a single event for the number of defects per domain, i.e., probability of formation of defects. Fig.10.5 shows probability of formation of single winding defects and anti-defects as a function of Ω. We note that both probabilities increase with Ω, with winding $+1$ defect probability increasing faster than the probability for winding -1 (anti-defects), reflecting biasing in the formation of defects over anti-defects.

Fig.10.6 shows probability of formation of winding two defects and anti-defects as a function of Ω. We find an increase in the formation probabilities of winding number two defects and anti-defects as a function of Ω. Probabilities for both the cases become

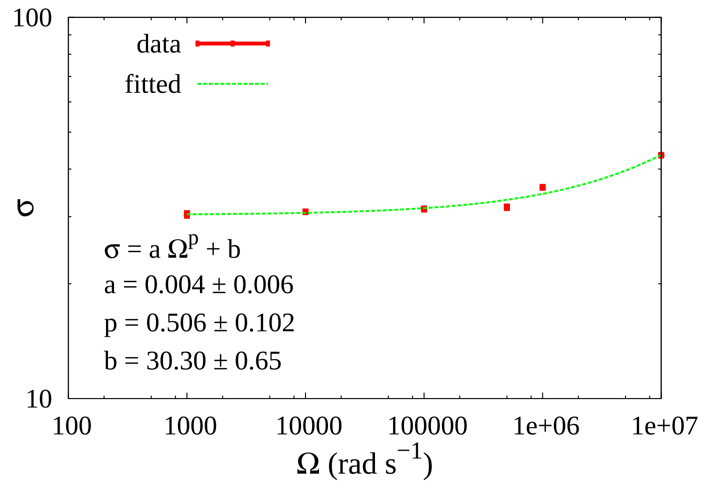

Figure 4.3: This plot shows that gaussian width changes with Ω and follow 1/2 power law dependence. Both the axes are in the Log-Log scale.

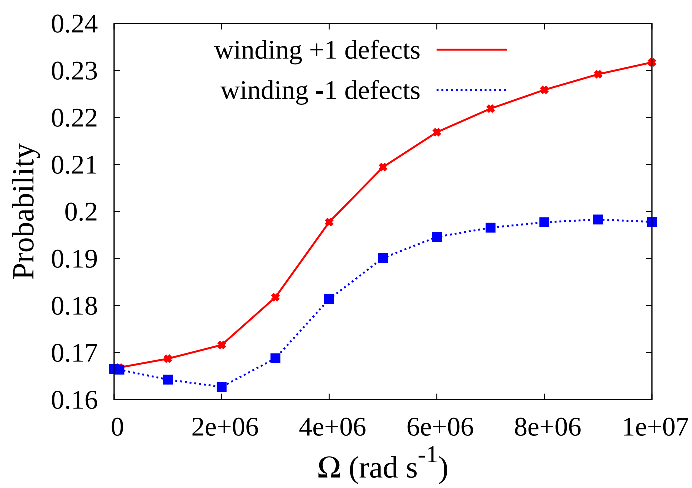

Figure 4.4: Plot shows probability of formation of single winding defects and anti-defects as a function of Ω. Probabilities for both the cases changes differently with Ω and causing biasing in the formation of defects over anti-defects.

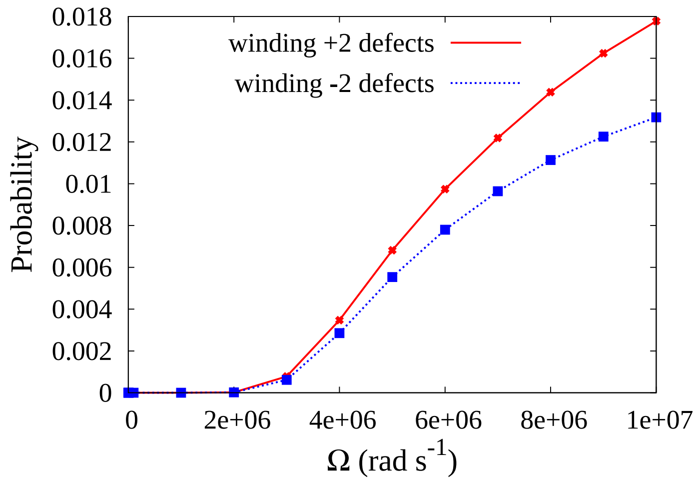

Figure 4.5: Plot shows probability of formation of winding two defects and anti-defects as a function of Ω. Probabilities for both the cases become non-zero at $\Omega > 2 \times 10^6$ $rad\ s^{-1}$ and changes differently with Ω and also causing biasing in the formation of defects over anti-defects. Winding number two defects are unstable in superfluid systems and split into two single winding defects and enhance single winding defects formation probabilities.

non-zero at $\Omega > 2 \times 10^6$ $rad\ s^{-1}$ and changes differently with Ω, again reflecting biasing in the formation of defects over anti-defects. It is well known fact that winding number two defects are unstable in superfluid systems and split into two single winding defects eventually enhancing single winding defects formation probabilities.

We note that while increase of vortex formation probability is expected as a function of increasing angular velocity, it may appear puzzling why anti-defect probability also increases with the rotation. The explanation for this may lie in the correlation of defects and antidefects which is an important and non-trivial prediction of the Kibble mechanism. As we see from Table 4.1, the defect-antidefect correlation exponent ν, while increasing slightly with angular velocity to a value of about 0.28, still remains far below the value of 0.5 for uncorrelated case. Thus, while vortex probability increases naturally with the rotation, the underlying domain structure forces larger probability of formation of anti-vortices close to vortices for winding number 1 as well as for winding number 2 case. (Basically from the fact that positive winding across two domains appears as anti-winding for the neighboring region.)

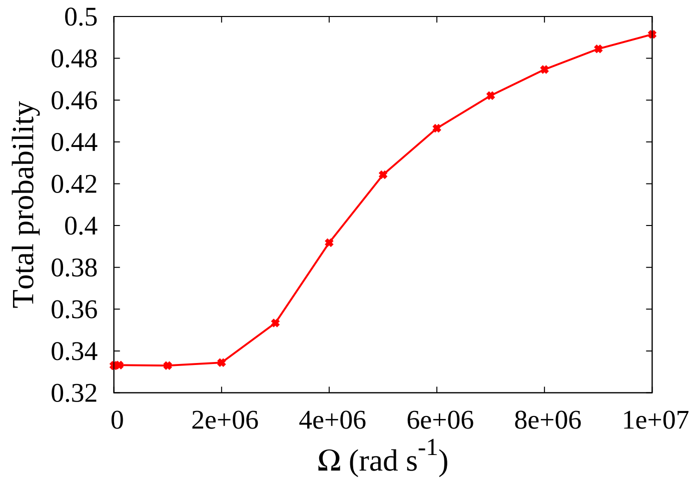

Figure 4.6: Plot shows the total formation probability of topological defects in the system with Ω (including winding number two and three defects with appropriate their weight in probability of single winding defects). Winding number three defects appear at $\Omega = 10^7\ rad\ s^{-1}$.

Fig.10.7 shows the total formation probability of topological defects in the system with Ω. Here we have included winding number two and three defects with their weight two and three respectively in probability of single winding defects formation as these defects are not stable and split into winding one defects. Winding number three defects appear at $\Omega = 10^7\ rad\ s^{-1}$. The total defect number (defects + anti-defects) probability increases with Ω as expected.

We have also checked the effects of varying the inter-domain separation d on our results. For $\Omega = 10^6$, increase of d from $d = 2\AA$ to $d = 40\AA$ increases probabilities for winding one defect as well as antidefect by about 15 %. Change in winding two defect probabilities is very small and dominated by fluctuations. For $\Omega \leq 10^5$ the change in probabilities is very small and dominated by fluctuations. The effect of d on various probabilities is a complex issue and we plan to study it systematically in future.

Experimental tests of our predictions based on this modified Kibble mechanism will lend strong support to the whole underlying picture of the Kibble mechanism which is adaptable for varying experimental conditions such as biased formation of flux tubes in superconductors in the presence of external field etc. We mention here an important aspect of vortex formation in superfluids via the Kibble mechanism which is not present for other types of topological defects (as emphasized in our earlier work [5]). We mentioned above that we assume that part of normal component which undergoes superfluid condensation carries the same angular momentum as it had before the transition (along an arc at the center of the domain). This just reflects the local conservation of linear momentum during the superfluid transition on that arc. However, even if there was no initial motion of the fluid, still during phase transition, spontaneous generation of flow of the superfluid will arise simply from the spatial variation of the condensate phase. Indeed, it is this (random) phase variation from one domain to another which leads to formation of vortex network and hence spontaneous generation of superflow. What happens then to local linear momentum conservation? Basically, some fraction of (^{4}He) atoms form the superfluid condensate during the transition and develop momentum due to the non-zero gradient of the phase of the condensate. The only possibility is that the remaining fraction of atoms (which form the normal component of fluid in the two-fluid picture) develop opposite linear momentum so that the momentum is locally conserved. (Here we avoid conceptual question of an ideal instantaneous quench to almost zero temperature where there is no normal component left). This means that there is no net momentum flow anywhere right after the transition. For superfluid transition in a rotating vessel, same consideration will apply to the normal component in a domain in regions away from the central arc as in those regions superflow will in general not match with the initial flow due to rotation implying generation of extra counterbalancing normal flow component. Note, this argument is quite different from the conventional argument of net angular momentum conservation for Kibble superfluid vortices where one knows that spontaneous generation of net rotation of the superfluid has to be counter balanced by the opposite rotation of the vessel containing the superfluid [3]. Here, we are arguing for local linear momentum conservation which implies generation of complex flow pattern for normal component depending on the generation of spontaneous part of the superflow during the transition. The final picture is then that, the original rotation of the normal fluid (before the transition) is simply transferred to the rotation of the superfluid which, via our modified Kibble mechanism, accounts for the net bias of vortices over anti-vortices. At the same time generation of extra vortices and anti-vortices via the random domain formation (via the Kibble mechanism) leads to extra local superfluid circulation in the system which will be accompanied by opposite circulation being generated in the normal component of the fluid (to balance the momentum conservation). To incorporate both these contributions accurately, one must carry out simulations of the transition with a two fluid picture in a rotating vessel. These consideration must be incorporated for any experimental test of the Kibble mechanism (either the conventional one, or the modified one presented here). It is possible that a due consideration of this spontaneously generated counterbalancing flow of the normal fluid may improve agreement of the results of various superfluid helium experiments with the Kibble mechanism. We plan to carry out a detailed investigation of this issue in a future work.

4.5 Conclusions

In conclusion, we have proposed a modification of the conventional Kibble mechanism for the situation of production of topological defects when physical situation requires excess of windings of one sign over the opposite ones. We have considered the case of formation of vortices for superfluid ^4He system when the transition is carried out in a rotating vessel. As our results show, this biased formation of defects can strongly affect the estimates of net defect density. Also, these studies may be crucial in discussing the predictions relating to defect-anti-defect correlations. The modified Kibble mechanism we presented here has very specific predictions about net defect number which shows a clear pattern of larger fluctuations (about mean value governed by the net rotation) compared to the conventional Kibble prediction. This can be easily tested in experiments. Further, even the average net defect number deviates from the number obtained from energetics considerations, especially for low values of Ω. This implies that exactly at the time of transition, a different net defect number will be formed on the average, which will slowly evolve to a value obtained from energetics considerations. These considerations can be extended for the case of flux tube formation in superconductors (with appropriate modifications for the gauged case), and we hope to present it in a future work. Such a modified Kibble mechanism is also needed to study formation of baryons at finite chemical potential in the framework of chiral sigma model where baryons appear as Skyrmions which are topological solitons (extending our earlier work on 1+1 D Skyrmion formation to 3+1 D [17]). Our results will have implications for superfluid transition in rotating neutron stars (where phase transition induced density fluctuations could be detected by observing pulsar signal changes, as proposed by some of us [18]). In an earlier work [5], we considered the possibility of superfluid phases of QCD, e.g. neutron superfluid and color-flavor-locked phase, in low energy heavy-ion collisions and showed that this will lead to production of few vortices via the (conventional) Kibble mechanism which can strongly affect the hydrodynamical evolution of the system and can be detected by measuring flow fluctuations. For low energy non-central collisions superfluid phase transition is likely to happen in the presence of an overall rotation of the plasma region. Resulting vortex production for such a case must be studied by a modified Kibble mechanism, as we have proposed here.

Bibliography

[1] Shreyansh S. Dave and Ajit M. Srivastava, arXiv: 1805.09377.

[2] T.W.B. Kibble, J. Phys. **A9**, 1387 (1976); Phys. Rept. **67**, 183 (1980).

[3] W.H. Zurek, Nature **317**, 505 (1985).

[4] W.H. Zurek, Phys. Rep. **276**, 177 (1996).

[5] A. Rajantie, Int. J. Mod. Phys. **A17**, 1 (2002).

[6] P.C. Hendry et al, Nature (London) **368**, 315 (1994); V.M.H. Ruutu et al, Nature (London) **382**, 334 (1996); M.E. Dodd et al, Phys. Rev. Lett. **81**, 3703 (1998); R. Carmi et al, Phys. Rev. Lett. **84**, 4966 (2000); see also, G.E. Volovik, Czech. J. Phys. **46**, 3048 (1996).

[7] R. Carmi, E. Polturak, and G. Koren, Phys. Rev. Lett. **84**, 4966 (2000); A. Maniv, E. Polturak, and G. Koren, cond-mat/0304359; R.J. Rivers and A. Swarup, cond-mat/0312082; E. Kavoussanaki, R. Monaco, and R.J. Rivers, Phys. Rev. Lett. **85**, 3452 (2000); S. Rudaz, A.M. Srivastava and S. Varma, Int. J. Mod. Phys. **A14**, 1591 (1999)1.

[8] I. Chuang, R. Durrer, N. Turok and B. Yurke, Science 251, 1336 (1991); R. Snyder et al. Phys. Rev. **A45**, R2169 (1992); I. Chuang et al. Phys. Rev. **E47**, 3343 (1993).

[9] M.J. Bowick, L. Chandar, E.A. Schiff and A.M. Srivastava, Science 263, 943 (1994).

[10] S. Digal, R. Ray, and A.M. Srivastava, Phys. Rev. Lett. **83**, 5030 (1999); R. Ray and A.M. Srivastava, hep-ph/0110165.

[11] L.D. Landau and E.F. Lifshitz, **Statistical Physics Part 2**, Pergamon Press Ltd. (1980).

[12] G.B. Hess, Phys. Rev. **161**, 189 (1967).

[13] S. Rudaz and A.M. Srivastava, Mod. Phys. Lett. A8, 1443 (1993).

[14] G.B. Hess and W.M. Fairbank, Phys. Rev. Lett. **19**, 216 (1967).

[15] L. Landau, Phys. Rev. **60**, 356 (1941).

[16] D.R. Tilley and J. Tilley, **Superfluidity and Superconductivity**, Third Edition, Overseas Press (2005).

[17] V.S. Kumar, B. Layek, A.M. Srivastava, S. Sanyal, and V.K. Tiwari, IJMP A **21**, 1199-1219 (2006).

[18] P. Bagchi, A. Das, B. Layek, A. M. Srivastava, Phys.Lett. **B747**, 120-124 (2015).

[19] A. Das, S.S. Dave, S. De, A.M. Srivastava, Mod. Phys. Lett. A **32**, 1750170 (2017).

Chapter 5

Quantum Chromodynamics and its Phases

The experiments of proton-proton and electron-proton collisions, with very high energies, revealed many unexpected fact about the substructure of proton and showed that the proton is a very complicated object which has a very rich internal structure in terms of its constituents, named *partons*. From the observation of distribution of outgoing particles in the experiments, it was realized that partons are almost free inside the proton and incapable of exchanging very high momentum through strong interaction in the high energy collisions. From electron-proton collisions, a very important result came out which is known as the *Bjorken scaling* of deep inelastic cross section. This shows that the cross section only depends on the fraction of longitudinal momentum carried by partons but not on the momentum transfer by the electron (or energy of the collisions) [1]. This implies that, an electromagnetic probe sees same structure of proton irrespective of the momentum transfer. Note that the interaction time scale of partons inside a proton is of the order of inverse of protons mass. This time scale is much larger than the electron - proton scattering time in the high energy experiment. It was observed that, during such short scattering time, partons behave almost freely inside proton. Partons have stronger interaction on a longer time scale.

This picture of free partons inside proton, during a short scattering time, raises a very fundamental question in the quantum field theory. Quantum field theory allows interaction of partons by *virtual particle* exchange in a very arbitrary small time duration with arbitrarily high momentum, see Ref. [1]. The question arose, which thing is stopping for the large momentum transfer between partons during the scattering time. Latter, it was realized that *non-abelian gauge theories* have *asymptotic freedom*, which means, large-momentum-transfer or short-time processes lead to lesser interaction between the particles. This feature of non-abelian gauge theory can address the above issue and therefore it was realized that underlying theory of partons interaction should be a non-abelian gauge theory. In the *non-abelian* gauge theory of strong interaction, interactions between partons happen through vector bosons exchange, named gluons, which also carry *charge* allowing self interaction between them. This feature is not available in QED where photons (vector boson of the theory) do not carry any charge and hence don't interact with other photons.

Experimental investigation of the interaction of partons through vector bosons (which carry charges) supports the non-abelian character of the strong interaction. The underlying theory of strong interaction is named *Quantum Chromodynamics* (QCD). The vector bosons in this theory are called gluons which carry charges named *color charges.* The self interaction among gluons through color charge is responsible for the QCD asymptotic freedom at high energy and due to that perturbative quantum field theoretical techniques can be used for the determination of scattering cross section of a process. At low momentum transfer or for a longer time process, interaction among partons become very strong and due to this, perturbation theory breaks down.

The fundamental particles, which participate in the strong interaction, are quarks, anti-quarks and gluons. There are many possible bound states of quarks, some of them are three quark (fermion) states, e.g. proton, neutron, etc., called as *baryons*, while others are quark - anti-quark (boson) states, e.g. pion, called as *mesons.* Quarks remain confined inside *baryons* and *mesons* (collectively called as *hadrons*). In the experiments only hadrons are observed; an isolated quark never appears.

We now discuss the original reason for introducing the *color quantum number* in the quark model. The physical properties of Δ^{++} particle shows that it consists of three identical u quarks, where all the quarks, in uuu bound state, have to lie in the ground state in a symmetric state to satisfy the property of Δ^{++}. But, this clearly violates the Fermi statistics. Also, other unavoidable question can arise that why qq, $\bar{q}\bar{q}$ or q particles are not seen in nature. To handle these issues another quantum number associated with quarks was introduced known as the *color quantum numbers, red (r), green (g), blue(b)*. This quantum number distinguishes all three u quarks in Δ^{++} and protect the violation of Fermi statistics. Thus, by this, quarks form the bound state not due to electromagnetic interaction (in Δ^{++} all quarks have same e.m. charge) but due to color (strong) interaction. As isolated quarks are not seen, the notion of color confinement was introduced. Quarks combine in such a way that only *colorless* (*white*), or more precisely, *color singlet* (invariant under the rotation transformation in r,g,b space) hadrons form. This disallows the possibility of qq, $\bar{q}\bar{q}$ or q states in the nature, see Ref. [2]. All hadrons are color singlet objects. Anti-quarks have color antired ($\bar{r}$), antigreen ($\bar{g}$), and antiblue ($\bar{b}$). For the detail discussion on the combination of colors to the color singlet object, see Ref. [2]. The bound state of quarks arises due to color exchange through *gluons* (vector boson of the strong interaction) which also carry color charge due to the non-abelian nature of QCD. There can be nine gluons which have bicolor charges (in linear combination of colors), $r\bar{r}$, $r\bar{g}$, $r\bar{b}$, $g\bar{r}$, $g\bar{g}$, $g\bar{b}$, $b\bar{r}$, $b\bar{g}$, and $b\bar{b}$. Out of nine gluon states, $r\bar{r}+g\bar{g}+b\bar{b}$ state is color singlet and therefore can not have its role in the color interaction. So in the theory of QCD, there are eight gluons which lead to the quark interaction. The $SU(3)$ theory has exactly same number of generators, and therefore can account for eight gluons. Thus, theory of strong interaction can be described by $SU(3)$ gauge theory which is known as the QCD. Note that since gluons also carry the color charge, therefore they can interact with themselves, which lead to a very important feature of QCD discussed below.

The fact that gluons have color charges gives a completely different polarizability of QCD vacuum from the QED. We know that electric charge of an electron is screened by vacuum polarization; electron-positron cloud around a test electron is generated in such a way that, positrons remain closer to test electron via electric attraction. Due to this, in the long distance measurement, charge of test electron shows lesser value. Towards the shorter distance, test charge increases. In the case of QCD also, around a color charge, vaccum becomes polarized and quark - anti-quark pairs distribute such that they color screen the color charge of quark (like electric charge in QED), but since gluons also carry charges, and can self interact themselves, therefore they also form a cloud of gluons around the color charge such that, instead of screening they create anti-screening of color charge; for example if test quark has red color, then around this, due to gluons cloud, an effective distribution of red color forms. For QCD, the effect of anti-screening dominates over any other kind of screening effects created by quark - anti-quark pairs. Therefore, in the long distance, color charge strongly gets enhanced due to such gluonic distribution. QCD vacuum, therefore is a paramagnetic medium (QED vacuum is a dielectric medium). Towards the shorter distance, color charge of quark reduces. This is the reason that, at sufficiently short distance or high energies, two quarks interact weakly (because they have lesser effective color charge in this regime), this feature of QCD is known as the *asymptotic freedom*. Note that in the thermal medium (in the quark-gluon plasma) the property of anti-screening goes away and charges only have Debye screening like in the case of QED plasma.

If one tries to pull apart quark - anti-quark pair, the interaction strength between them becomes stronger and stronger with increasing distance. Since gluons can interact with themselves, therefore with the distance, the color field between the pair squeezes in the transverse direction of stretching, and by this, behaves as a string of fixed string tension. When we pull further the string, it breaks into two pieces of strings (hadrons) of smaller length with the production of one more pair of quark - anti-quark. This is the reason, no isolated quark can be found in nature. This is known as the *color confinement*.

All hadrons are color singlet object but when they are brought sufficiently close to each other, quark of one hadron start seeing quark of other hadron. This interaction is responsible for the binding of neutron and protons into nuclei.

5.1 Quantum Chromodynamics (QCD)

The demand of local gauge invariance of the Lagrangian provides interactions between fermions with vector gauge bosons. QED is one of such local gauge theory which is invariant under transformation of fermion and photon field at each space-time points. This theory is an abelian gauge theory which is very well tested experimentally. This suggests that the local gauge invariance is a *fundamental principle* of the nature and leads to a specific form of the Lagrangian. We have discussed that gluons have color charge and hence can self interact with themselves. Quarks come in three colors which form three dimensional color vector space. Therefore the quark field forms a triplet state (ψ_r ψ_g ψ_b) which transforms with the 3×3 matrices, where ψ is a Dirac field for quarks. These transformation matrices form a group, known as color $SU(3)_c$ group. The QCD Lagrangian is invariant under this group. $SU(3)_c$ group has total 8 generators, therefore local gauge invariance of the theory requires 8 vector fields. These are the gluons, responsible for the strong interaction.

Lagrangian density of QCD, following local gauge invariance under $SU(3)_c$, is given by [3],

$$\mathcal{L} = \sum_{f=1}^{6} \bar{\Psi}_f \big(i\gamma^\mu D_\mu - m_f\big)\Psi_f - \frac{1}{4} F^a_{\mu\nu} F^{\mu\nu}_a, \tag{5.1}$$

where Ψ is the 3×1 matrix of the quark field containing three color quantum states red, green, blue of quark, which is the triplet of $SU(3)_c$,

$$\Psi = \begin{pmatrix} \psi_r \\ \psi_g \\ \psi_b \end{pmatrix}.$$

The label f in Ψ_f corresponds to flavor of quarks. There are 6 quarks in nature, up (u), down (d), charm (c), strange (s), top (t), and bottom (b). Masses (m_f) of all the quarks are vastly different and till now there is no physical understanding of why this is so. γ^μ are the Gamma-matrices. D_μ is called the covariant derivative which acts on the color triplet of the quark field. Local gauge invariance of Lagrangian density leads the form of covariant derivative,

$$D_\mu = \partial_\mu - igA^a_\mu t^a, \tag{5.2}$$

where g is the dimensionless coupling constant of QCD. A^a_μ represent eight gauge fields, i.e. gluon fields, with $a = 1, .., 8$ corresponding to eight generators t^a (Hermitian matrices) of $SU(3)_c$ algebra. The gluon fields form octet of $SU(3)_c$. These generators are in the fundamental (irreducible) representation of the $SU(3)_c$ algebra, i.e. come in 3×3 matrices. These generators satisfy the following commutation relation,

$$[t^a, t^b] = if_{abc}t^c, \tag{5.3}$$

and normalization condition,

$$tr(t^a t^b) = \frac{1}{2}\delta^{ab}, \tag{5.4}$$

where f_{abc} are the structure constants which are anti-symmetric in its indices. The structure constants, which have non-zero values, are [3],

$f_{123} = 1,$

$f_{147} = -f_{156} = f_{246} = f_{257} = f_{345} = -f_{367} = 1/2,$

$f_{458} = f_{678} = \sqrt{3}/2.$

t^a are 3×3 matrices and equal to $\frac{1}{2}\lambda^a$, where λ^a are the *Gell-Mann matrices*, see the Ref. [3] for the form of these matrices.

To incorporate the dynamics of gauge field, field strength tensor is introduced in the Lagrangian. In the case of non-abelian theory, field strength tensor contains quadratic term of gauge fields,

$$F^a_{\mu\nu} = \partial_\mu A^a_\nu - \partial_\nu A^a_\mu - g f_{abc} A^b_\mu A^c_\nu, \tag{5.5}$$

This expression of field strength tensor can also be written in a simpler form by introducing $A_\mu \equiv t^a A^a_\mu$ and $F_{\mu\nu} \equiv t^a F^a_{\mu\nu}$,

$$F_{\mu\nu} = \partial_\mu A_\nu - \partial_\nu A_\mu + ig[A_\mu, A_\nu]. \tag{5.6}$$

This clearly shows that in QCD, gluons can interact with each other (Lagrangian of QCD contains cubic and quartic terms of gauge field). This is what makes the theory asymptotically free. The color electric field and color magnetic field can be written as,

$$E^i = F^{i0}, \quad B^i = -\frac{1}{2}\epsilon_{ijk}F^{jk}, \tag{5.7}$$

where ϵ_{ijk} is the third rank Levi-Civita tensor. The equation of motion of quark field and gluon field can be obtained from the QCD Lagrangian,

$$(i\gamma^\mu D_\mu - m)\Psi = 0, \tag{5.8}$$

$$[D_\nu, F^{\nu\mu}] = gj^\mu, \tag{5.9}$$

where $j^\mu = t^a j^{\mu a}$ and $j^{\mu a} = \bar{\Psi}\gamma^\mu t^a \Psi$. The element of $SU(3)_c$, under which QCD Lagrangian is invariant, is given by, $U(x) = exp\big(-i\theta^a(x)t^a\big)$. The transformation of quark field and gluonic field under $SU(3)_c$ is given by,

$$\Psi(x) \to U(x)\Psi(x), \quad gA_\mu(x) \to U(x)\big(gA_\mu(x) - i\partial_\mu\big)U^\dagger(x), \tag{5.10}$$

Under these transformation, QCD Lagrangian is invariant. Under $SU(3)_c$ transformation covariant derivative of the quark field transforms in the same way as the quark field. In the abelian gauge theory, field strength tensor $F^{\mu\nu}$ is invariant under gauge transformation, but in the non-abelian case, $F_{\mu\nu} \equiv t^a F^a_{\mu\nu}$ is not invariant under the gauge transformation. The gauge transformations of $F_{\mu\nu}$ and D_μ are,

$$F_{\mu\nu}(x) \rightarrow U(x)F_{\mu\nu}(x)U^\dagger(x), \quad D_\mu(x)\Psi(x) \rightarrow U(x)D_\mu(x)\Psi(x)U^\dagger(x). \tag{5.11}$$

Note that quark field comes in a triplet, therefore transforms under irreducible (fundamental) representation of $SU(3)_c$, i.e. transformation elements are 3×3 matrices. But gluonic field forms an octet, therefore transforms by 8×8 matrices, which is known as the adjoint representation of $SU(3)_c$ algebra [1,3].

To get the description in terms of particles and their interactions allowed by quantum theory, one needs to quantize the QCD Lagrangian. There are mainly two methods by which one can quantize the fields, one is the canonical quantization and the other is the Feynman Path integral method. The popular one is the Feynman path integral method, in which one writes the transition amplitude from vacuum to vacuum from $-\infty$ to $+\infty$ time. This incorporates all possible quantum effects in the theory, by considering all possible paths of fields from initial configuration state to the final configuration state. This transition amplitude is the generating functional of the full Green's function (all possible diagrams). We are mainly interested in the connected diagrams, which can be easily obtained by taking logarithms of generating functional. Finally, one particle irreducible diagrams (1PI diagrams) are obtained by calculating the Legendre transform of logarithms of generating functional (connected diagrams). This is known as the *effective action* of the theory.

In the evaluation of the generating functional, one problem arises due to presence of infinite number of possible paths which are connected by gauge transformation. All such paths contribute the same amount in the generating functional, and because of this, generating functional become divergent. To avoid this problem, gauge fixing is performed, so that only one representative point of a gauge orbit (in one orbit, all gauge fields are connected through the gauge transformation) is taken into account. The famous technique for the gauge fixing is the Faddeev - Popov method. Finally, after gauge fixing, a modified generating functional and Lagrangian density of the theory is obtained, which is written with the introduction of new field variables, known as ghost and anti-ghost field. Although, this new Lagrangian density is not gauge invariant (classical gauge invariant), but it is invariant under the BRST transformation (quantum gauge invariant). With all this, generating functional can be evaluated which generates all possible diagrams. As we mentioned, one is interested in the connected 1PI diagrams, which control the divergence structure of the theory. For detail discussion see Refs. [1, 3].

To regulate the ultraviolet divergences in the loop integrals, a momentum cut-off scale is introduced. This makes *scattering amplitude* finite, but cut-off dependent. To make experimentally measured quantities cut-off independent, one renormalizes the theory by adding some extra counter terms in the *bare* Lagrangian. By this, the *bare* parameters of the Lagrangian get redefined such that the generating functional of the theory remain independent from the momentum cut-off scale. With this, quantities like coupling constant change with the energy scale κ (at which the divergences are renormalized) by the following the *flow equation* [3],

$$\kappa\frac{\partial g}{\partial\kappa} = \beta, \tag{5.12}$$

where β can be calculated in the small g limit. β depends upon g, by following a series expansion,

$$\beta(g) = -\beta_0 g^3 - \beta_1 g^5 + ... \tag{5.13}$$

where,

$$\beta_0 = \frac{1}{(4\pi)^2}\Big(11 - \frac{2}{3}N_f\Big), \quad \beta_1 = \frac{1}{(4\pi)^4}\Big(102 - \frac{38}{3}N_f\Big). \tag{5.14}$$

It should be noted that for $N_f \leq 8$, both β_0 and β_1 are positive numbers. If $8 < N_f \leq 16$, β_1 becomes negative, but β_0 still remain positive. For $N_f > 16$, both β_0 and β_1 become negative. We know that there are six quarks in nature, so for this, β is negative, which indicates that with increasing momentum cut-off scale, strong interaction coupling decreases. One can obtain the fine structure constant of the strong interaction, $\alpha_s = g^2/4\pi$, in terms of β_0 and β_1 as,

$$\alpha_s(\kappa) = \frac{1}{4\pi\beta_0 ln(\kappa^2/\Lambda_{QCD}^2)}\left[1 - \frac{\beta_1}{\beta_0^2}\frac{ln(ln(\kappa^2/\Lambda_{QCD}^2))}{ln(\kappa^2/\Lambda_{QCD}^2)} + ...\right], \tag{5.15}$$

which shows that when κ increases, α_s decreases. Λ_{QCD}, called *QCD scale parameter*, is determined by experimentally which has value $\sim 200\ MeV$. It is independent from

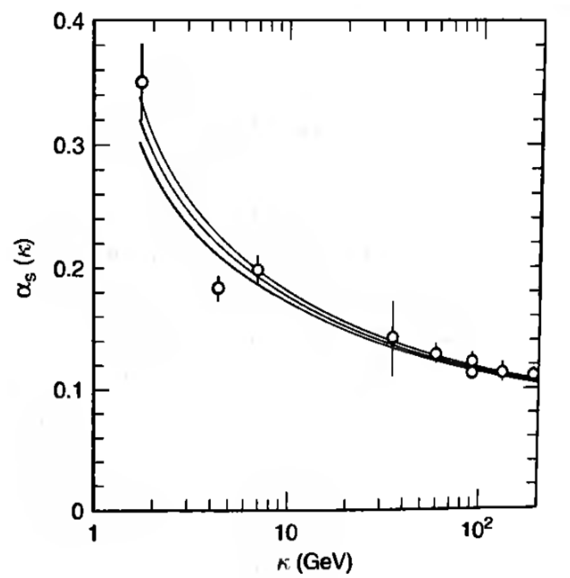

Figure 5.1: Figure shows the running of QCD coupling constant with the energy scale κ. The points on the plot is from the various experiments. Running of QCD coupling constant clearly shows that QCD is a asymptotically free theory. Figure has been taken from the Ref. [3].

κ. Fig. 5.1 shows the dependence of α_s on κ; data points are experimental measured values. This shows that QCD is an asymptotically free theory. This asymptotic freedom arises due to the non-abelian nature (and hence due to self-interaction between gauge (gluonic) field). Due to the same reason gluons in the QCD vacuum anti-screen a color charge, which makes the QCD vacuum a *paramagnetic medium*, see Ref. [3]. In the presence of matter (at finite temperature), this anti-screening goes away. That is the reason why quark-gluon plasma exhibits the screening of the color interaction, just like QED plasma does for the electromagnetic interaction [3].

Chiral symmetry in QCD : As we have discussed, QCD Lagrangian is invariant under the local $SU(3)_c$ gauge transformation. Now we discuss that QCD also has some global symmetries, the chiral symmetry is one of them [3]. Let us consider the QCD Lagrangian density, without the kinetic term of gauge field,

$$\mathcal{L} = \sum_{f=1}^{6} \bar{\Psi}_f \big(i\gamma^\mu D_\mu - m_f \big) \Psi_f. \tag{5.16}$$

The current quark mass of u and d quarks are $m_u, m_d \sim 5-10\ MeV$. The masses of the strange and charm quarks are $m_s \sim 95\ MeV$, $m_c \sim 1.3\ GeV$, respectively; the masses of top and bottom quarks are much higher than the masses of these quarks. In the comparison with the QCD scale $\Lambda_{QCD} \sim 200\ MeV$, in an approximation, one can neglect the masses of u and d quark, while in a poor approximation one neglects the mass of the s quark also, with respect to QCD scale. Let us consider $m_u \simeq m_d \simeq 0$, then we can write the QCD Lagrangian density as,

$$\mathcal{L} = \bar{\psi}\big(i\gamma^\mu D_\mu\big)\psi + \sum_{f=3}^{6} \bar{\Psi}_f\big(i\gamma^\mu D_\mu - m_f\big)\Psi_f, \tag{5.17}$$

where,

$$\psi = \begin{pmatrix} \Psi_u \\ \Psi_d \end{pmatrix},\ \bar{\psi} = \begin{pmatrix} \bar{\Psi}_u \bar{\Psi}_d \end{pmatrix},\ \Psi_{u,d} = \begin{pmatrix} \psi_r \\ \psi_g \\ \psi_b \end{pmatrix}.$$

One can project ψ_u and ψ_d fields into their left and right chiral components as,

$$\psi_{_L} = \frac{1}{2}(1-\gamma_5)\psi, \quad \psi_{_R} = \frac{1}{2}(1+\gamma_5)\psi, \tag{5.18}$$

where,

$$\psi_{_L} = \begin{pmatrix} \Psi_{u_L} \\ \Psi_{d_L} \end{pmatrix},\ \psi_{_R} = \begin{pmatrix} \Psi_{u_R} \\ \Psi_{d_R} \end{pmatrix},$$

and $\gamma_5 = i\gamma^0\gamma^1\gamma^2\gamma^3$. γ_5 anti-commutes with the other Dirac's matrices, $\{\gamma_5, \gamma^\mu\} = 0$. In the *Weyl representation*, γ^5 =diag$(-I, I)$. It is a hermitian matrix, $\gamma_5^\dagger = \gamma_5$. In terms of $\psi_{_L}$ and $\psi_{_R}$ one can write the first term of Eq. 5.17 as,

$$\mathcal{L}_{u,d} = \bar{\psi}_{_L}\big(i\gamma^\mu D_\mu\big)\psi_{_L} + \bar{\psi}_{_R}\big(i\gamma^\mu D_\mu\big)\psi_{_R}, \tag{5.19}$$

where $\bar{\psi}_{_L} = \psi_{_L}^\dagger\gamma^0 = \frac{1}{2}\psi^\dagger(1-\gamma_5)\gamma^0 = \frac{1}{2}\bar{\psi}(1+\gamma_5)$ and $\bar{\psi}_{_R} = \frac{1}{2}\bar{\psi}(1-\gamma_5)$. The above equation shows that in the zero mass limit, the left chiral part and the right chiral part completely get decoupled and their equation of motion are also independent. This is known as the *chiral symmetry*. Note that in the presence of the mass term $m\bar{\psi}\psi = m\bar{\psi}_{_R}\psi_{_L} + m\bar{\psi}_{_L}\psi_{_R}$, left and right chirality are not decoupled, and therefore mass term breaks the chiral symmetry.

The Lagrangian density in Eq. 5.19 is invariant under the separate unitary transformations of $\psi_{_L}$ and $\psi_{_R}$ fields. The symmetry group of this Lagrangian density is

$SU(2)_L \times SU(2)_R$ whose elements transform the u and d quark fields as,

$$\psi_L \to e^{-i\frac{1}{2}\tau^a\theta^a_L}\psi_L, \quad \psi_R \to e^{-i\frac{1}{2}\tau^a\theta^a_R}\psi_R \tag{5.20}$$

$$\bar{\psi}_L \to \bar{\psi}_L e^{i\frac{1}{2}\tau^a\theta^a_L}, \quad \bar{\psi}_R \to \bar{\psi}_R e^{i\frac{1}{2}\tau^a\theta^a_R} \tag{5.21}$$

These are the global transformations which acts independently on the ψ_L and ψ_R fields. Under these transformations the Lagrangian 5.19 is invariant. This is known as the *chiral symmetry* which arises in the mass zero limit.

The chiral symmetry can also be realized by directly looking the first term of the QCD Lagrangian Eq. 5.17,

$$\mathcal{L}_{u,d} = \bar{\psi}\big(i\gamma^\mu D_\mu\big)\psi, \tag{5.22}$$

This Lagrangian density is invariant under the transformations of $SU(2)_V \times SU(2)_A$,

$$\psi \to e^{-i\frac{1}{2}\tau^a\theta^a_V}\psi, \quad \psi \to e^{-i\frac{1}{2}\tau^a\theta^a_A\gamma_5}\psi, \tag{5.23}$$

$$\bar{\psi} \to \bar{\psi}e^{i\frac{1}{2}\tau^a\theta^a_V}, \quad \bar{\psi} \to \bar{\psi}e^{-i\frac{1}{2}\tau^a\theta^a_A\gamma_5}. \tag{5.24}$$

The symmetry associated with the $SU(2)_V$ transformations is called the *vector* or *isospin symmetry*, while with the $SU(2)_A$ transformations is called the *axial symmetry*. Note that both the chiral symmetry transformations, mentioned above, are equivalent, since the groups, $SU(2)_L \times SU(2)_R$ and $SU(2)_V \times SU(2)_A$, are isomorphic to each other. If the chiral symmetry of QCD is followed by its ground state, then this must be reflected in the hadronic multiplet structure. But, in the hadronic spectrum, in the consideration of $m_u \simeq m_d$, we only see the isospin $SU(2)_V$ symmetry, where three pions form isospin-1 multiplet structure. Thus, we conclude that $SU(2)_L \times SU(2)_R \sim SU(2)_V \times SU(2)_A$ chiral symmetry should be spontaneously broken by the QCD ground state with remaining $SU(2)_V$ isospin symmetry. The ground state breaks three generators, therefore according to the Goldstone's theorem, three massless Goldstone's bosons arise which are three pions in this case. These pions acquire their masses due to the explicitly breaking of the chiral symmetry due to non-zero current quark mass of u and d quarks. If we consider $m_u \simeq m_d \simeq m_s \simeq 0$, then the QCD Lagrangian density for these flavors show the chiral symmetry, $SU(3)_L \times SU(3)_R \sim SU(3)_V \times SU(3)_A$, which get broken by the ground state, with remaining isospin $SU(3)_V$ symmetry, where there will be eight Goldstone's bosons associated with the eight broken generators.

5.2 QCD at Finite Temperature

To describe thermodynamic phases of QCD, *finite temperature field theory* (or many body field theory) is required. Here, we briefly introduce this subject by following the discussion from the Refs. [3–5]. We discuss the phases of QCD, basically transition from thermal gas of hadrons to the quark-gluon plasma by showing the Lattice QCD results. The quark-gluon plasma (QGP) phase is expected to arise due to asymptotic freedom of QCD interaction at sufficient high energies or very short distances. Therefore it was expected that the plasma of quarks, anti-quarks and gluons should be weakly coupled, but this was not the case when observed in the experiment. The experiment data have showed that the produced plasma at the relativistic heavy-ion collider (RHIC) is strongly interacting and behaves almost like a perfect fluid.

In the low energy or long distance limit, a plasma of hadrons is formed. Since strong interaction, by nature, is a short range, therefore as distance increases, interactions among the hadrons are expected to decrease. These hadrons form a phase which is known as the *ideal hadron gas*. These phases of QCD (hadron gas and QGP) can arise at finite temperature ($T \neq 0, \mu = 0$), at finite chemical potential ($T = 0, \mu \neq 0$) or the case when both are non-zero ($T \neq 0, \mu \neq 0$). The quantum field theory ($T = 0$ and $\mu = 0$) describes the interaction among particles in the vacuum. The transition amplitude from vacuum to vacuum gives the generating functional for the QCD processes in the Feynman path integral formalism,

$$Z = \int \mathcal{D}\mathcal{A}^a_\mu(x)\mathcal{D}\bar{\Psi}(x)\mathcal{D}\Psi(x)e^{i\int d^4x\mathcal{L}[\mathcal{A}^a_\mu,\bar{\Psi},\Psi]}. \tag{5.25}$$

In the saddle point approximation, the most contribution in the generating functional comes from the field configurations of $(\mathcal{A}^a_\mu(x), \bar{\Psi}(x), \Psi(x))$ which satisfies the classical Euler-Lagrange equation of motion of the QCD Lagrangian. The other field configurations of $(\mathcal{A}^a_\mu(x), \bar{\Psi}(x), \Psi(x))$ around the classical one also contribute in the generating functional which incorporate all possible QCD quantum processes (loop diagrams). Note that fermion fields $\bar{\Psi}(x)$ and $\Psi(x)$) are *Grassmann variables* which satisfy anti-commutation relations, e.g. $\{\Psi(x_1), \Psi(x_2)\} = 0$ and $\{\bar{\Psi}(x_1), \bar{\Psi}(x_2)\} = 0$.

To describe the equilibrium properties of the strongly interacting quarks, anti-quarks and gluons one needs to write the *grand canonical partition function* for this system. Note that here we are avoiding the discussion of QCD at finite chemical potential. From the computational point of view, this system faces a problem known as *QCD sign problem*, which disallow the computation of partition function in the lattice simulation. For discussion on the QCD sign problem see Ref. [4]. (We mention that, in the perturbative regime, it is possible to perform the thermal field theory calculations at finite chemical potential). From the *quantum statistical mechanics*, the partition function for the grand canonical ensemble is given by,

$$\mathcal{Z} = tr(e^{-\beta\hat{H}}) = \sum_n \langle n|e^{-\beta\hat{H}}|n\rangle, \tag{5.26}$$

where $\beta = 1/T$, where T is the temperature of the system, $\hat{H}$ is the Hamiltonian of the theory and $|n\rangle$ forms a complete set of basis.

Let us consider transition amplitude from state $|n_i\rangle$ at time t_i to state $|n_f\rangle$ at time t_f [3],

$$K_{n_f n_i}(t_f, t_i) = \langle n_f|e^{i\hat{H}(t_f - t_i)}|n_i\rangle. \tag{5.27}$$

The form of the partition function has similarity with the transition amplitude if one takes initial and final state same, i.e. $|n_f\rangle \to |n_i\rangle$, and replaces $t_f - t_i \to i\beta$.

To write the transition amplitude in the form of the path integral (as written above the generating function for QCD theory), one needs to compactify the time axis t such that it varies from 0 to $t_f - t_i$. Then, from the above analogy, to obtain the generating functional at finite temperature, one also replaces $t \to i\tau$ everywhere, such that imaginary time τ varies from 0 to β. Note that τ is not the time coordinate here, although it looks analogous to the time axis. In fact, in the thermal equilibrium all the state variables are time independent. So variation of τ from 0 to β is nothing to do with the time evolution or temperature change. This is just a method by which one can perform calculation for the partition function. We do the following replacements in the generating functional to get the partition function for the field theoretical system,

$$x_\mu \to (x_\mu)_E = (\mathbf{x}, \tau = -it), \quad \partial_\mu \to (\partial_\mu)_E = (\nabla, \partial_\tau = i\partial_t),$$
$$\gamma_\mu \to (\gamma_\mu)_E = (\gamma_i, \gamma_4 = -i\gamma_0), \quad \mathcal{A}^a_\mu \to (\mathcal{A}^a_\mu)_E = (\mathcal{A}^a_i, \mathcal{A}^a_4 = -i\mathcal{A}^a_0),$$

With these replacements, QCD Lagragian density $\mathcal{L}$ is replaced by the *Euclidean Lagrangian density* $\mathcal{L}_E$. With all this, the partition function for the quark-gluon plasma at zero chemical potential in terms of *Euclidean Lagrangian density* $\mathcal{L}_E$ is given by,

$$\mathcal{Z} = \int \mathcal{D}\mathcal{A}^a_\mu(\mathbf{x},\tau)\mathcal{D}\bar{\Psi}(\mathbf{x},\tau)\mathcal{D}\Psi(\mathbf{x},\tau)e^{-\int_0^\beta d\tau \int d^3x \mathcal{L}_E[\mathcal{A}^a_\mu,\bar{\Psi},\Psi]}. \tag{5.28}$$

The replacements of time coordinates of various variables restrict the allowed field configurations. The gluon field configurations which follow periodic boundary condition, and Grassmann fermion fields which follow anti-periodic boundary conditions, are allowed, i.e., $\mathcal{A}^a_\mu(\mathbf{x},\tau) = \mathcal{A}^a_\mu(\mathbf{x},\tau+\beta)$ and $\Psi(\mathbf{x},\tau) = -\Psi(\mathbf{x},\tau+\beta)$ etc. These restrictions come because of invariance of partition function under the cyclic permutations of fields $\mathcal{A}^a_\mu, \bar{\Psi}, \Psi$ inside the *trace*, see Eq. 5.26.

The *thermal equilibrium ensemble average* $<\hat{\mathcal{O}}> = tr(e^{-\beta\hat{H}}\hat{\mathcal{O}})$ of any observable $\hat{\mathcal{O}}[\mathcal{A}^a_\mu, \bar{\Psi}, \Psi]$ can be calculated by,

$$<\hat{\mathcal{O}}> = \frac{\int \mathcal{D}\mathcal{A}^a_\mu(\mathbf{x},\tau)\mathcal{D}\bar{\Psi}(\mathbf{x},\tau)\mathcal{D}\Psi(\mathbf{x},\tau)\mathcal{O}[\mathcal{A}^a_\mu,\bar{\Psi},\Psi]e^{-\int_0^\beta d\tau \int d^3x \mathcal{L}_E[\mathcal{A}^a_\mu,\bar{\Psi},\Psi]}}{\int \mathcal{D}\mathcal{A}^a_\mu(\mathbf{x},\tau)\mathcal{D}\bar{\Psi}(\mathbf{x},\tau)\mathcal{D}\Psi(\mathbf{x},\tau)e^{-\int_0^\beta d\tau \int d^3x \mathcal{L}_E[\mathcal{A}^a_\mu,\bar{\Psi},\Psi]}}. \tag{5.29}$$

5.3 QCD Phase Transitions

To describe a phase transition from one phase to the other, one requires an order parameter which has its magnitude zero in one phase and non-zero in the other phase. For the QCD transition two order parameters can be defined, which characterizes/distinguishes hadronic and QGP phases. One is obtained by the thermal expectation value of the *Polyakov loop operator*,

$$L = \frac{1}{3}tr\left(\mathcal{P}e^{ig\int_0^\beta \mathcal{A}_4(\mathbf{x},\tau)d\tau}\right), \tag{5.30}$$

i.e. $\langle L\rangle$, which characterizes QCD confinement-deconfinement transition, where $\mathcal{A}_4 = \mathcal{A}^a_4\frac{\lambda^a}{2}$ and $\mathcal{P}$ stands for the *path ordering* in time direction. The other one is the thermal expectation value of *chiral condensate* $\bar{\Psi}(x)\Psi(x)$, i.e. $\langle\bar{\Psi}\Psi\rangle$, which characterizes the QCD *chiral transition*.

The exponent in the Polyakov loop operator is a gauge dependent field, but Polyakov loop operator itself is a gauge independent operator (due to presence of trace and periodic boundary condition of $\mathcal{A}^a_4$). To make $\mathcal{A}^a_4$ field τ-independent one chooses a gauge such that τ-dependence goes away. Therefore the exponent becomes $ig\int_0^\beta \mathcal{A}_4(\mathbf{x},\tau)d\tau = ig\beta\mathcal{A}^a_4(\mathbf{x})\frac{\lambda^a}{2}$. Now, one can put a test heavy quark at $\mathbf{x}$, in the medium of gauge field $\mathcal{A}_\mu^a(\mathbf{y})$, and calculate its interaction with the medium (L_{int} is in the Euclidean space),

$$H_{int} = -L_{int} = \sum_{\mu=1}^{4} \int d^3y J_\mu^a(\mathbf{y}) \mathcal{A}_\mu^a(\mathbf{y}), \tag{5.31}$$

where Euclidean four color current density for this quark is given by, $J_\mu^a(\mathbf{y}) = -ig\frac{\lambda^a}{2}\delta(\mathbf{y}-\mathbf{x})(1,0,0,0)$. Therefore,

$$H_{int} = -\int d^3y J_4^a(\mathbf{y}) \mathcal{A}_4^a(\mathbf{y}) = -ig\mathcal{A}_4^a(\mathbf{x})\frac{\lambda^a}{2}. \tag{5.32}$$

With this result, the exponent in the Polyakov loop operator can be written as $e^{ig\beta\mathcal{A}_4^a(\mathbf{x})\frac{\lambda^a}{2}} = e^{-\beta H_{int}}$. So, if the thermal expectation value of the Polyakov loop operator $\langle L \rangle$ becomes zero, the energy of the free quark becomes infinite, which indicates that the pure gluon medium is in the *confined* state which does not allow the existence of a free quark. On the other hand if thermal expectation value $\langle L \rangle$ is not zero, then the energy of the free quark will be finite and the medium will be in the deconfined phase. Therefore $\langle L \rangle$ properly distinguishes the two phases and therefore can be treated as an order parameter of the confinement - deconfinement transitions.

$\langle L \rangle$ for the pure gluon theory (without any quark and anti-quark) shows a sudden jump in its value at the transition temperature, which indicates that, the transition is of *first order*. It gets a non-zero value in the deconfined phase and zero in the confined phase. At finite temperature, the system allows for a $\mathcal{Z}_3$ symmetry (center of $SU(3)_c$), which corresponds to twist in the gauge transformation in time direction. This $\mathcal{Z}_3$ symmetry is spontaneously broken in the deconfined phase (due to non-zero value of $\langle L \rangle$), while it is restored in the confined phase. In the deconfined phase, vacuum becomes 3-fold degenerate, and form a *disconnected order parameter space*. For this space, zeroth-homotopy group is non-trivial and therefore *topological domain walls* ($\mathcal{Z}_3$ wall) can exist in the deconfined gluonic medium. In the presence of quark and anti-quark fields, this symmetry is explicitly broken and transition becomes cross-over. The Lattice QCD result for the confinement-deconfinement transition at zero chemical potential has been shown in the left of the Fig. 5.2. At low temperature the value of $\langle L \rangle$ is very small. It rises very quickly near the transition temperature and become saturated at higher temperatures. This behavior of $\langle L \rangle$ indicates that there is cross-over transition from confined phase to the deconfined phase. The derivative of

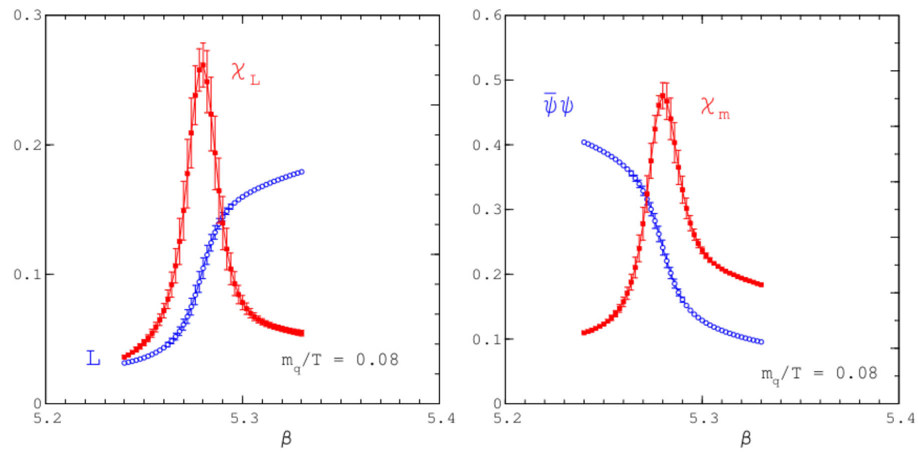

Figure 5.2: Figure shows a strong temperature dependence of the thermal expectation value of the Polyakov loop operator $\langle L \rangle$ and $\langle \bar{\Psi}\Psi \rangle$ where both the expectation values are independent from x due to translational invariance of the medium. The temperature derivative of these thermal expectation values provides the the peak position where cross-over transition happens and in both the cases, location of the peak lie at the same temperature. Here β is different parameter $\beta = 6/g^2$ which is monotonically related with the temperature. Figure has been taken from Ref. [4]

this with respect to temperature (in the figure β plays the role of temperature) shows a peak at a point, which indicates the exact value of the transition temperature.

In the case of chiral transition, in the QGP phase, constituent quark mass (effective mass of quark generated due to chiral transition) vanishes. The current quark mass of u and d are small ($5 - 10\ MeV$) compare to QCD scale so that one can neglect their masses. The right of the Fig. 5.2 shows the Lattice QCD result for the chiral transition. In the high temperature regime, $\langle \bar{\Psi}\Psi \rangle$ condensate approaches zero value which indicates that chiral symmetry gets restored in this phase. Near the transition temperature, chiral condensate $\langle \bar{\Psi}\Psi \rangle$ changes very quickly to a higher value and symmetry gets broken in this phase. This symmetry breaking provides 1 GeV masses to protons and neutrons by generating an effective masses of u and d quarks (also s quark) in the medium, which is known as the *constituent* quark mass. If masses of all three quarks (u, d, and s) are considered to be zero, then in such situation the chiral transition is a first order symmetry breaking phase transition [6]. However, if one considers the actual masses of all three quarks, then the chiral transition becomes a cross-over transition [6], which is shown in right in the Fig.5.2. Due to explicit symmetry breaking of QCD in presence of quark masses, pions (also other Goldstone bosons) become *pseudo Goldstone boson* with the small mass $\sim 140\ MeV$. In the figure the derivative of the chiral condensate with respect to the temperature shows a peak, and the position of the peak matches with the confinement-deconfinement transition temperature which indicates that both the transition happen at the same temperature.

The deconfinement transition leads to the liberation of large number of gluons and quarks - anti-quarks and results in the quark-gluon plasma. The chiral symmetry restoration transition leads to small dynamical masses (smaller than the transition temperature) of the u, d and s quarks which makes their production cross section larger and therefore these quarks get produced in a bulk amount and form an equilibrated plasma.

Fig. 5.3 shows the Lattice results which indicates that required energy density to achieve QGP is larger than $\sim 1\ GeV/fm^3$. As number of degrees of freedom of the deconfined plasma is very large compared to confined phase, therefore to have QGP, required energy density is also very large. The transition temperature for the hadron to QGP transition is $\sim 170\ MeV$. It is clear from the plot that at the transition temperature, the rise in the energy density is very fast. From the calculation of grand canonical ensemble of massless gas of quarks and gluons, the energy density is $\epsilon_{SB} = \left(g_b + \frac{7}{8} g_f\right) \frac{\pi^2}{30} T^4$, where g_b is the bosonic degree of freedom, here it is 2(helicity)$\times$ 8(color)=16 gluon degrees of freedom and g_f is the fermionic degrees of freedom, here it is 2(spin)$\times$3(color)$\times$3(flavor)$\times$2($q+\bar{q}$)=36 massless quark and antiquark degrees of freedom. This is known as *Stefan-Boltzmann limit* which is also indicated in the figure by the right arrow. This limit, within the given range of temperature, is not achieved by QGP in lattice calculations.

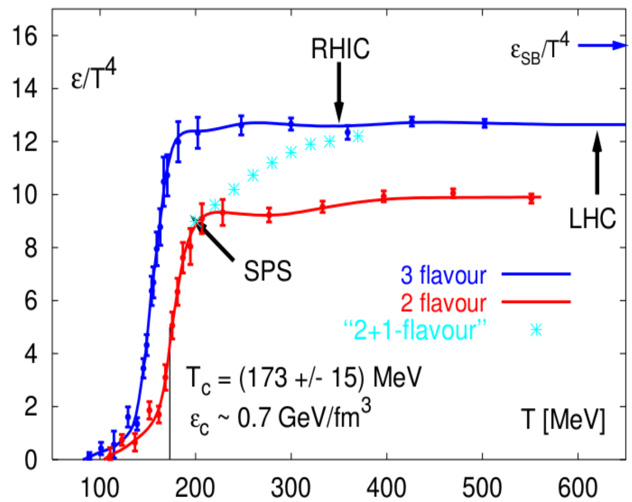

Figure 5.3: Figure shows the increase in the energy density with increasing temperature from the confined phase to the deconfined phase which happens due to increase in the degrees of freedom in the deconfined phase. Blue plot corresponds to the three flavor case where we have more degrees of freedom and hence higher energy density, while red plot corresponds to two flavor case and therefore has lower energy density. In both the cases masses of the quarks has been taken $\frac{m_q}{T} = 0.4$. Blue plot corresponds to the case when mass of strange quark is considered to be $\frac{m_q}{T} = 1$ keeping mass of u and d same. Energy density in this case matches with the 2 flavor case at lower T value, while at higher T, it approaches to 3 flavor case. The transition temperature for QGP phase is obtained $\sim 170\ MeV$ and energy density, required to have QGP, is comes out in the same order as in the core of a proton $\sim 1\ GeV/fm^3$. Figure has been taken from Ref. [4]

5.4 Superfluid Phases of QCD

5.4.1 Color-flavor Locked (CFL) Phase

As we have discussed, QCD is an asymptotically free theory. Therefore at sufficiently high baryon density, quarks can not remain bound inside hadrons and form deconfined phase of QCD. If the temperature of the system is sufficiently low, i.e. $T \ll \mu_B$, then quarks form a degenerate Fermi liquid. At non-zero baryon densities, more number of quarks exist in the system than anti-quarks. Therefore in such systems, interactions among the quarks are more relevant for deciding the physical properties of the system. According to the BCS theory, to form Cooper pairs near the Fermi surface, an attractive interaction (irrespective of the strength of interaction, even incredibly weaker interaction gives bound state) between particles is required. A pair of particles, having attractive interaction near the Fermi surface, reduces the free energy of the system. Therefore system strongly supports the formation of more and more number of Copper pairs near the Fermi surface. These Cooper pairs Bose condense and give rise to charged or uncharged superfluidity (depending upon the charge state of the cooper pairs). The charged superfluidity is known as the superconductivity.

At very high densities, near the Fermi surface quarks are almost free, so the perturbative calculations can be performed [7]. The quark-quark pairs can have both, anti-symmetric and symmetric color combinations, which form triplet and sextet states, respectively, as $3 \otimes 3 = 3^* \oplus 6$. The quark-quark anti-symmetric color combinations $\big((rg - gr)/\sqrt{2},\ (gb - bg)/\sqrt{2},\ (br - rb)/\sqrt{2},\big)$ has attractive interaction through one gluon exchange [8]. Therefore near the Fermi surface in the anti-symmetric color combination, quarks form Cooper-pairs and Bose condensate. Since this combination of quarks is not *color singlet*, therefore the condensate breaks the color gauge symmetry of the QCD Lagrangian. Since these phases of QCD breaks color gauge symmetry of QCD Lagrangian, that is the reason, these phases are called *color superconductor*. Since quarks have many degrees of freedom, spin, flavor, and color, therefore depending upon the quark-quark Cooper pair combinations, several kind of color superconducting phases are possible. Since such superconducting phases break color gauge symmetry spontaneously, therefore in these phases gauge bosons of the theory, which are gluons, become massive and give rise to *color Meissner effects*.

At very high baryon chemical potential $\sim 1500\ MeV$ (quark chemical potential $\sim 500\ MeV$), Fermi energy of the system becomes so high that, with respect to this, one can neglect the effect of masses of u, d, s quarks in medium [7]. In this regime u, d, s quarks can be considered on the same footing. In this regime all three quarks have their common Fermi momenta. Therefore all the spin-color-flavor combinations of Cooper pairs occur just above the (same) Fermi momenta in such a high density regime, and conventional zero momentum spin-less BCS Cooper pairs form. This phase of QCD is known as the *color-flavor locked* (CFL) phase in which all eight gluons become massive.

The quark-quark pair condensate is characterized in the gauge-variant way. The quark-quark pairing is given by the ground state expectation value of quark-quark two-point function. In the CFL phase, it is given by [7],

$$\begin{aligned} \langle \psi_i^\alpha \mathcal{C}\gamma_5 \psi_j^\beta \rangle &\propto \Delta_{_{CFL}}(\kappa+1)\delta_i^\alpha\delta_j^\beta + \Delta_{_{CFL}}(\kappa-1)\delta_j^\alpha\delta_i^\beta \\ &= \Delta_{_{CFL}}\epsilon^{\alpha\beta A}\epsilon_{ijA} + \Delta_{_{CFL}}\kappa(\delta_i^\alpha\delta_j^\beta + \delta_j^\alpha\delta_i^\beta). \end{aligned} \tag{5.33}$$

Here ψ is the quark field operator. This expression has all possible combinations of quark-quark interactions including symmetric combinations (second term in second line in the equation) which have repulsive interaction. Since repulsive part of quark-quark interaction is not of interest for Cooper pairs formation, therefore we ignore the κ term in the last line of the above expression. In the above expression, $\mathcal{C}$ is the Dirac charge conjugation matrix which is given by $\mathcal{C} = i\gamma_2\gamma_0$. Here $\Delta_{_{CFL}}$ is the CFL gap parameter. α, β are color indices which range over red, green, blue (r, g, b) 1-3 indices, and i, j are flavor indices which range over up, down, strange (u, d, s) 1-3 indices. Here the combinations of quarks has been taken such that they form parity-even (quark-quark pair with equal and opposite momenta) and spin-singlet (so that gap remain isotropic in momentum space) state. Since Dirac structure $\mathcal{C}\gamma_5$ is a Lorentz singlet, therefore total state is anti-symmetric in the spinor Dirac indices (spinor Dirac indices are not written here). This implies that color-flavor combinations should be in the symmetric state. As we have mentioned that only anti-symmetric color combinations of quarks have attractive interaction therefore flavor combinations should also be anti-symmetric such that color-flavor state form a symmetric state. Note that momentum zero and spin-less quark combination implies that quarks which are participating in the formation of a Cooper pair will have same chirality (quark masses are considered to be zero).

The above combinations of quarks near the Fermi surface breaks the symmetry of the (zero mass) QCD Lagrangian (this symmetry is also followed by the quark-gluon plasma phase). The symmetry breaking pattern from QGP to CFL phase is,

$$SU(3)_c \times SU(3)_L \times SU(3)_R \times U(1)_B \rightarrow SU(3)_{c+L+R} \times \mathcal{Z}_2. \tag{5.34}$$

It is clear from the combinations of the quarks that they are colored objects. Therefore when such combinations condense in the ground state, it breaks the color gauge symmetry of the QCD Lagrangian. Due to this condensation, all eight gluons become massive in the CFL phase, which gives rise the *color Meissner effect*. This phase also breaks the chiral symmetry of the QCD Lagrangian but in a different way as broken by the $\langle\bar{\psi}\psi\rangle$ condensate in the QGP to hadron chiral transition. In the Eq.5.33, Kronecker deltas mix color and flavor indices, therefore only under the equal and opposite global $SU(3)$ rotation in color and flavor (vector transformation) spaces, the condensate remains invariant, and by this way, a global $SU(3)_{c+L+R}$ symmetry survive in this phase. Therefore, since in this phase, pairing of quarks show invariance under locked transformation of color and flavor basis ($SU(3)_{c+L+R}$), that is the reason why this phase is called *color-flavor locked phase*. This phase breaks the color and axial symmetry of QCD Lagrangian.

In the CFL phase, the global baryon number $U(1)_B$ symmetry breaks to discrete $\mathcal{Z}_2$ symmetry. Because of this reason, CFL phase is a superfluid phase of QCD. The order parameter for a superfluid phase should be a gauge invariant quantity (should be color and electric charge neutral). Therefore to characterize superfluidity in the CFL phase, gauge invariant six-quarks order parameter is used, which has color and flavor structure of two Λ baryons, $\langle\Lambda\Lambda\rangle$, where $\Lambda = \epsilon^{abc}\epsilon_{ijk}\psi^a_i\psi^b_j\psi^c_k$. Due to breaking of $U(1)_B$ symmetry, a massless Goldstone mode arises in this phase which governs the dynamics of superfluid. Since in this phase $U(1)_B$ breaks to $\mathcal{Z}_2$, therefore coset space (order parameter space) of this phase is $U(1)/\mathcal{Z}_2$ which is homeomorphic to a circle S^1. As we know that S^1 order parameter space has non-trivial fundamental group, i.e. $\pi_1(S^1) = \mathcal{Z}$. Therefore in this phase, string like defects can exist, which are superfluid vortices. There are studies which show that, the superfluid vortex in CFL phase is energetically unfavorable (in some parametric regime) compared to well-separated triplets of semi-superfluid color flux tubes [9], therefore it decays into three such semi-superfluid color flux tubes [10].

In the medium, quark's effective (constituent) masses are density dependent, which is expected to decrease with increasing density of the medium [7]. For the discussion, we ignore the effective masses of u and d quarks. At relatively lower densities, effective mass of strange quark shows its effect in the pairing with the u and d quarks. At a given baryon chemical potential, due to presence of larger mass of strange quark, the Fermi momenta of s quark gets a different value from Fermi momenta of u and d quarks. Therefore, BCS pairing between s and u,d quarks with equal and opposite momenta, implies that strange quark can not lie near its Fermi momenta. Such kind of BCS Cooper pairing costs energy and therefore Cooper pairs feel stress in such cases. Such stress becomes more and more stronger (with respect to gap parameter Δ) as baryon density decreases. At sufficiently lower baryon density CFL pairing disappears. In this regime, some exotic, non-BCS, paring of quarks still may be possible which can give even more exotic phase of QCD. However, the BCS paring between u and d quarks still can be possible in lower densities which leads to a different kind of phase known as the 2SC phase (two flavor superconducting phase) in the QCD phase diagram [7].

5.4.2 Neutron Superfluidity

Just after the BCS theory for metal superconductivity was proposed, N.N. Bogoliubov in 1958 and A.B. Migdal in 1959 proposed that neutron and proton also can form Cooper pairs through nucleon-nucleon potential (residual of strong interaction) near the Fermi surface in the nuclear-matter (inside nuclei and in a neutron star), and give rise to uncharged and charged superfluidity, respectively. Such superfluidity arises in the inner crust region and in the core of a neutron star. In the inner crust, density varies from 0.16×10^{-3} fm^{-3} to 0.16 fm^{-3}. This density region of the star belong to the neutron drip line, where protons capture electron and produce neutrino and neutron. With a very large number of production of neutrons, these neutrons can not remain bound inside nuclei and come out from nuclei and form a degenerate Fermi liquid (usually temperature remain very low inside neutron star). In this density range, neutrons feel the attractive part of the long range nucleon-nucleon potential, therefore

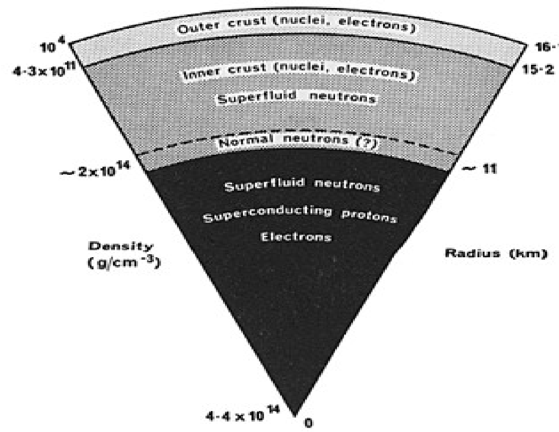

Figure 5.4: Figure shows the cross-sectional view of a typical neutron star. This figure shows the density range in which different superfluid phases of neutron and superconducting phase of protons lies. Figure has been taken from Ref. [11].

form Cooper pairs near the Fermi surface and Bose condensate. In such density regime neutron star has $^1S_0$ neutron superfluidity. At higher density regime (in the core of star), star has $^3P_2$ neutron superfluidity, since in this density regime repulsive part of the nucleon-nucleon potential makes $^1S_0$ state unstable, and instead of this, calculations support to have $^3P_2$ pairing. In this density region, protons and neutron both become free from nuclei. Protons also form Cooper pairs in $^1S_0$ channel and give rise to proton superconductivity, see Fig.5.4. The transition temperature for these superfluids are model dependent (depending upon the potential used). Therefore there are wide range of superfluid transition temperatures are possible. Estimates for transition temperature vary from 0.2 MeV to 5 MeV.

Since neutron star contains free state of nuclei, protons, and electrons, when it rotates it radiates electromagnetic radiation and looses its total energy. Due to this, a rotating neutron star slows down with time, see Fig.5.5. Apart from this, It is also observed that angular velocity of neutron star suddenly gets increased, and this happens periodically, see Fig.5.5. This phenomena is known as glitches. Such periodic glitches can not be satisfactorily explained by any other model except superfluidity and superfluid vortices. The glitches, therefore give a very strong support to have neutron superfluidity and superfluid vortices inside neutron star. The explanation of such phenomena is as follows. Due to the rotation of neutron star, in the inner

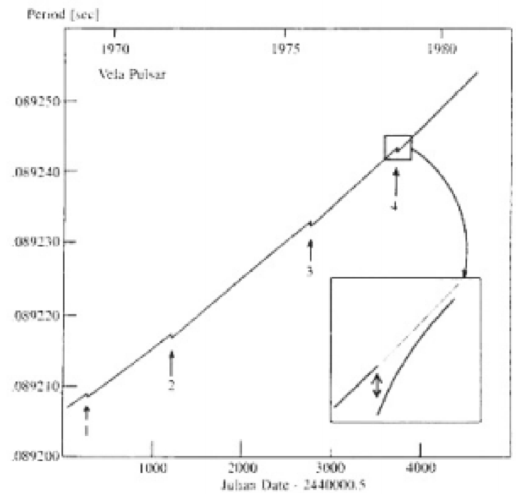

Figure 5.5: Figure shows the observation of periodic change in the angular velocity (glitches) of a neutron star in time. Figure has been taken from Ref. [11].

crust and core region, a superfluid vortex lattice forms. Note that superfluid vortex contains angular momentum (superfluid component rotates around each superfluid vortex). Now, though the angular velocity of a neutron star decreases with time due to electromagnetic radiation, but since it contains neutron superfluid, and superfluid has the property that it does not transfer its energy and momentum to other part of the system, therefore superfluid part of the star continue to rotate with its original angular velocity. The time reaches when the system becomes energetically highly unstable. It is more favorable that, a bunch of superfluid vortices get depin from the boundary of inner crust and core, and transfer its angular momentum to the outer crust. This gives rise the glitches phenomena. Again, with time, vortex lattice forms, and by this, such phenomena repeatedly occurs. The explanation of this phenomena has a unique requirement which is only satisfied by superfluid and superfluid vortex. Therefore periodic glitches are the strongest support to have neutron superfluidity and superfluid vortices inside a neutron star. The post-glitch exponential relaxation can also be explained by the two fluid model (normal fluid + superfluid), at least qualitatively [11]. Other models also use the presence of superfluidity inside neutron star to fit the data. Presence of neutron superfluidity also affects cooling of neutron star [11].

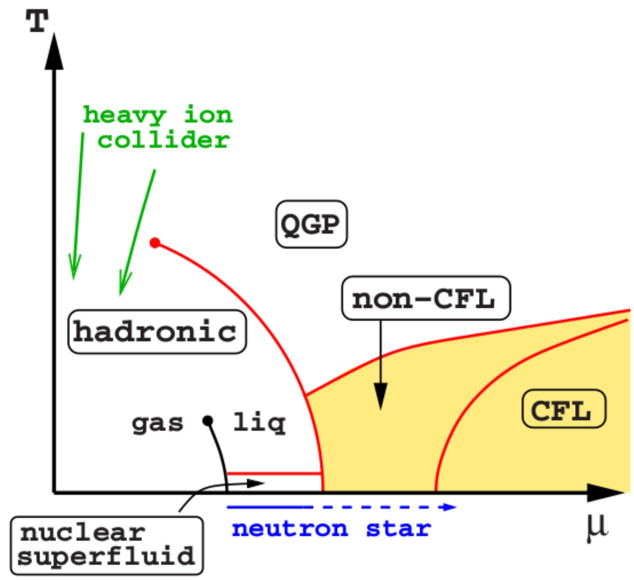

Figure 5.6: Figure shows the QCD phase diagram. Along y-axis we have temperature while along x-axis we have baryon chemical potential. Figure has been taken from Ref. [7]

QCD Phase Diagram

We end this chapter by briefly discussing the QCD phase diagram. From Fig.5.6, it is clear that QCD has very rich phase structure. At very high temperature and baryon density due to asymptotic freedom of QCD, quarks become deconfined from hadrons and form a medium which is known as the quark-gluon plasma (QGP). To have QGP, energy density of a system should be higher than 1 GeV/fm^3. Below this density, we have confined phase of QCD which are hadrons. The confined phase QCD itself has very reach phase structure. In the hadronic phase, there is gas to liquid first order phase boundary which ends at a critical point. At sufficiently low temperature there is possibility to have neutron superfluidity and proton superconductivity. There is also a first order phase boundary present from hadronic phase to the QGP phase at finite chemical potential which ends at the critical point of QCD. At very low chemical potential, there is a cross-over transition from hadron to QGP. Heavy-ion collision experiments at RHIC and LHC probe the QCD phase diagram in this regime, where system produced in these experiments encounter cross-over transition from

QGP to hadrons. At extremely high baryon density and sufficiently low temperature we have various color superconducting phases of QCD. Existence of such phases may be possibly inside a neutron star.

Bibliography

[1] M.E. Peskin, D.V. Schroeder, **An Introduction to Quantum Field Theory**, Addison-Wesley Publishing Company (1996).

[2] F. Halzen, A.D. Martin, **Quarks and Leptons: An Introductory Course in Modern Particle Physics**, John Wiley & Sons (1984).

[3] K. Yagi, T. Hatsuda, A. Miake, **Quark-Gluon Plasma : From Big Bang to Little Bang**, Cambridge University Press (2005).

[4] Ulrich Heinz, Concepts of Heavy-Ion Physics, **arXiv:**hep-ph/0407360.

[5] Larry McLerran, Rev. Mod. Phys. **58**, (1986).

[6] C. Bonati, P. de Forcrand, M. DElia, O. Philipsen, F. Sanfilippo, Proceedings of science, CERN-PH-TH/2012-003, YITP-12-2, IFUP-TH/2012-01, arXiv:1201.2769.

[7] M.G. Alford, A. Schmitt, K. Rajagopal, T. Schäfer, Rev. Mod. Phys. **80**, 1455 (2008).

[8] D. Griffiths, **Introduction to Elementary Particles**, WILEY-VCH Verlag GmbH & Co. KGaA (2004).

[9] A.P. Balachandran, S. Digal, and T. Matsuura, Phys. Rev. D **73**, 074009 (2006).

[10] M.G. Alford, S.K. Mallavarapu, T. Vachaspati, and A. Windisch, Phys. Rev. C **93**, 045801 (2016).

[11] Ka Wai Lo, **Neutron Star and Superfuidity**, (2010).

Chapter 6

Hydrodynamics: Formalism

6.1 Relativistic Ideal Hydrodynamics

Hydrodynamic description of a system requires (at least) local thermodynamic equilibrium, i.e., *mean free path* of two successive collisions should be sufficiently smaller than the typical size of the local region. Hydrodynamic description does not depend upon the nature of the constituents of fluid element, whether constituents are classical or quantum, but it depends on the *equation of state*, a thermodynamic property of the system, which depends upon their underlying microscopic interactions Ref. [1]. The requirement of local thermodynamic equilibrium allows to describe the system with its local thermodynamic variables, e.g. energy density ϵ, pressure P, temperature T, entropy density s, etc. These variables can vary in space, which is against the *global thermodynamic equilibrium*, and hence there can be presence of flow in the system. The assumption of local thermodynamic equilibrium is the *ideal hydrodynamic approximation* where there is no transfer of momentum between two nearby fluid elements (no heat conduction and viscosity). This kind of fluid is called *ideal fluid* or *inviscid fluid*. For an *ideal fluid* there is no entropy production and therefore its evolution is known as *isentropic* Ref. [1]. The *ideal hydrodynamics* gives a good description of the *quark-gluon plasma* produced in relativistic heavy-ion collisions.

Relativistic hydrodynamics is needed when either fluid velocity is relativistic or its constituents are relativistic particles Ref. [2]. To discuss the formalism of relativistic hydrodynamics, we begin by defining fluid element, its four velocity, fluid local rest frame, and the energy-momentum tensor.

Fluid element: is a part of the system where one can assume the local thermodynamic equilibrium. A fluid element contains sufficiently large number of particles such that there is sufficient interactions among particles and statistical average makes sense. In a fluid element, particles have very small mean free path compared to the size of fluid element.

Fluid four velocity: in the laboratory frame, in the four vector notation is defined as,

$$u^\mu = \gamma(1, \vec{v}), \quad \gamma = \frac{1}{\sqrt{1-\vec{v}^2}}, \tag{6.1}$$

where $\vec{v}$ is the three velocity of fluid element in the *laboratory frame* which is, in general, function of (t, x, y, z); fluid velocity is also called *collective velocity.* We will be working in the natural units with $\hbar = c = 1$. In this chapter, We will follow the Minkowski metric $g^{\mu\nu} = (1, -1, -1, -1)$. We can easily see with the definition of u^μ and $g^{\mu\nu}$ that,

$$u^\mu u_\mu = 1. \tag{6.2}$$

Fluid rest frame: is defined as a frame in which fluid element under consideration is at rest; its momentum and hence its three velocity $\vec{v}$ is equal to zero. Therefore in the fluid rest frame, four velocity is given by $u^\mu = (1, 0)$. All the thermodynamic quantities, e.g. energy density ϵ, pressure P, number density n, etc., associated with the fluid element are defined in the rest frame of fluid and they are *Lorentz scalars* by construction Ref. [1]. In the fluid rest frame, all the properties of the fluid element are isotropic which gives a specific structure to energy momentum tensor discussed below.

Energy-momentum tensor $T^{\mu\nu}$: is a rank-2 *contravariant tensor*, whose elements are functions of local fluid variables ϵ, P, $\vec{v}$ and have their physical meaning as [1],

i) $T^{00} \equiv$ energy density of the fluid element.
ii) $T^{0i} \equiv$ momentum density along i-axis.
iii) $T^{i0} \equiv$ energy flux along i-axis.
iv) $T^{ij} \equiv$ jth component of momentum flux along i-axis.

The *momentum flux* T^{ij} is usually called the *pressure tensor* P^{ij}. $T^{\mu\nu}$ is a conserved quantity which follows the energy-momentum conservation laws,

$$\partial_\mu T^{\mu\nu} = 0. \tag{6.3}$$

Along with energy-momentum, there can be more conserved quantities (conserved charges) present in the system, e.g., baryon number. So we have another conservation equation as,

$$\partial_\mu N^\mu = 0, \quad N^\mu = n u^\mu, \tag{6.4}$$

where $N^0 = n\gamma$, n is the *baryon density* in the fluid rest frame and $\vec{N} = n\gamma\vec{v}$ is the *baryon flux*. In the local rest frame the *isotropic* property of the fluid element (in the *inviscid hydrodynamics*) demands that the *baryon flux* should vanish in this frame (otherwise the directionality of such flow destroy local equilibrium). This is not true in the case of *dissipative hydrodynamics* where the *baryon flux* can be non-zero even in the fluid rest frame.

In the ideal or inviscid hydrodynamics, there is no heat exchange between two nearby fluid elements, therefore entropy is also conserved in this fluid. Therefore the evolution of inviscid hydrodynamics is an *isentropic process* (adiabatic process), which follows the local entropy conservation equation,

$$\partial_\mu s^\mu = 0, \quad s^\mu = s u^\mu, \tag{6.5}$$

where s is entropy density in the fluid rest frame.

With all these definitions, we can now construct the energy-momentum tensor in the laboratory frame. We first write $T^{\mu\nu}$ in the fluid local rest frame, where the isotropy property of the fluid element demands that all off-diagonal components of $T^{\mu\nu}$ should be zero. Thus in the fluid rest frame, momentum density T^{0i} and energy flux T^{i0} becomes zero, and pressure tensor becomes diagonal, i.e. $P^{ij} = P\delta^{ij}$, where P is the thermodynamic pressure. Therefore in the fluid rest frame, $T^{\mu\nu}$ is given by,

$$T^{\mu\nu}_{LRF} = \begin{pmatrix} \epsilon & 0 & 0 & 0 \\ 0 & P & 0 & 0 \\ 0 & 0 & P & 0 \\ 0 & 0 & 0 & P \end{pmatrix}$$

In the fluid rest frame, baryon 4-current and entropy 4-currents are given by,

$$N^{\mu}_{LRF} = \begin{pmatrix} n \\ 0 \\ 0 \\ 0 \\ 0 \end{pmatrix} \quad ; \quad s^{\mu}_{LRF} = \begin{pmatrix} s \\ 0 \\ 0 \\ 0 \\ 0 \end{pmatrix} .$$

To obtain $T^{\mu\nu}$ in the laboratory frame one can do Lorentz transformation of $T^{\mu\nu}_{LRF}$ and obtain, $T^{\mu\nu} = \Lambda^{\mu}_{\alpha}\Lambda^{\nu}_{\beta}T^{\alpha\beta}_{LRF}$, where Λ is the *Lorentz transformation matrix*. But here we adopt the trick used in the Ref. [3]. As $T^{\mu\nu}$ is a double rank tensor it can only be a function of u^{μ} and $g^{\mu\nu}$. Therefore $T^{\mu\nu}$ in the laboratory frame can be written uniquely as,

$$T^{\mu\nu} = c_1 u^{\mu}u^{\nu} + c_2 g^{\mu\nu}, \tag{6.6}$$

where c_1 and c_2 are unknown coefficients which we have to determine. Similarly in the laboratory frame N^{μ} and s^{μ} can be written as,

$$N^{\mu} = c_3 u^{\mu}, \quad s^{\mu} = c_4 u^{\mu}. \tag{6.7}$$

So from the above equations in the fluid local rest frame, where $u^{\mu} = (1, 0, 0, 0)$ we have,

$$T^{\mu\nu}_{LRF} = \begin{pmatrix} c_1 + c_2 & 0 & 0 & 0 \\ 0 & -c_2 & 0 & 0 \\ 0 & 0 & -c_2 & 0 \\ 0 & 0 & 0 & -c_2 \end{pmatrix}$$

$$N^{\mu}_{LRF} = \begin{pmatrix} c_3 \\ 0 \\ 0 \\ 0 \\ 0 \end{pmatrix} \quad ; \quad s^{\mu}_{LRF} = \begin{pmatrix} c_4 \\ 0 \\ 0 \\ 0 \\ 0 \end{pmatrix} .$$

From the previous expressions, we know the form of $T^{\mu\nu}_{LRF}$, N^{μ}_{LRF}, and s^{μ}_{LRF} in the local rest frame. Therefore we get, $c_1 + c_2 = \epsilon, -c_2 = P, c_3 = n, c_4 = s$. By putting these coefficients in the Eq.(6.6) we get $T^{\mu\nu}$ in the laboratory frame as,

$$T^{\mu\nu} = (\epsilon + P)u^{\mu}u^{\nu} - Pg^{\mu\nu}. \tag{6.8}$$

Similarly in the laboratory frame N^μ and s^μ are,

$$N^\mu = nu^\mu, \quad s^\mu = su^\mu. \tag{6.9}$$

Therefore all the conservation equations in the *inviscid hydrodynamics* are,

$$\partial_\mu T^{\mu\nu} = 0, \quad \partial_\mu N^\mu = 0, \quad \partial_\mu s^\mu = 0. \tag{6.10}$$

Eqs.(6.8),(6.9) and (6.10) are the *ideal hydrodynamics* equations. With the use of *equation of state* (relation between ϵ and P) the above equations become close system of equations in the sense that number of independent variables present in the equations become equal to number of available equations to determine them.

$T^{\mu\nu}$ obtained above is a symmetric tensor. The component T^{0i} has physical meaning of momentum density along i-axis can be understood by writing its form from Eq.(6.8) by keeping only term in the first order in velocity, $T^{0i} = (\epsilon + P)v^i$ which has the form of momentum density in the non-relativistic system, ρv^i (ρ is the mass density). In the non-relativistic system pressure $P \ll \epsilon$, therefore pressure does not contribute in the inertia. But in the relativistic system, pressure is comparable to the energy density of the fluid, therefore inertia of the fluid in the relativistic system is given by $(\epsilon + P)$ [1].

To write Eqs.(6.8),(6.9) and (6.10) in a convenient form, we introduce two index tensor which is a projection operator,

$$\Delta^{\mu\nu} = g^{\mu\nu} - u^\mu u^\nu. \tag{6.11}$$

This operator is perpendicular to the fluid four velocity since,

$$u_\mu \Delta^{\mu\nu} = 0. \tag{6.12}$$

Also it has the property that $\Delta^{\mu\alpha}\Delta_\alpha^\nu = \Delta^{\mu\nu}$. From the expression of $T^{\mu\nu}$, it can be deduced that,

$$\epsilon = u^\mu u^\nu T^{\mu\nu}, \quad P = -\frac{1}{3}\Delta_{\mu\nu}T^{\mu\nu}. \tag{6.13}$$

Now we define derivative called co-moving or convective derivative (derivative acting along the motion of the fluid)

$$D = u^\mu \partial_\mu. \tag{6.14}$$

Four divergence is defined as,

$$\Theta = \partial_\mu u^\mu \tag{6.15}$$

and let $\nabla_\mu = \Delta_\mu^\alpha \partial_\alpha$. With these definitions we can write our conservation equations by using identity $u_\nu \partial_\mu T^{\mu\nu} = 0$,

$$D\epsilon + (\epsilon + P)\Theta = 0. \tag{6.16}$$

This equation is known as the *cooling equation*. By using identity $\Delta_\mu^\alpha \partial_\nu T^{\mu\nu} = 0$, we get,

$$(\epsilon + P)Du^\alpha - \nabla^\alpha P = 0, \tag{6.17}$$

which is known as the *Euler's equations*. The baryon number and entropy conservation equations can be written in the form,

$$Dn + n\Theta = 0, \quad Ds + s\Theta = 0. \tag{6.18}$$

Sound wave: Let us consider a fluid with uniform energy density ϵ_0 and pressure P_0. Consider a small perturbation on the top of the energy density and pressure, $\delta\epsilon$ and δP, given by [1],

$$\epsilon(t, x, y, z) = \epsilon_0 + \delta\epsilon(t, x, y, z), \quad P(t, x, y, z) = P_0 + \delta P(t, x, y, z). \tag{6.19}$$

The sound speed is the speed by which small perturbations propagate in a uniform fluid which is at rest. For the evolution of this perturbation, we use linearized form of equation $\partial_\mu T^{\mu\nu} = 0$ by keeping only linear terms in $\delta\epsilon$, δP and $\vec{v}$. Therefore from Eqs.(6.8) and (6.10) we have,

$$\frac{\partial\epsilon}{\partial t} + \vec{\nabla}.((\epsilon + P)\vec{v}) = 0, \quad \frac{\partial}{\partial t}((\epsilon + P)\vec{v}) + \vec{\nabla}P = \vec{0}. \tag{6.20}$$

Writing for small perturbation in the uniform fluid, we get,

$$\frac{\partial(\delta\epsilon)}{\partial t} + (\epsilon_0 + P_0)\vec{\nabla}.\vec{v} = 0, \quad (\epsilon_0 + P_0)\frac{\partial\vec{v}}{\partial t} + \vec{\nabla}(\delta P) = \vec{0}, \tag{6.21}$$

where we have neglected second order terms in the perturbations. Now, the velocity of sound is define as,

$$c_s = \left(\frac{\partial P}{\partial\epsilon}\right)^{1/2}, \tag{6.22}$$

which is inversely related to the *compressibility* of the fluid; smaller sound speed corresponds to the *softer equation of state*. Therefore in the above equations using $\delta P = c_s^2 \delta\epsilon$ and eliminating $\vec{v}$ we get,

$$\frac{\partial^2(\delta\epsilon)}{\partial t^2} - c_s^2 \Delta(\delta\epsilon) = 0, \tag{6.23}$$

which is a wave equation in $3+1$ dimensions showing that any arbitrary perturbation in uniform ideal fluid propagates with the sound speed c_s.

In Chapter 8 we discuss application of the *inviscid hydrodynamic equations* in the evolution of *quark-gluon plasma* in relativistic heavy-ion collisions.

6.2 Discussion on Dissipative hydrodynamics

It is inevitable fact that every fluid has dissipation and because of that it is necessity to incorporate dissipation in the hydrodynamics equations. We will discuss its consequence in the assumption of the local thermodynamic equilibrium and on the structure of $T^{\mu\nu}$. From the kinetic theory of gases the coefficient of viscosity η is given by [4],

$$\eta \approx \frac{1}{3} \sum_i (n\langle p\rangle\lambda)_i, \tag{6.24}$$

where n_i is the density of i-th quanta which transports an average momenta $\langle p\rangle_i$ to a nearby fluid cell in a length scale λ_i. According to the uncertainty principle, these quanta can not be localized within a distance shorter than $\langle p\rangle^{-1}$. Therefore the momentum exchange length scale will always be greater than this value, i.e. $\lambda \gtrsim \langle p\rangle^{-1}$. This sets a lower bound on η as,

$$\eta \gtrsim \frac{1}{3} n, \tag{6.25}$$

where $n = \sum_i n_i$, total density of all the quanta present in the fluid cell. It is very clear from the above equation that the lower bound on η is independent from the detailed dynamics of the system. Another lower bound on η comes due to the fact that λ can not be shorter than inter-particle distance, which implies, $\lambda \gtrsim n^{-1/3}$. This gives,

$$\eta \gtrsim \frac{1}{3} \langle p\rangle n^{2/3}. \tag{6.26}$$

Eq.(6.25) and (6.26) show that every system has a non-zero viscosity. These two lower bounds for the uniform energy density $\epsilon \sim \langle p \rangle n$ (massless case) will be equal if $n = \epsilon^{3/4}$, which gives,

$$\eta \gtrsim \frac{1}{3}\epsilon^{3/4} \tag{6.27}$$

For QGP at zero chemical potential ($\mu = 0$), energy density and temperature are related by $\epsilon = 12.2\, T^4$ (for 2-flavor case). After substituting this in the above equation we get lower bound on η for QGP,

$$\eta \gtrsim 2T^3. \tag{6.28}$$

QGP in heavy-ion collisions might be the hottest system in the present universe which has temperature, 200-600 MeV (depending upon RHIC and LHC Expts.). So it means that QGP has very high viscosity, but it also has very high entropy density in relativistic heavy-ion collisions which also goes with temperature as $s = 16.3\ T^3$ (for 2-flavor case). Therefore η/s ratio for QGP can be very small. The observations show that QGP has the lowest η/s ratio ever observed for any system, see Fig.(6.1) (Ref. [5]). AdS/CFT correspondence also sets a lower bound on the η/s ratio for the strongly coupled Super-Yang-Mills theory, which is $\eta/s \gtrsim 1/4\pi$, see Ref. [6].

When in the system *dissipation* is present, it is not possible to justify local thermodynamic equilibrium due to continuous momentum exchange in between nearby fluid elements [3]. As we have discussed, every fluid has dissipation, therefore assumption of local thermodynamics equilibrium is a strongly restrictive consideration. Even if there is no motion in fluid, because of inhomogeneity in the energy density, momentum exchange takes place (heat flow) which makes momentum distribution of particles in the fluid elements anisotropic. Also, we have already mentioned that a moving fluid always has some viscous effects. Therefore all these effects disturb the local thermodynamic equilibrium and assumption of ideal hydrodynamics will not be valid any more. However, to develop formalism for the dissipative hydrodynamics one assumes that momentum exchange is sufficiently small that one can (at least) define local thermodynamic quantities.

In the dissipative hydrodynamics, due to presence of dissipation and hence absence of *isotropic* property in the fluid rest frame, $T^{\mu\nu}$ of the system is no longer diagonal. And also in this case, in the fluid rest frame baryon current can be non-zero. Therefore

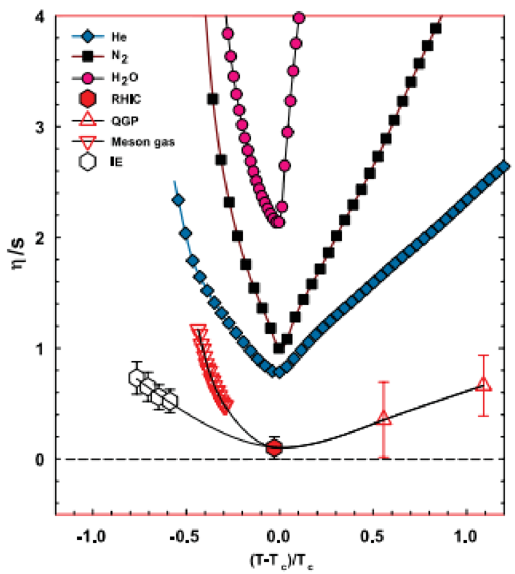

Figure 6.1: Figure shows the η/s ratio with the temperature for different systems. It clearly shows that η/s ratio for QCD matter is lowest. Figure has been taken from the Ref. [5].

to account for the dissipation, dissipative currents $\tau^{\mu\nu}$ and n^μ are added in the ideal $T^{\mu\nu}$ and N^μ, respectively, such that new $T^{\mu\nu}$ and N^μ follow the conservation laws,

$$\partial_\mu T^{\mu\nu} = 0, \quad \partial_\mu N^\mu = 0, \tag{6.29}$$

where,

$$T^{\mu\nu} = (\epsilon + P)u^\mu u^\nu - Pg^{\mu\nu} + \tau^{\mu\nu}, \tag{6.30}$$

$$N^\mu = nu^\mu + n^\mu, \tag{6.31}$$

where $\tau^{\mu\nu}$ is a symmetric tensor. In this case total entropy of the system is not conserved due to dissipation, therefore condition $\partial_\mu s^\mu \geq 0$ is imposed on the fluid. For the review on *dissipative hydrodynamics* we refer to reader Refs. [3, 7].

Bibliography

[1] J. Ollitrault, Eur. J. Phys. **29**, 275302 (2008).

[2] L.D. Landau and E.M. Lifshitz **Fluid Mechanics**, Second Edition, Pergamon Press (1987).

[3] A. Jaiswal and V. Roy, Advances in High Energy Physics, Volume 2016, Article ID 9623034 (2016).

[4] P. Danielewicz and M. Gyulassy, Phys. Rev. D **31**, 53 (1985).

[5] Roy A. Lacey et al., Phys. Rrev. Lett. **98**, 092301 (2007).

[6] P. Romatschke and U. Romatschke, Phys.Rev. Lett. **99**, 172301 (2007).

[7] P. Romatschke, IJMP E **19**, 1-53 (2010).

Chapter 7

Ideal Magneto-hydrodynamics: Formalism

In the previous chapter we studied the dynamics of a fluid in the local thermodynamic equilibrium in the absence of any kind of force. In the presence of force, dynamics of the fluid gets modified. Viscous force is an internal force which reduces the velocity gradient, via momentum transfer, between two nearby layers of fluid and affects the dynamics of the fluid. In astrophysics and cosmology gravitational force, an external force, very strongly affects the dynamics of the fluid. If the constituents of fluid elements are charge particles then dynamics of fluid is affected by the electromagnetic field present in it. We know when a conductor passes through a non-uniform magnetic field, magnetic field exerts force on it (Lenz's law) and opposes its motion. Similarly when a conducting fluid moves in the presence of magnetic field, it feels force and hence its dynamics gets modified; the dynamics of the fluid affects the magnetic field in back also. The dynamics of the fluid is not only affected by electromagnetic field if constituents of fluid elements are charge particles, but if fluid is polarizable (electric or magnetic) then also electromagnetic field affects its dynamics through interaction. Electromagnetic field also changes the thermodynamic pressure of the fluid and makes the sound speed direction dependent in the fluid causing its anisotropic evolution.

In this thesis, we will consider charge neutral conducting fluid. We work in the framework of ideal approximations where in the fluid, viscosity, thermal conduction remain absent throughout its evolution and electric conductivity of the fluid σ is infinity. This is called ideal magneto-hydrodynamics approximation. First we briefly discuss the non-relativistic version of ideal MHD fluid and then move to the relativistic covariant form of ideal MHD equations. We use flat metric of space-time. Note that like in the case of ideal hydrodynamics, in the ideal MHD fluid also the length and time scale of evolution of the fluid always remain sufficiently larger than microscopic length scale (mean free path) and interaction time scale. So the length scale and time scale of any charge current in the fluid must be much smaller than the typical length and time scale of the evolution of the fluid; so no macroscopic current is allowed in the fluid.

The medium response to the electromagnetic field, e.g. polarizability or permeability, affect the strength of electromagnetic field. In vacuum there is no difference between electric field and electric displacement vector, and similarly between magnetic induction and magnetic field. But in medium these fields differ from each other and this difference comes completely due to response of the system. These properties of system also decide the dynamics of electromagnetic field, e.g. electric conductivity of the plasma determines time scale of diffusion of magnetic field in the fluid. Maxwell's equations for electromagnetic fields in a medium in three dimensions are given by [1],

$$\vec{\nabla}.\vec{B} = 0, \quad \vec{\nabla} \times \vec{E} = -\frac{1}{c}\frac{\partial \vec{B}}{\partial t}, \tag{7.1}$$

$$\vec{\nabla}.\vec{D} = 4\pi\rho, \quad \vec{\nabla} \times \vec{H} = \frac{4\pi}{c}\vec{J} + \frac{1}{c}\frac{\partial \vec{D}}{\partial t}, \tag{7.2}$$

where, $\vec{E}$ is the electric field, $\vec{D}$ is the electric displacement, $\vec{B}$ is the magnetic induction, $\vec{H}$ is the magnetic field, ρ is the electric charge density, and $\vec{j}$ is the electric current. $\vec{D} = \epsilon\vec{E}$, $\vec{B} = \mu\vec{H}$, where ϵ is the *electric permittivity* and μ is the *magnetic permeability.*

7.1 Non-relativistic Ideal Magneto-hydrodynamics Equations

Ideal magneto-hydrodynamics (MHD) deals with the combined system of magnetic field and fluid. In MHD, fluid elements consist of charged particles, however, each fluid element is locally charge neutral. Therefore no electric charge separation is allowed in the ideal MHD fluid. In the fluid, magnetic field exerts force on charge particles. By maintaining charge neutrality of the fluid-elements, fluid as a whole moves under the influence of magnetic field, and modifies the field also. Because ideal MHD fluid has infinite electrical conductivity, therefore due to presence of unlimited number of freely moving charge particles, electric field does not survive in the ideal MHD fluid.

Now, we write the non-relativistic ideal magneto-hydrodynamics equations following Ref. [2]. First ideal MHD equation is the Gauss law for magnetism in medium,

$$\vec{\nabla}.\vec{H} = 0. \tag{7.3}$$

Using the Ohm's law in the moving frame $\vec{j} = \sigma(\vec{E} + \vec{v} \times \vec{B}/c)$ (relation between the current and the electromagnetic field in a moving homogeneous conductor); by ignoring displacement current with respect to electric current in the Maxwell's equation (second equation of Eq.7.2); and by using second equations of Eqs.7.1,7.2, with infinite electric conductivity $\sigma \to \infty$ of the fluid (considering permeability $\mu = 1$ for whole fluid), we get [2],

$$\frac{\partial \vec{H}}{\partial t} = \vec{\nabla} \times (\vec{v} \times \vec{H}). \tag{7.4}$$

This equation shows that magnetic field lines of force move with the fluid element and never decay and remain frozen in the infinite conducting fluid; but the strength of the magnetic field may change if the volume of the fluid element changes. The equation of continuity is given by,

$$\frac{\partial \vec{\rho}}{\partial t} + \vec{\nabla}.(\rho\vec{v}) = 0, \tag{7.5}$$

where ρ is the fluid density. Navier-Stokes (Euler) equation in the presence of magnetic force is given by,

$$\frac{\partial \vec{v}}{\partial t} + (\vec{v}.\vec{\nabla})\vec{v} = -\frac{1}{\rho}\vec{\nabla}P - \frac{1}{4\pi\rho}(\vec{H} \times (\vec{\nabla} \times \vec{H})). \tag{7.6}$$

To solve the all independent variables, equation of state of the fluid is required,

$$P = P(\rho, T), \tag{7.7}$$

where P and T are pressure and temperature of the fluid. Because the ideal MHD evolution does not have dissipation therefore the process is adiabatic and therefore entropy is a conserved quantity,

$$\frac{\partial \vec{s}}{\partial t} + (\vec{v}.\vec{\nabla})\vec{s} = 0, \tag{7.8}$$

where s is the entropy per unit mass of the fluid. Eqs. 7.3, 7.4,7.5,7.6,7.7, and 7.8 are form the system of the *ideal magneto-hydrodynamics equations.*

We mention that due to presence of magnetic field in the fluid, momentum flux density tensor, energy density (hence pressure), energy flux density get modified, see [2] for detail. In the ideal MHD fluid, electric displacement current is neglected. From the Ohm's law, the infinite conductivity of the fluid implies that, $\vec{E} = -\vec{v}\times\vec{H}/c$ (since conduction current is finite). Therefore using these facts and Eq.7.6 one gets condition on magnetic field $H^2 \ll \rho c^2$ [2].

Let us consider a homogeneous ideal fluid in the presence of a uniform magnetic field. We are interested in the evolution of a small disturbance in this fluid. Due to this disturbance, Magnetic field, fluid density, pressure get perturbed while velocity of the fluid becomes non-zero, from the zero, equilibrium value. These perturbations are small enough in the magnitude such that one can neglect the higher order term in these perturbations. For the evolution of these perturbations only four equations of the ideal magneto-hydrodynamics, Eqs. 7.3, 7.4, 7.5, and 7.6 are relevant. If we look for the solution of the plane wave of these perturbations, $\exp[i(\vec{k}.\vec{r} - \omega t)]$, then the Eq. 7.3 and 7.4 shows that the wave vector $\vec{k}$ is always perpendicular to the direction of the perturbation in the magnetic field, Ref. [2]. Now, depending upon the direction of wave vector and the fluid velocity there are three kinds of waves are possible in the MHD fluid, Ref. [2].

If the fluid motion is perpendicular to the magnetic field, then since field lines are frozen in the fluid, therefore due to the motion of the fluid, field lines also get stretched in the perpendicular direction with the fluid. Due to this motion field lines feel tension and try to restore it previous configuration. These two motions generate a transverse wave in the direction of magnetic field; the wave vector becomes parallel to the magnetic field, i.e., $\vec{k}\|\vec{H}$. This transverse wave in the fluid is known as the $Alfv\acute{e}n$ *wave* with group velocity given by,

$$\vec{c}_A = \frac{\vec{H}}{\sqrt{4\pi\rho}}. \tag{7.9}$$

In the MHD fluid, there are two kinds of *magnetosonic waves* are present, *fast* and *slow magnetosonic waves*. Depending upon the direction of the wave vector, one of the wave becomes non-zero. If the wave vector is along the direction of magnetic field, i.e., $\vec{k}\|\vec{H}$, then the slow magnetosonic wave becomes non-zero. The speed of this wave is the same as the usual hydrodynamics wave in the fluid which is given by,

$$c_{\|} = c_s = \left(\frac{\partial P}{\partial \rho}\right)^{1/2}. \tag{7.10}$$

While if the wave vector is perpendicular to the magnetic field, i.e., $\vec{k}\perp\vec{H}$, then the fast magnetosonic wave becomes non-zero. The speed of this wave is higher than the slow magnetosonic wave and given by,

$$c_{\perp} = \sqrt{c_s^2 + c_A^2}. \tag{7.11}$$

Note that both the magnetosonic waves are independent from the direction of the fluid motion. If the direction of wave vector is arbitrary with the magnetic field then all three kinds of waves can be present in the fluid.

In Ref. [2], it has been shown that for an arbitrary perturbation (not necessarily small), if the magnetic field is uniform in the fluid, say along y-axis, then the fluid acceleration along the x-axis becomes stronger compare to the ideal hydrodynamics due to the change in the equation of state (and hence larger sound speed) in this direction,

$$\frac{\partial v_x}{\partial t} + v_x \frac{\partial v_x}{\partial x} = -\frac{1}{\rho}\frac{\partial}{\partial x}\left(P + \frac{b^2}{8\pi}\rho^2\right), \tag{7.12}$$

where $b = H/\rho$ is a constant number for a homogeneous fluid. This equation looks like an Euler's equation for the ideal fluid dynamics, only difference here is the change in the equation of sate, $P = P(\rho)$ to a new equation of state in the x-direction arising due to the magnetic field (in the y-direction), i.e., $P^*(\rho) = P(\rho) + b^2\rho^2/8\pi$. Therefore the velocity of sound in this case is higher from the ideal hydrodynamics case,

$$c^* = \sqrt{\left(\frac{\partial P^*}{\partial \rho}\right)} = \sqrt{c_s^2 + \frac{b^2}{4\pi}\rho} = \sqrt{c_s^2 + \frac{H^2}{4\pi\rho}} = \sqrt{c_s^2 + c_A^2}. \tag{7.13}$$

This result can play a very important role in the evolution of the fluid produced in relativistic heavy-ion collisions, see Chapters 8 and 10 in this regard.

7.2 Relativistic Ideal Magneto-hydrodynamics Equations

As we mentioned earlier, whenever either fluid elements or constituents of fluid elements are relativistic, we have to deal with the relativistic formalism of hydrodynamic equations. Here we discuss the covariant form of relativistic ideal magneto-hydrodynamics (RMHD) equations. We follow the derivation of RMHD equations from the Refs. [1,3].

To study the effect of electromagnetic field on the dynamics of conducting fluid, energy momentum tensor $T^{\alpha\beta}$ of the system is required. As electromagnetic field also carries energy and momentum, therefore the form of $T^{\alpha\beta}$ used in the previous chapter will get modified in the present case. In the presence of electromagnetic field, form of $T^{\alpha\beta}$ strongly depends upon the thermodynamic properties of the fluid under study. Here we consider a simple picture of the system by assuming ideal MHD approximations. Our goal is to derive $T^{\alpha\beta}$, which follows energy-momentum conservation law,

$$\partial_\alpha T^{\alpha\beta} = 0 \tag{7.14}$$

for a polarizable medium. We begin by defining some known electromagnetic quantities. The electromagnetic field-strength tensor is define as,

$$F^{\alpha\beta} = \partial^\alpha A^\beta - \partial^\beta A^\alpha, \tag{7.15}$$

where A^α is the electromagnetic four-potential; $A^\alpha = (\phi, \vec{A})$. The dual field-strength tensor is given by,

$$\Im^{\alpha\beta} = \frac{1}{2}\varepsilon^{\alpha\beta\gamma\delta}F_{\gamma\delta}, \tag{7.16}$$

where $\varepsilon^{\alpha\beta\gamma\delta}$ is anti-symmetric fourth-rank Levi-Civita tensor. The inhomogeneous Maxwell's equations in vacuum,

$$\partial_\alpha F^{\alpha\beta} = 4\pi J^\beta, \tag{7.17}$$

where J^α is four vector electric charge current, satisfying conservation law $\partial_\alpha J^\alpha = 0$, where $J^\alpha = (\rho_e, \vec{j})$; ρ_e is electric charge density and $\vec{j} = \rho_e \vec{v}$ is the current density of (dilute) charge distribution. The homogeneous Maxwell's equations in vacuum,

$$\partial_\alpha \Im^{\alpha\beta} = 0. \tag{7.18}$$

Here we are working in the natural units, therefore c=1.

In a polarizable medium, the electromagnetic field get modified. In a conductor, electric charge current density $\vec{j}$ also get modified. In the medium, vectors $\vec{P}$, $\vec{M}$ and $\vec{j_c}$ defined by, Ref. [1],

$$4\pi\vec{P} = \vec{D} - \vec{E}, \quad 4\pi\vec{M} = \vec{B} - \vec{H}, \quad \vec{j_c} = \vec{j} - \rho_e\vec{v}, \tag{7.19}$$

where these vectors are the *polarization*, the *magnetization* and the *conduction current* respectively. These vectors arise due to medium effect which have their values depending upon the type of media, and vanish in the vacuum or in a media whose internal structure does not get affected by electromagnetic field. In the medium field-strength tensor get replaced as,

$$F^{\alpha\beta}(\mathbf{E},\mathbf{B}) \longrightarrow I^{\alpha\beta}(\mathbf{D},\mathbf{H}), \tag{7.20}$$

where $I^{\alpha\beta}$ is the electromagnetic induction tensor; $\mathbf{D}$ and $\mathbf{H}$ are electric displacement and magnetic field vectors respectively. (Note that there is a huge confusion in the name of $\vec{B}$ and $\vec{H}$ fields. Traditionally, in most of the literature, vector $\vec{B}$ is named as the *magnetic induction field* and $\vec{H}$ as the *magnetic field*, although former is the magnetic field in the vacuum while latter in the medium. We also follow the traditional name of these two fields to avoid any kind of confusion.) The matrix form of all these tensors are as follow,

$$F^{\alpha\beta} = \begin{pmatrix} 0 & -E_1 & -E_2 & -E_3 \\ E_1 & 0 & -B_3 & B_2 \\ E_2 & B_3 & 0 & -B_1 \\ E_3 & -B_2 & B_1 & 0 \end{pmatrix},$$

$$I^{\alpha\beta} = \begin{pmatrix} 0 & -D_1 & -D_2 & -D_3 \\ D_1 & 0 & -H_3 & H_2 \\ D_2 & H_3 & 0 & -H_1 \\ D_3 & -H_2 & H_1 & 0 \end{pmatrix},$$

$$\Im^{\alpha\beta} = \begin{pmatrix} 0 & -B_1 & -B_2 & -B_3 \\ B_1 & 0 & E_3 & -E_2 \\ B_2 & -E_3 & 0 & E_1 \\ B_3 & E_2 & -E_1 & 0 \end{pmatrix}.$$

Therefore Maxwell's equations in an electrically charged, non-conducting, but polarizable media is given by,

$$\partial_\alpha I^{\alpha\beta} = 4\pi J^\beta, \quad \partial_\alpha \Im^{\alpha\beta} = 0, \tag{7.21}$$

where J^α is charge current in the media. For electrically neutral ($\rho_e = 0$), non-conducting ($\vec{j_c} = 0$), but polarizable ($\vec{E} \neq \vec{D}$ and $\vec{B} \neq \vec{H}$) media $J^\alpha = (0, 0)$, and first equation will also become homogeneous. For conducting media with finite conductivity, an applied electric field on the fluid generates microscopic conduction (drift) current $\vec{j_c}$ of charge particles in the background of the macroscopic motion of the fluid. For this case it become difficult to define actual electromagnetic field and tensor inside the media because of accumulation of charge particles at the interface between media and hole (vacuum inside media), and the prescription followed to define fields in the media breakdown (for detailed discussion see Ref. [1]). But from the microscopic description of the media, it is possible to define the electromagnetic field and tensor in the conducting media also and it can be shown that the Eq.(7.21) remains valid, Refs. [1, 4], with $\rho_e = 0$ inside the media. The *polarization tensor* can be constructed with the $F^{\alpha\beta}$ and $I^{\alpha\beta}$ as,

$$4\pi P^{\alpha\beta} = F^{\alpha\beta} - I^{\alpha\beta}, \tag{7.22}$$

where

$$P^{\alpha\beta} = \begin{pmatrix} 0 & -P_1 & -P_2 & -P_3 \\ P_1 & 0 & -M_3 & M_2 \\ P_2 & M_3 & 0 & -M_1 \\ P_3 & -M_2 & M_1 & 0 \end{pmatrix}.$$

Electromagnetic field carries energy momentum tensor in the vacuum. It is quite obvious that when one applies an electromagnetic field on a distribution of freely moving charge particles (called charge dust cloud), its dynamics get affected by electromagnetic field. It can be shown that the energy-momentum tensor for this charge distribution, without considering electromagnetic part, can not be conserved, but when added with the other factors coming from the electromagnetic part, then the total energy-momentum tensor is conserved. This extra factors are the energy-momentum tensor of the electromagnetic field in the vacuum, which is given by,

$$T^{\alpha\beta}_{em} = \frac{1}{4\pi}[F^\alpha_\gamma F^{\beta\gamma} - \frac{1}{4} F_{\gamma\delta} F^{\gamma\delta} \eta^{\alpha\beta}], \tag{7.23}$$

while the energy-momentum tensor for charge distribution $T_d^{\alpha\beta}$ is given by (pressure=0),

$$T_d^{\alpha\beta} = \rho_m v^\alpha v^\beta, \tag{7.24}$$

where ρ_m is the mass density of charge particles. Both $T_d^{\alpha\beta}$ and $T_{em}^{\alpha\beta}$ are symmetric double rank tensors. So total energy-momentum tensor of the system is,

$$T^{\alpha\beta} = T_d^{\alpha\beta} + T_{em}^{\alpha\beta}, \tag{7.25}$$

where energy-momentum conservation law is,

$$\partial_\alpha T^{\alpha\beta} = 0. \tag{7.26}$$

So in the presence of electromagnetic field energy-momentum tensor of the system get modified and electromagnetic field also become part of the system and contribute in the $T^{\alpha\beta}$.

In the last chapter we have given the physical interpretation of components $T^{\alpha\beta}$ for fluid without electromagnetic field. The components of $T_{em}^{\alpha\beta}$ also have the same physical meaning but in terms of electromagnetic variables,

i) $T_{em}^{00} \equiv$ energy density $\epsilon_{em} = \frac{1}{8\pi}(E^2 + B^2)$.

ii) $T_{em}^{0i} \equiv$ momentum density along i-axis, $S^i/c^2 = S^i = \frac{1}{4\pi}(\vec{E} \times \vec{B})^i$.

iii) $T_{em}^{i0} \equiv$ energy flux along i-axis, S^i.

iv) $T_{em}^{ij} \equiv$ flux of jth component of momenta along i-axis, $\frac{1}{4\pi}[E^iE^j + B^iB^j - \frac{1}{2}\delta^{ij}(E^2 + B^2)]$,

where $\vec{S}$ is known as the *Poynting vector* and T_{em}^{ij} as the *Maxwell stress tensor*.

The total energy-momentum tensor of a system should be conserved, therefore in the medium also, it is expected that the energy-momentum tensor (fluid+electromagnetic field) remain conserved. The difference comes due to the medium response to the electromagnetic field which modifies this field. The energy-momentum tensor for electromagnetic part $T_{em}^{\alpha\beta}$ in the medium is given by [1, 3],

$$T_{em}^{\alpha\beta} = \frac{1}{4\pi}[F_\gamma^\alpha I^{\beta\gamma} - \frac{1}{4}F_{\gamma\delta}I^{\gamma\delta}\eta^{\alpha\beta}]. \tag{7.27}$$

We know the energy-momentum tensor for the thermalized matter field (now including pressure) is given by,

$$T_f^{\alpha\beta} = (\epsilon + P)u^\alpha u^\beta + P\eta^{\alpha\beta}. \tag{7.28}$$

Note that here we use metric $\eta^{\alpha\beta}$ =diag$(-1,1,1,1)$, therefore sign before the last term is different from previous chapter. We will see that the total energy-momentum tensor for a fluid interacting with electromagnetic fields is not just $T^{\alpha\beta} = T_f^{\alpha\beta} + T_{em}^{\alpha\beta}$, but more kind of tensors arise, these extra tensors will go away when we take the ideal MHD approximation, i.e., $\sigma \to \infty$, and consider the *electric* and *magnetic susceptibility* to be uniform in the medium. Ultimately we get the energy-momentum conservation law for the ideal MHD fluid as,

$$\partial_\alpha T^{\alpha\beta} = 0. \tag{7.29}$$

These equations governs the dynamics of an ideal relativistic magnetized fluid. Note that as happen in the case of hydrodynamics, all physical variables, e.g. $T_f^{\alpha\beta}$, n^α and s^α, flow along the direction of fluid velocity u^α; in this case also, including $T_{em}^{\alpha\beta}$, all physical variables flow along the direction of fluid. An equilibrium state is a steady state of both, matter as well as electromagnetic field, Ref. [1].

$F^{\alpha\beta}$ and $I^{\alpha\beta}$ can be decomposed with respect to u^α, and new vectors and tensors can be defined as [1, 3],

$$E^\alpha \equiv F^{\alpha\beta} u_\beta, \quad B^{\alpha\beta} \equiv F^{\alpha\beta} - 2u^{[\alpha} E^{\beta]}, \tag{7.30}$$

$$D^\alpha \equiv I^{\alpha\beta} u_\beta, \quad H^{\alpha\beta} \equiv I^{\alpha\beta} - 2u^{[\alpha} D^{\beta]}, \tag{7.31}$$

where, $[\alpha\beta]$ is anti-symmetrization with respect to indices α, β. Since $F^{\alpha\beta}$ and $I^{\alpha\beta}$ are anti-symmetric tensors, therefore contraction with $u_\alpha u_\beta$ of these tensors give zero, Ref. [1]. This shows that vectors defined above, E^α and D^α, are orthogonal to the four-velocity u^α. In the rest frame of the fluid, $E^\alpha = (\vec{E}, 0)$, $D^\alpha = (\vec{D}, 0)$, $B^{\alpha\beta} = F^{\alpha\beta}$ without electric field, and $H^{\alpha\beta} = I^{\alpha\beta}$ without electric displacement. Therefore E^α and D^α represent electric field and electric displacement, while $B^{\alpha\beta}$ and $H^{\alpha\beta}$ represent magnetic induction and magnetic field in the fluid rest frame. $B^{\alpha\beta}$ and $H^{\alpha\beta}$ are anti-symmetric tensors.

Using the analogy with Eq.(7.19), in the medium, relation between E^α and D^α, and in between $B^{\alpha\beta}$ and $H^{\alpha\beta}$ are given by defining new vector and tensor,

$$D^\alpha = E^\alpha + 4\pi P^\alpha, \quad B^{\alpha\beta} = H^{\alpha\beta} + 4\pi M^{\alpha\beta}, \tag{7.32}$$

where,

$$P^\alpha = -P^{\alpha\beta} u_\beta, \quad M^{\alpha\beta} = P^{\alpha\beta} + 2u^{[\alpha} P^{\beta]}, \tag{7.33}$$

where, $P^{\alpha\beta}$ is the *polarization tensor* as defined in Eq.(7.22). In the fluid rest frame $P^\alpha = (\vec{P}, 0)$ is the polarization vector, and $M^{\alpha\beta} = P^{\alpha\beta}$ without $\vec{P}$. So P^α and $M^{\alpha\beta}$ defined the electric polarization and magnetization of the fluid in the rest frame. The *linear constitutive relations* of the material is given by [1],

$$P^\alpha = \kappa(\rho, T)E^\alpha, \quad M^{\alpha\beta} = \chi(\rho, T)B^{\alpha\beta}, \tag{7.34}$$

where, the parameters κ and χ are *electric* and *magnetic susceptibility* respectively. ρ is the *conserved charge or mass density* (in the relativistic system it corresponds to the baryon density) and T is the *absolute temperature* of the system. Therefore we have,

$$D^\alpha = (1 + 4\pi k)E^\alpha, \quad H^{\alpha\beta} = (1 - 4\pi\chi)B^{\alpha\beta}. \tag{7.35}$$

By imposing the local thermodynamic equilibrium on the system, Dixon in Ref. [1] showed that there are four kind of energy-momentum tensor present in the magnetized fluid which add up to give total energy-momentum tensor of the fluid. Dixon used the fact that for a perfect fluid, in the equilibrium state, entropy production is zero, i.e. $\partial_\alpha s^\alpha = 0$, where $s^\alpha = su^\alpha$. By writing the entropy flux, s^α, as function of $T^{\alpha\beta}$, ρ^α, $F_{\alpha\beta}$ and $I^{\alpha\beta}$, Dixon obtained the form of the total energy-momentum tensor for the fluid interacting with the electromagnetic field,

$$T^{\alpha\beta} = T_1^{\alpha\beta} + T_2^{\alpha\beta} + T_3^{\alpha\beta} + T_4^{\alpha\beta}, \tag{7.36}$$

which follows the conservation law,

$$\partial_\alpha T^{\alpha\beta} = 0, \tag{7.37}$$

(Note that Dixon in Ref. [1] has taken a polarizable non-conducting charged medium with finite charge density ρ_e for the development of the formalism to derive $T^{\alpha\beta}$. We are interested in the $T^{\alpha\beta}$ for a polarizable conductor. For this, only difference is in the presence of conduction current $\vec{j_c}$. We assume that the whole formalism goes through for a conducting fluid also as assumed by Anile in Ref. [3].) where,

$$T_1^{\alpha\beta} = (\epsilon + p_g)u^\alpha u^\beta + p_g\eta^{\alpha\beta}, \tag{7.38}$$

is the usual energy-momentum tensor for the matter part. p_g is the thermal pressure of the fluid.

$$T_2^{\alpha\beta} = \frac{1}{2}T\left(\frac{\partial\kappa}{\partial T}E^2 + \frac{\partial\chi}{\partial T}B^2\right)u^\alpha u^\beta - \frac{1}{2}\rho\left(\frac{\partial\kappa}{\partial\rho}E^2 + \frac{\partial\chi}{\partial\rho}B^2\right)(\eta^{\alpha\beta} + u^\alpha u^\beta), \tag{7.39}$$

where $E^2 = E^\alpha E_\alpha$ and $B^2 = \frac{1}{2}B^{\alpha\beta}B_{\alpha\beta}$.

$$T_3^{\alpha\beta} = \frac{1}{2\pi}F_\gamma^{[\alpha}I^{\mu]\gamma}u_\mu u^\beta, \tag{7.40}$$

and

$$T_4^{\alpha\beta} = \frac{1}{4\pi}[F_\gamma^\alpha I^{\beta\gamma} - \frac{1}{4}F_{\gamma\delta}I^{\gamma\delta}\eta^{\alpha\beta}]. \tag{7.41}$$

In $T^{\alpha\beta}$, $T_1^{\alpha\beta}$ has the contribution, which depends upon the fluid property mostly. Successively fluid-property dependent contributions decreases from $T_1^{\alpha\beta}$ to $T_4^{\alpha\beta}$ in the $T^{\alpha\beta}$ and electromagnetic field contribution increases. $T_4^{\alpha\beta}$ is the *Minkowski tensor* (proposed by Minkowski in 1908) and $T_3^{\alpha\beta} + T_4^{\alpha\beta}$ is the *Abraham tensor* (proposed by Abraham in 1909) which give the contribution of electromagnetic field to the medium. The forms of these tensors are independent from the property of the medium. Note that $T^{\alpha\beta}$, $T_1^{\alpha\beta}$ and $T_2^{\alpha\beta}$ are symmetric tensors, but $T_3^{\alpha\beta}$ and $T_4^{\alpha\beta}$ are not. However, $T_3^{\alpha\beta} + T_4^{\alpha\beta}$ is a symmetric tensor known as the *explicitly symmetric tensor*.

Consider the charge 4-current in the conductor which can be decomposed in terms of four-velocity u^α and conduction current j^α,

$$J^\alpha = \rho_e u^\alpha + j^\alpha,$$

such that $j^\alpha u_\alpha = 0$; j^α and u_α are orthogonal vectors and $\rho_e = -J^\alpha u_\alpha$ is the proper charge density. Assuming linear constitutive relation between j^α and E^α (Ohm's law),

$$j^\alpha = \sigma^{\alpha\beta}E_\beta, \tag{7.42}$$

where $\sigma^{\alpha\beta}$ is the *conductivity tensor*. Generally, in the presence of magnetic field conductivity tensor becomes anisotropic and depends upon density, temperature and magnetic field in the fluid, Ref. [3]. We assume that magnetic field is sufficiently weak such that there is no non-diagonal terms present in the conductivity tensor. With this assumption we have,

$$\sigma^{\alpha\beta} = \sigma(\rho, T)\eta^{\alpha\beta}. \tag{7.43}$$

Now, in the ideal MHD approximation, $\sigma \to \infty \Rightarrow E_\alpha = 0$ from the Eq.(7.42). So there is no electric field present in the ideal MHD fluid. This occurs because in the infinite conducting fluid an unlimited number of freely moving charge particles remain present, so if there is any electric field arises in the fluid, these charge particles move in such a way that the field disappears. By taking $\sigma \to \infty$ (i.e. $E_\alpha = 0$) in Eq.(7.35), we get $D_\alpha = 0$. Therefore by Eq.(7.31) we have $I^{\alpha\beta} u_\beta = 0$, and hence from Eq.(7.40) it is clear that $T_3^{\alpha\beta}$ becomes zero in the ideal RMHD fluid. Also, from Eqs.(7.30) and (7.31) we get $B^{\alpha\beta} = F^{\alpha\beta}$ and $H^{\alpha\beta} = I^{\alpha\beta}$, therefore by using Eq.(7.35) we get,

$$I^{\alpha\beta} = (1 - 4\pi\chi) F^{\alpha\beta}. \tag{7.44}$$

This can be written in terms of μ, the *magnetic permeability* of the media as,

$$I^{\alpha\beta} = \frac{1}{\mu} F^{\alpha\beta}. \tag{7.45}$$

For simplicity we assume that κ and χ are uniform in space and independent from density and temperature. Therefore in such case $T_2^{\alpha\beta}$ becomes zero. The approximations which we have taken here may not be true for the quark-gluon plasma produced in relativistic heavy-ion collisions; the system in which we are interested. This plasma has very strong variation in energy density and temperature (may be the strongest in the present universe). The electric conductivity of this plasma is finite and varies with the temperature. κ and χ may also have variation with energy density and temperature. But considering the real situation may make system mathematically as well as numerically very difficult. Therefore we continue with these approximations. We now introduce magnetic induction four-vector as,

$$B_\alpha = \frac{1}{2} \varepsilon_{\alpha\beta\gamma\delta} u^\beta F^{\gamma\delta}, \tag{7.46}$$

where $\varepsilon_{\alpha\beta\gamma\delta}$ is the Levi-Civita anti-symmetric fourth rank tensor. Since $E^\alpha = 0$ in the ideal RMHD fluid, therefore from Eq.(7.30),

$$F^{\alpha\beta} u_\beta = 0. \tag{7.47}$$

Let us calculate the quantity $\varepsilon^{\alpha\mu\nu\sigma} B_\alpha u_\mu$,

$$\varepsilon^{\alpha\mu\nu\sigma} B_\alpha u_\mu = \frac{1}{2} \varepsilon^{\alpha\mu\nu\sigma} \varepsilon_{\alpha\beta\gamma\delta} u^\beta F^{\gamma\delta} u_\mu. \tag{7.48}$$

Using the property of the Levi-Civita tensor,

$$\varepsilon_{i_1 \ldots i_k i_{k+1} \ldots i_n} \varepsilon^{i_1 \ldots i_k j_{k+1} \ldots j_n} = k! \delta^{j_{k+1} \ldots j_n}_{i_{k+1} \ldots i_n},$$

where,

$$\delta^{j_{k+1}\cdots j_n}_{i_{k+1}\cdots i_n} = \begin{vmatrix} \delta^{j_{k+1}}_{i_{k+1}} & \cdots & \delta^{j_{k+1}}_{i_n} \\ \vdots & \ddots & \vdots \\ \delta^{j_n}_{i_{k+1}} & \cdots & \delta^{j_n}_{i_n} \end{vmatrix}.$$

We get,

$$\varepsilon^{\alpha\mu\nu\sigma}\varepsilon_{\alpha\beta\gamma\delta} = \delta^{\mu}_{\beta}(\delta^{\nu}_{\gamma}\delta^{\sigma}_{\delta} - \delta^{\nu}_{\delta}\delta^{\sigma}_{\gamma}) - \delta^{\mu}_{\gamma}(\delta^{\nu}_{\beta}\delta^{\sigma}_{\delta} - \delta^{\nu}_{\delta}\delta^{\sigma}_{\beta}) + \delta^{\mu}_{\delta}(\delta^{\nu}_{\beta}\delta^{\sigma}_{\gamma} - \delta^{\nu}_{\gamma}\delta^{\sigma}_{\beta}).$$

Using this identity in Eq.(7.48), last four terms give zero due to Eq.(7.47) and the first two terms by using $u_\beta u^\beta = -1$ and $F^{\nu\sigma} = -F^{\sigma\nu}$ give,

$$\varepsilon^{\alpha\mu\nu\sigma}B_\alpha u_\mu = \tfrac{1}{2}(u_\beta u^\beta F^{\nu\sigma} - u_\beta u^\beta F^{\sigma\nu}) = -F^{\nu\sigma}.$$

Therefore,

$$F^{\nu\sigma} = -\varepsilon^{\alpha\mu\nu\sigma}B_\alpha u_\mu. \tag{7.49}$$

Using the Eqs.(7.45, 7.46, and 7.49) in Eq.(7.41), we get,

$$4\pi\mu T^{\alpha\beta}_{em} = -B^\alpha B^\beta + \frac{1}{2}B_\sigma B^\sigma \eta^{\alpha\beta} + B_\sigma B^\sigma u^\alpha u^\beta. \tag{7.50}$$

By introducing the vector, $b^\alpha = \frac{1}{4\pi\mu}B^\alpha$, one gets total energy-momentum tensor for ideal RMHD fluid as,

$$T^{\alpha\beta} = (\epsilon + p_g + |b|^2)u^\alpha u^\beta - b^\alpha b^\beta + (p_g + \frac{|b|^2}{2})\eta^{\alpha\beta}. \tag{7.51}$$

By substitution of $F^{\alpha\beta}$ from Eq.(7.49) in terms of B^α in the *homogeneous Maxwell's equations* and taking the dual (multiplying by $\varepsilon^{\alpha\mu\beta\gamma}$) one gets,

$$\partial_\alpha(u^\alpha b^\beta - u^\beta b^\alpha) = 0. \tag{7.52}$$

The *inhomogeneous Maxwell's equation* can be used for the calculation of the charge current for a given b^α [3].

If the constituents of fluid elements are non-relativistic particles (though the fluid velocity is relativistic), then during the fluid evolution mass number remain conserved. But if constituents of the fluid elements are relativistic, then mass number may get change, therefore only baryon number conservation condition can be imposed on the fluid evolution. Thus the equations of relativistic magneto-fluid dynamics are as follow:

The mass / baryon number conservation equation :

$$\partial_\alpha(\rho u^\alpha) = 0 \quad or \quad \partial_\alpha(n u^\alpha) = 0, \tag{7.53}$$

The energy-momentum conservation equation :

$$\partial_\alpha\Bigg((\epsilon + p_g + |b|^2)u^\alpha u^\beta - b^\alpha b^\beta + (p_g + \frac{|b|^2}{2})\eta^{\alpha\beta}\Bigg) = 0, \tag{7.54}$$

The Maxwell's equations :

$$\partial_\alpha(u^\alpha b^\beta - u^\beta b^\alpha) = 0, \tag{7.55}$$

where fluid four velocity is given by $u^\alpha = \gamma(1, \vec{v})$. Minkowski metric is $\eta^{\alpha\beta}$ =diag$(-1, 1, 1, 1)$. We need equation of state (EoS) to solve these equation $\epsilon \equiv \epsilon(p_g)$. The four-vector b^α is related with the magnetic field and fluid velocity by, Ref. [5],

$$b^\alpha = \gamma\Bigg(\vec{v}.\vec{B}, \frac{\vec{B}}{\gamma^2} + \vec{v}(\vec{v}.\vec{B})\Bigg), \tag{7.56}$$

with this $u_\alpha b^\alpha = 0$. Therefore,

$$|b|^2 = b^\alpha b_\alpha = \frac{|\vec{B}|^2}{\gamma^2} + (\vec{v}.\vec{B})^2. \tag{7.57}$$

From Eq.7.54 it is clear that in the ideal MHD fluid the total pressure of the plasma is not just p_g, but sum of thermal pressure p_g and magnetic pressure $\frac{|b|^2}{2}$; $p = p_g + \frac{|b|^2}{2}$. Therefore,

$$p = p_g + \frac{|\vec{B}|^2}{2\gamma^2} + \frac{(\vec{v}.\vec{B})^2}{2}. \tag{7.58}$$

In the Chapter 10, by following the Ref. [5], we discuss method for solving ideal RMHD equations.

Bibliography

[1] W.G. Dixon, **Special Relativity: The foundation of macroscopic physics**, Cambridge University Press (1982).

[2] L.D. Landau and E.M. Lifshitz, **Electrodynamics of Continuous Media**, Pergamon Press, Second Edition (1984).

[3] A.M. Anile, **Relativistic Fluids and Magneto-fluids**, Cambridge University Press (2005).

[4] S.R. de Groot, L.G. Suttorp, **Foundations of Electrodynamics**, Amsterdam: North-Holland Publ. Co. (1972).

[5] A. Mignone and G. Bodo, Mon. Not. R. Astron. Soc. 368, 1040 (2006).

Chapter 8

Heavy-Ion Collisions and Initial Magnetic Field

8.1 Introduction

In the *Big Bang cosmology*, from the *Planck epoch* to a few microsecond, the energy density of the Universe was so high that quarks, anti-quarks and gluons (basically color degrees of freedom) could not be remain in the bound state of *hadrons*. These color degrees of freedom remained present in the early Universe, and by interacting among themselves could form a thermal medium. This plasma of quarks, anti-quarks and gluons is known as the *quark-gluon plasma* (QGP) which survived up to the time $\sim 10^{-6}$ *sec*, at which the temperature of the Universe was about 170 MeV. Below this temperature these colored objects become confined inside hadrons, and become color singlet object by forming bound state. The possibility of thermal medium of quarks, anti-quarks and gluons in the early Universe up to time scale of 1 μs is due to the fact that QCD at that energy scale has interaction time scale $\sim 1\ fm$ (10^{-23} *sec*), which is much shorter than time scale in which Universe evolved from the Planck epoch $\sim 1\ \mu s$, therefore this time is sufficient to have enough interaction between these particles to form a thermal medium.

In the present day Universe, a deconfined phase of the quark and gluon may exist in the core of a compact object, like *neutron star*. The quark-gluon plasma in these objects arises due to high compression of baryonic matter due to gravitational attraction. Therefore quark-gluon plasma phase in this system has finite baryon chemical potential (more number of baryons over anti-baryons).

The CMBR power spectrum corresponds to the era of the Universe when its age was about 300000 years. On the basis of the measurement of CMBR power spectrum, there are many predictions regarding the evolution of the Universe before this time, e.g. *inflation* etc. But the soup of quark-gluon plasma, which was existed much before the CMBR decoupling, remain hidden behind the present observation reach and there is no clue from the CMBR measurement about the actual physical property of this plasma. The same problem remains with the QGP inside a neutron star, where there is no direct way to study the physical properties of the QGP (even its existence is questionable inside the neutron star). Therefore to produce the quark-gluon plasma and study its physics, there seems no way other than colliding two heavy nuclei with relativistic energies. The purpose of the *relativistic heavy-ion collision* at RHIC (the Relativistic Heavy Ion Collider, since 2000) and heavy-ion collision at LHC (the Large Hadron Collider at CERN, since 2008) is to recreate the condition of the early Universe when its age was less than few microsecond. In these kinds of experiments, it is possible to have a thermal medium of quarks, anti-quarks and gluons, as it is expected that, the total time duration of system which remain in the deconfined state is larger ($\sim 10\ fm$) than the QCD interaction time scale ($\sim 1\ fm$). In such kind of experiments local thermalization may occur in time lesser than 1 fm, and energy density can be much higher than the critical energy density ($1\ GeV/fm^3$) to form the quark-gluon plasma.

In relativistic heavy-ion collider experiments two opposite moving nuclei (along $\pm$ z-axis) are collided with relativistic energies. RHIC and LHC experiments are carried out to perform such kind of collisions and produce the hottest medium in the present Universe. FAIR and NICA are also upcoming facilities with relatively lower energy of collision and are motivated to create a very high baryon density medium and study its physical properties. This kind of medium is expected to exist inside a neutron star. The main goal of all these experiments to investigate QCD phase diagram and study physical properties of QCD matter in various conditions.

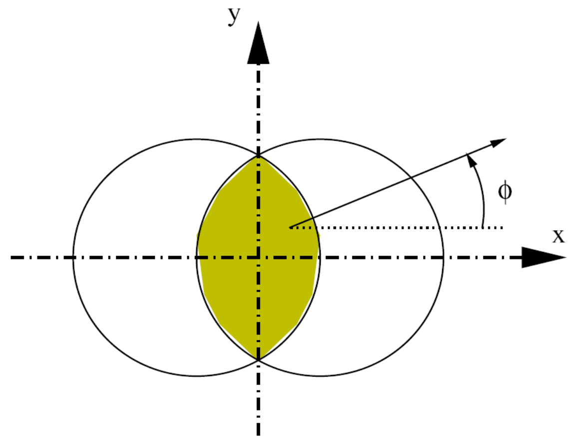

Figure 8.1: Figure shows the overlapping of two nuclei in the transverse plane in the non-central collision. Figure has been taken from the Ref. [1].

8.2 Various stages of Relativistic Heavy-ion Collisions and Probes of Quark-gluon Plasma

First we describe some important terminology used in the context of heavy-ion collisions (HIC). The HIC experiments are performed either by two similar nuclei, called as *symmetric collision*, or with the different nuclei, the *asymmetric collisions*. Usually lighter nuclei is called the projectile and heavier nuclei as target, while in the case of symmetric collisions, any one of the two nuclei can be given any name. From the center of the target to the projectile, hypothetical vector drawn in the plane perpendicular to the motion is called the impact parameter vector and its magnitude is called impact parameter. For the central collisions impact parameter is almost zero, while it is non-zero in the case of non-central collisions. Impact parameter vector and longitudinal axis (z-axis) form a plane known as the *reaction plane*. In Fig.8.1 we have shown the situation for the non-central collisions in the transverse plane (xy-plane).

Fig.8.2 shows the successive stages of relativistic heavy-ion collisions. At relativistic energy, due to huge Lorentz contraction, width of nuclei in the longitudinal direction gets contracted with the large γ factor. But due to presence of low momentum ($\sim$ 200 MeV) *wee partons* inside protons and neutrons, width of nuclei never gets contracted below 1 fm. In the very high energy collisions, due to asymptotic

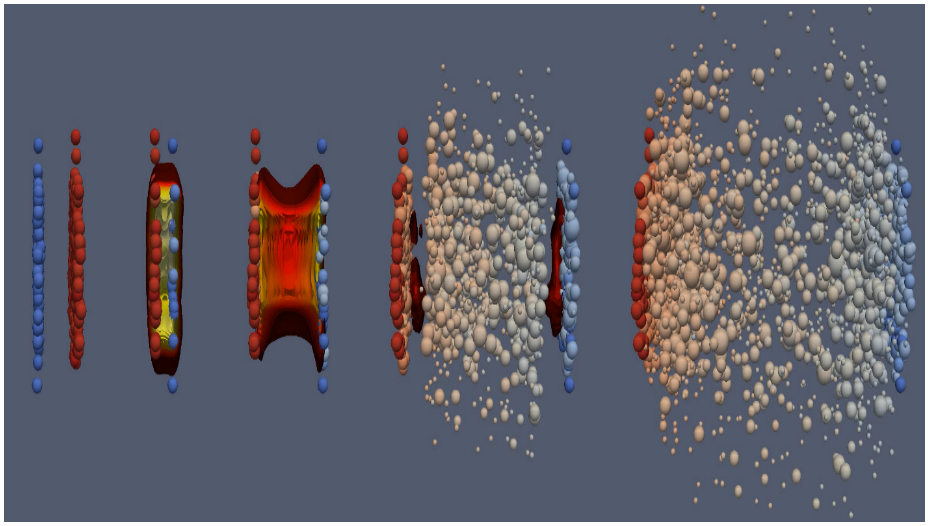

Figure 8.2: Figure shows the successive stages of relativistic heavy-ion collisions. Figure has been taken from Ref. [2]

freedom of QCD, nuclei cross through each other with relativistic speed without much interacting, therefore a very less amount of initial matter gets stopped in the overlap region. In such an energy regime, nuclei become almost transparent to each other because of asymptotic freedom. Only a small interaction among nuclei stores energy in the intermediate region, which further creates particles, mainly partons. These particles scatter elastically and inelastically with each other due to very high parton density, which is absent in the case of pp collisions. Therefore it is expected that in the heavy-ion collision experiment, in a time less than $\sim 1\ fm$, partons get thermalized and form quark-gluon plasma (initial energy density at RHIC and LHC is much higher than the critical energy density required to have QGP).

The hydrodynamics description of a system is only possible if the mean free path and the time scale of the interaction among the particles are much smaller than the system size and the time scale of the evolution of the system, respectively. The system of particles produced in the relativistic heavy-ion collisions satisfies both of these criteria. Bjorken (Ref. [3]) estimated the mean free path of partons $\sim 0.1 - 0.01\ fm$, which is much smaller than the typical size of the system $\sim 10\ fm$. Similarly, QCD interaction time scale is $\sim 1\ fm$ and the QGP system is expected to last for at least $\sim 10\ fm$ time. This indicates that local thermodynamic equilibrium is justified and the hydrodynamic description of the system is possible. This supports the formation of a thermalized medium of quarks, anti-quarks and gluon in relativistic heavy-ion collisions.

In the relatively low energy collisions, plasma forms at finite chemical potential. At these energies baryon stopping cross-section is higher, due to which, a good fraction of initial baryons are stopped in the interaction region, thereby forming QGP or hadronic matter at finite chemical potential. The study of this system is useful in the context of neutron star physics.

After achieving local thermodynamic equilibrium, system expands very fast hydrodynamically as the central pressure of the plasma is much higher than the vacuum outside. This decreases the central energy density of the plasma, and eventually QGP to hadron cross-over transition occurs. As the hadronic phase has lesser degrees of freedom than the QGP phase, from the QGP to hadronic phase entropy density of the system decreases by a very large amount in a small range of temperature. Since the total entropy of a system can not decrease, therefore to compensate this, volume of the system has to increase very fast by keeping temperature approximately constant, such that total entropy remain conserved [4]. Since the increment in the volume takes some time, therefore system spends a significant amount of time near the transition temperature [4]. When the transition is over, in the hadronic phase not much growth in the expansion rate occurs, because speed of sound in the hadronic phase is much smaller than in the QGP, and fluid acceleration is directly related to the sound speed in the fluid. All these features are expected to be detected in the experiment.

After the hadronization, system continues to expand with relatively slower rate by maintaining thermodynamic equilibrium. At a certain stage it becomes so dilute that the mean free path of hadrons becomes comparable to the system size, and local thermodynamic equilibrium is destroyed. This stage is known as the *thermal* of *kinetic freeze-out*. Before reaching this stage, hadrons scatter among themselves elastically and inelastically. Since inelastic cross section is only small fraction of the total cross-section, therefore these process get stopped much before the elastic scattering processes. Since only inelastic collision can change the species of hadrons, therefore this kind of chemical composition changing processes stop much before the thermal freeze-out. This stage of the evolution of the system where chemical composition of hadronic species freezes is known as the *chemical freeze-out*. After this stage hadrons only scatter elastically and maintain thermal equilibrium. One more component plays important role in maintaining of the thermal equilibrium in this stage is the *resonance process* in which two hadrons by combining form a shortly lived resonance state which subsequently, again decays into the parent hadrons. This is also treated as the elastic process. As mentioned earlier, at the stage where even this elastic scattering get stopped is known as the *thermal or kinetic freeze-out*. After this no scattering happen and hadrons come out directly to the detectors with specific momenta. With the hadronic momentum distribution, people analyse what happened during the evolution of the system and determine its various stages and physical properties of the quark-gluon plasma and its transition to the hadronic phase. Thus, heavy-ion collision experiments probe confinement transition. The final hadronic spectra, which comes out to the detectors, is blue shifted due to hydrodynamic expansion and show higher temperature (than the actual temperature of the system in the rest frame of the plasma). This blue shift in the spectra is compensated by production of soft pions due to resonance decay process (these soft pions show relatively lower temperature than the temperature of blue shifted parent hadrons), see Ref. [4].

Now we discuss various signals in the relativistic heavy-ion collisions which mainly probe the presence of the medium and have dependence on the properties of the medium, e.g whether it is a deconfined medium or confined medium etc. At the very early stage of the collision it is more probable to have hard particles (either large mass or large transverse momentum $p_T \gg 1\ GeV$ particles) because according to the *uncertainty principle*, time required for production of these particles is short. The time scale for the production of hard particles from uncertainty principle is $\tau \sim 1/\sqrt{Q^2}$, where Q^2 is the momentum transfer, which is of the order of $p_T^2 \gg 1\ GeV^2$, see Ref. [4]. Therefore hard partons dominate in the very early stage of the collision and play a very important role in the study of the whole evolution of the system. These hard partons can produce jets of high-p_T by fragmentation. If such jets get produced at the edge of the system and one one part of the jet moves inward then it has to travel about 10 fm distance (this is transverse size of the system in the central collisions). During this period of motion of such a jet, soft partons get thermalized, expand eventually hydrodynamically, hadronizing, and then freezing-out. All this evolution of the system can be probed by such jets due to the momentum exchange with the soft particles. By this process, jet looses its energy. This energy loss is proportional to density of the medium times the scattering cross section between the probe and the medium constituents, integrated along the probes trajectory, see Ref. [4]. This process is known as *jet quenching* which probes the properties of the medium formed in relativistic HIC.

There are various channels for the fragmentation of these hard particles. One of the fragmentation mode is the $c\bar{c}$ (J/ψ) production. These mesons can be produced at the early stages of both relativistic heavy-ion as well as in the pp collisions. The difference is that, in the relativistic heavy-ion collisions due to medium effect, these mesons can melt due to the *Debye screening* in the medium. This happens because QGP medium screens the color force between the constituents of $c\bar{c}$ and these pairs melt. Eventually, after hadronization, they form other hadrons (open charm). This is known as J/ψ *suppression*.

At the very early stage of the collision, direct photons and lepton-antilepton pairs (known as *dileptons*) are also produced. The production cross-section of photons is proportional to the fine structure constant of the electromagnetic interaction, $\alpha_e = \frac{1}{137}$ which is very small. However, once these photons get created they have the interaction cross-section with the medium also of the same order and therefore come out of the medium directly without much interacting. Their detection gives very important information about the momentum-distribution of partons at the early stages. The photons/dileptons can be created in both stages, early stage as well during expansion of the thermal medium. However, the probability of production of photons at late stage is very less [4].

An important effect of the formation of thermal medium is the development of the momentum anisotropy in the plasma in the case of non-central collisions. This is expected to be absent in the pp collisions where produced particles come out without much subsequent collisions and therefore there is no chance of formation of thermal medium. (Though recently collective effects have been seen in high multiplicity pp collisions at LHC). In relativistic HIC (at RHIC) it has been experimentally observed a momentum anisotropy in the system evolution in the transverse plane in the case of non-central collisions which signals the formation of thermal medium at a certain stage. The hydrodynamic description of system, which requires local thermodynamic equilibrium, can naturally explain the origin of this momentum anisotropy. Hydrodynamics explains that, the spatial anisotropy present in the plasma in the non-central collision leads to different pressure gradients in different direction in the transverse plane causing stronger flow in the direction where pressure gradient is more. This can generate the *elliptic flow*, which is explained by hydrodynamics where an elliptical spatial anisotropy present in the plasma ultimately transfers to the observed momentum anisotropy. We will discuss this in the next section in more detail. Important point is that hydrodynamics requires local thermodynamic equilibrium and hence medium formation. Therefore elliptic flow is a signal of the equilibrated medium formation in relativistic HIC. As we have discussed, the energy density produced in the relativistic HIC is much higher that the critical energy density for the formation of QGP, and also, elliptic flow depends upon the equation of state of the medium which is very different for QGP and hadrons. Therefore the observation of elliptic flow determines which kind of thermal medium has formed after the collision. The observed value of elliptic flow supports the formation of the quark-gluon plasma in relativistic heavy-ion collision experiments.

Another important probe for the QGP formation in the relativistic HIC is the *strangeness enhancement* which is highly suppressed in the *pp* collision case. This happens due to the chiral symmetry restoration in the QGP phase which makes the dynamical mass of the strange quark lighter. Because of this, its production cross-section becomes significantly large in this medium (compared to much heavier strange hadrons). Thus the strange partons are produced abundantly in the QGP phase and chemical equilibrate with the other lighter partons.

8.3 Inviscid Relativistic Hydrodynamics For Heavy-Ion Collision and Elliptic Flow

The hydrodynamic description of a system requires initial values of the energy density and fluid velocity at each space points. Hydrodynamic equations are first order differential equation which can only be solved if the initial conditions are given along with the equation of state of the plasma. These initial conditions are given at the thermalization time, say at proper time $\tau_0 < 1\ fm$. For the initial energy density in the relativistic HIC there are many models are available, the most popular models are *Glauber model*, Ref. [5], and the *color-glass-condensate*, Ref. [6, 7]. First, we discuss the *Glauber model* by which one can generate the initial energy density profile for the plasma which undergoes hydrodynamic expansion in the relativistic heavy-ion collisions. The other method to produce initial energy density is the *color glass condensate* for which one can follow Refs. [6, 7].

We take the z-axis, the longitudinal axis, to be along the motion of the nuclei, and therefore xy-plane forms the transverse plane. We choose x-axis along the impact parameter vector. The xz-plane is known as the *reaction plane*. We consider the starting time for the collision as $t = 0$ at the position $z = 0$. This is the stage of complete overlap of the two nuclei. At the very initial stage due to large Lorentz contraction along the z-axis, z-width of the system is very small compare to the transverse size (diameter of the nuclei for the central collisions).

Optical Glauber Model : In the Glauber model the initial energy or entropy density is parameterized in two dimension (transverse plane) by the geometry of the collisions. In the *optical Glauber method*, the density distribution of nucleons inside incoming nuclei is considered to be *Woods-Saxon distribution*. Let us denote the two nuclei by A and B, therefore the Woods-Saxon profile of density distribution of nucleons inside incoming nuclei is given by,

$$\rho_{A,B}(r) = \frac{\rho_0}{e^{(r-R_{A,B})/\xi} + 1}, \tag{8.1}$$

where, $\rho_0 = 0.16\ fm^{-3}$ is the normal nuclear density at the center of nuclei, r is the radial coordinate, $R_{A,B}$ is the radius of nuclei (1.2(mass number)$^{1/3}$ fm) and ξ is the *skin thickness* of the nuclei. The nuclear thickness function along the z-axis in the transverse plane is given by,

$$T_{A,B}(x, y) = \int_{-\infty}^{\infty} dz \rho_{A,B}(x, y, z). \tag{8.2}$$

The transverse energy density deposited after the collision is the function of $T_{A,B}$ and is determined by the expression [5, 8],

$$e(x,y,b) = K\Bigg[T_A(x+b/2,y)\Bigg(1-\Big(1-\frac{\sigma T_B(x-b/2,y)}{B}\Big)^B\Bigg) \\ +T_B(x-b/2,y)\Bigg(1-\Big(1-\frac{\sigma T_A(x+b/2,y)}{A}\Big)^A\Bigg)\Bigg], \tag{8.3}$$

where, K is a phenomenological parameter which is set so that the experimentally observed rapidity density of charged hadrons with the centrality of the collisions is reproduce, Ref. [5, 8]. σ is the total inelastic nucleon-nucleon cross section at the given collision energy. This gives the initial energy density in the transverse plane. For the energy density profile along the z-axis, a Woods-Saxon profile which satisfies the geometry of the collision along z-axis is used with proper Lorentz contraction.

Monte Carlo Glauber Model : This model is also based on the geometry of the collision, but in this method, unlike the optical Glauber, individual nucleon-nucleon collisions are considered for the energy deposition, Ref. [9]. First, inside the incoming nuclei, nucleons are randomly distributed following the Woods-Saxon probability distribution. Depending upon the interaction cross-section, an effective area of nucleons during the collisions is considered. The effective diameter of the nucleons during the collisions is taken as $d = \sqrt{\sigma/\pi}$. The locations at which the effective area of individual nucleons of target overlap in the transverse plane with the nucleons of projectile, *Gaussian distribution* of energy density with certain height and width is put by hand. These individual Gaussians, representing individual nucleon-nucleon collisions, which add up to give the total deposited energy density by the passing of two nuclei through each other. In the z-direction the distribution is taken by considering these randomly distributed individual Gaussians following Woods-Saxon distribution with appropriate Lorentz contraction. The energy density profile generated with this method can capture all possible fluctuations present in the relativistic HIC experiments.

In the relativistic HIC, since the thermalization time is expected to be short, it may be a good approximation to take the initial transverse flow velocity to be zero, i.e., $v_x = v_y = 0$. It can be justified on the basis that the partons produced just after the collision should have isotropic momentum distribution, therefore initially there should not be a preferred direction of the flow in the transverse plane [1].

According to the Bjorken picture, Ref. [3], in the longitudinal direction fluid velocity linearly increases with z, i.e., $v_z = z/t$, where t is the time in the laboratory frame. We will see that this velocity profile is only valid for the case when the central rapidity distribution $\frac{dN}{dY}$ vs. Y is completely flat. However, it is not completely true, in fact Bjorken picture is valid only approximately (valid up to a proportionality factor). The Bjorken velocity profile is the *boost-invariant* velocity profile; i.e. under the Lorentz transformation of z, t and v_z, all these variables get transformed as $z' = \gamma(z - vt)$, $t' = \gamma(t - \frac{v}{c^2}z)$, and $v'_z = (v_z - v)/(1 - \frac{v}{c^2}v_z)$ by preserving the velocity profile invariant, i.e., in the new frame also $v'_z = z'/t'$.

With the spacetime rapidity $\eta_s = \frac{1}{2}\ln\left(\frac{t+z}{t-z}\right)$, and the fluid rapidity $Y = \frac{1}{2}\ln\left(\frac{p_0+p_z}{p_0-p_z}\right)$ (fluid 4-momenta $p^\mu = (p_0, p_x, p_y, p_z)$, where $p_z = v_z p_0$), Bjorken prescription $v_z = z/t$ translates into $Y = \eta_s$, i.e. the fluid rapidity equals the spacetime rapidity. Using proper time $\tau = \sqrt{t^2 - z^2}$, one gets $t = \tau\cosh\eta_s$, $z = \tau\sinh\eta_s$, $v_z = \tanh Y$.

As we have discussed, for the hydrodynamic description of the system, we need initial conditions for energy density or entropy density. Here for the analytic estimate and for the sake of simplicity we assume that initial energy density or entropy density profile of the system as a *Gaussian* distribution as taken in Ref. [1],

$$s(x, y) \propto exp\left(-\frac{x^2}{2\sigma_x^2} - \frac{y^2}{2\sigma_y^2} - \frac{\eta_s^2}{2\sigma_\eta^2}\right), \tag{8.4}$$

where σ_x and σ_y are the widths of the transverse distribution. In the case of non-central collisions, as we have considered the x-axis along the impact parameter vector, therefore $\sigma_x < \sigma_y$, while in the case of central collisions both widths are equal. σ_η is a dimensionless parameter, representing the width of the distribution along rapidity. σ_η can be estimated by using the fact that particle multiplicity is proportional to the entropy [1].

At very early stage of the system evolution, longitudinal expansion dominates over the transverse expansion, therefore in the time shorter than $t \ll \sigma_x/c_s, \sigma_y/c_s$, Ref. [1], one can use $1 + 1$ dimensional hydrodynamic evolution of the plasma (here c_s is the sound velocity in the plasma given by $c_s = (\partial P/\partial\epsilon)^{1/2}$). Time greater than this, transverse expansion starts dominating and system undergoes full $3 + 1$ dimensional hydrodynamic expansion.

Now we discuss with the given initial conditions how ideal hydrodynamics explains the flow. The energy-momentum tensor for the inviscid hydrodynamics is given by,

$$T^{\mu\nu} = (\epsilon + P)u^\mu u^\nu - Pg^{\mu\nu}, \tag{8.5}$$

where $g^{\mu\nu} \equiv$ diag(1,-1,-1,-1) is the Minskowski metric tensor. The 4-velocity of fluid element u^μ is given by,

$$u^0 = \frac{1}{\sqrt{1-\vec{v}^2}}, \quad \vec{u} = \frac{\vec{v}}{\sqrt{1-\vec{v}^2}}. \tag{8.6}$$

The energy-momentum conservation equations are,

$$\partial_\mu T^{\mu\nu} = 0. \tag{8.7}$$

Longitudinal expansion and cooling : First we will consider the situation when the Bjorken picture is valid throughout plasma evolution, this requires $\sigma_\eta \to \infty$. Then we discuss how Bjorken picture gets modified for finite σ_η. We consider the evolution of the plasma near $z = 0$ with fluid velocity $v_z \simeq 0$. In Eqs.8.5,8.7 by taking $\nu = 3$, to the first order in velocity, we have,

$$\frac{\partial}{\partial t}((\epsilon + P)v_z) + \frac{\partial}{\partial z}P = 0. \tag{8.8}$$

Since initial fluid velocity is very small near $z = 0$ and remain very small in infinitesimal time dt, therefore the initial acceleration,

$$\frac{\partial v_z}{\partial t} = -\frac{1}{(\epsilon+P)}\frac{\partial P}{\partial z} = -\frac{1}{(\epsilon+P)}\frac{\partial \epsilon}{\partial z}\frac{\partial P}{\partial \epsilon}. \tag{8.9}$$

Now since the ideal hydrodynamics evolution is an adiabatic evolution therefore total entropy of the system is conserved, i.e. $dS = 0$, which implies that $d(sV) = 0$, where s is the entropy density. This gives, for the *isentropic process*, $\frac{ds}{s} = -\frac{dV}{V}$. From the first law of thermodynamics $dU = -PdV + TdS$, since $dS = 0$, therefore $d(\epsilon V) = -PdV$, which implies that, $\frac{d\epsilon}{(\epsilon+P)} = -\frac{dV}{V}$. Therefore for the isentropic process,

$$\frac{ds}{s} = d(\ln s) = \frac{d\epsilon}{(\epsilon+P)}. \tag{8.10}$$

By using above expression and the definition of the sound, Eq.8.9 can be written as,

$$\frac{\partial v_z}{\partial t} = -c_s^2\frac{\partial(\ln s)}{\partial z}. \tag{8.11}$$

Thus it is clear from this equation that if the entropy density varies with z, then fluid will accelerate, and near $z = 0$, fluid velocity will increase and deviate from the Bjorken velocity profile. Now we rewrite the above equation in the τ, η_s and Y coordinates. Near $z = 0$, $v_z \approx Y$, $dt \approx d\tau$, $dz \approx \tau d\eta_s$, therefore

$$\frac{\partial Y}{\partial \tau} = -\frac{c_s^2}{\tau}\frac{\partial(\ln s)}{\partial \eta_s}. \tag{8.12}$$

Therefore to have the Bjorken picture throughout the system evolution, the condition $\frac{\partial(\ln s)}{\partial \eta_s} = 0$ must satisfy, which implies that $\sigma_\eta \to \infty$. This corresponds to a flat rapidity spectra. If σ_η is finite then the above equation gives,

$$\frac{\partial Y}{\partial \tau} = \frac{c_s^2}{\tau}\frac{\eta_s}{\sigma_\eta}. \tag{8.13}$$

When we integrate this equation from proper time τ_0 to τ with the Bjorken's initial condition $Y = \eta_s$, we get,

$$Y(\tau) = \left(1 + \frac{c_s^2 \ln(\tau/\tau_0)}{\sigma_\eta^2}\right)\eta_s \tag{8.14}$$

This shows that even if the rapidity distribution is not completely flat, Bjorken picture can be valid up to an proportionality factor. Since with increasing energy, rapidity distribution becomes more and more flatter. Therefore the Bjorken picture becomes more and more valid with the increasing energy of the collision.

Now we discuss the longitudinal cooling, baryon number density and entropy density changes with time in the Bjorken picture in 1+1 dimension. Let us consider $\nu = 0$ in Eqs.8.5,8.7. We get,

$$\frac{\partial \epsilon}{\partial t} + \frac{\partial((\epsilon + P)v_z)}{\partial z} = 0. \tag{8.15}$$

We are interested in the evolution of energy density at $z = 0$, therefore fluid velocity $v_z = z/t$ will be zero at $z = 0$. Since $\partial v_z/\partial z = 1/t$, therefore under these conditions above equation becomes,

$$\frac{\partial \epsilon}{\partial t} + \frac{\epsilon + P}{t} = 0. \tag{8.16}$$

Now let us use the ideal gas equation of state (EoS) for the QGP, i.e, $P = \epsilon/3$. The above equation gives,

$$\epsilon \propto t^{-4/3}. \tag{8.17}$$

This shows that at $z = 0$, energy density of plasma with ideal gas EoS in 1+1 dimension in the Bjorken scenario decreases with time as $t^{-4/3}$. Since $\epsilon \propto T^4$, where T is the temperature, therefore $T \propto t^{-1/3}$. Now if we consider the baryon number conservation equation and the entropy conservation equation,

$$\partial_\mu (n u^\mu) = 0, \quad \partial_\mu s^\mu = 0, \tag{8.18}$$

and perform same kind of calculation in the Bjorken picture, we get,

$$\frac{\partial n}{\partial t} + \frac{n}{t} = 0, \quad \frac{\partial s}{\partial t} + \frac{s}{t} = 0. \tag{8.19}$$

This gives nt = constant and st = constant, which shows that baryon density and entropy density both decrease with t^{-1}. This is expected, as in 1+1 dimension volume of the system increases as t.

Transverse expansion : As done earlier, we now take $\nu = 1, 2$ in Eqs.8.5,8.7, and consider first order terms in velocities. We get (at $z = 0$),

$$\frac{\partial}{\partial t}((\epsilon + P)v_x) + \frac{\partial}{\partial x} P = 0, \tag{8.20}$$

$$\frac{\partial}{\partial t}((\epsilon + P)v_y) + \frac{\partial}{\partial y} P = 0. \tag{8.21}$$

Again, since initial fluid velocity is zero and very small in time dt, therefore initial acceleration of fluid at $z = 0$ is given by,

$$\frac{\partial v_x}{\partial t} = -\frac{1}{(\epsilon + P)} \frac{\partial P}{\partial x}, \tag{8.22}$$

$$\frac{\partial v_y}{\partial t} = -\frac{1}{(\epsilon + P)} \frac{\partial P}{\partial y}. \tag{8.23}$$

Again, by using the fact that ideal hydrodynamics evolution is an adiabatic process so the total entropy is conserved and by using the definition of speed of sound we get,

$$\frac{\partial v_x}{\partial t} = -c_s^2 \frac{\partial (\ln s)}{\partial x}, \tag{8.24}$$

$$\frac{\partial v_y}{\partial t} = -c_s^2 \frac{\partial (\ln s)}{\partial y}. \tag{8.25}$$

Therefore for the given entropy density profile, the obtained transverse velocity for small t is,

$$v_x = \frac{c_s^2 x}{\sigma_x^2} t, \tag{8.26}$$

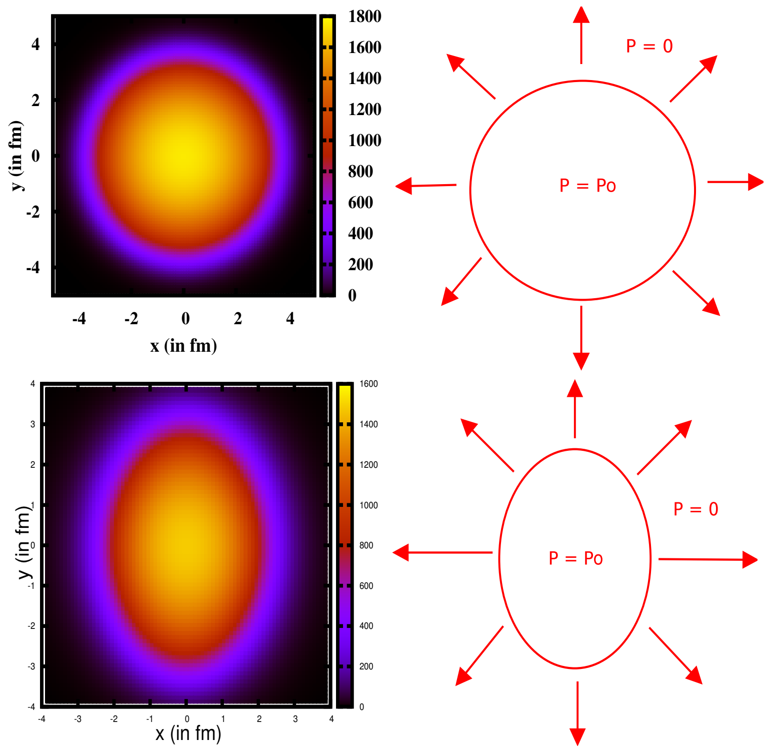

Figure 8.3: Figure shows how spatial distribution of energy density affects the momentum distribution of plasma evolution in the transverse plane.

$$v_y = \frac{c_s^2 y}{\sigma_y^2} t. \tag{8.27}$$

Here first we should note that fluid velocity is directly related with the sound speed. This fact plays a very important in the evolution of the fluid, since the sound speed is related with the EoS which dictates the property of the fluid. The dependence of the fluid velocity on sound speed plays a very important role in the MHD fluid where sound speed is direction dependent in this fluid and leads to the anisotropic evolution of the plasma depending upon the direction of magnetic field. Now, since $\sigma_x < \sigma_y$ for the non-central collisions, therefore $v_x > v_y$ which shows that spatial anisotropy present in the plasma leads to momentum anisotropy in the hydrodynamic evolution. This happens due to presence of larger pressure gradient along x-axis than along y-axis in non-central collisions. The left part of Fig.8.3 shows the initial energy density created with the *optical Glauber method* for the cases of central collision (up) and non-central collision (down). This shows that in the case of central collision plasma region has isotropic distribution of energy density while in the case of non-central collisions there is a spatial anisotropy present in the plasma. Right part of Fig.8.3 shows that due to presence of different initial conditions, plasma evolution for the central collision (up) and non-central collision (down) is different. In the case of non-central collision, there is a momentum anisotropy in the plasma evolution.

Elliptic Flow : To quantify the momentum anisotropy, one introduces the *elliptic flow* which can be defined in various ways. Note that in the detector freeze-out hadrons reach which carry this momentum anisotropy. So the particle distribution function is needed for the full characterization of this anisotropy. However, Here we only discuss at the level of hydrodynamics evolution which is the main cause of the momentum anisotropy. Here we discuss two hydrodynamic variables which can characterize the momentum anisotropy,

$$\epsilon_p = \frac{T^{xx} - T^{yy}}{T^{xx} + T^{yy}} = \frac{v_x^2 - v_y^2}{v_x^2 + v_y^2 + \frac{1}{2\gamma^2}}, \tag{8.28}$$

and

$$v_2 = \frac{T^{0x} - T^{0y}}{T^{0x} + T^{0y}} = \frac{v_x - v_y}{v_x + v_y}, \tag{8.29}$$

where we have used the EoS, $\epsilon = 3P$, to get the finial expression of ϵ_p. Both these variables are measure of momentum anisotropy. In the case of non-central collision, one gets $v_x > v_y$, so both the variables become non-zero, while in the case of central collisions both are zero. The difference is that former depends upon the EoS, while latter does not. Also the time evolution of former and latter is different. v_2 gets a sudden jump as soon as the flow develops, while ϵ_p varies smoothly with time. This can be seen as follows: let us consider the time at which a flow just has developed, in this case both v_x and v_y will be very small. Let us consider, as an example, $v_x = 2v_y$. Then the above expressions for both the quantities for very small initial velocity, $\gamma \approx 1$, gives,

$$\epsilon_p = \frac{3}{5 + \frac{1}{2\gamma^2 v_y^2}} \approx 6v_y^2, \tag{8.30}$$

which is very small number and hence ϵ_p varies with time smoothly, while

$$v_2 = \frac{1}{3}, \tag{8.31}$$

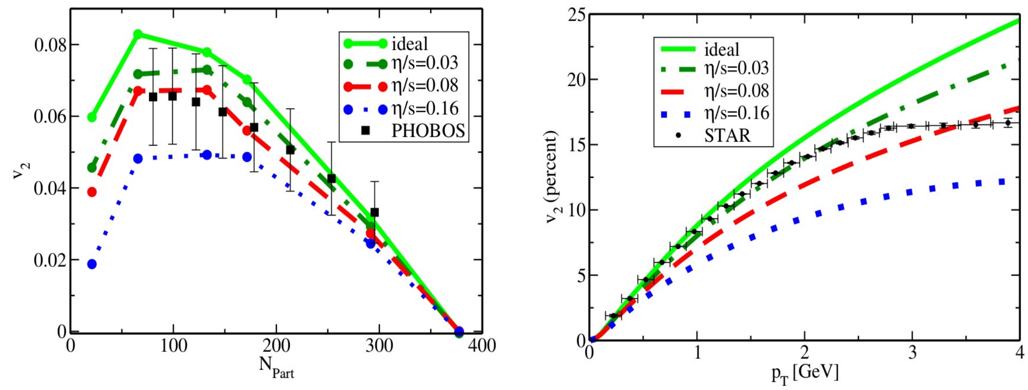

Figure 8.4: v_2 for charged particles in Au Au collisions at $\sqrt{s} = 200$ GeV, compared to hydrodynamic model for various viscosity ratios η/s. Figure has been taken from Ref. [10].

which is independent from the initial small values of flow velocity and has sudden jump. Although both the quantities have different character, both are measure of the momentum anisotropy which arises due to elliptic shape of the plasma in the non-central collisions and therefore are called *elliptic flow*.

As shown in Fig.8.4 the ideal hydrodynamics can explain experimental data very well on the qualitative ground. But it does not fit the data exactly, because QGP has non-zero η/s. It has been argued that due to quantum uncertainty principle, there is a lower bound on η/s. AdS/CFT also sets a lower bound on viscosity as $\eta/s \geq 1/4\pi \sim 0.08$ for certain Super-Yang-Mills theory. So to fit the data, viscous Hydrodynamics is required. The best fitting gives the value of η/s of QGP. It is clear from the figure that viscosity in the fluid reduces the elliptic flow by reducing velocity gradient.

Although the left Figure in Fig.8.4 satisfies the lower bound, right does not. The reason may be that in the simulation in Ref. [10], Glauber initial condition has been used and magnitude of elliptic flow depends upon initial energy density profile. When one uses color glass condensate initial condition, then there is no violation of the lower bound of η/s, see Ref. [11] and Fig.8.5. In fact, magnitude of elliptic flow depends upon initial energy density (CGC or Glauber), viscosity of QGP, EoS, etc. In the Chapter 10 of this thesis, we will see that elliptic flow also depends upon the strength

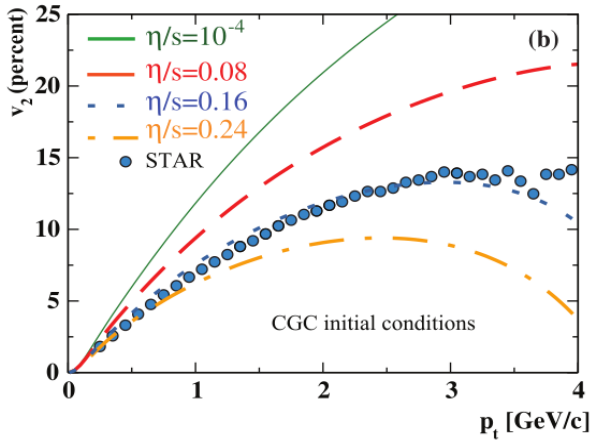

Figure 8.5: v_2 from experimental data fitted using initial conditions by the color glass condensate model in the viscous hydrodynamics. Figure has been taken from Ref. [11].

and profile of the initial magnetic field in the plasma.

8.4 Fourier Analysis for Flow in Heavy-Ion Collisions

Firstly, here we summarize the above discussion, and discuss the Fourier analysis of transverse momentum distribution. In relativistic heavy-ion collision experiments two heavy nuclei collide with very high energy and pass through each other (direction of motion of nuclei is along $\pm z$-axis). In the overlap region, partons get produced, which through sufficient interactions thermalize locally, due to which system undergoes hydrodynamic expansion. Impact parameter vector is a vector drawn from the center of target to projectile center in the plane transverse to the beam axis (i.e. in the xy-plane). Impact parameter vector and z-axis form a plane is known as the reaction plane. We take x-axis along the impact parameter vector and therefore y-axis is perpendicular to the reaction plane.

For the central (head on) collisions, impact parameter is zero. So if we don't consider the fluctuations in the initial energy density profile, because of isotropic pressure gradient, plasma expands isotropically following hydrodynamic evolution.

In the case of non-central collisions, impact parameter is non-zero and there is a spatial anisotropy in the plasma of the elliptical shape. As in this case, there is more pressure gradient along x-axis compared to y-axis, therefore fluid will accelerate more along x-axis than y-axis. This kind of flow is generated because of initial elliptical shape of the plasma that is why this is called the elliptic flow.

In the presence of fluctuations energy density distribution of the plasma has random components and can generate very complicated kind of flow. To study such kind of complicated flow, the Fourier analysis of the transverse momentum distribution is performed Ref. [12]. For the analysis, we first construct an azimuthal (or transverse) distribution function. In heavy-ion collision, experimentalist observe hadrons and their momenta. So they construct azimuthal distribution function by using hadron momentum distribution. But in our work we have not performed simulations until the freeze-out, therefore we construct azimuthal distribution function with the help of fluid momenta.

We solve ideal hydrodynamics equations $\partial_\mu T^{\mu\nu} = 0$ (see Chapter 6), where ideal energy-momentum tensor is given by, $T^{\mu\nu} = (\epsilon + P)u^\mu u^\nu - Pg^{\mu\nu}$. Here $g^{\mu\nu} = (1, -1, -1, -1)$ is the Minkowski metric, $u^\mu = \gamma(1, \vec{v})$ is fluid 4-velocity, ϵ is the local energy density, P is the local pressure of the plasma, and last two are related by the equation of state. After solving energy-momentum conservation equations, we have all the components of $T^{\mu\nu}$. T^{0i} components of $T^{\mu\nu}$ are the momentum density along i-th direction. Let us call $p^i = T^{0i}$.

We divide our transverse plane into small angular bins and calculate average momenta in each bin which gives us $p(\phi)$. We also calculate average momenta in the whole transverse plane, say $\bar{p}$. By this, we construct our azimuthal distribution function $r(\phi) = \frac{\delta p}{\bar{p}} = \frac{p(\phi)-\bar{p}}{\bar{p}}$, which can be written as a Fourier series as follows:

$$r(\phi) = \frac{\delta p}{\bar{p}} = \frac{x_0}{2\pi} + \sum_{n=1}^{\infty}[x_n \cos(n\phi) + y_n \sin(n\phi)], \tag{8.32}$$

where,

$$x_n = \frac{1}{\pi}\int_0^{2\pi} r(\phi)\cos(n\phi)\, d\phi, \tag{8.33}$$

$$y_n = \frac{1}{\pi}\int_0^{2\pi} r(\phi)\sin(n\phi)\, d\phi. \tag{8.34}$$

A non-zero value of x_n and y_n indicates n-th type of flow, which is characterized by the magnitude $v_n^{rms} = v_n = \sqrt{x_n^2 + y_n^2}$, and the direction ψ_n, where $0 \leq \psi_n < 2\pi/n$. Here $x_n = v_n \cos(n\psi_n)$ and $y_n = v_n \sin(n\psi_n)$. Therefore the azimuthal distribution function in terms of v_n and ψ_n is given by,

$$r(\phi) = \frac{v_0}{2\pi} + \frac{1}{\pi}\sum_{n=1}^{\infty} v_n \cos[n(\phi - \psi_n)] \tag{8.35}$$

If there is no flow anisotropy, all higher coefficients become zero and only x_0 or v_0 remain non-zero. The first flow coefficient v_1 is known as the *directed flow* which becomes non-zero if there is a flow along a particular direction in the plasma. The direction of directed flow is given by ψ_1. The second flow coefficient v_2 is known as the *elliptic flow* which becomes non-zero if therefore is equal and opposite directional flow present in the plasma. The direction of elliptic flow is characterized by the angle ψ_2 and $\psi_2 + \pi$. Similarly, the third flow coefficient v_3 is known as the *triangular flow* which becomes non-zero if there is equal amount of flow present in plasma in three directions with angles ψ_3, $\psi_3 + \frac{2\pi}{3}$, and $\psi_3 + \frac{4\pi}{3}$. Similarly, higher flow coefficients can be present in the plasma.

In the case of central collisions if there are no fluctuations present in the plasma then the plasma region will be completely azimuthal symmetric and in that case evolution of the plasma will be isotropic, therefore $r(\phi)$ becomes independent of ϕ and all flow coefficients become zero except v_0. But if the fluctuations are present in the plasma then all flow coefficients become non-zero.

In the case of non-central collisions if there are no fluctuations present, plasma region will have a reflection symmetry. Because of this, generated flow also have a reflection symmetry, which makes only even flow coefficients non-zero. Therefore if in the plasma a reflection symmetry is present, then one expects even-odd separation in the power of flow coefficients. In the presence of fluctuations, reflection symmetry in plasma is suppressed, due to which all the flow coefficients become non-zero and the even-odd separation in the flow coefficients is washed out.

In the following chapters we see that even if the plasma is azimuthal symmetric due to presence of vortices or magnetic field, flow becomes such that it can generate an even-odd separation in the flow coefficients. In both the cases, vortices and magnetic field, a strong elliptic flow gets generated which drives other even harmonics and gives rise to even-odd separation. Of course due to fluctuations, this separation gets suppressed. The main conclusion of these results can be summarized as follows:

If the plasma evolution has a reflection symmetry, then irrespective of the cause of this symmetry, there always be an even-odd separation in the flow coefficients.

8.5 Magnetic Field in Heavy-Ion Collisions

As we have discussed, in the relativistic HIC experiment two heavy nuclei collide with each other and produce particles which after interaction form a thermal medium. As the nuclei is made of protons and neutrons, due to its motion, magnetic field get produced around the individual nuclei. In the case of central collisions, if we consider the uniform charge distribution of protons inside nuclei, the magnetic field generated by one nuclei exactly gets canceled by the magnetic field of the other nuclei in the $z = 0$ plane, therefore no magnetic field will be present there. But if we consider the actual charge distribution inside a nuclei which may not be uniform due to the random positions of protons inside nuclei (following Woods-Saxon distribution), then in the case of central collision also magnetic field can be generated. However, this magnetic field is completely arbitrary and if one performs the event average over it, then the net magnetic field and its effects may not seen. In the Fig. 8.6 we have shown the magnetic field in the central collision, where we have considered the position coordinates of protons randomly inside the nuclei (following Woods-Saxon distribution). Since the distribution of protons in both the nuclei is completely independent, therefore magnetic field generated by both the nuclei do not get canceled in general. Left plot is the magnetic field at the earlier time while right plot is for the magnetic field at some late time, which is clearly smoother than the left one.

In the case of non-central collisions, because of the asymmetry in the collisions, even if we consider the uniform charge distribution inside nuclei, strong magnetic field arises (mainly due to spectators) in the region where plasma forms. The direction of this magnetic field is perpendicular to the reaction plane (along y-axis) at $x = 0$ plane, and the magnitude of this magnetic field is the strongest at the center of the system. The magnitude of magnetic field at the center can be as high as $\sim 10^{15}$ Tesla (~ 0.1 GeV^2) at LHC energies [13]. This magnitude is 10^4 times stronger than the

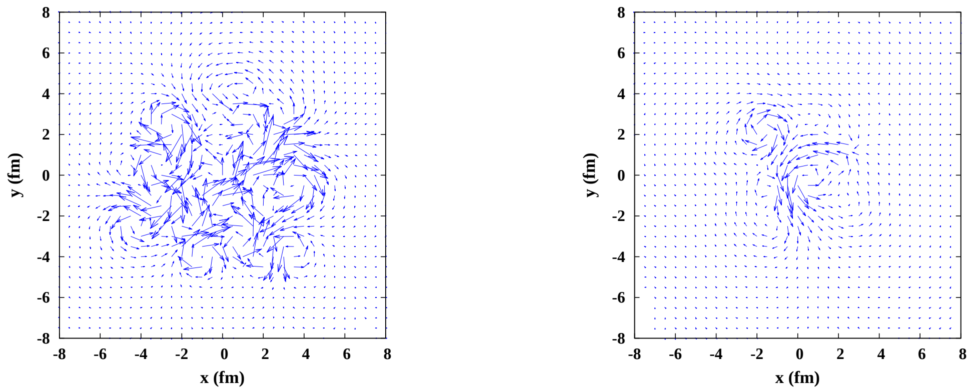

Figure 8.6: The magnetic field is generated in the central collision by considering random distribution of protons inside nuclei following Woods-Saxon distribution. The left plot is at the earlier time and right is at the latter time. The magnitude of magnetic field is proportional to the length of the vector in the plot. We are not giving here any number since our purpose is to show a qualitative profile of magnetic field in the central collision.

magnetic field present in a *Magnetar*. In the Fig. 8.7 the situation of the non-central collision has been shown. Left figure shows how a magnetic field can be generated due to the motion of two nuclei in the HIC experiments. The direction of the magnetic field, where plasma forms, is along the y-axis and significantly strong. The right plot shows the whole magnetic field profile in the case of non-central collision in the $z = 0$ plane. This plot has been generated by considering the uniform charge distribution inside the nuclei.

The magnetic field generated by a charge particle moving along z-axis in vacuum with speed v is given by [15],

$$\vec{H} = \frac{e\gamma}{4\pi}\frac{v|\vec{b}-\vec{b'}|\hat{\phi}}{(|\vec{b}-\vec{b'}|+\gamma^2(vt-z)^2)^{\frac{3}{2}}}, \tag{8.36}$$

where e is the electric charge of the particle, $\vec{b}$ is the observation point and $\vec{b'}$ is the location of the particle from the origin in the transverse plane. This expression can be obtained by solving Maxwell's equations or by doing Lorentz transformation of the electric field from the rest frame of the particle to the moving frame. If we consider a uniform charge distribution inside each nuclei, i.e., charge density, $\rho(r') = Z/(\frac{4}{3}\pi R_A^3)$,

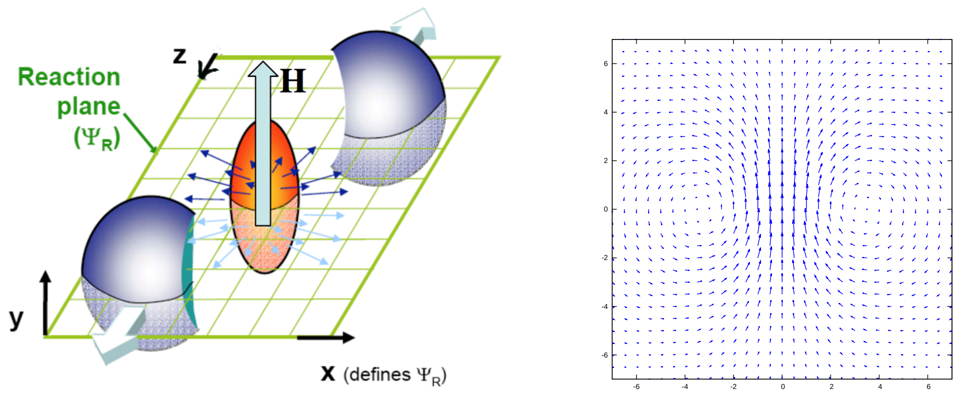

Figure 8.7: The left figure shows how magnetic field can be generated in the HIC experiments due to motion of two nuclei. Figure has been taken from Ref. [14]. Right figure shows the profile of the magnetic field in the $z = 0$ plane.

then the magnetic field generated by moving nuclei in HIC can be calculated by the expression, Ref. [15],

$$\vec{H}_{Nuclei} = \int \vec{H}\rho(r')d^3r', \tag{8.37}$$

where R_A is the radius of the nuclei. The total magnetic field in HIC arising from both moving nuclei can be calculated by adding magnetic fields due to the individual nuclei, see Ref. [15].

The important point here is that the strength of the magnetic field is proportional to the Lorentz γ factor, so when energy of the collision increases, the strength of the produced magnetic field also increases. But the Lorentz γ factor is also present in front of the time factor in the denominator in the above expression, therefore with the increasing γ factor, strength of the magnetic field also decreases very fast with time. On the other hand, in the low energy collisions the strength of the initial magnetic field is relatively weaker but it decreases with relatively slower rate also. This time decaying magnetic field can be protected if the conducting medium forms very quickly. From the Maxwell's equations we know that, in a medium, a time varying magnetic field generates an electric field, which induces an electric current in the medium which again generate the magnetic field in the same direction. Because of this, the decay rate of the magnetic field gets suppressed in a conducting medium. If the conductivity of the medium is high then due to the above process magnetic field decays very slowly in the medium. If the conductivity of the medium is infinite then magnetic field never decays and remains frozen in the medium.

Now let us see how a magnetic field changes with time in a conducting medium (Ref. [16]). We see that if the conductivity of the fluid is finite then the magnetic field lines diffuse in the medium with certain diffusion time while if the conductivity of the medium is infinite then magnetic field lines never decay and remain frozen in the medium. Let us consider an electrically neutral, conducting fluid in the presence of magnetic field. In a high conductivity fluid, electric field is almost zero due to availability of large number of free charges in the medium. The *Ohm's law* in the rest frame of the fluid is given by,

$$\vec{J} = \sigma \vec{E}, \tag{8.38}$$

where σ is the electrical conductivity of the medium. This shows that if the medium has infinite conductivity, then in the rest frame of the fluid, there is no electric field. Now, Maxwell's equations is given by (ignoring displacement current in a good conducting medium),

$$\vec{\nabla} \times \vec{E} + \frac{\partial \vec{B}}{\partial t} = 0, \tag{8.39}$$

$$\vec{\nabla} \times \vec{B} = 4\pi \vec{J}. \tag{8.40}$$

Using Maxwell's equation and Ohm's law we get,

$$\frac{\partial \vec{B}}{\partial t} = \frac{1}{4\pi\sigma} \nabla^2 \vec{B}. \tag{8.41}$$

This is a diffusion equation, which shows that in a medium with finite conductivity, an initial magnetic field gets diffused in a diffusion time (obtained by solving above diffusion equation),

$$\tau = 4\pi\sigma L^2. \tag{8.42}$$

where L is the characteristic length of the spatial variation of $\vec{B}$. In Chapter 10 we have estimated the diffusion time (in different unit system) for QGP in relativistic HIC, which we find to be less than 1 fm. Note that this time should be counted after the formation of thermal medium in HIC. Up to the thermalization time a significant amount of the initial magnetic field already decays in the vacuum. The above equation also shows that if the conductivity of the medium is infinite then magnetic field never decays in the medium. It remains frozen and moves with the medium. Since within

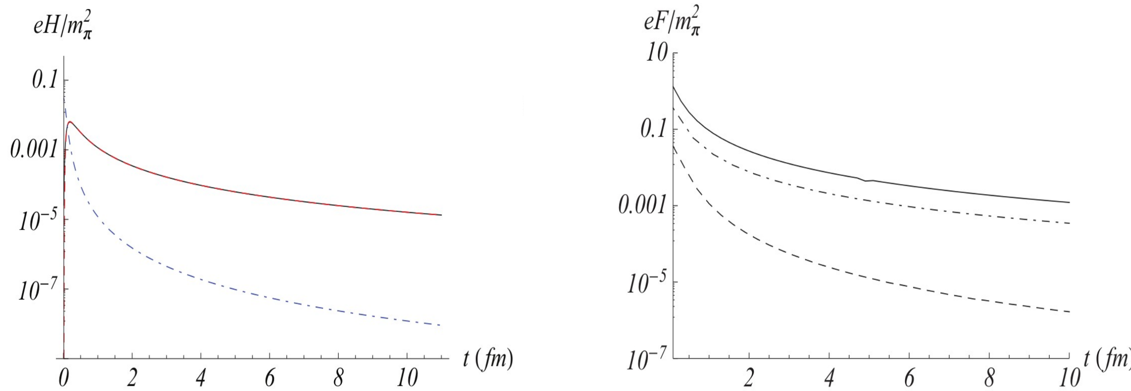

Figure 8.8: Calculations have been performed at $z = 0$ with $\gamma = 100$. Left figure shows the time evolution of the magnetic field at the center created by a point unit charge in vacuum (blue) and in the medium of conductivity $\sigma = 5.8\ MeV$ (red). Here $|\vec{b}| = 0$ and $|\vec{b}'| = 7.4\ fm$. Right figure shows the time dependence of the electromagnetic field created due to the motion of two nuclei with impact parameter 7 fm in HIC experiment. The solid line shows the time variation of H_y at $x = y = 0$; the dashed line for H_x and dashed-dotted line for E_y at $x = y = 1\ fm$. Figures has been taken from the Ref. [15].

the diffusion time magnetic field lines does not decay much, therefore within this time interval, the ideal MHD approximation can be considered for the fluid evolution.

In Ref. [15], by considering the presence of a finite conducting medium of conductivity $\sigma = 5.8\ MeV$, it has been shown that time decay of magnetic field in the medium is much slower than in the vacuum. Fig. 8.8 shows that a time varying magnetic field decays with the slower rate in medium compared to the vacuum. Calculations have been performed at $z = 0$ with $\gamma = 100$. Left figure shows the time evolution of the magnetic field at the center created by a point unit charge in vacuum (blue) and in the medium of conductivity $\sigma = 5.8\ MeV$ (red). Here $|\vec{b}| = 0$ and $|\vec{b}'| = 7.4\ fm$. Right figure shows the time dependence of the electromagnetic field created due to the motion of two nuclei with impact parameter 7 fm in HIC experiment. The solid line shows the time variation of H_y at $x = y = 0$; the dashed line for H_x and dashed-dotted line for E_y at $x = y = 1\ fm$.

In relativistic heavy-ion collisions, medium forms at thermalization time $\tau_0 < 1\ fm$ in the presence of time varying magnetic field. The thermalization time may also get modified due to presence of the magnetic field. Although charged particles remain present from the very beginning of the collision, but since at this stage system remain out of equilibrium, therefore system does not have the conductivity of a thermalized QGP medium. After the formation of the thermal medium, the time decay of magnetic field gets slower down. A quick thermalization and large conductivity of the plasma may protect magnetic field (of high magnitude) from decay.

In heavy-ion collisions, temperature of the medium varies strongly from center of the plasma with value, $\sim 200 - 300\ MeV$ to zero value outside in vacuum. The conductivity is a function of temperature. The Lattice simulation results for the QGP gives $\sigma_{QGP} = 0.04T$. Therefore conductivity should also vary in space in such a medium. For the sake of simplicity, in Chapter 10, we have considered the fluid in HIC as an ideal RMHD fluid, which has infinite electric conductivity everywhere, spatially as well as temporally.

Now we discuss the effect of magnetic field on the medium evolution. First we discuss that if we consider the ideal RMHD fluid evolution of the medium in relativistic HIC, how its evolution differs from the ideal hydrodynamic evolution. We find that the presence of magnetic field can enhance the *elliptic flow*. We know that the ideal hydrodynamics has only one kind of longitudinal (pressure) sound wave, speed of which is given by,

$$c_s = \left(\frac{\partial p}{\partial \epsilon}\right)^{1/2}. \tag{8.43}$$

In this case EoS of the whole fluid is isotropic (although equation of state can be a function of temperature itself), therefore c_s is isotropic in the ideal hydrodynamics. In ideal RMHD fluid, different kinds of waves are possible as discussed in the last chapter. Consider fluid motion perpendicular to the magnetic field direction. Since field lines remain frozen in the ideal RMHD fluid, therefore due to perpendicular motion of the fluid, magnetic lines get deformed as shown in the Fig.8.9. This bending of magnetic lines cost energy, magnetic lines feel tension, and try to become straight again. Due to this, EoS perpendicular to magnetic field becomes stiffer and hence sound speed becomes larger in this direction. As we have discussed in the ideal hydrodynamics case, and also have seen in the last chapter in the case ideal MHD fluid, that fluid velocity is directly related with the sound speed of the fluid in the direction of the

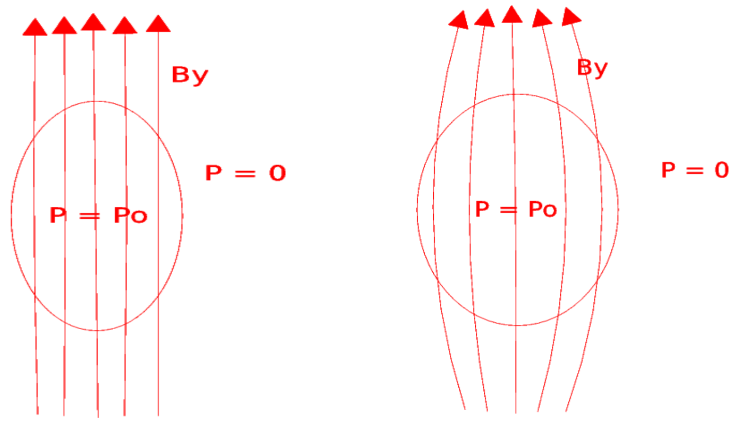

Figure 8.9: Figures show the evolution of an ideal RMHD fluid in relativistic HIC. Due to the expansion of the fluid along x-axis, magnetic field lines get bend in the right figure.

fluid motion, therefore along the x-axis (if we consider uniform magnetic field along y-axis), fluid velocity get enhanced, therefore from the expression of the elliptic flow we can see that its magnitude gets enhanced due to this. Therefore magnetic field in the fluid can enhance the elliptic flow, see Ref. [17].

In Ref. [18], the effect of a strong magnetic field, which can probe the topology of QCD vacuum structure in the context of relativistic HIC, has been discussed. We know that QCD has infinite degenerate vacua. Each vacuum is characterized by different winding number associated with the gauge field configurations. As in Chapter 2 we have discussed that there is a topological barrier when one tries to go from one winding number configuration to the other; i.e. no continuous deformation is possible which can change one winding number configuration to the other. But quantum physics allows the quantum tunneling between different winding number vacua mediated by the *instanton process*. Because there is an energy barrier, given in term of $F^{\mu\nu}$ between two vacua, therefore during the instanton process $F^{\mu\nu}$ becomes non-zero. Further, instanton configurations have non-zero value of $F^{\mu\nu}\widetilde{F}_{\mu\nu}$, with the winding number associated with the instanton being given by integral of $F^{\mu\nu}\widetilde{F}_{\mu\nu}$. Now, we know by the *chiral anomaly* that for zero mass fermions, if $F^{\mu\nu}\widetilde{F}_{\mu\nu}$ becomes non-zero, then depending upon the sign of the winding number of the instanton, one chirality prefers over the other in the system. In relativistic HIC, at the stage when magnetic field is very strong, i.e. $eB \gg p^2$ (p is momentum of particle), spin of the positive charge particles align along the magnetic field direction while spin of the negative charge particles align opposite to the magnetic field. Now if an instanton process occurs in the system then due to this, system will have a chirality imbalance. To have correct chiral particles in the system, particles flip their momentum [18]. Thus by this, there will be more number of one chiral particles than the other. This leads to the motion of the positive and negative charge particles in the opposite direction in the line of magnetic field, i.e. perpendicular to the *reaction plane*. This causes a charge separation. Therefore it is expected that in HIC experiment, in the detectors there should be accumulation of opposite charges in the opposite direction, perpendicular to the reaction plane. This is known as the *chiral magnetic effect*.

Bibliography

[1] J. Ollitrault, Eur. J. Phys. **29**, 275302 (2008).

[2] https://www.opensciencegrid.org.

[3] J.D. Bjorken, Phys. Rev. D **27**, 140 (1983).

[4] Ulrich Heinz, Concepts of Heavy-Ion Physics, **arXiv:** hep-ph/0407360.

[5] Peter F. Kolb, Ulrich Heinz, Hydrodynamic description of ultrarelativistic heavy-ion collisions, **arXiv:** nucl-th/0305084.

[6] Edmond Iancu, Raju Venugopalan, The Color Glass Condensate and High Energy Scattering in QCD, **arXiv:** hep-ph/0303204.

[7] Edmond Iancu, QCD in heavy ion collisions, **arXiv:** 1205.0579.

[8] P.F. Kolb, J. Sollfrank, and U. Heinz, Phys.L Rev. C **62**, 054909 (2000).

[9] M.L. Miller, K. Reygers, S.J. Sanders, and P. Steinberg, Annu. Rev. Nucl. Part. Sci. **57**, 205-243 (2007).

[10] P. Romatschke, U. Romatschke, Phys. Rev. Lett. **99**, 172301 (2007).

[11] R. Snellings, New J. Phys. **13**, 055008 (2011).

[12] S. Voloshin, Y. Zhang, Z. Phys. C **70**, 665 (1996).

[13] Y. Zhong, C-B Yang, X. Cai, and S-Q Feng, Advances in High Energy Physics **2014**, 193039 (2014).

[14] D.E. Kharzeev, Prog. Part. Nucl. Phys. **75**, 133 (2014).

[15] K. Tuchin, Phys. Rev. C, 88, 024911 (2013).

[16] J.D. Jackson, **Classical Electrodynamics**, John Wiley & Sons (1962).

[17] R.K. Mohapatra, P.S. Saumia, Ajit M. Srivastava, Mod. Phys. Lett. A **26**, 2477 (2011).

[18] D.E. Kharzeev, L.D. McLerran, H.J. Warringa, Nucl. Phys. A **803**, 227 (2008).

Chapter 9

Superfluid Phases of QCD in Heavy-ion Collisions

Topological defects arise in a variety of systems, e.g. vortices in superfluid helium to cosmic strings in the early universe. There is an indirect evidence of neutron superfluid vortices from glitches in pulsars. One also expects that topological defects may arise in various high baryon density phases of quantum chromodynamics (QCD), e.g. superfluid topological vortices in the color flavor locked (CFL) phase. Though vastly different in energy/length scales, there are universal features, e.g. in the formation of all these defects. Utilizing this universality, in this chapter, we investigate the possibility of detecting these topological superfluid vortices in laboratory experiments, namely heavy-ion collisions. Using hydrodynamic simulations, we show that vortices can qualitatively affect the power spectrum of flow fluctuations. This can give unambiguous signal for superfluid transition resulting in vortices, allowing for check of defect formation theories in a relativistic quantum field theory system, and the detection of superfluid phases of QCD. Detection of nucleonic superfluid vortices in low energy heavy-ion collisions will give opportunity for laboratory controlled study of their properties, providing crucial inputs for the physics of pulsars. Results discussed in this chapter have been presented in Ref. [1].

9.1 Introduction

Topological defects are typically associated with symmetry breaking phase transitions. Due to their topological nature, they display various universal properties, especially in their formation mechanism and evolution. This has led to experimental studies of defect formation in a range of low energy condensed matter systems, e.g., superfluid helium, superconductors, liquid crystals etc. [2,3] which have utilized this universality and have provided experimental checks on different aspects of the theory of cosmic defect formation, usually known as the Kibble mechanism [4]. However, it is clearly desirable to experimentally test these theories also in a relativistic quantum field theory system for a more direct correspondence with the theory of cosmic strings and other cosmic defects.

We address this possibility in this chapter and focus on heavy-ion collision (HIC) experiments. One of the main aims of these experiments is to probe the QCD phase diagram which shows very rich features, especially in the regime of high baryon density and low temperatures. FAIR and NICA are upcoming facilities for HIC, dedicated to the investigation of high baryon density phases of QCD. Exotic partonic phases e.g. two flavor color superconducting (2SC) phase, crystalline color superconducting phase, color flavor locked (CFL) phase, [5] etc. are possible at very high baryon density. Transitions to these phases is associated with complex symmetry breaking patterns allowing for a very rich variety of topological defects in different phases. Even at moderately low baryon densities, nucleon superfluidity (neutron superfluidity and proton superconductivity) arises. The CFL phase occurs at very high baryon densities, with baryon densities at least an order of magnitude higher than the nuclear saturation density (ρ_0), and temperatures up to about 50 MeV, whereas nucleonic superfluidity occurs at much lower densities, of order $(10^{-3}-1)\rho_0$, and temperatures as low as 0.3 MeV. Interestingly, this entire vast range of densities and temperatures may be accessible at the facilities such a FAIR and NICA. As we noted above, irrespective of the energy scale, universality of defect formation allows us to infer reasonably model independent predictions about qualitative effects arising from vortex formation from these different phase transitions.

In the present day universe, superfluid phases of nucleons are expected to exist inside neutron stars [6] and resulting vortices are supposed to be responsible for the phenomenon of glitches [7]. No such observational support exists yet for the high density phases of QCD (e.g. CFL phase) in any astrophysical object. In an earlier paper, some of us have proposed the detection of such phase transitions by studying density fluctuations arising from topological defect formation and its effects on pulsar timings and gravitational wave emission [8, 9].

All of the HIC investigations in the literature probing the high baryon density regime of QCD have focused primarily on signals related to the quark-hadron transition. We propose a somewhat different line of focus at these experiments. Some of these exotic high baryon density partonic phases also have superfluidity. For example, the CFL phase corresponds to the spontaneous symmetry breaking pattern, $SU(3)_{color} \times SU(3)_L \times SU(3)_R \times U(1)_B \rightarrow SU(3)_{color+L+R} \times Z_2$. Superfluidity arises from spontaneous breaking of $U(1)_B$ to Z_2 as the diquark condensate for the CFL phase is not invariant under $U(1)_B$ baryon number transformations. This is also expected in somewhat lower density phases (where effects of heavier strange quark become important) such as the CFL+K^0 phase [10]. In HIC, if any of these phases arise, a superfluid transition will inevitably lead to production of superfluid vortices via the Kibble mechanism [4].

Similarly, for relatively lower energy heavy-ion collisions, the hot nucleonic system formed in the collisions may undergo transition to nucleonic superfluid phase as it expands and cools. This will again lead to the formation of nucleonic superfluid vortices via the Kibble mechanism. Note, these are precisely the same vortices which are believed to play crucial role in pulsar glitches, though there they form due to rotation of the neutron star. As we will discuss later, universality of defect formation in the Kibble mechanism tells that defect density of order one will be produced per correlation domain [4]. (For a second order transition, critical slowing down can affect defect formation in important ways, and is described by the Kibble-Zurek mechanism [2].)

It is immediately obvious that the most dramatic effect of presence of any vortices will be on the resulting flow pattern. We carry out detailed simulations of development of flow in the presence of vortices and study qualitative changes in the flow pattern.

9.2 Kibble mechanism, vortex formation and local linear momentum conservation

We briefly recall the basic physics of the Kibble mechanism which originates from the formation of a sort of domain structure during a phase transition. The order parameter field (superfluid condensate in this case) is correlated (hence can be approximately taken to be uniform) inside a domain while it varies randomly from one domain to another. Such a picture of domains is very natural for a first order transition via bubble nucleation with each bubble being an independent domain. Even for a second order transition, correlation length size regions correspond to such domains. For a superfluid transition, the phase of the order parameter varies randomly from one domain to another (the magnitude of the order parameter being fixed by the temperature). As the gradient of the phase directly correspond to superfluid velocity, spontaneous generation of flow is inevitable in a phase transition. Further, at the junction of several domains one can find non-zero circulation of flow if the order parameter phase winds non-trivially around the junction. These are superfluid vortices. This picture of formation of vortices is actually very general and applies to the formation of all types of topological defects in symmetry breaking transitions.

However, spontaneous formation of superfluid vortices via Kibble mechanism in a transition from normal to superfluid phase has certain non-trivial aspects which are not present in the formation of other types of topological defects. During phase transition, the spontaneous generation of flow of the superfluid, as mentioned above, is not allowed by local linear momentum conservation. Basically, some fraction of atoms (e.g. ^{4}He atoms) form the superfluid condensate during the transition and develop momentum due to the non-zero gradient of the phase of the condensate. The only possibility is that the remaining fraction of atoms (which form the normal component of fluid in the two-fluid picture) develop opposite linear momentum so that the momentum is locally conserved. This means that even though order parameter phase gradients are present across different domains generating superfluid flow across different domain junctions, there is no net momentum flow anywhere in the beginning. Note, this argument is somewhat different from the conventional argument of angular momentum conservation for Kibble superfluid vortices where one knows that spontaneous generation of net rotation of the superfluid has to be counter balanced by the opposite rotation of the vessel containing the superfluid. Here, we are arguing for local linear momentum conservation.

The immediate implication of this local linear momentum conservation is that the initial velocity profile for the normal fluid around each vortex formed via the Kibble mechanism should be exactly the same as the velocity profile of the superfluid velocity profile (as determined by the local momentum conservation at the time of vortex formation, depending on relative fraction of the normal fluid and the superfluid). The momentum balance is being achieved locally here, simply by the normal component of fluid recoiling to balance the local momentum generated for the superfluid component. So, basically, some particles fall into a quantum state with non-zero momentum, which, for an isolated system, is only possible when other particles in that part of the system develop equal and opposite momentum. The final picture is then that, spontaneous generation of vortex via the Kibble mechanism leading to superfluid circulation in such a system will be accompanied by opposite circulation being generated in the normal component of the fluid (to balance the momentum conservation).

We mention here an important implication of the above discussion. In standard application of the Kibble mechanism for superfluid ^{4}He transition one expects a dense network of superfluid vortices which should be detectable in experiments. However, above arguments show that at the time of formation, superflow and normal flow have opposite flows, so experimental detection may become very complicated. As normal flow will be expected to change in time due to viscous effects one may expect easier detection at later times. However, the vortex network itself evolves and coarsens rapidly in time, thus complicating inference regarding Kibble estimate of vortex formation. In conclusion, counter balancing normal fluid flow which necessarily arises in Kibble mechanism must be accounted for when comparing theoretical predictions with data. We plan to carry out a detailed investigation of this issue in a future work.

9.3 Hydrodynamical simulation of flow fluctuations with vortices

We will first focus on superfluid transitions in the high baryon density partonic phase of QCD and later comment on the possibility of low baryon density nucleonic superfluid phase transition. We carry out hydrodynamical simulations of the evolution of a partonic system in the presence of vortices using a two-fluid picture of superfluid. We also consider a range of values for the density fraction of superfluid to normal fluid and study its effect on the signals. The two fluids are evolved, as in our earlier simulations [11], with Woods-Saxon profile of energy density with and without additional density fluctuations (though it does not appear to have crucial effects on our results). It is known that various high baryon density partonic phases (QGP, 2SC, CFL etc.) do not differ much in energy density and pressure [5]. Thus, we evolve the superfluid component with the same equation of state as the normal fluid, which is taken simply to be an ideal gas of quarks and gluons at temperature T and quark chemical potential μ_q with the energy density ϵ given as (for two light flavors) [12],

$$\epsilon = \frac{6}{\pi^2}\left(\frac{7\pi^4}{60}T^4 + \frac{\pi^2}{2}T^2\mu_q^2 + \frac{1}{4}\mu_q^4\right) + \frac{8\pi^2}{15}T^4, \tag{9.1}$$

with pressure $P = \epsilon/3$. Note, as our interest is only in discussing the hydrodynamics in the partonic phase (and not in the quark-hadron transition), we do not include the bag constant. The energy-momentum tensor is taken to have the perfect fluid form,

$$T^{\mu\nu} = (\epsilon + P)u^\mu u^\nu - Pg^{\mu\nu}, \tag{9.2}$$

where u^μ is the fluid four-velocity. The hydrodynamical evolution is carried out using the equations, $\partial_\mu T^{\mu\nu} = 0$. Note that we do not need to use conservation equation for the baryon current as our interest is only in flow pattern requiring knowledge of ϵ and P and the ideal gas equation of state relating P and ϵ does not involve μ_q. The simulation is carried out using a 3+1 dimensional code with leapfrog algorithm of 2nd order accuracy. For various simulation details we refer to the earlier work [11]. The initial energy density profile for both fluid components (normal fluid as well as superfluid) is taken as a Woods-Saxon background of radius 3.0 fm with skin width of 0.3 fm (with appropriate fractions of energy density). We take the initial central energy density ϵ_0 with temperature $T_0 = 25$ MeV and $\mu_q = 500$ MeV as representative values [5]. Initial random fluctuations are incorporated in terms of 10 randomly placed Gaussian of half-width 0.8 fm, added to the background energy density, with central amplitude taken to be $0.4\epsilon_0$.

The initial velocity profile is determined by the fluid rotation around the vortices. For the superfluid part, The magnitude of the fluid rotational velocity at distance r from the vortex center is taken as

$$v(r) = v_0 \frac{r}{\xi} \quad (r \leq \xi); \qquad v(r) = v_0 \frac{\xi}{r} \quad (r > \xi). \tag{9.3}$$

Here ξ is the coherence length. For CFL vortex, estimates in ref. [6] give $v_0 = 1/(2\mu_q \xi)$ and the coherence length is given by

$$\xi \simeq 0.26 \left(\frac{100\text{MeV}}{T_c} \right) \left(1 - \frac{T}{T_c} \right)^{-1/2} \quad \text{fm}. \tag{9.4}$$

As we mentioned above, exactly at the time of formation of the vortex, the velocity profile of the normal component will be opposite, having exactly the same form as that of the superfluid vortex, but with a magnitude appropriate for the fraction of the normal fluid. So, for the normal fluid, the initial velocity profile is taken to be exactly the same as given by Eqn.(9.3), but with v_0 having opposite sign, and suitably scaled for local momentum conservation depending on superfluid density fraction. This will remain as correct profile if the normal fluid has very low viscosity (note, QGP at RHIC energies has low viscosity). However, if the viscosity is significant, then this velocity profile will not be sustained due to differential rotation, and will change in time. We have accounted for this possibility also by considering admixture of velocity profile for viscous fluid with a velocity profile $v(r) \propto r$ at different times (even though we use inviscid hydrodynamics). We find that this does not affect the qualitative features of our results at all, except that with large fraction of this viscous velocity profile one also gets a non-zero directed flow in the presence of vortices.

We take value of superfluid transition temperature $T_c = 50$ MeV [6]. For the initial central temperature $T_0 = 25$ MeV, resulting values of $\xi = 0.7$ fm and $v_0 = 0.3$ (we take $c = 1$). (Note, even though we use 2-flavor equation of state, we use the estimates of the vortex velocity profile for the CFL phase for order of magnitude estimates.)

Formation of vortices in superfluid transition will be in accordance with the Kibble mechanism as we discussed above. We will not actually simulate the Kibble mechanism here as our interest is not in getting a statistical network of defects. Rather, we want to see effect of a couple of vortices on the resulting flow pattern. As we will see below, for the size of QGP region expected here, the number of superfluid vortices expected here is of order 1. We do not simulate coupled dynamics of normal and superfluid components. Instead, we evolve the two components using separate conservation equations for the two energy momentum tensors. This allows us to simulate a delayed superfluid transition. This models the situation when initial partonic system has too high a temperature (but with appropriate baryon density) to be in the superfluid phase, though it is still in the QGP phase, and subsequent expansion and cooling leads to crossing the phase boundary to the superfluid phase. Also, for the case of nucleon superfluidity (to be discussed below), initial high temperatures will lead to normal nucleonic phase, and only at late stages of expansion superfluid phase may arise. In a coupled fluid dynamics, this cannot be achieved as one always has a normal fluid as well as a superfluid component.

For observational signatures, we focus on the power spectrum of flow fluctuations. In a series of papers some of us have demonstrated that just like the power spectrum of CMBR, in HIC also the power spectrum of flow fluctuations has valuable information about the initial state fluctuations of the plasma [13, 14]. We will calculate the power spectrum of flow fluctuations and study the information contained in the power spectrum about the initial vortex induced velocity fields. We focus on the central rapidity region (focusing on a thin slab of width 2 fm in z direction at z = 0) and study the angular anisotropy of the fractional fluctuation in the transverse fluid momentum, $\delta p(\phi)/p_{av}$, where ϕ is the azimuthal angle, p_{av} is the angular average of the transverse fluid momentum, and $\delta p(\phi) = p(\phi) - p_{av}$. This fluid momentum anisotropy is eventually observed as momentum anisotropy of the hadrons which are finally detected. The power spectrum of flow fluctuations is obtained by calculating the root mean square values v_n^{rms} of the n_{th} Fourier coefficient v_n of the momentum anisotropy $\delta p(\phi)/p_{av}$. We use lab fixed coordinates, so event averaged value of v_n is zero.

We use standard Kibble mechanism, as described above, to estimate the probability of vortex formation. In the CFL phase, superfluidity corresponds to spontaneous breaking of U(1) symmetry (just like the case for superfluid ^{4}He, though for ^{4}He case U(1) is completely broken while for the CFL phase, U(1) breaks to Z_2). In two space dimensions, this leads to probability 1/4 for the formation of a vortex (V) or antivortex (AV) per correlation domain [4]. For the azimuthal momentum anisotropy in the central rapidity region, the relevant velocity field is essentially two-dimensional. With the correlation length of order 1 fm, and the plasma region which we are taking to have a radius of 3 fm, we expect number of superfluid vortices to be about 2. For definiteness, we will consider cases of 1 vortex, and a V-V pair and a V-AV pair. The locations of these are taken to be randomly distributed in the plasma region. To have clear signals, we have taken definite orientations for the vortices. We consider vortices either pointing along z axis (with random locations) or pointing along x axis (passing through the origin).

9.4 Results of the simulation

We now present results of the simulations. Fig. 9.1 shows the effect of vortices on the flow power spectrum for a central collision at $\tau - \tau_0 = 1.68$ fm, (with $\tau_0 = 1.0$ fm). We mention that with our numerical code, fluid evolution becomes unstable for large times, especially in with complex flow pattern with high velocities, hence we show the results at relatively shorter times. However, these qualitative signals will be expected to survive even for longer times, though with possibly smaller magnitudes. As such these will apply to situations of early freezeout, e.g. for smaller nuclei, or for peripheral collisions. Fig. 9.1 shows plots of v_n^{rms} for the cases of no vortex, one vortex, a V-V pair, and a V-AV pair. In all cases, vortices are taken along the z axis with random positions. Noteworthy is a large value of the elliptic flow for the V-AV case (even though this is a central collision). For all cases with vortices we find that the elliptic flow is very large initially (see, also, Fig. 9.2). This is clearly seen in the inset of Fig. 9.1 for the V-AV case which also shows the dependence of elliptic flow on superfluid fraction and its time evolution. This can be detected by its effects on photon or dilepton elliptic flow [15] which is sensitive to flow effects at very early stages.

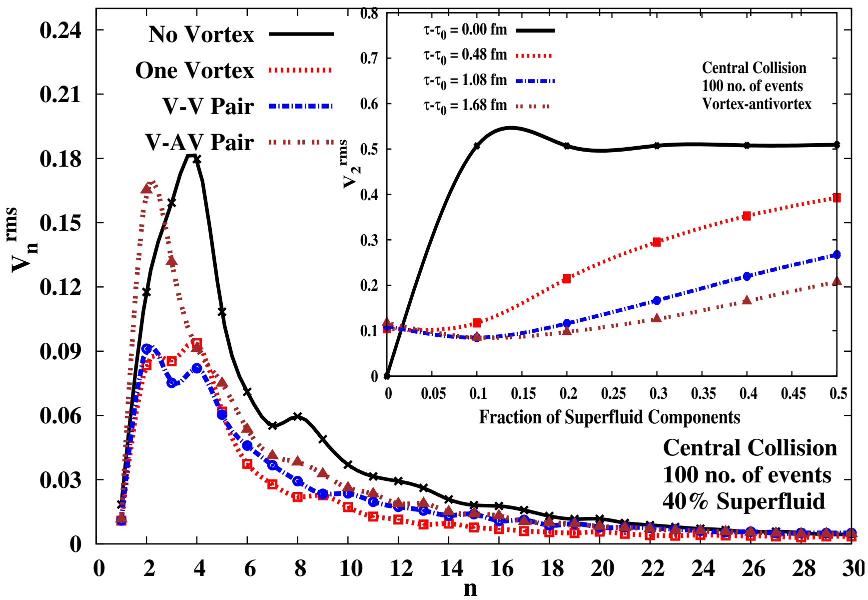

Figure 9.1: Power spectrum at $\tau - \tau_0 = 1.68$ fm for central collision. Different plots show the power spectrum for the cases of no vortex, single vortex, a V-V pair, and a V-AV pair. Inset shows dependence of elliptic flow at different times on the superfluid fraction for the V-AV case showing very large initial elliptic flow.

Fig. 9.2 shows the time evolution of the power spectrum for the case with a V-V pair (we find similar results for V-AV case as well). Note difference in the power for even and odd Fourier coefficients at earlier times. (Such a qualitatively different pattern in HIC has only been predicted in the presence of strong magnetic field, as reported in ref. [16]). This result also has interesting implications for the CMBR power spectrum. It is known that low l modes of CMBR power spectrum also show difference in even-odd modes [17]. It is possible that this feature may be indicative of the presence of a magnetic field, or presence of some vorticity during the very early stages of the inflation.

Fig. 9.3 presents the case of non-central collisions. Here we consider an ellipsoidal shape for the plasma region as appropriate for a non-central collision with semi-minor axis along the x-axis, and initial spatial eccentricity = 0.6. Here we plot v_2 for a single event (not the rms value), for two cases, a V-AV pair pointing in z direction and located on the x-axis at $x = \pm 1.5 fm$ respectively, and the other case with a

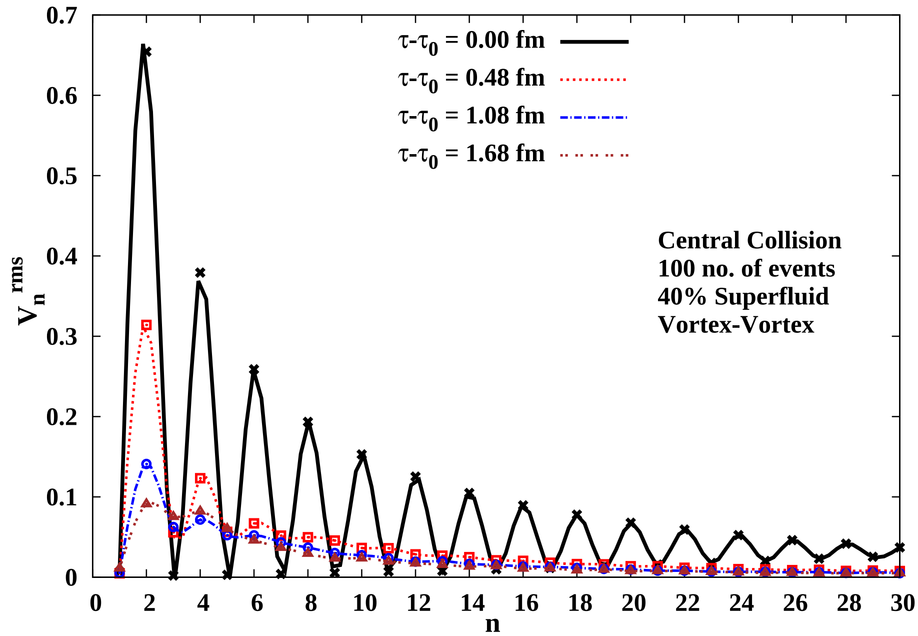

Figure 9.2: Time evolution of the power spectrum for the case with a V-V pair showing the difference in the power for even and odd Fourier coefficients for early times.

single vortex lying along the x-axis. Both cases show strongly negative elliptic flow at initial stages. Fig. 9.3 also shows large (negative) values of v_4 for both these cases which arises from vortex induced elliptic flow being in the orthogonal direction to the shape induced elliptic flow. These large values of negative elliptic flow as well as v_4 may be observed if the freezeout occurs at early times (in smaller systems, or in peripheral collisions) and should also leave imprints on other observables such as on v_2 for photons [15]. Note that negative elliptic flow can arise in relatively low energy HIC due to squeeze-out effects [18]. However, for low energy collisions (as we discuss below for nucleonic superfluidity), a vortex induced negative elliptic flow is completely uncorrelated to the elliptic shape of the event (which can be inferred from independent observables), hence can be distinguished from the squeeze-out effect. Further, at higher energies (where CFL phase may be expect to arise), no squeeze-out is expected, so a negative elliptic flow can signal vortex formation.

We have also carried out all the simulations with a delay of up to 1 fm in the onset of superfluid transition (following our modeling of the two fluid picture as explained above). The results remain essentially unchanged with various plots showing changes of order only few percent.

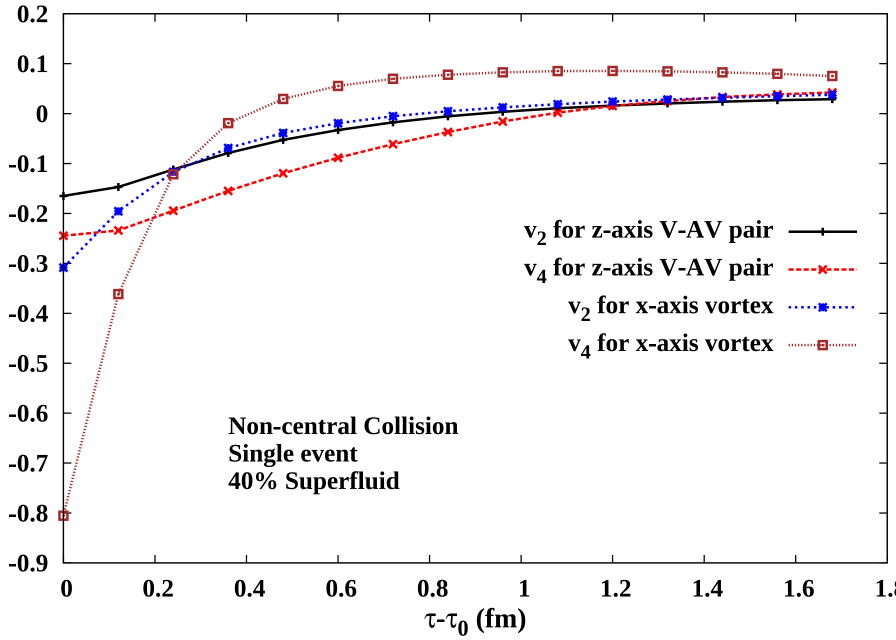

Figure 9.3: Plot of v_2 and v_4 for non-central collisions for a V-AV pair along z axis, and a single vortex along the x axis, showing negative elliptic flow at initial stages as well as large (negative) values of v_4.

9.5 Nucleonic superfluidity for low energy collisions

We now discuss the possibility of detecting nucleonic superfluidity in HIC. Though neutron superfluid condensate is expected to exist inside several nuclei, these systems are typically too small to demonstrate bulk superfluid phase and its associated superfluid vortices, as are expected inside a neutron star. Calculations for neutron stars show that nucleonic superfluidity is expected in range of densities from $10^{-3}\rho_0$ (for $^1S_0$ pairing of neutrons) to few times ρ_0 (for $^3P_2 -^3 F_2$ pairing). The critical temperature can range from 0.2 MeV to 5 MeV (depending on the nuclear potential used [19, 20]). Temperatures and densities of this order are easily reached in HIC at relatively low energies. For example, at the FOPI-facility at GSI Darmstadt, temperatures of about 17 MeV (with $\rho \sim 0.4\rho_0$) were reported in Au-Au collisions at

150 MeV/nucleon lab energy [21]. Temperatures of order 4-5 MeV were reported in Au-Au collisions at E/A = 50 MeV, at heavy-ion synchrotron SIS [22]. Thus temperatures/densities appropriate for the transition to the nucleonic superfluid phase can easily be reached in HIC. Universality of defect formation implies that the qualitative aspects of our results in this paper (for the CFL phase) will continue to hold even in this lower density regime. FAIR and NICA are ideal facilities for probing even this low energy regime with detectors suitable for measurements with which flow power spectrum analysis can be performed. Detection of signals as discussed in this paper can provide a clean detection of nucleonic superfluid vortices. It is worth emphasizing the importance of focused experiments for creating a nucleonic system of several fm size which can accommodate nucleonic superfluid vortices. Direct experimental evidence of these vortices and controlled studies of their properties can provide a firm basis for our understanding of neutron stars. This is all the more important in view of the fact that gravitational waves from rotating neutron stars and their collisions will be thoroughly probed by LIGO and upcoming gravitational wave detectors.

UrQMD Analysis for possibility of Neutron Superfluidity in low energy Heavy-ion Collisions

Ultra-relativistic quantum molecular dynamics model (UrQMD) [24, 25] is a microscopic description of relativistic heavy-ion collisions (HIC), which uses N-body transport theory and evolves the system from initial stage to freeze-out time in $8N$-dimensional phase space, where $6N$ degrees of freedom corresponds to configuration- and momentum-space and rest $2N$, time and energy of each particles. Two-body elastic and inelastic collisions, and many-body resonance decay are ingredients for changing momenta and particles species in this model. UrQMD is applicable from several MeV to several TeV per nucleon laboratory energies. At low energies ($\sqrt{s} < 5$ GeV) it deals with phenomenology of hadronic interactions by considering hadrons, their excited states and resonances. At higher energies ($\sqrt{s} > 5$ GeV) it incorporates string mechanism for hadronic interaction, string excitation and its subsequent fragmentation into multiple hadrons.

We use urqmd-3.3p2 model [24] to generate 10000 events at different times for $^{238}_{92}\mathbf{U}$-$^{238}_{92}\mathbf{U}$ central collisions with lab. energy 50A MeV. In our simulations, we have ignored the deformation of Uranium nuclei, and considered it as a spherical nuclei. For our simulations, we have considered such a low energy and heavy nuclei because we are looking for the possibility of neutron superfluidity in the overlap region where plasma forms, and to have neutron suerfluidity baryon density must be higher than 0.16×10^{-3} fm^{-3} and temperature must be lower than few MeV (transition temperature is model dependent), which only can be possible by colliding a neutron rich nuclei with low energy.

We start our analysis from time 20 fm by considering only nucleons (only protons & neutrons) (because we are interested in the temperature and density of nucleon system). For the fluid description of the system, one should have at least local thermodynamic equilibrium (LTE). To check LTE, usually one takes, either cubical or spherical cell around the center of the system. Firstly, to check equilibrium, we consider cubical cell of volume $4\times4\times4$ fm^3 centered around the center of mass of the system (i.e. at the origin). We follow the same procedure for checking equilibrium in the cell as followed in Ref. [25]. First, we check whether velocity distributions $\frac{dN}{dv_i}$ (vs. v_i), follow Maxwell-Boltzman (MB) velocity distribution, $\exp(-m_N v_i^2/2T)$, and overlap with each other or not. If these distributions overlap with each other, i.e. if momentum is isotropic, then LTE can be possible in this cell. Here dN is the number of nucleons in the velocity bin dv_i, where v_i is the velocity of individual nucleons in $i \equiv (x, y, z)$ direction, m_N is mass of nucleons, T is the temperature of the cell. We find that in this cell, 20 fm time is too short to achieve LTE. At this time, transverse and longitudinal MB velocity distributions do not overlap with each other (even, longitudinal velocity distribution does not follow MB distribution at this time), see Fig. 9.4. Full equilibrium is achieved in a cubical cell of volume $6\times6\times6$ fm^3 at 150 fm time, where all velocity components completely overlap with each other and follow MB velocity distribution, see Fig. 9.4. We get, on an average, 7.5 nucleons inside the cell, which gives the nucleon density about 3.5×10^{-2} fm^{-3} which is more than 200 times larger than the required density to have neutron superfluidity (note that we have only considered protons and neutrons, consideration of other baryons will give even more baryon density).

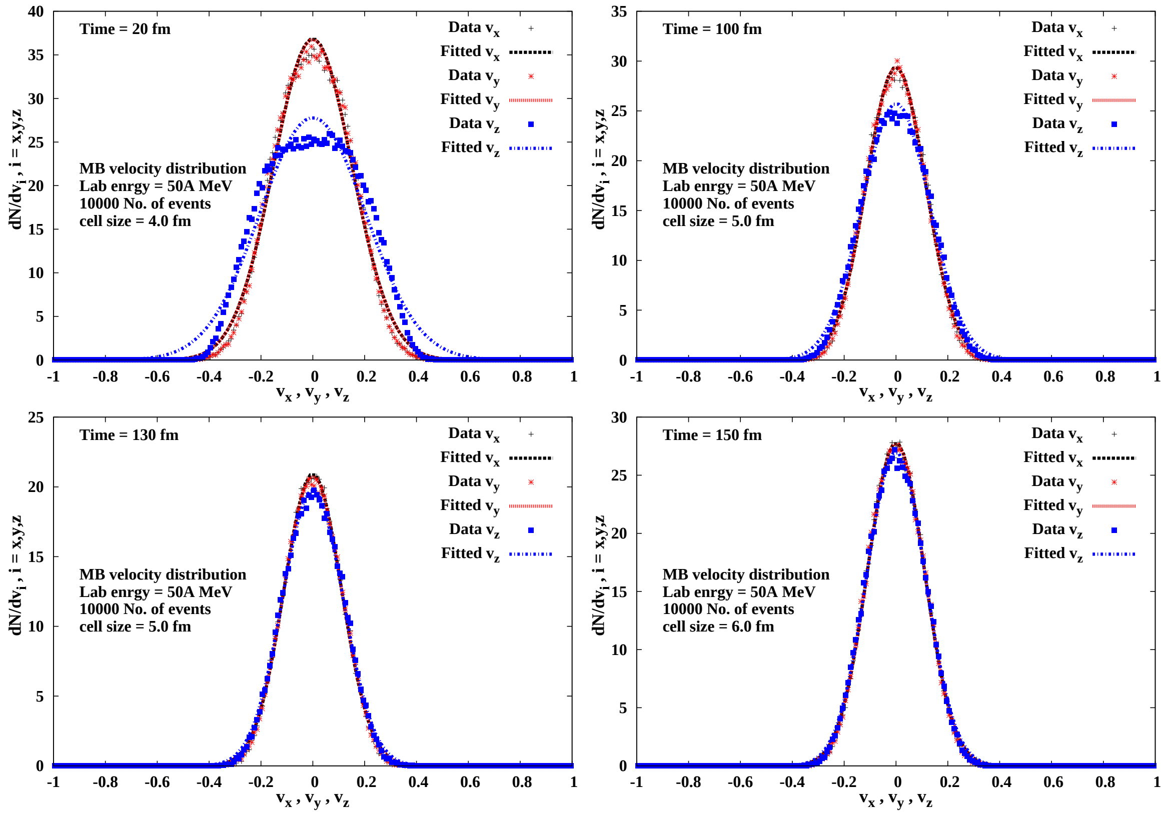

Figure 9.4: Figures show velocity distribution of all three components of velocity of nucleons (protons and neutrons) at different times. At $t = 150$ fm we see the complete overlap of velocity distribution which indicates that, in the cubical cell of 6 fm size, local thermodynamic equilibrium is possible.

At 150 fm time, in this cell, the momentum spectrum of nucleons, i.e. $\frac{dN}{d^3p}$ vs. $(E-m)$, follows Fermi-Dirac distribution (may be fitted with the Boltzman distribution also),

$$\frac{dN}{d^3p} = \frac{1}{4\pi}\frac{dN}{pEdE} = \frac{a}{\exp(\frac{E-\mu_B}{T})+1}, \tag{9.5}$$

where μ_B is the baryon chemical potential. By fitting, we obtain the temperature of the cell to be about 9.7 MeV. This indicates the presence of thermodynamic equilibrium in the cell, see Fig. 9.5.

Although the temperature of the cell is higher than the required temperature to have neutron superfluidity, but it is not much higher and gives a hint that in the heavy-ion collision experiments it might be possible that one can achieve the appropriate condition to have neutron superfluidity. The detailed analysis for such

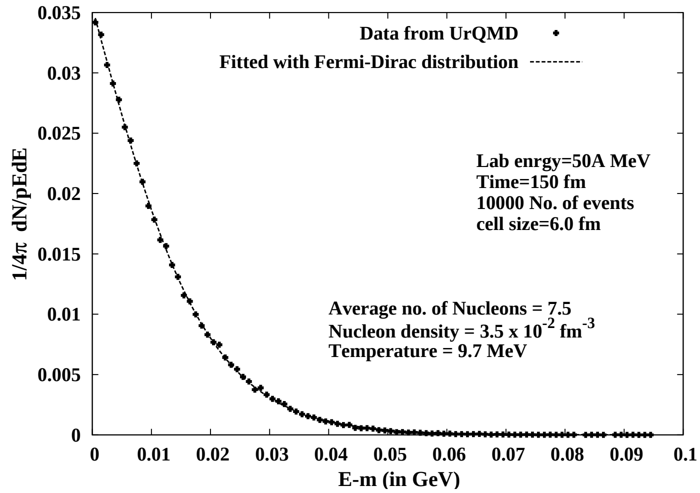

Figure 9.5: Figure shows particle momentum distribution, $\frac{dN}{d^3p}$ vs. $(E-m)$ at time 150 fm in the 6 fm cell. We have fitted it with the Fermi-Dirac distribution function (though it may be fitted with the Boltzman distribution function). By fitting we obtain the temperature of the cell to be about 9.7 MeV.

situation is under investigation which we will present it in future.

9.6 Conclusions

We conclude by pointing out the importance of searching for the superfluid vortices during transition to high baryon density QCD phases, or to nucleonic superfluid phase, at FAIR and NICA. Due to universal features of vortex (topological defect) formation, these vortices directly probe the symmetry breaking pattern of the phase transition providing very useful information about the QCD phase diagram. Various high density phases of QCD such as CFL phase etc. are associated with definite symmetry breaking patterns leading to different topological defects. Detection of defects thus directly probes precise nature of symmetry breaking transition occurring in the system. In this sense, this technique has advantage over other observational signatures which depend on equation of state etc. as those quantities can be strongly model dependent (in contrast to the symmetry patterns which are the most universal features of any phase transition). In this context we mention that there has been study of stability of CFL vortices etc. and it is found that for certain parameter range these vortices may be unstable [23]. Even for the unstable case, typical decay time for the vortices will be expected to be at least of order few fm which, though very short time for astrophysical relevance, should be long enough time for these vortices to leave their observational signature in heavy-ion collisions.

It is hard to overemphasize the importance of detecting nucleonic superfluid phase and associated vortices in these experiments which have capability of providing a controlled experimental investigation of the properties of these vortices and associated phases. Till date, there is no direct experimental observation of nucleonic superfluid vortices, though they provide probably the most accurate explanations of pulsar glitches. Thus detection of these in laboratory experiments will strengthen our understanding of pulsar dynamics. The signals we have discussed show qualitatively new features in flow anisotropies signaling the presence of vortices and the underlying superfluid phase in the evolving plasma. These qualitative features are expected to be almost model independent, solely arising from the vortex velocity fields. We mention that one has to properly account for the effects due to jets, resonance decays etc. to properly account for genuine hydrodynamic flow fluctuations. We hope to address these issues in a future work. Also, we have not included error bars in our plots to avoid overcrowding of the plots. The number of events was chosen suitably large (100 events) so that the main qualitative features of the plot are above any statistical fluctuations. (Our focus is mainly on the qualitative patterns of the plots, in the spirit of the universal features of topological vortices forming at varying energy scales, and not on precise numerical value.) As we mentioned, due to universality of defect formation, similar signals are expected from nucleonic superfluid vortices which can arise in low energy HIC providing direct experimental access to the physics of pulsars.

In our UrQMD analysis we obtain the nucleon density more than 200 times larger than the required baryon density, and the temperature of such system comes out to be 9.7 MeV which is not much higher than that required to have neutron superfluidity. It gives a good hint about the possibility of neutron superfluidity in the low energy heavy-ion collision experiments. More dedicated and appropriate analysis may give even lower temperature which can reveal the possibility to have neutron superfluidity in heavy-ion collisions.

Bibliography

[1] Arpan Das, Shreyansh S. Dave, Somnath De, and Ajit M. Srivastava, Mod. Phys. Lett. A **32**, 1750170 (2017), arXiv: 1607.00480.

[2] W.H. Zurek, Phys. Rep. **276**, 177 (1996).

[3] See, for example, special section on condensed matter analogues of cosmology, J. Phys. **G 25** (2013).

[4] T.W.B. Kibble, J. Phys. **A 9**, 1387 (1976).

[5] M.G. Alford, A. Schmitt, K. Rajagopal, and T. Schafer, Rev. Mod. Phys. **80**, 1455 (2008).

[6] K. Iida and G. Baym, Phys. Rev. **D 66**, 014015 (2002).

[7] J.M. Lattimer and M. Prakash, Astrophys. J. **550**, 426 (2001).

[8] P. Bagchi, A. Das, B. Layek, and A.M. Srivastava, Phys. Lett. **B 747**, 120 (2015).

[9] P. Bagchi, A. Das, B. Layek, and A.M. Srivastava, arXiv: 1412.4279.

[10] M.M. Forbes and A.R. Zhitnitsky, Phys. Rev. **D 65**, 085009 (2002).

[11] Saumia P.S. and A.M. Srivastava, Mod. Phys. Lett. A 31, 1650197 (2016).

[12] J. Cleymans, R.V. Gavai, and E. Suhonen, Phys. Rep. **130**, 217 (1986).

[13] A. P. Mishra, R. K. Mohapatra, P. S. Saumia, and A. M. Srivastava, Phys. Rev. **C 77**, 064902 (2008).

[14] A. P. Mishra, R. K. Mohapatra, P. S. Saumia, and A. M. Srivastava, Phys. Rev. **C 81**, 034903 (2010).

[15] R. Chatterjee and D. K. Srivastava, Nucl.Phys. **A 830**, 503C (2009).

[16] Arpan Das, Shreyansh S. Dave, P.S. Saumia, and Ajit M. Srivastava, Phys. Rev. C. **96**, 034902 (2017), arXiv: 1703.08162.

[17] P. K. Aluri and P. Jain, Mon. Not. Roy. Astron. Soc. **419**, 3378 (2012).

[18] A. Andronic, FOPI Collaboration, Phys. Lett. **B 612**, 173 (2005).

[19] L. Amundsen and E.Ostgaard, Nucl. Phys. **A 442**, 163 (1985).

[20] L. Amundsen and E.Ostgaard, Nucl. Phys. **A 437**, 487 (1985).

[21] W. Reisdorf, et al., Nucl. Phys. **A 612**, 493 (1997).

[22] V. Serfling et al., Phys. Rev. Lett. **80**, 3928 (1998).

[23] M.G. Alford, S.K. Mallavarapu, T. Vachaspati, A. Windisch, Phys.Rev. **C93**, 045801 (2016).

[24] S.A. Bass et al., Prog. Part. Nucl. Phys. **41**, 225 (1998); M. Bleicher et al., J. Phys. G **25**, 1859 (1999).

[25] L.V. Braivina et al., Phys. Lett. B **434**, 379 (1998).

Chapter 10

Magneto-hydrodynamic Simulations for Relativistic Heavy-ion Collisions

Very strong magnetic fields can arise in non-central heavy-ion collisions at ultrarelativistic energies, which may not decay quickly in a conducting plasma. We carry out relativistic magnetohydrodynamics (RMHD) simulations to study the effects of this magnetic field on the evolution of the plasma and on resulting flow fluctuations in the ideal RMHD limit. Our results show that magnetic field leads to enhancement in elliptic flow for small impact parameters while it suppresses it for large impact parameters (which may provide a signal for initial stage magnetic field). Interestingly, we find that magnetic field in localized regions can temporarily increase in time as evolving plasma energy density fluctuations lead to reorganization of magnetic flux. This can have important effects on chiral magnetic effect. Magnetic field has nontrivial effects on the power spectrum of flow fluctuations. For very strong magnetic field case one sees a pattern of even-odd difference in the power spectrum of flow coefficients arising from reflection symmetry about the magnetic field direction if initial state fluctuations are not dominant. We discuss the situation of nontrivial magnetic field configurations arising from collision of deformed nuclei and show that it can lead to anomalous elliptic flow. Special (crossed body-body) configurations of deformed nuclei collision can lead to presence of quadrupolar magnetic field which can have very important effects on the rapidity dependence of transverse expansion (similar to *beam focusing* from quadrupole fields in accelerators). Results discussed in this chapter have been presented in Ref. [1].

10.1 Introduction

Extensive efforts have focused on the discovery of the quark-gluon plasma (QGP) phase of QCD in relativistic heavy-ion collision experiments (RHICE). There is mounting evidence that QGP phase is created in these experiments. It is no more possible to explain the wealth of experimental data at RHIC and LHC without assuming a transient phase of QGP. While it is certainly desirable to have *smoking gun* signal for QGP, it is also an appropriate stage for the exploration of the rich spectrum of physics unfolded by the (most likely) presence of this transient stage of QGP in relativistic heavy-ion collisions. Search for exciting possibilities like the critical point in the QCD phase diagram, possible exotic high baryon density phases (in upcoming facilities FAIR and NICA) are some of these directions.

An entire new line of explorations has been initiated in recent years by the very exciting possibility that in relativistic heavy-ion collision experiments extremely high magnetic fields are expected to arise, especially in non-central collisions. During earliest stages, magnetic field in the plasma can be of order 10^{15} Tesla (few m_π^2), which is several orders of magnitude larger than the magnetic field even in magnetars. Such a strong magnetic field in QGP will lead to important effects. Much of the discussion in literature has focused on the exciting possibility of observing CP violation effects [2]. Relevant effects are generally known as *chiral magnetic effect* and more recently discussed *chiral vortical effect*. Along with such effects, there are many other important consequences of the magnetic field for QGP evolution. Some of us had earlier utilized the fact that an important effect of the presence of magnetic fields in the plasma will be to lead to variations in velocities of different types of waves in the plasma [4]. In particular the group velocity varies with the angle between the wave vector and the direction of the magnetic field. Its obvious effect will be to qualitatively modify the development of anisotropic flow. In ref. [4], it was argued that the flow coefficients can be significantly affected by these effects, in particular, the presence of magnetic field can lead to enhancement in the elliptic flow coefficient v_2 by almost 30%. As pointed out in ref. [4], it raises the interesting possibility of whether a larger value of η/s can be accommodated by RHIC data when these effects are incorporated using full magnetohydrodynamical simulations. This possibility can be viewed as either leading to the QGP η/s being higher than the AdS/CFT bound, or in the context of results in ref. [5] which suggested crossing the AdS/CFT bound, to restore the bound when proper effects of magnetic field are incorporated. The issue of magnetic field dependence of elliptic flow was discussed by Tuchin [6] (including viscous effects as well) with results in agreement with [4].

The arguments in ref. [4] utilized directional dependence of sound velocity in the presence of magnetic field and modeled its effect on development of elliptic flow. Those results were not based on any magnetohydrodynamical simulation. In this chapter, we have carried out detailed relativistic magnetohydrodynamics simulations. We indeed confirm the results in [4,6] that elliptic flow can increase in the presence of magnetic field. However, our results show that the dependence of v_2 on magnetic field is much more complex than assumed in these earlier works, with several factors at play. In certain situations (e.g. for small impact parameters) the magnetic field enhances the elliptic flow, while in a different situation (large impact parameter), magnetic field suppresses the elliptic flow. These underlying factors are important to understand (especially in view of other recent relativistic magnetohydrodynamics simulations [7] where it was found that magnetic field has no effect on elliptic flow, in contrast to the results in [4,6]). Along with the effect on elliptic flow, we will demonstrate several other important effects of magnetic field showing how flow evolution is qualitatively affected. These effects are important as they show that an understanding of flow pattern is not complete without including effects of magnetic field in the early stages of plasma evolution.

Another important reason to focus on different qualitative effects of magnetic field on flow evolution is that it can provide signal for the presence of strong magnetic field during early stages of the plasma evolution. It must be emphasized that although for the earliest stage of collision, magnetic field can be calculated with reasonably accurate approximations, its evolution even in immediately successive stages is poorly understood. All the important effects of the magnetic field, such as chiral magnetic effect as well as various effects on flow pattern as we have discussed here (and in [4,6]) require that reasonably strong magnetic field survives for at least several fm proper time. Earlier it was thought that magnetic field rapidly decays after the collision. It is strong for a very short time, essentially the passing time of the Lorentz contracted nuclei (~ 0.2 fm for RHIC energies). Subsequently it rapidly decays [3, 8]. In such a situation the effect of magnetic field on flow evolution as well effects such as chiral magnetic effect will be strongly suppressed as time scale for the development of flow and for charge separation (for latter effects) is several fm. Similar situation is expected at higher energies, e.g. at LHC.

It was later pointed out by Tuchin [9] that magnetic field does not decay very rapidly due to induced currents arising from rapidly decreasing external magnetic field. In fact, the magnetic field satisfies a diffusion equation with the diffusion constant equal to $1/(\sigma\mu)$ where μ is the magnetic permeability and σ is the electrical conductivity [10, 11]. With $\mu \sim 1$ and $\sigma \simeq 0.04T$ ($= 0.04$ fm^{-1} for T $\simeq$ 200 MeV) from refs. [12], one finds that the time scale τ over which the magnetic field remains reasonably strong [9] over length scale L is, $\tau \simeq L^2\sigma/4$. For $L = 6 - 10$ fm, we get τ less than 1 fm. Indeed, one sees that magnetic field decreases fast initially, though at later times matter effects become more important slowing down decrease of magnetic field significantly [13]. For higher temperatures σ will be larger increasing the value of τ. σ is also expected to increase due to the effects of magnetic field in the plasma [14], further increasing the value of τ.

Even if one takes this optimistic picture that due to non-zero conductivity of QGP, magnetic field doe not decay extremely rapidly, and may survive for significant time scales, the self-consistency of this picture can be questioned due to uncertainties of the initial non-equilibrium stages of the parton system. Initially there is no plasma, so no conductivity. If the parton system is assumed to have the QGP conductivity during its formation stages, question arises as to how magnetic field can penetrate the conducting plasma. For simplicity consider the plasma (say during early stage for less than 1 fm lab time) to be a thick disk of nuclear diameter and thickness of 1-2 fm. If the plasma was static then one could just consider the penetration depth $\delta \sim (\mu\sigma\omega)^{-1/2}$ where ω is the angular frequency of electromagnetic wave. Initial magnetic field, being a narrow pulse of time duration $t \simeq 0.2$ fm (typically the width of Lorentz contracted Nuclei, for RHIC energies), can be taken to have $\omega \simeq 30$ fm^{-1}. This gives the penetration depth of order 1 fm (note it was mistakenly written as 3 fm in ref. [4]). In such a situation, though magnetic field cannot penetrate from the perimeter of the disc (nuclear radius being about 6-7 fm), it may be able to penetrate significantly in the interior from the longitudinal direction (from both sides), with disk thickness being only about 1 fm. In such a situation, the picture of magnetic field diffusing through the entire region of the plasma with typical length scale of several fm, and lasting with a value close to the high initial peak values for time scales of several fm, may be self consistent.

However, the plasma is not static in the longitudinal direction. Far from it, the plasma is relativistically expanding in the longitudinal direction. The above argument of penetration depth cannot be applied to a conducting plasma which is relativistically expanding. The conclusion being that if the plasma is taken to be conducting from the very beginning, we do not know how much fraction of the original magnetic field penetrates the plasma. Only that fraction can then be assumed to follow the diffusion equation as in ref. [9] and survive for few fm time scale. A proper treatment of the problem will require treatment of the early parton system as a non-equilibrium system, whose response to ambient magnetic field then needs to be estimated. As the plasma equilibrates, it will develop conductivity as appropriate for the QGP phase, and one needs to determine how much magnetic field is trapped in the conducting plasma. Its subsequent evolution then can be followed as in ref. [9].

Having stated all these issues, we will take a simple path. We will assume, for simplicity, that strong magnetic field exists inside the plasma. The strength of magnetic field will be estimated close to its peak value, and will be assumed to survive in the plasma for the duration of evolution we carry out evolving according to the equations of relativistic magnetohydrodynamics (RMHD). We assume ideal RMHD with infinite conductivity, so magnetic field lines are frozen in the plasma. Due to our computer limitations (for our 3+1 dimensional simulations), we are only able to consider small lattice, hence evolve for short times up to about 3 fm (to avoid boundary effects). This being a rather short time, our assumption of ideal MHD may not be very inappropriate. Our focus in the chapter is mainly on the qualitative aspects of results, and not on actual numbers. We are not claiming to give numbers which can be compared to the experimental data. Rather we demonstrate qualitative patterns of flow evolution, which one can look for in the experiments. Primary emphasis being on these being signals of the presence of strong magnetic field during early stages of plasma evolution.

The chapter is organized in the following manner. In Sec.II, we briefly review the formalism we have adopted for the relativistic MHD simulation from ref. [15]. Sec.III presents details of our numerical simulation. In Sec.IV we first discuss the issue of effect of magnetic field on elliptic flow (in view of conflicting conclusions in [4, 6, 7]). Sec.V presents results of the simulations which show that magnetic field can lead to qualitatively new effects. Sec.VI presents conclusions and discussions.

10.2 The Formalism

We here provide a brief summary of the formalism we have followed for our relativistic magnetohydrodynamical (RMHD) simulations. For this we have followed ref. [15] and for the benefit of the reader we provide essential steps from that ref. in the following. We will be assuming zero baryon chemical potential situation so there will not be any baryon number conservation equation. Equations for ideal RMHD for the evolution of fluid and magnetic field are as follows.

Conservation of total energy momentum tensor (for QGP as well as the magnetic field) is given by

$$\partial_\alpha[(\rho + p_g + |b|^2)u^\alpha u^\beta - b^\alpha b^\beta + (p_g + \frac{|b|^2}{2})\eta^{\alpha\beta}] = 0, \tag{10.1}$$

where we have used perfect fluid form for the QGP energy-momentum tensor,

$$T^{\mu\nu} = (\rho + p_g)u^\mu u^\nu + p_g\eta^{\mu\nu}. \tag{10.2}$$

Maxwell's equations are

$$\partial_\alpha(u^\alpha b^\beta - b^\alpha u^\beta) = 0. \tag{10.3}$$

Here ρ and p_g are the energy density and pressure of QGP which we assume to be related by an ideal gas equation of state, $p_g = \frac{\rho}{3}$. u^α is the four-velocity with

$u^\alpha u_\alpha = -1$. Four-vector b^α is related to the magnetic field $\vec{B}$ as,

$$b^\alpha = \gamma[\vec{v}.\vec{B}, \frac{\vec{B}}{\gamma^2} + \vec{v}(\vec{v}.\vec{B})]. \tag{10.4}$$

γ is the Lorentz factor for velocity $\vec{v}$ and we have following normalizations

$$u^\alpha b_\alpha = 0, \text{ and } |b|^2 \equiv b^\alpha b_\alpha = \frac{|\vec{B}|^2}{\gamma^2} + (\vec{v}.\vec{B})^2. \tag{10.5}$$

For numerical simulation, the above equations are cast in the following form

$$\frac{\partial U}{\partial t} + \sum_k \frac{\partial F^k}{\partial x^k} = 0. \tag{10.6}$$

This is the evolution equation for the vector U where

$$U = (m_x, m_y, m_z, B_x, B_y, B_z, E), \tag{10.7}$$

where

$$m_k = [\rho h \gamma^2 + |\vec{B}|^2] v_k - (\vec{v}.\vec{B}) B_k, \tag{10.8}$$

and

$$E = \rho h \gamma^2 - p_g + \frac{|\vec{B}|^2}{2} + \frac{v^2 |\vec{B}|^2 - (\vec{v}.\vec{B})^2}{2}. \tag{10.9}$$

h is the specific enthalpy ($4p_g/3$ with the ideal gas equation of state we are using for QGP) and F^k are the fluxes in Eqn.(10.6) along directions $x^k \equiv (x, y, z)$ given as follows.

$$F^x = \begin{pmatrix} m_x v_x - B_x \frac{b_x}{\gamma} + p \\ m_y v_x - B_x \frac{b_y}{\gamma} \\ m_z v_x - B_x \frac{b_z}{\gamma} \\ 0 \\ B_y v_x - B_x v_y \\ B_z v_x - B_x v_z \\ m_x \end{pmatrix}. \tag{10.10}$$

Similar expressions hold for F^y and F^z by appropriate replacement of indices. Here $p = p_g + \frac{|b|^2}{2}$ is the total pressure. Evolution is carried out using Eqn.(10.6) for the vector U from which the independent variables $(p_g, \vec{v}, \vec{B})$ have to be extracted. For this we define $W = \rho h \gamma^2$ and $S = \vec{m}.\vec{B}$. With this we can write,

$$E = W - p_g + (1 - \frac{1}{2\gamma^2})|\vec{B}|^2 - \frac{S^2}{2W^2}, \quad (10.11)$$

$$|m|^2 = (W + |\vec{B}|^2)^2(1 - \frac{1}{\gamma^2}) - \frac{S^2}{W^2}(2W + |\vec{B}|^2). \quad (10.12)$$

This equation is used to express γ as a function of W and known variables $\vec{m}$, $\vec{B}$, and hence S (from the knowledge of vector U).

$$\gamma = \left(1 - \frac{S^2(2W + |\vec{B}|^2) + |m|^2W^2}{(W + |\vec{B}|^2)^2W^2}\right)^{-1/2}. \quad (10.13)$$

With the ideal gas equation of state we have $p_g = \frac{W}{4\gamma^2}$. Eqn.(10.9) then can be entirely written in terms of unknown quantity W and other known quantities $\vec{B}$, S and E as follows

$$f(W) \equiv W - p_g + (1 - \frac{1}{2\gamma^2})|\vec{B}|^2 - \frac{S^2}{2W^2} - E = 0. \quad (10.14)$$

We solve this equation using Newton-Raphson method to get W using expressions for various derivatives as in ref. [15]. (Except for one derivative, we obtain dp_g/dW using the equation $p_g = \frac{W}{4\gamma^2}$ for our choice of equation of state. This expression differs from the expression in ref. [15].). From the value of W thus obtained, γ can be calculated using Eqn.(10.13). With this, we get value of p_g. Equation for m_k (Eqn.(10.8)) can then be used to obtain velocity components v_k. This completes the procedure of recovery of independent variables from time evolved vector U. For further details, we refer to ref. [15].

10.3 Details of Numerical Simulation

We have developed a 3+1 dimensional code and use lattice of size $200 \times 200 \times 200$ (and in some cases, for example for power spectrum for very strong magnetic field case, to get averages over several events we use smaller lattice $150 \times 150 \times 150$). For evolution we use leapfrog algorithm of 2nd order accuracy. Due to small size of the lattice (due to computer limitations) we are able to evolve only for times up to 3 fm to avoid boundary effects. In some cases we evolve for shorter times as we will mention for the respective cases.

Glauber like initial conditions are used for the initial energy density profile where a nucleus-nucleus collision is viewed as a sequence of independent binary nucleon-nucleon collisions [16]. The enhancement of v_2 is studied using smooth Glauber initial conditions in the X-Y plane. The parameters are tuned to an initial central temperature of 160 - 180 MeV assuming energy density of ideal gas of quarks and gluons for the two flavor case with zero chemical potential. A smooth Woods-Saxon profile is used along z-axis with extent equal to the extent of the colliding region along Y-axis. While studying the other effects like flux re-organisation, any possibility of vorticity generation, and the power spectrum, we use Glauber Monte Carlo initial conditions with parameters tuned to obtain the desired temperature range of 160 - 180 MeV. We distribute the energy density from the collision of participants along z-axis following a Gaussian distribution. As we mentioned above, ideal gas equation of state is used for QGP. We also add a constant background energy density of about 1% of the maximum initial energy density of the plasma, it gave better stability for the simulation, especially in the presence of fluctuations. (This energy density addition is not needed due to any instability of the program. Our algorithm of extracting the primitive variable does not work effectively when magnetic field energy density is much larger than the plasma density, as was noted in ref.6 also. Hence a non-zero energy density is used in the outer region. Such a small energy density should not affect any results strongly. Indeed, it is hard to argue that surroundings of the QGP region do not have some small energy density.) For some of the results, we have neglected fluctuations and have used Glauber optical initial conditions along the x-y plane. This is done so that one can isolate the effects of magnetic field on the specific features of plasma evolution. Fluctuations lead to magnetic flux rearrangement which makes evolution highly complex, as we will demonstrate in the section on results. So, in the presence of fluctuations it becomes hard to associate specific patterns of flow with the magnetic field. Certainly, for experimental comparison one will need to combine all the effects together, and make special efforts to identify specific regimes of collision energy, nuclear size, centrality etc. to enhance the effects due to magnetic field. When we present results we specify where fluctuations are included and where not.

For the initial configuration of magnetic field we have used several methods. For most of the results we use magnetic field produced by two oppositely moving uniformly charged spheres (representing colliding nuclei), in vacuum, with appropriate Lorentz gamma factor [11, 13]. This neglects modifications due to participants, but that is not expected to be very significant. This works fine with the range of magnetic fields expected in relativistic heavy-ion collisions, though we restrict our simulation to lower energy collisions about $\sqrt{s} = 20$ GeV. For most of the simulations below, the magnetic field profile is obtained in this manner. We typically give two sets of results, labeled by B_{time} which is the time at which the magnetic field profile is calculated after the collision. We use $B_{time} = 0.4$ fm and 0.6 fm. Smaller value gives larger value of the magnetic field, but may not be very realistic in view of finite conductivity of the plasma. If we use very large Lorentz gamma factor, then the magnetic field is sharply peaked at receding (Lorentz contracted) nuclei, and our 3+1 dimensional simulation is not able to run for reasonable times, especially in the presence of fluctuations. For some cases just to show some interesting effects (e.g. systematic difference in the power of even-odd flow coefficients) we needed to use very high magnetic fields (of order 15 m_π^2). Such large magnetic field are completely unrealistic here, and we use this value only to show how completely new effects may arise for very large magnetic field. The simulation with realistic magnetic field profile develops instabilities, primarily because in this case magnetic field energy density is much larger than the plasma density everywhere. Such difficulties have been noticed in other simulations as well [7] where it is mentioned that the numerical code was not able to handle configurations where the magnetic pressure is much larger than the thermal pressure, which typically is the case in regions outside the plasma region. To avoid these difficulties, for the large magnetic field case, we use a simpler profile for magnetic field where the profile in the (x-z) plane is chosen to be proportional to the energy density profile in the (x-z) plane at y = 0 obtained from the Glauber Monte Carlo like procedure as described above. z axis is the collision axis and the impact parameter is along the x axis, with resulting magnetic field pointing along the y axis. The peak value of the magnetic field is chosen by hand. The magnetic field is then taken to be constant along the y axis, as consistent with Gauss' law. Clearly this magnetic field profile is not realistic along the y axis, but is only used to illustrate special effects of magnetic field on plasma evolution. The possibility remains that large magnetic fields may not be very unrealistic for example for deformed nucleus case.

We mention here that for low energy collisions with $\sqrt{s} = 20$ GeV it is not appropriate to work with the simple zero chemical potential ideal relativistic gas equation of state which we have used. Also, at such low energies, chemical potential is sizeable and one cannot ignore baryon current. We use these approximations (simple equation of state and zero chemical potential) for simplicity, just as we have used ideal MHD equations for the evolution of the plasma. Our aim in this work is not to give definite numbers which can be compared with the experiments. Rather we look for basic physics for new effects. These qualitative patterns will not be expected to depend on the presence (or absence) of baryon current, or on the exact nature of the equation of state, though the numerical values will certainly depend on the factors. We thus expect that the qualitative patterns we find and the basic physics of new phenomena we discuss, will apply from low energy collisions (e.g. at FAIR and NICA) to high energy collisions at LHC.

As the simulation is carried out using (x,y,z) coordinates, with complete 3-dimensional profile for the initial energy density and magnetic field, we incorporate longitudinal expansion by assuming a maximum value of the velocity (of 0.7) at maximum z value for the Lorentz contracted energy density profile. (Note that this maximum velocity represents the velocity of the equilibrated plasma, and not that of the receding nuclei.) For intermediate distances, velocity is assumed to vary linearly as appropriate for Bjorken scaling. We use the lab time coordinate for time evolution. For the initial energy density profile, we first assume energy density profile as appropriate for an initial constant proper time hypersurface, evolving locally by longitudinal Bjorken scaling law, and then transform it to the constant lab time. This neglects nonlinear effects of inhomogeneities on evolution for a very short proper time period (the initial time for the beginning of plasma evolution), but should not be important for later time evolution. All our results are for the central rapidity region with unit rapidity window (suitably translated to Δz). This further makes our results reasonably reliable as the difference between the proper time and lab time are significant only for larger rapidities. Due to limitation of lattice size we have only considered small nucleus, copper in our case. Even for that, we have taken the radius to vary from about

3 fm to 4.5 fm (depending on consideration of fluctuations etc.). We again emphasize that the spirit of our work here is to demonstrate various important qualitative patterns in the flow in the presence of magnetic fields, rather than precise numbers.

10.4 Effect of Magnetic Field on Elliptic Flow

Before we present results of our simulations for different aspects of flow evolution, including the elliptic flow, we discuss previous results in the literature regarding effects of magnetic field on elliptic flow. In an earlier paper [4], some of us had argued that magnetic field can lead to enhancement of elliptic flow by up to about 30%. We first briefly recall physical arguments for such an enhancement as discussed in ref. [4]. Basic argument in [4] relied on the the effects of an external magnetic field on sound waves in QGP produced in RHICE. For relativistic magnetohydrodynamics, the waves which are relevant for the case of discussion of flow are the *magnetosonic waves* as they involve density perturbations. Phase velocities for these waves are given by [17]

$$\mathbf{v}_{ph} = v_{ph}\mathbf{n} = \mathbf{n}(\frac{1}{2}[(\rho_0 h_0/\omega_0)c_s^2 + v_A^2])^{1/2}(1 + \delta\cos^2\theta \pm a)^{1/2}. \tag{10.15}$$

Here $+$ and $-$ signs correspond to the fast and slow magnetosonic waves respectively, $v_A = B_0/\sqrt{\omega_0}$ is the Alfvén speed, and δ and a are defined below. Mean local values of various quantities are denoted by subscript o and θ is the angle between the magnetic field and $\mathbf{n}$.

$$a^2 = (1 + \delta\cos^2\theta)^2 - \sigma\cos^2\theta, \tag{10.16}$$

$$\delta = \frac{c_s^2 v_A^2}{[(\rho_0 h_0/\omega_0)c_s^2 + v_A^2]}, \quad \sigma = \frac{4c_s^2 v_A^2}{[(\rho_0 h_0/\omega_0)c_s^2 + v_A^2]^2}. \tag{10.17}$$

(Note, σ is defined above, and should not be confused with the conductivity as used above.) For propagation of density perturbations, as relevant for the evolution of flow anisotropies, the relevant wave velocity is the group velocity for the magnetosonic waves,

$$\mathbf{v}_{gr} = v_{ph}\left[\mathbf{n} \pm \mathbf{t}\frac{[\sigma \mp 2\delta(a \pm (1+\delta\cos^2\theta))]\sin\theta\cos\theta}{2(1+\delta\cos^2\theta \pm a)a}\right]. \qquad (10.18)$$

Here $\mathbf{t} = [(\mathbf{B_0}/B_0) \times \mathbf{n}] \times \mathbf{n}$, and again the upper and lower signs ($\pm$ or $\mp$) correspond to the fast and the slow magnetosonic waves respectively. For a given magnetic field $\mathbf{B_0}$, the direction of $\mathbf{n}$ can be varied to generate group velocities of these waves in different directions. Fig. 10.1 shows a typical situation of various vectors in Eq.(10.18) expected in RHICE. It is important to note that the direction of $\mathbf{v}_{gr}$ depends on the relative factors multiplying $\mathbf{n}$ and $\mathbf{t}$ in Eq.(10.18). This in turn depends on properties of the plasma like energy density. Thus due to the presence of spatial gradients in RHICE, especially due to initial state fluctuations, even along a fixed azimuthal direction, we expect the direction of $\mathbf{v}_{gr}$ to keep varying with the radial distance. This can lead to the development of very complex flow patterns. This raises a very interesting possibly of generation of vorticity in the plasma entirely from the effect of magnetic field. We are not able to fully explore this possibility as yet due to our limitation of relatively small time evolution of the plasma. (Vorticity will be expected to arise at later times when the flow pattern gets significantly twisted due to magnetic field effects.) Any such vorticity will have important implications, especially in view of chiral vortical effect.

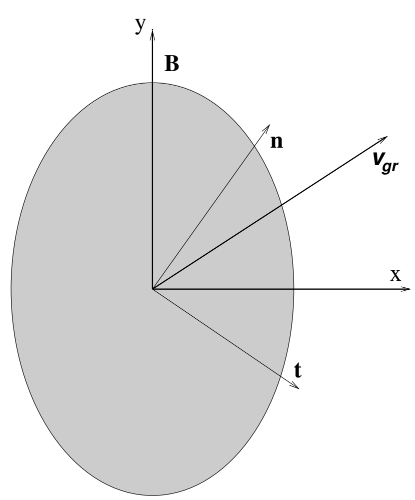

Figure 10.1: A typical situation expected in relativistic heavy-ion collisions with the magnetic field pointing in the y direction. The direction of the group velocity $\mathbf{v}_{gr}$ is obtained from $\mathbf{n}$ and $\mathbf{t}$ via Eq.(10.18). (figure taken from ref. [4]).

The effect of magnetic field on propagation of sound waves here comes from an effective magnetic pressure arising from the freezing of magnetic field lines in the plasma in the magnetohydrodynamics limit. The distortions of magnetic field lines in the presence of density perturbations cost energy leading to an extra contribution to pressure from the presence of magnetic field. This is what is responsible for increasing the effective sound speed as given above. The estimate of the effect of magnetic field on elliptic flow in ref. [4] was based on the fact that the flow coefficients are proportional to the sound velocity [18], which now becomes dependent on the directions of the magnetic field and that of the phase velocity. This directly affects the flow pattern and hence elliptic flow.

We mention that these arguments are rather crude. Elliptic flow is a complex phenomenon and cannot be directly related to the anisotropy of the stiffness of equation of state and resulting sound velocity. Our intention here is to point out the underlying physics of the phenomena and why one may expect an increased elliptic flow from the presence of magnetic field. A more detailed analysis of the effects of magnetic field on elliptic flow was carried out by Tuchin in [6] with results in agreement with the estimates of [4]. Later, in the section of results we will present results of our numerical simulation where again magnetic field is found to enhance elliptic flow. However, quite different results are reported in a recent numerical RMHD simulations where magnetic field was found to have no effect on elliptic flow [7]. It is important to understand possible reasons for the discrepancies between these different works. For this purpose we have carried out simulations to study elliptic flow evolution with different values of impact parameters which lead to different types of magnetic field profiles. Our conclusion is that in the end the effects of magnetic field on flow pattern has many complex features. The picture used in [4] was indeed too simplistic where the magnetic field dependent sound speed was directly assumed to affect the elliptic flow. In fact quite opposite arguments could be given using Lenz's law from which one expects that induced magnetic fields will always oppose the change which causes magnetic flux changes. Basically this should imply that expansion along x axis should be suppressed as this leads to decrease in magnetic flux, while expansion along y axis should not be affected, thereby decreasing elliptic flow. The actual situation is much more complex. For example, Lenz's law argument does not distinguish between uniform expansion along x axis and the distortion of a localized plasma by transverse expansion. The latter leads to distortion of field lines, and not just decrease in magnetic flux, which has implications for extra pressure, and hence on sound waves. Some of the complexities have been discussed recently in refs. [19, 20], though exact time dependence used for magnetic field in ref. [20] seems difficult to justify, (also for the Gaussian profile of the magnetic field in the x-y plane in ref. [19], one needs to ensure that Gauss' law is satisfied.)

As we will see later, net effect of magnetic field on elliptic flow depends very sensitively on the profile of magnetic field in relation to the profile of plasma energy density. When magnetic field is entirely localized within the plasma, we typically find enhancement of elliptic flow, in accordance with the physical arguments in [4]. However, when the magnetic field profile extends significantly beyond the plasma profile, plasma expansion seems to be hindered by the squeezing of external field lines, thereby suppressing elliptic flow. Presence of initial state fluctuations introduces extra complications due to flux re-arrangements, as we will discuss below. It is possible that a combination of such effects may be responsible for discrepancies between these various results on the expected magnetic field dependence of elliptic flow.

10.5 Results

We now present results of our simulations. As we mentioned, due to small lattice size, we are able to consider evolution for a maximum of only 3 fm time to avoid boundary effects. We first present results for elliptic flow.

10.5.1 Magnetic field dependence of elliptic flow

We carry out simulations with different impact parameters and calculate elliptic flow with magnetic field and without magnetic field. The latter is calculated by repeating the same simulation, but with magnetic field switched off.

First we present results for the conventional momentum anisotropy defined as $\epsilon_p = \frac{T^{xx} - T^{yy}}{T^{xx} + T^{yy}}$. We calculate ϵ_p at different times with and without magnetic field. Fig. 10.2 shows these plots. As expected, ϵ_p increases gradually with time. However, we see that ϵ_p in the presence of magnetic field increases more rapidly, clearly showing enhancement of momentum anisotropy due to magnetic field (for this choice of parameters, in particular, with impact parameter of 4 fm).

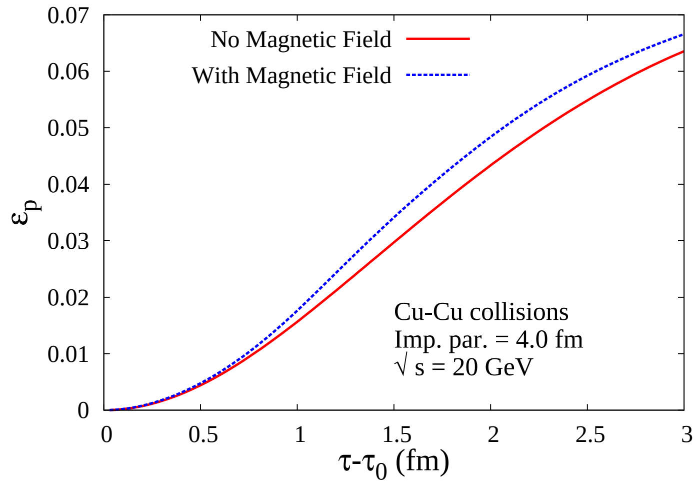

Figure 10.2: Effect of magnetic field on build up of momentum anisotropy ϵ_p, showing clear enhancement of ϵ_p with magnetic field, for this set of parameters, in particular for impact parameter of 4 fm.

Though this expression for momentum anisotropy represents the expected development of momentum anisotropy, we will not use this definition of momentum anisotropy. Instead, we will use Fourier expansion of the following normalized momentum anisotropy

$$f(\phi) = \frac{\Delta p(\phi)}{\bar{p}} = \frac{p(\phi) - \bar{p}}{\bar{p}} \tag{10.19}$$

v_2 is taken to be the 2nd Fourier coefficient in the Fourier series expansion of $f(\phi)$. Here $p(\phi)$ is the fluid momentum in a bin at azimuthal angle ϕ calculated from momentum components of the energy momentum tensor, i.e. from T^{x0} and T^{y0}, integrating over the plasma volume in the central rapidity region of unit rapidity width. We believe that the expression for v_2 obtained from Eqn.(10.19) is more appropriate as it directly gives the momentum anisotropy as measured in the experiment, rather than expected momentum anisotropy ϵ defined in terms of T^{xx} and T^{yy}. Interestingly, this definition of v_2 has a specific advantage over ϵ_p. As Fig. 10.2 shows, ϵ_p

increases gradually, and becomes sizeable only after significant time (in Fig. 10.2 at $t = 3$ fm). So, to study effects of magnetic field on momentum anisotropy in various conditions, it requires running simulation every time upto significant time. In contrast, the definition in Eqn.(10.19) gives a value of v_2 which has a large value right from the beginning (after first few time steps), it very slowly changes afterwards due to evolving shape of the plasma region. This may appear surprising, but there is a simple physical explanation for this behavior. Consider a definition of $v_2 = \frac{T^{x0}-T^{y0}}{T^{x0}+T^{y0}}$. (It is simple to see that the arguments given for this v_2 apply to the definition of v_2 obtained from Fourier expansion of $f(\phi)$ in Eqn.(10.19).) One can see from the form of QGP energy-momentum tensor (Eqn.(10.2)) that for small velocities (at initial times), this v_2 equals $\frac{v_x-v_y}{v_x+v_y}$. With initial fluid velocity directly proportional to the pressure gradient (as one can see from Euler's equation, see, e.g. [18]), we see that v_2 captures complete information about spatial anisotropy right from the beginning. It does not depend on the magnitude of the velocity, but only on the fractional difference in v_x and v_y. As long as the fluid acceleration remains roughly constant, the value of v_2 above will remain roughly the same. essentially, the velocities (both v_x, and v_y, hence also fluid momenta) will simply increase with time. End result will be that time will not play much role for this definition of v_2. Same argument applies to $f(\phi)$ in Eqn.(10.19) and v_2 obtained from its Fourier expansion. That is the reason we find that v_2 assumes a large, roughly constant value right from the beginning stages, and starts changing later only with changes in the spatial anisotropy (and effects of fluctuations etc.). In contrast, the usual definition of momentum anisotropy ϵ_p is equal to (again, for small velocities at initial times) $\frac{v_x^2-v_y^2}{v_x^2+v_y^2+\frac{1}{2\gamma^2}}$ with the equation of state $\rho = 3p_g$. This value increases from zero smoothly to finite value due to extra factor of $\frac{1}{2\gamma^2}$ in the denominator as velocity magnitude increases in time. This is why we see ϵ_p in Fig. 10.2 gradually increasing in time (for both cases, with and without magnetic field). For our case, v_2 in Eqn.(10.19) increases rapidly to a finite value simply because at the first stage itself the acceleration of the fluid (and hence the instantaneous velocity) completely originates from the anisotropy of pressure gradient arising from the spatial anisotropy. We find little change in the value of v_2 for significant initial time (of order 2-3 fm), and after that it evolves primarily because of the changes in the spatial anisotropy, as expected. Thus, we believe it is much more appropriate to use the expression for v_2 obtained from Eqn.(10.19) rather than the usual one based on T^{xx} and T^{yy}. This also helped us in collecting results for many runs with different impact parameters, with and without magnetic field, as the initial v_2 was itself found to be close to the time evolved value of v_2 up to several fm time.

Fig. 10.3 shows the effect of magnetic field on elliptic flow. Top figure in Fig. 10.3 shows the plot of $v_2(B)/v_2(0)$ vs. the impact parameter. We see clear enhancement in v_2 due to magnetic field which reaches a peak value at the impact parameter of about 3 fm, decreasing subsequently. Interestingly, for large impact parameter (near about 6.5 fm) there is no effect of magnetic field on v_2 and for larger impact parameters, magnetic field actually leads to suppression of v_2, with suppression being strong for impact parameter of 8 fm. The bottom figure in Fig. 10.3 shows the behavior of v_2 for the cases of without magnetic field (solid, red curve) and with magnetic field (dashed and dotted curves) separately, clearly showing that for large impact parameters, magnetic field strongly suppresses the elliptic flow. This is despite the fact that the magnetic field is monotonically increasing function of the impact parameter almost for the entire range considered, as can be seen in Fig. 10.4, with only slight decrease for the case $B_{time} = 0.4$ fm (that cannot account for the decrease of $v_2(B)$ which is seen for both values of $B_{time} = 0.4$ and 0.6 fm). We will discuss below the physical reasons for this behavior which will also explain the discrepancies in the results of refs. [4,6] and ref. [7]. In all the figures, we typically give two curves labeled by B_{time} which is the time at which the magnetic field profile is calculated after the collision. Smaller value of B_{time} gives larger value of the magnetic field, but may not be very realistic in view of finite conductivity of the plasma.

We have studied the reason for this non-trivial behavior of magnetic field dependence of elliptic flow and it appears to originate from the differences in the profiles of magnetic field vs. the energy density profile. For smaller values of impact parameters, the magnetic field profile is reasonably confined while the plasma density profile extends for larger regions. This is the regime where arguments in [4, 6] seem to be valid and enhancement of v_2 is seen in the presence of magnetic field. This situation is shown in Fig. 10.5 which shows the initial profile of the magnetic field as well as the initial energy density profile for impact parameter of 1 fm.

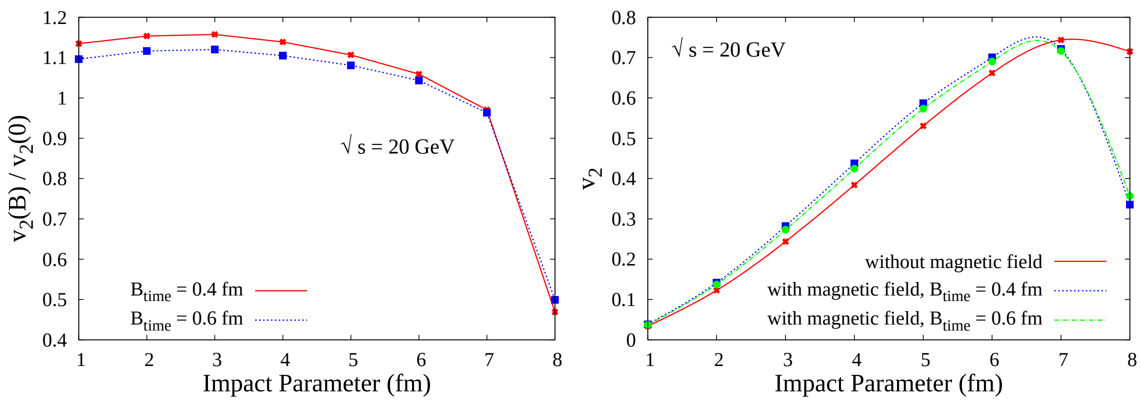

Figure 10.3: Top figure shows the plot of $v_2(B)/v_2(0)$ vs the impact parameter. The ratio peaks at the impact parameter of about 3 fm, decreasing afterwards, and actually becomes less than 1 (meaning suppression of elliptic flow due to magnetic field) for large impact parameters. Bottom figure shows the plots of v_2 for the cases of without magnetic field (solid,red, curve) and with magnetic field (dashed and dotted curves) separately, clearly showing that for large impact parameters, magnetic field strongly suppresses the elliptic flow.

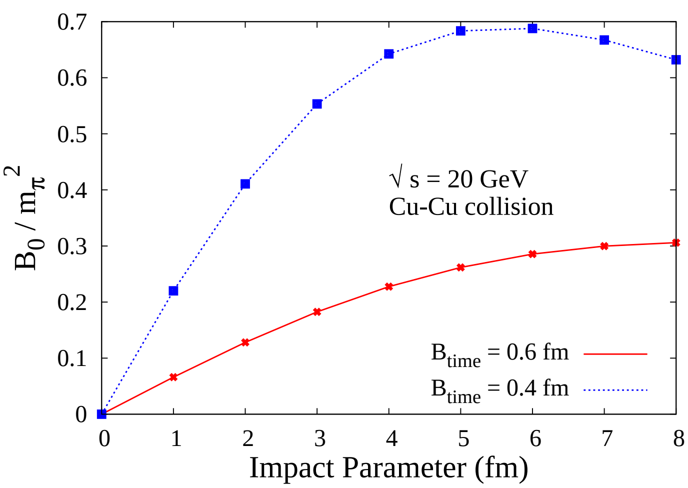

Figure 10.4: Central value of magnetic field as a function of the impact parameter. Note that magnetic field almost monotonically increases with the impact parameter.

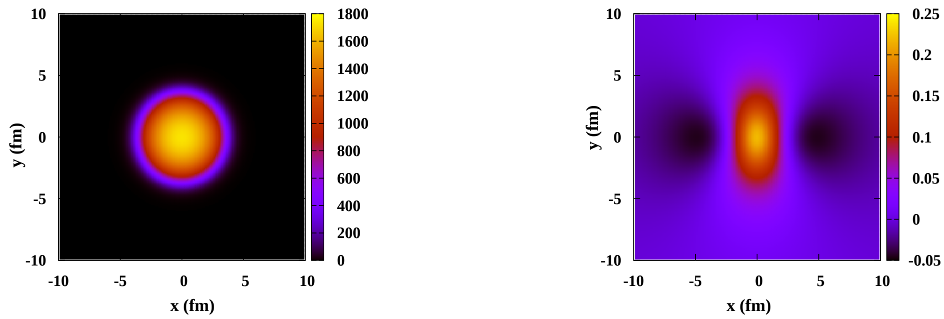

Figure 10.5: Left figure shows the initial plasma energy density profile for impact parameter of 1 fm. Right figure shows the initial magnetic field profile for the same case. Note that for this small value of impact parameter, plasma extends well beyond the region along x-axis where magnetic field is significant. Here and in Fig. 10.6 we show the y component of the magnetic field (in the units of m_π^2, the energy density in the units of MeV/fm^3).

Quite opposite profiles are seen in Fig. 10.6 which shows initial profiles for magnetic field and energy density for a large impact parameter of 7 fm. (For both Figs. 10.5,10.6 we have used $B_{time} = 0.4$ fm.) Extension of significant strength of magnetic field profile beyond the plasma profile along x axis (semi-minor axis of the elliptical QGP shape) squeezes plasma expansion in x-direction as magnetic field lines in the outer regions offer stiffness against distortion. This seems to be the cause of decrease in $v_2(B)/v_2(0)$ for larger impact parameters. This is especially demonstrated by the very strong decrease in $v_2(B)$ for impact parameter beyond 7 fm in the bottom figure in Fig. 10.3. (Note in this context, that simulations in [7], where no effect of magnetic field was found on the elliptic flow, were carried out for Au-Au collisions with large impact parameter.).

Our conclusion of this investigation is that the effect of magnetic field on elliptic flow is quite complex. There are several physical effects at play here, from anisotropic sound speed due to magnetic field direction (which tends to increase elliptic flow), to Lenz's law which suppresses plasma expansion in the regime of external magnetic field (which tends to suppress elliptic flow). Net effect on the elliptic flow depends

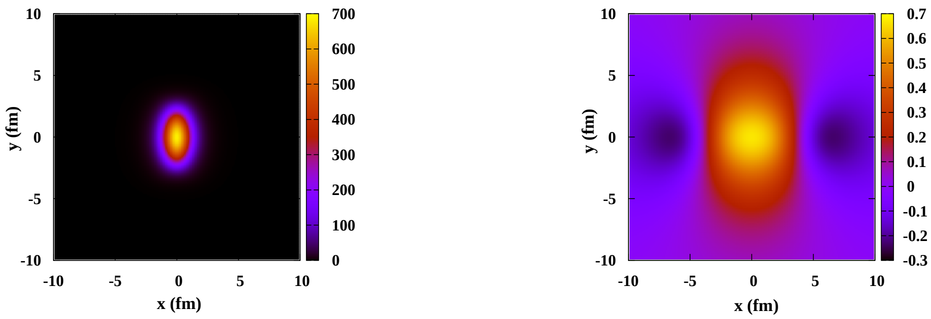

Figure 10.6: Left figure shows the initial plasma energy density profile for impact parameter of 7 fm. Right figure shows the initial magnetic field profile for the same case. Note that for this large value of impact parameter, the two profiles show opposite behavior compared to Fig. 10.5. Here we see that the magnetic field profile extends beyond the region along x-axis compared to the plasma energy density profile.

on which factors dominate. We are not attempting to provide a definitive answer to the discrepancies between different results for $v_2(B)/v_2(0)$ in the literature, but pointing out possible factors which may be responsible for this. Nonetheless, the strong suppression of elliptic flow in the presence of magnetic field for large impact parameters may provide a signal for the presence of strong magnetic field during early stages of plasma evolutions.

10.5.2 Magnetic flux re-arrangement due to fluctuations

One usually expects that magnetic field decreases as plasma evolves. It is indeed true at an average level. However we know that the plasma has strong initial state fluctuations in the energy density. As fluctuations evolve, the dynamics of magnetic flux lines (which are mostly frozen in the plasma) become very complex. It is clearly possible that in some region plasma expansion dilutes the magnetic flux, while due to energy density inhomogeneities, the neighboring region may get concentration of magnetic flux, thereby locally increasing the magnetic field. We find that indeed this happens. Fig. 10.7 shows the plot of central magnetic field for two different cases. The thin curve (with stars) shows the case for Gaussian width of 0.3 fm for the energy deposition in each binary collision in Glauber Monte Carlo, while the thick curve (with solid squares) represents the case of Gaussian width of 0.4 fm, thereby representing a much smoother background for the plasma. We see that for this smoother plasma case, the magnetic field roughly monotonically decreases with time (after a very little initial increase, again due to relatively small fluctuations) as expected. However, for the case of smaller Gaussian width, representing stronger fluctuations, the magnetic field initially increases significantly almost by about 10%, and eventually decreases. This is only a sample case, and it is clear that for stronger fluctuations, one may expect even stronger temporary increase of the magnetic field during plasma evolution. This can have important consequences for effects like chiral magnetic effect and chiral vortical effect (with a possibility that complex flow pattern arising from magnetic field in the presence of fluctuations can in principle lead to generation of vortices). These effects strongly depend on the presence of topological charge density (for chiral magnetic effect) and vorticity (for chiral vortical effect). These quantities are reasonably localized, and if the magnetic field in these *relevant* regions tends to increase in time (for some time) it can lead to strong enhancement of these effects compared to the usual expectation based on decreasing magnetic field.

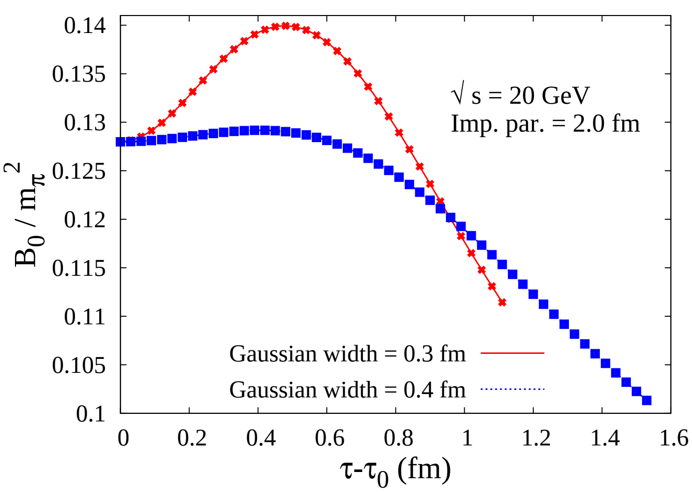

Figure 10.7: Plot of central magnetic field in the presence of fluctuations and for relatively smoother plasma back ground. We see that for the smoother case, the magnetic field monotonically decreases as expected. However, for the case of stronger fluctuations, the magnetic field initially increases, and eventually decreases.

10.5.3 Effects of magnetic field on the power spectrum of flow fluctuations

We now consider the effects of magnetic field on the power spectrum of flow fluctuations. Power spectrum of flow fluctuations for a large number of flow coefficients can be a very valuable source for investigating early stages of plasma evolution [21]. The reason for departure from conventional focus on only first few even flow coefficients was the recognition that initial state fluctuations contribute to development of all flow coefficients (including the odd ones) even for a central collisions. Many subsequent investigations confirmed this expectation [22] and indeed now one routinely measures odd coefficients (e.g. the triangular flow coefficient v_3) and there have also been several investigations of power spectrum of flow coefficients upto a large value of n of about 10-12. From the discussion above it is obvious that magnetic field will affect the power spectrum in non-trivial manner. Indeed, it was an earlier calculation of effects of primordial magnetic field on CMBR power spectrum [23] which prompted some of us to explore the possibility of magnetic field effects on the power spectrum of flow fluctuations in RHICE [4].

We use same methods for calculating flow anisotropies as in our earlier work [21]. v_n denotes the n_{th} Fourier coefficient of the resulting momentum anisotropy in $\delta p/p$. We do not calculate the average values of the flow coefficients v_n, instead we calculate root-mean square values of the flow coefficients v_n^{rms}. Further, these calculations are performed in a lab fixed frame, without any reference to the event planes of different events. Average values of v_n are zero due to random orientations of different events. As v_n^{rms} will have necessarily non-zero values, physically useful information will be contained in the non-trivial shape of the power spectrum (i.e. the plot of v_n^{rms} vs. n). We show below in Fig. 10.8 the effects of magnetic field on the power spectrum calculated after time evolution of about 2 fm. These results are for realistic magnetic field for the collision energy considered here ($\sqrt{s}$ = 20 GeV) for copper nuclei with central field strength of 0.1 m_π^2 and 0.4 m_π^2 corresponding to B_{time} = 0.6 and 0.4 fm respectively (with initial state fluctuations). (For the results for the power spectrum calculations, we have taken initial longitudinal velocity of the plasma to be zero for the stability of the program in the presence of strong fluctuations.) As we can see, the effects of magnetic field are very tiny, though they are clearly present. As we will see below, the effects of magnetic field are not seen prominently here due to the effects of fluctuations being dominant for the power spectrum. Limited particle statistics may make it very difficult to observe such tiny effects.

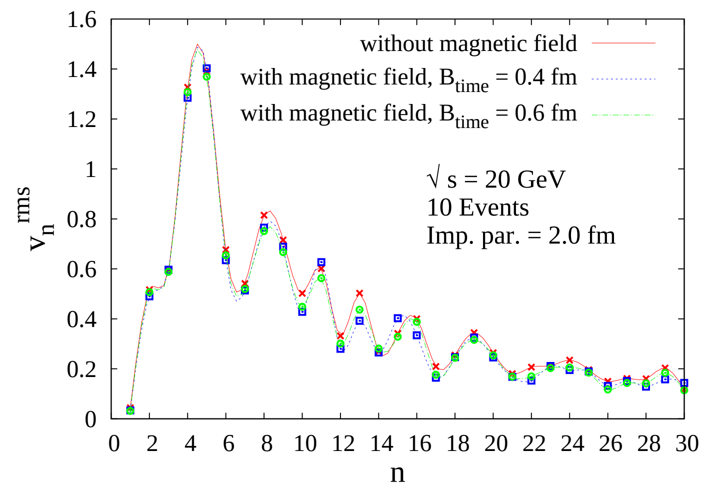

Figure 10.8: Plot of v_n^{rms} with and without magnetic field. Even though magnetic field affects the power spectrum, its effects are very tiny here for the magnetic field considered here (0.1 and 0.4 m_π^2).

As we mentioned in the Introduction, it is of great importance to find signals which can indicate the presence of strong magnetic field during the initial stages. Fig. 10.8 shows possible effects of magnetic field, though the effects are very insignificant for these low magnetic fields (for much larger field appropriate for large values of $\sqrt{s}$, e.g. at LHC, these effects may become significant. We are not able to carry out simulations for such large values of $\sqrt{s}$ at present.) Further, the effects seen in Fig. 10.8 do not show any qualitatively distinct pattern for the power spectrum. We show qualitatively different result below for very strong magnetic fields. We consider magnetic field strength to be $5m_\pi^2$ and $15m_\pi^2$. These values are completely unrealistic here (unless unexpected things happen, say for deformed nuclei), and we use these only to show how completely new effects can arise for very large magnetic field. As we mentioned in Sect.III, for large magnetic fields, requiring large Lorentz gamma factor, the realistic magnetic field profile (as used for Fig. 10.8) causes problems with simulation. Thus for these cases (for Figs. 10.9,10.10,10.11 below), we use a simpler profile for magnetic field where the profile in the (x-z) plane is chosen to be proportional to the energy density profile in the (x-z) plane at y = 0. The peak value of the magnetic field is chosen by hand. The magnetic field is then taken to be constant along the y axis, as consistent with the Gauss's law. Fig. 10.9 and Fig. 10.10 below show the power spectrum for magnetic field of strength $5m_\pi^2$ and $15m_\pi^2$ respectively. As these are runs for very strong magnetic field, simulation could be carried out only for relatively short time of 0.6 fm. We see strong pattern of different powers in even and odd v_n^{rms} coefficients. This is expected from the reflection symmetry about the magnetic field direction if initial state fluctuations are not dominant. Note that for $5m_\pi^2$ case, even-odd pattern is seen for only first few flow coefficients as fluctuation effects wash out the effect for larger v_n for the event average over 10 events. For $15m_\pi^2$ case the magnetic field is very strong and fluctuation effects are not able to wash out the even-odd pattern arising from the magnetic field. This is a qualitatively distinct result and can give unambiguous signal for the presence of strong magnetic field during early stages.

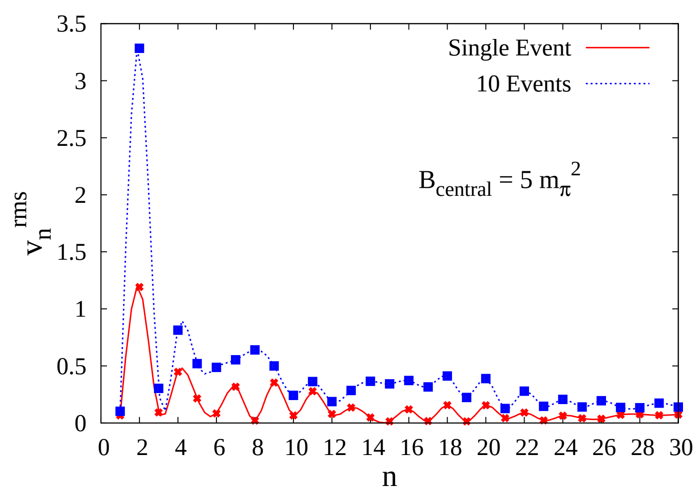

Figure 10.9: Plot of v_n^{rms} for magnetic field with strength $5m_\pi^2$. Even-odd power difference is seen in first few flow coefficients as fluctuations wash out the effect for large v_ns.

The reason one needs very strong magnetic field is that although magnetic field tends to develop clear pattern of even-odd power difference, there are strong effects of initial state fluctuations on the power spectrum. The final power spectrum is a

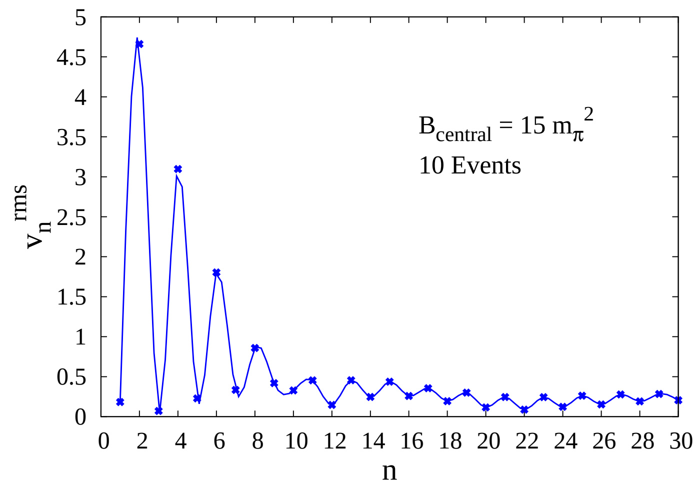

Figure 10.10: Plot of v_n^{rms} for very strong magnetic field with strength $15m_\pi^2$. Strong difference in the power of even and odd values of v_n^{rms} are seen. Though such large magnetic field are completely unexpected here, such effects may provide unambiguous signal for the presence of any unexpected strong initial magnetic field.

combined effect of the two patterns. Strong magnetic field is needed to dominate over the effects of fluctuations in Fig. 10.9,10.10. To illustrate this, we show in Fig. 10.11 flow fluctuations for a smooth isotropic plasma region (without any fluctuations) in the presence of magnetic field. We now take a more reasonable value of magnetic field strength equal to m_π^2. Due to smaller magnetic field and smooth plasma profile, the evolution could be run up to 3 fm time (after which boundary effects could not be neglected). We see that strong even-odd power difference is present in the power spectrum.

We mention that such even-odd power difference can arise due to presence of vortices also during early plasma evolution, as demonstrated in our earlier work [24]. Thus, we may conclude that even-odd difference in the power spectrum indicates either strong magnetic field or presence of vortices in the initial plasma. (We know that to some extent the effect of magnetic field in a plasma is similar to the presence of vortices as the Lorentz force due to magnetic field has similar form as the Coriolis force in the presence of vortices.) This result also has interesting implications for the CMBR power spectrum. It is known that low l modes of CMBR power spectrum also show possible difference in even-odd modes [25]. It is possible that this feature may

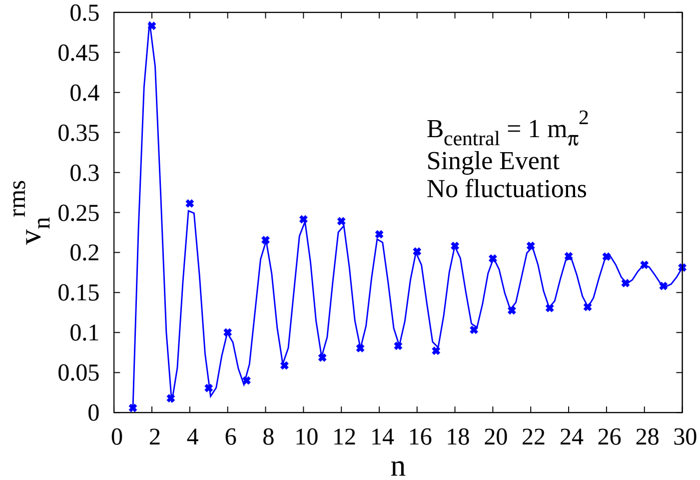

Figure 10.11: Plot of v_n^{rms} for magnetic field with strength m_π^2. Here we consider isotropic region with smooth plasma profile without any fluctuations. Strong difference in the power of even and odd values of v_n^{rms} are present arising from the effect of magnetic field.

be indicative of the presence of a magnetic field, or presence of some vorticity, during the very early stages of the inflation.

10.5.4 Anomalous elliptic flow for deformed nucleus

Collision of deformed nuclei opens up entirely new range of possibilities for heavy-ion collisions. This is especially true when considering possible magnetic field configurations for a given shape of plasma. For non-central collisions of spherical nuclei, one is constrained to consider the magnetic field pointing along the semi-major axis of the elliptical QGP region. (Though due to fluctuations, deviations from this will happen but roughly the picture remains the same.) For deformed nuclei, entirely new possibilities can arise. As an example, Fig. 10.12 shows ellipsoidal nuclei, with longer axes of both along the y axis, with impact parameter also along the y axis. As one can see from Fig. 10.12, different impact parameters can lead to following anomalous magnetic field configurations (in the sense that they cannot arise for spherical nuclei).

a) QGP region being elliptical in shape but the magnetic field pointing along the semi-minor axis, x-axis in this case as seen in Fig. 10.12a.

b) QGP region being roughly spherical, but still strong magnetic field is present due to strong components coming from spectators, as seen in Fig. 10.12b.

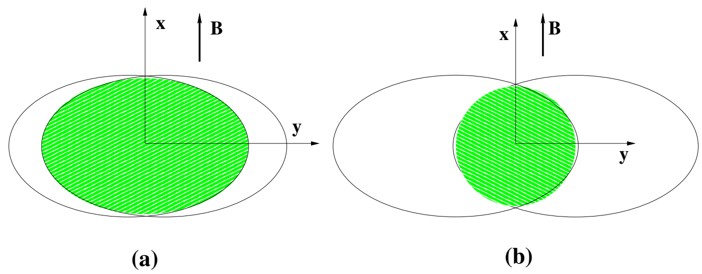

Figure 10.12: (a) shows the situation of the case when the QGP region is elliptical in shape but the magnetic field points along the semi-minor axis. (b) shows the case when the QGP region is roughly spherical, but still strong magnetic field is present due to strong components coming from spectators.

With the physics of effects of magnetic field as described above, one can immediately guess what to expect in both these cases. For (a) we expect suppression of elliptic flow as the magnetic field induced anisotropy leads to larger momentum flowing in the direction of semi-major axis of the elliptical QGP shape, even though the usual fluid pressure gradient develops larger flow along the semi-minor axis. This leads to strong suppression of elliptic flow due to this anomalous magnetic field. (For very strong magnetic field the net v_2 may even be completely dominated by the magnetic field, leading to negative elliptic flow.) For (b) one would have expected no elliptic flow for the smooth plasma profile considered here, (non-zero v_2 may only arise from any fluctuations), as the QGP is roughly isotropic. However, the presence of strong magnetic field introduces anisotropic pressure, leading to development of non-zero v_2, even though QGP region is spherical. Figs. 10.13,10.14 confirm these expectations. Again, the anomalous elliptic flow in these situations may provide a signal for initial stage magnetic field.

Note that here we are not simulating collision of deformed nuclei. We use the plasma profile for Fig. 10.12a and Fig. 10.12b by using collisions of spherical nuclei (copper) with non-zero and zero impact parameter respectively. But for the magnetic field we calculate the magnetic field as in Sects.5A and 5B, rotate it along the x axis, and use that for the evolution of the above plasma profiles. This, in some sense,

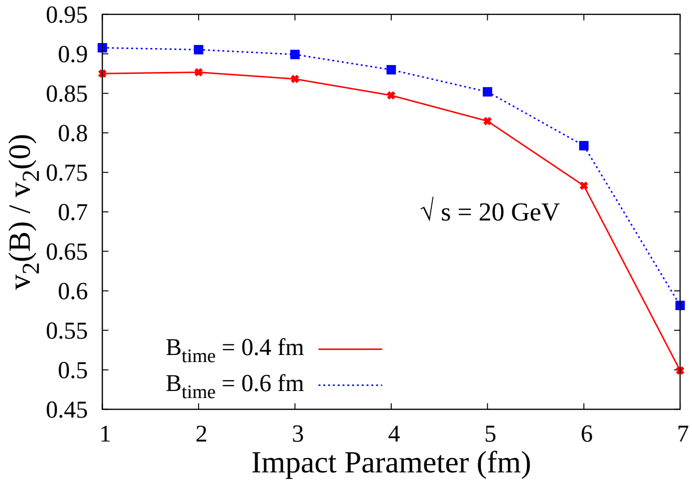

Figure 10.13: v_2 for the case when the QGP region is elliptical in shape but the magnetic field points along the semi-minor axis, x-axis in this case. Strong suppression of elliptic flow arises with larger momentum flowing in the direction of semi-major axis of the elliptical QGP shape due to magnetic field induced anisotropy.

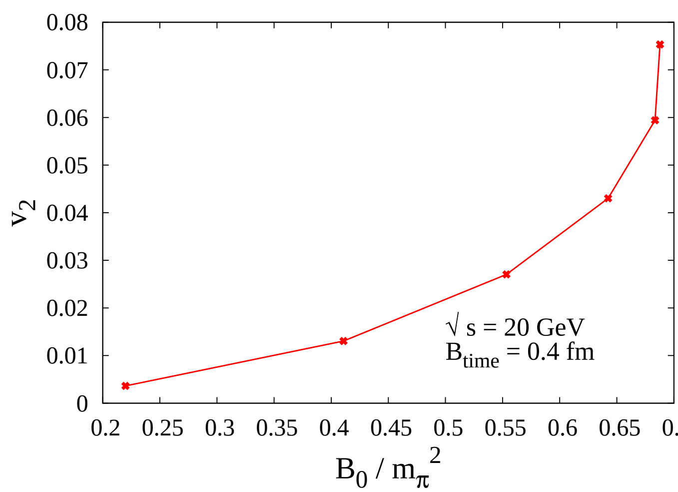

Figure 10.14: v_2 for the case when the QGP region is roughly isotropic in shape but still non-zero magnetic field is present leading to non-zero v_2, monotonically increasing with the strength of magnetic field, even though no elliptic flow is expected in this case.

models different situations of collisions of deformed nuclei as in Fig. 10.12a,b. A full simulation for deformed nuclei is presently under investigation and will be presented in a future work.

10.5.5 Quadrupole magnetic field from deformed nucleus

A very interesting possibility arises when considering collision of deformed nuclei. Consider again ellipsoidal nuclei with long axes in the transverse plane (as in the above), but now in crossed configuration. Fig. 10.15 shows this crossed configuration for Uranium nucleus with the semi-minor and semi-major axes being about 6.7 fm and 8.7 fm respectively. Magnetic field is calculated at time of 0.4 fm after the collision for $\sqrt{s} = 20$ GeV. It is clear that while the resulting QGP region is roughly isotropic (possibly with strong v_4 component), spectators will generate quadrupolar magnetic field as one can see from Fig. 10.16 showing the magnetic field lines for this crossed configuration of colliding nuclei. (Magnetic field here has been calculated by extending the calculation of Sec.V A,B for the case of deformed nucleus, Uranium in this case. We calculate magnetic field from uniformly charged ellipsoidal nuclei [11, 26], oppositely moving, with appropriate Lorentz transformations.) This raises very important possibilities. Quadrupolar field will itself contribute to v_4, thereby affecting final value of v_4 of the plasma. Further, quadrupolar field will tend to focus plasma motion along the longitudinal direction, thereby affecting Bjorken longitudinal expansion itself. For charged plasma with finite conductivity one may expect charge separation in the transverse direction as a function of rapidity, while a focusing effect should be seen along the beam axis for the plasma. This should lead to suppression of transverse flow at non-zero rapidity. Further, if focusing is strong, it may lead to hot extended regions along the longitudinal axis. This requires a detailed investigation of plasma dynamics with such a crossed configuration collision of deformed nuclei properly represented in Glauber Monte Carlo. This is under study and will be presented in a future work.

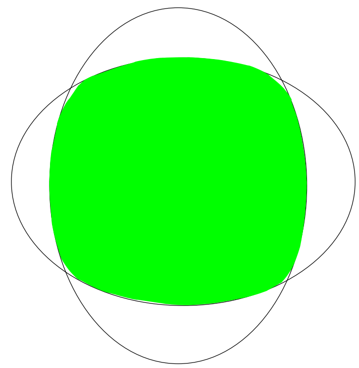

Figure 10.15: Crossed configuration of collision of deformed nuclei. Note that the overlap region will be reasonably isotropic, with possibly strong v_4 component. Importantly now there are four spectator parts whose motion should lead to quadrupolar magnetic field configuration.

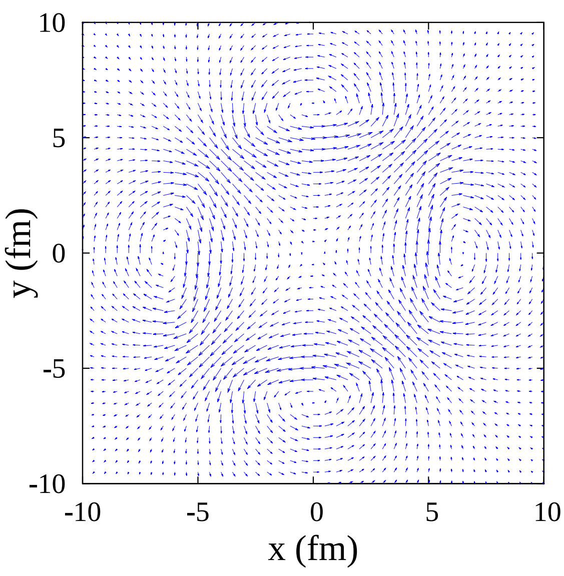

Figure 10.16: Magnetic field configuration arising from collision of crossed deformed nuclei (Uranium) as in Fig. 10.15. Quadrupolar nature of the field is clear.

10.6 MHD Simulations for Deformed Nuclei

Results discussed above in this Chapter have been presented in ref. [1]. We have briefly discussed above the case of deformed nuclei and the new possibilities which arise from considering such collisions. As we mentioned, the results for deformed nucleus case, in ref. [1], were modeled using the magnetic field calculated from the non-central collision of spherical nuclei, but considering plasma shape, in first case, elliptical with semi-minor axis along y-axis and in the second case, circularly symmetric in the transverse plane. The results for elliptic for these two cases are shown in Fig.10.13 and Fig.10.14 respectively. These configurations of magnetic field and plasma region were chosen to model the specific magnetic field configurations expected for different orientations of colliding deformed nuclei, see Fig. 10.12.

In this sub-section, we present results of ongoing work for deformed nuclei case where we have carried out full simulations of deformed nucleus-nucleus collision using Glauber model initial condition. For these results, deformed nuclei geometry (with ellipsoidal shape) has been incorporated in the Glauber model so that with different choices of orientations of colliding Uranium nuclei, correct distribution of initial energy density is obtained. The magnetic field is again calculated (as above) starting with the electric fields of ellipsoidal nuclei in their rest frames and Lorentz transforming to the center of mass frame. We have carried out MHD simulations, with lattice spacing 0.2 fm, for Uranium-Uranium collision at $\sqrt{s} = 20$ GeV.

Fig. 10.17 presents results for the effects of magnetic field on elliptic flow for body-body collision of Uranium nuclei. The behavior of the plot is qualitatively similar to the plot shown in right of Fig. 10.3 for spherical nuclei case, but there are important differences. Recall Fig. 10.12, where it has been shown that in the case of body-body collision, at low impact parameter regime, magnetic field will be along semi-minor axis of the plasma region (in the case of spherical nuclei magnetic field is always along the semi-major axis). Without the magnetic field, in such case, usual hydrodynamics gives negative elliptic flow as shown with the solid (red) curve in the Fig. 10.17. But, as we argued that magnetic field can enhance the sound speed in perpendicular direction, therefore it should suppress the negative elliptic flow, which is clear from the Fig. 10.17 that dotted (blue) curve is going from above the solid (red) curve

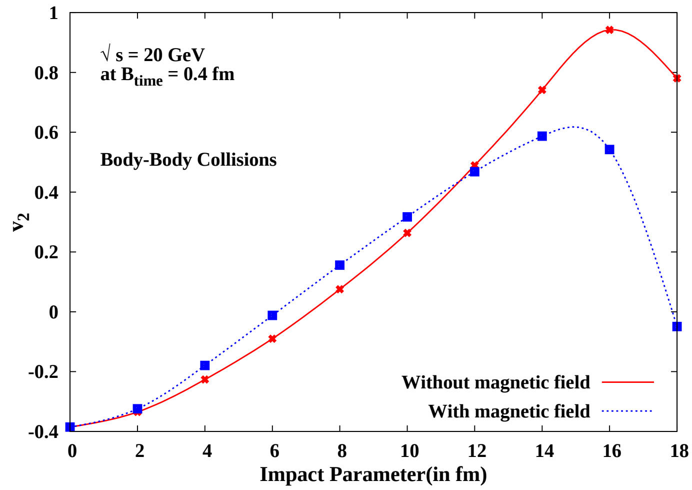

Figure 10.17: Plots of v_2 for the cases of without magnetic field (solid, red, curve) and with magnetic field (dotted, blue, curves) for body-body collision of Uranium nuclei.

(see the modeling in Fig. 10.13 in this regard). It also should be noted from the Fig. 10.17 that at impact parameter about 7 fm, solid (red) curve has zero value of elliptic flow, which corresponds to the circularly symmetric plasma region in the transverse plane. But in this case magnetic field is also present (spectators are present see Fig. 10.12b) and due to this elliptic flow becomes non-zero, shows that magnetic field can generate momentum anisotropy in the plasma (see the modeling in Fig. 10.14 in this regard). At higher impact parameter also, there is a qualitative difference in between Fig.10.3b and Fig.10.17. Note that in Fig.10.3b, magnetic field induced enhancement of v_2 survives up to a value of impact parameter where v_2 reaches its maximum. In contrast, in Fig.10.17, v_2 with magnetic field becomes less than v_2 without magnetic field much before that point.

10.7 Conclusions

We have demonstrated qualitatively new effects on the flow pattern of QGP in the presence of initial magnetic field. As we emphasized, due to various limitations of our simulation, we are not in a position to provide numbers which can be compared to experimental data. Our intention is to show possibilities of new physical phenomena which one can try to look for in experiments. These qualitative patterns may be able to provide clear signal for the presence of strong magnetic field during early stages of the evolution, though actual value of magnetic field etc. will depend on more reliable numerical estimates of the numbers. Among our results one of the results shows that due to flux re-arrangement arising from evolving fluctuations, there may be local regions where magnetic field increases for some time (before it starts decreasing finally). If topological charges or vortices are also present in that region, it can lead to enhancement of chiral magnetic/vortical effects. We see very complex patterns of twisting flow developing due to magnetic field effects in the presence of fluctuations. For strong fluctuations and strong magnetic field, it seems entirely possible that localized vorticity may get generated at later times which we are not able to study due to limitations of our simulation. Our result on enhancement of elliptic flow in the presence of magnetic field confirms earlier expectation in refs. [4, 6]. At the same time our simulation also points out that the effects of magnetic field on elliptic flow are much more complex than envisaged in simple arguments of ref. [4]. In fact in some situations one finds decrease in the elliptic flow. This may resolve the discrepancy between the results of ref. [4, 6] and ref. [7] (see, also refs. [19, 20]). The strong suppression of elliptic flow for large impact parameters can provide a signal for initial stage strong magnetic field. (For this it is needed to have observations extended for very large impact parameters, to distinguish from the suppression from usual hydrodynamics resulting from decreased plasma pressure at large impact parameters.) We show non-trivial effects of magnetic field on the power spectrum of flow fluctuations. The strongest form of this effect being in the form of even-odd power difference in the flow power spectrum for strong magnetic fields which can be a very clean signal for strong magnetic field, or vortices [24], in RHICE. (At the same time, it can have important implications for the low l modes for CMBR power spectrum.) Our results for deformed nuclei provide possibilities of anomalous elliptic flow, which can be used to detect the magnetic field in such collisions. It points to a very interesting possibility of generating a quadrupolar magnetic field configuration which can have focusing effect on plasma in the longitudinal direction (along with a possibility of charge separation in the transverse direction.) These possibilities are under investigation at present and will be presented in a future work.

Bibliography

[1] Arpan Das, Shreyansh S. Dave, P.S. Saumia, and Ajit M. Srivastava, Phys. Rev. C. **96**, 034902 (2017), arXiv: 1703.08162.

[2] D. Kharzeev, R.D. Pisarski, and M.H.G. Tytgat, *Phys. Rev. Lett.* **81**, 512 (1998); S.A. Voloshin, *Phys. Rev. C* **70**, 057901 (2004).

[3] D.E. Kharzeev, L.D. McLerran, and H.J. Warringa, *Nucl. Phys. A* **803** 227 (2008).

[4] R. K. Mohapatra, P. S. Saumia, and A. M. Srivastava, Mod. Phys. Lett. **A 26**, 2477 (2011).

[5] P. Romatschke and U. Romatschke, Phys. Rev. Lett. **99**, 172301 (2007).

[6] K. Tuchin, J.Phys. G39, 025010 (2012).

[7] G. Inghirami et al. arXiv: 1609.03042; Eur. Phys. J. **C 76**, 659 (2016).

[8] M. Asakawa, A. Majumder, and B. Muller, *Phys. Rev. C* **81**, 064912 (2010).

[9] K. Tuchin, Phys.Rev. **C 83**, 017901 (2011); *Phys. Rev. C* **82**, 034904 (2010).

[10] L. Landau and E. Lifshitz, *Electrodynamics of Continuous Media* (Pergamon Press, N.Y., USA, 1984), Sect. 58.

[11] J.D. Jackson, *Classical Electrodynamics*, 3rd Edition (John Wiley & Sons, Inc., USA, 1999).

[12] H.-T. Ding et al. arXiv:1012.4963, Phys. Rev. **D 83**, 034504 (2011).

[13] K. Tuchin, Phys. Rev. **C 88**, 024911 (2013).

[14] P.V. Buividovich, et al., *Phys. Rev. Lett.* **105**, 132001 (2010).

[15] A. Mignone and G. Bodo, Mon. Not. R. Astron. Soc. **368**, 1040 (2006).

[16] M.L. Miller, K. Reygers, S.J. Sanders, and P. Steinberg, Ann. Rev. Nucl. Part. Sci. **57**, 205 (2007); P.F. Kolb, J. Sollfrank, and U. W. Heinz, Phys.Rev. **C 62**, 054909 (2000).

[17] J.P. (Hans) Goedbloed, R. Keppens, and S. Poedts, *Advanced Magnetohydrodynamics* (Cambridge University Press, UK, 2010).

[18] J.-Y. Ollitrault, *Eur. J. Phys.* **29**, 275 (2008); R. S. Bhalerao, J. P. Blaizot, N. Borghini, and J.-Y. Ollitrault, *Phys. Lett. B* **627**, 49 (2005).

[19] L.G. Pang, G. Endrodi, and H. Petersen, Phys. Rev. **C 93**, 044919 (2016).

[20] S. Pu and D.L. Yang, Phys. Rev. **D 93**, 054042 (2016).

[21] A. P. Mishra, R. K. Mohapatra, P. S. Saumia, and A. M. Srivastava, Phys. Rev. **C 77**, 064902 (2008); Phys. Rev. **C 81**, 034903 (2010).

[22] P. Sorensen, J.Phys. G 37 (2010) 094011; B. Alver and G. Roland, Phys. Rev. C 81 (2010) 054905; A. Mocsy and P. Sorensen, Nucl. Phys. **A 855** (2011) 241; J.I. Kapusta, Nucl. Phys. A 862-863 (2011) 47; J.Y. Ollitrault, J. Phys. Conf. Ser. 312 (2011) 012002; P. Sorensen, arXiv:0808.0503.

[23] J. Adams, U.H. Danielsson, D. Grasso, and H. Rubinstein, *Phys. Lett. B* **388**, 253 (1996).

[24] A. Das, S.S. Dave, S. De, and A.M. Srivastava, Mod. Phys. Lett. A **32**, 1750170 (2017), arXiv: 1607.00480.

[25] P.K. Aluri and P. Jain, Mon. Not. Roy. Soc. **419**, 3378 (2012).

[26] O.D. Kellogg, *Foundations of Potential Theory*, (Springer-Verlag, 1967).

Chapter 11

Summary

In this thesis, by introducing the concept of topological spaces and topological defects we have discussed how topological defects can form during a SSB phase transitions. The mechanism by which these defects form is known as the Kibble mechanism which predicts the equal formation probabilities of defects and anti-defects. However, in this thesis, we have discussed that there are some situations where one requires some modification in the Kibble mechanism which can account for biasing in the formation of topological objects over anti-objects and vice versa. We have considered the case of superfluid transition in the presence of rotation and ask what will be the vortex and anti-vortex formation probabilities in such a situation. In this work, we have proposed a modification in the conventional Kibble mechanism for the situation of production of topological defects when physical situation requires excess of winding of one sign over the opposite ones. We have considered the case of formation of vortices for superfluid ^4He system when the transition is carried out in a rotating vessel. As our results show, this biased formation of defects can strongly affect the estimates of net defect density. Also, these studies may be crucial in discussing the predictions relating to defect-anti-defect correlations. The modified Kibble mechanism we presented in this thesis has very specific predictions about net defect number which shows a clear pattern of larger fluctuations (about mean value governed by the net rotation) compared to the conventional Kibble prediction. This can be easily tested in experiments. Further, even the average net defect number deviates from the number obtained from energetics considerations, especially for low values of Ω. This implies that exactly at the time of transition, a different net defect number will be formed on the average, which will slowly evolve to a value obtained from energetics considerations.

After above discussion, we have introduced the theory of strong interaction known as Quantum Chromodyanmics (QCD). By introducing QCD and its symmetry properties we have discussed QCD at finite temperature and discussed its phase transitions. We show the Lattice QCD results and discuss the possibility of quark-gluon plasma phase. We also discuss other high baryon density superfluid phases of QCD. These are color-flavor locked phase and neutron superfluid phase. We also have discussed that topological vortices may be possible in these superfluid phases.

By discussing the formalism of ideal hydrodynamics and magneto-hydrodynamics, we finally introduce the physics of heavy-ion collisions. We introduce a very important hydrodynamic quantity known as the elliptic flow, which is one of the probes of the equilibrated medium formation in heavy-ion collision experiments. We also discuss the effect of magnetic field on the elliptic flow in heavy-ion collisions.

We then consider the possibility of superfluid phases of QCD in low energy heavy-ion collision and discuss that appearance of these phases leads to formation of superfluid vortices via Kibble mechanism which generate local circulation in the fluid and affect its hydrodynamic evolution. Then we have discussed that to account for the linear momentum conservation, when superfluid vortices form, normal components also start rotating about the vortex in the opposite direction, this leads to the generation of a strong elliptic flow. Using hydrodynamic simulations, we show that vortices can qualitatively affect the power spectrum of flow fluctuations. Even if the plasma region in the transverse plane is isotropic, a strong elliptic flow can be generated due to the formation of superfluid vortices. We also see that in the presence of pair of vortices, the power spectrum of flow can show differences in the power of even and odd flow coefficients. In the case of non-central collisions we can have negative value of elliptic flow, arising due to specific configuration of vortex/pair of vortices. All this can give unambiguous signal for superfluid transition resulting in vortices, allowing for check of defect formation theories in a relativistic quantum field theory system, and the detection of superfluid phases of QCD. Detection of nucleonic superfluid vortices in low energy heavy-ion collisions will give opportunity for laboratory controlled study of their properties, providing crucial inputs for the physics of pulsars. We also study the possibility of formation of neutron superfluidity in the low energy heavy-ion collisions. We see that there is a good possibility to have neutron superfluidity in this sufficiently low energy collisions of neutron rich nuclei. For this, we have performed the UrQMD simulations. Our result shows that in the case of Uranium-Uranium collisions (by ignoring deformation of nuclei) at 50 MeV, the condition reached in the central cell (center of the system) is very close to the normal to superfluid transition point (though detail investigations are required). The detection of these in laboratory experiments will strengthen our understanding of pulsar dynamics. The signals we have discussed show qualitatively new features in flow anisotropies signaling the presence of vortices and the underlying superfluid phase in the evolving plasma. These qualitative features are expected to be almost model independent, solely arising from the vortex velocity fields.

In the next part of our work, we have performed magneto-hydrodynamic simulations for relativistic heavy-ion collisions and have studies the effects of magnetic field on the flow fluctuations. We have calculated the magnetic field at the thermalization time and assumed that it gets trapped in the fluid due to medium conductivity. In this work, we carry out relativistic magnetohydrodynamics (RMHD) simulations to study the effects of this magnetic field on the evolution of the plasma using ideal RMHD equations and study resulting flow fluctuations. We have demonstrated qualitatively new effects on the flow pattern of QGP in the presence of initial magnetic field. These qualitative patterns may be able to provide clear signal for the presence of strong magnetic field during early stages of the evolution, though actual value of magnetic field etc. will depend on more reliable numerical estimates of the numbers. Our results show that magnetic field leads to enhancement in elliptic flow for small impact parameters while it suppresses the elliptic flow for large impact parameters (which may provide a signal for initial stage magnetic field). This result on the enhancement of elliptic flow in the presence of magnetic field confirms earlier expectation in Refs. [1, 2]. At the same time our simulation also points out that the effects of magnetic field on elliptic flow are much more complex than envisaged in simple arguments of Ref. [1], as in some situations one finds decrease in the elliptic flow. This may resolve the discrepancy between the results of Refs. [1, 2] and Ref. [3] (see, also Refs. [4, 5]). The strong suppression of elliptic flow for large impact parameters can provide a signal for strong magnetic field at initial stages. Interestingly, we find that magnetic field in localized regions can temporarily increase in time as evolving plasma energy density fluctuations lead to reorganization of magnetic flux. This can have important effects on chiral magnetic effect. Magnetic field has non-trivial effects on the power spectrum of flow fluctuations. For very strong magnetic field case one sees a pattern of even-odd difference in the power spectrum of flow coefficients arising from reflection symmetry about the magnetic field direction if initial state fluctuations are not dominant. We discuss the situation of nontrivial magnetic field configurations arising from collision of deformed nuclei and show that it can lead to anomalous elliptic flow. Special (crossed body-body) configurations of deformed nuclei collision can lead to presence of quadrupolar magnetic field which can have very important effects on the rapidity dependence of transverse expansion.

We have performed RMHD simulations for the case of deformed nucleus-nucleus collisions for the case of Uranium nuclei. We have generated the initial energy density by Glauber model, and magnetic field profile appropriate for Uranium-Uranium collisions. We have performed the RMHD simulations for the body-body collisions. Due to deformation of the nuclei, even in the zero impact parameter case there is spatial anisotropy in the plasma such that the semi-major axis of the ellipse lies along the x-axis therefore we get negative elliptic flow; in this case there is no magnetic field present. When we increase the impact parameter by a small amount, magnetic field gets generated along the y-axis (semi-minor axis of the plasma), due to this, overall magnitude of the elliptic flow gets suppressed. When we increase the impact parameter further, at a particular impact parameter, plasma region becomes isotropic in the transverse plane. For such case, ideal hydrodynamics gives zero value of the elliptic flow while due to presence of the magnetic field we get non zero elliptic flow showing that magnetic field itself can generate momentum anisotropy in the plasma. When we increase impact parameter further, the situation becomes similar as in the case of the spherical nuclei collisions and we first get enhancement and then suppression in the elliptic flow with increasing impact parameter.

Bibliography

[1] R. K. Mohapatra, P. S. Saumia, and A. M. Srivastava, Mod. Phys. Lett. A **26**, 2477 (2011).

[2] K. Tuchin, J. Phys. G **39**, 025010 (2012).

[3] G. Inghirami et al. arXiv: 1609.03042; Eur. Phys. J. C **76**, 659 (2016).

[4] L.G. Pang, G. Endrodi, and H. Petersen, Phys. Rev. C **93**, 044919 (2016).

[5] S. Pu and D.L. Yang, Phys. Rev. D **93**, 054042 (2016).